Water Oxidation Catalysis Using First Row Transition Metals

PRIMAVERA PELOSIN

UNIVERSITAT ROVIRA i VIRGILI

Water Oxidation Catalysis Using First Row Transition Metals

PRIMAVERA PELOSIN

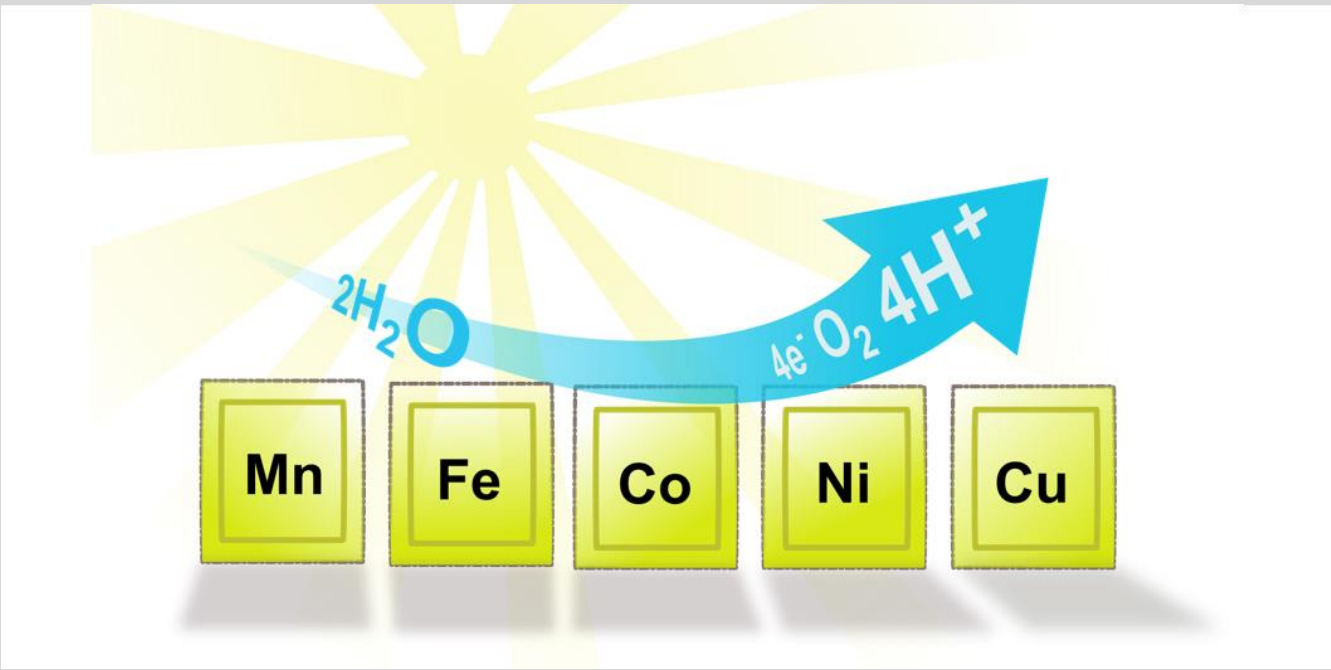

DOCTORAL THESIS
2020

UNIVERSITAT ROVIRA I VIRGILI
Water Oxidation Catalysis Using First Row Transition Metals
PRIMAVERA PELOSIN

Primavera Pelosin

Water Oxidation Catalysis Using First Row Transition Metals

DOCTORAL THESIS

Supervised by

Prof. Antoni Llobet

Institute of Chemical Research of Catalonia
Tarragona
2020

ICIQ - Institut Català d'Investigació Química
Avgda, Països Catalans 16,
43007 Tarragona (Spain)

I STATE that the present study, entitled "Water Oxidation Catalysis Using First Row Transition Metals" presented by Primavera Pelosin for the award of the degree of Doctor, has been carried out under my supervision in my group at the Institute of Chemical Research of Catalonia.

Tarragona, October 29th, 2020

Thesis Supervisor

Prof. Antoni Llobet

Acknowledgements

The work performed in this doctoral thesis has been possible thanks to the Institute of Chemical Research of Catalonia (ICIQ), the funding of: MINECO, FEDER and AGAUR (CTQ2016-80058-R,CTQ2015-73028-EXP, SEV 2013-0319, ENE2016-82025-REDT, CTQ2016-81923-REDC, 2017- SGR-1631) and the PhD grant from MINECO (Ref. BES-2017-080072).

List of Publications

(1) “Analysis of the Active Species Responsible for Water Oxidation Using a Pentanuclear Fe Complex” Pelosin, P.; Gil-Sepulcre, M.; Garrido-Barros, P.; Moonshiram, D.; Benet-Buchholz, J.; Gimbert-Surñiach, C.; Llobet, A. *iScience*, 2020, *23*, 101378.

(2) “Redox Metal–Ligand Cooperativity Enables Robust and Efficient Water Oxidation Catalysis at Neutral pH with Macrocyclic Copper Complexes” Garrido-Barros, P.; Moonshiram, D.; Gil-Sepulcre, M.; Pelosin, P.; Gimbert-Suriñach, C.; Benet-Buchholz, J.; Llobet, A. *J. Am. Chem. Soc.* 2020 142 (41), 17434-17446.

Abstracts

Chapter 1. General Introduction

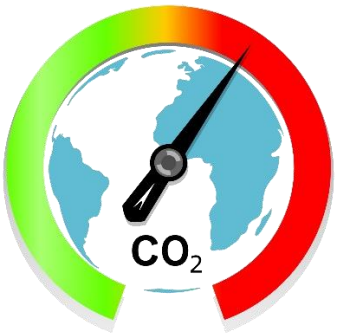

This chapter deals with the general description of the background and the remaining challenges in the field of molecular water oxidation catalysis (molecular WOC). Firstly, the solar fuels, produced through artificial photosynthesis, as the possible green alternative to the currently extensively used fossil fuels are described. The bottleneck in the development of the artificial photosynthetic technology is the oxidation of water, whose principles are introduced along with the development of molecular WOCs, which were of fundamental importance for the understanding of the water oxidation mechanism. Finally, the heterogenization of molecular WOCs on electrode surface for the generation of molecular anodes, which can be practically introduced in the photochemical cell are described.

Chapter 2. Objectives

Chapter 3. Redox Metal–Ligand Cooperativity Enables Robust and Efficient Water Oxidation Catalysis at Neutral pH with Macrocyclic Copper Complexes

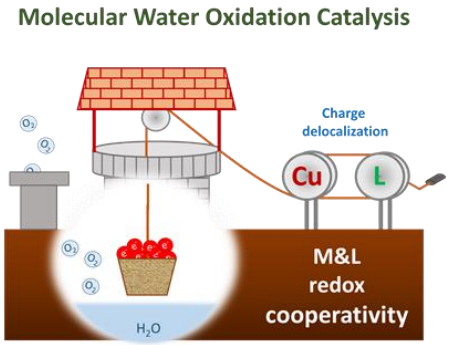

Chapter 3 shows the importance of the rational design of the ligand in the development of molecular WOCs based on first row transition metals. One Cu-based complex with a π delocalized tetraamido macrocycle ligand (TAML) was studied as a WOC and compared with other similar systems featuring a lower delocalization. The first complex showed a large activity and stability due to the metal-ligand cooperativity in the formation of the positive holes necessary to guest the electrons from water, which did not occur in the other two complexes, leading to lower performances or even decomposition. Further, the macrocycle effect could be appreciated when the catalyst, bearing a macrocycle as ligand, proved to be stable at neutral pH while an acyclic complex was decomposing.

Chapter 4. Polymeric Cu-based Molecular Anodes: Application in Water Oxidation Catalysis

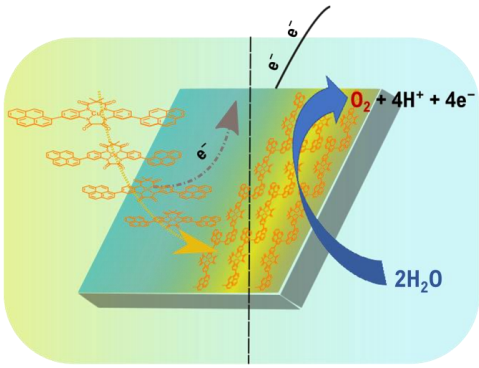

Chapter 4 describes the generation of molecular anodes based on first row transition metal WOCs. A reported rugged Cu-based molecular WOC was modified introducing two pyrenes in the ligand backbone, leading to the formation of two regioisomeric complexes, which were anchored on ITO electrodes through polymerization of the pyrene moieties. The new materials were tested toward water oxidation at pH between 7.5 and 10.

Chapter 5. Analysis of the Active Species Responsible for Water Oxidation Using a Pentanuclear Fe Complex

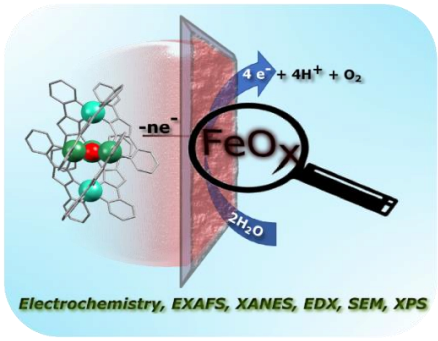

Chapter 5 is the revisited study of a pentanuclear iron complex claimed to work as molecular water oxidation catalyst. A deep analysis of the system after catalysis through techniques such as electrochemistry, UV-Vis, EDX, SEM, XPS and XAS, confirmed hematite as the real catalyst. This report with a detailed described methodology, can be considered as a user manual for researchers working with molecular non-noble metal based WOCs.

Chapter 6. General Conclusions

Contents

Chapter 1

General Introduction

This chapter deals with the general description of the background and the remaining challenges in the field of molecular water oxidation catalysis (molecular WOC). Firstly, the solar fuels, produced through artificial photosynthesis, as the possible green alternative to the currently extensively used fossil fuels are described. The bottleneck in the development of the artificial photosynthetic technology is the oxidation of water, whose principles are introduced along with the development of molecular WOCs, which were of fundamental importance for the understanding of the water oxidation mechanism. Finally, the heterogenization of molecular WOCs on electrode surface for the generation of molecular anodes, which can be practically introduced in the photochemical cell are described.

1.1 The energetic problem

Fossil fuels, have been used as a primary source of energy for centuries and even today constitute over 80% of the world energy supply.[1] Figure 1 shows a comparison between the composition of world total primary energy supply (TPES) in 1971 and 2018. In these 47 years the TPES increased by 2.5 times and it is going to escalate exponentially because of the fast demographic growth. As can be seen from the graph the most used sources of energy are still coal (25%), oil (35%) and natural gas (25%).

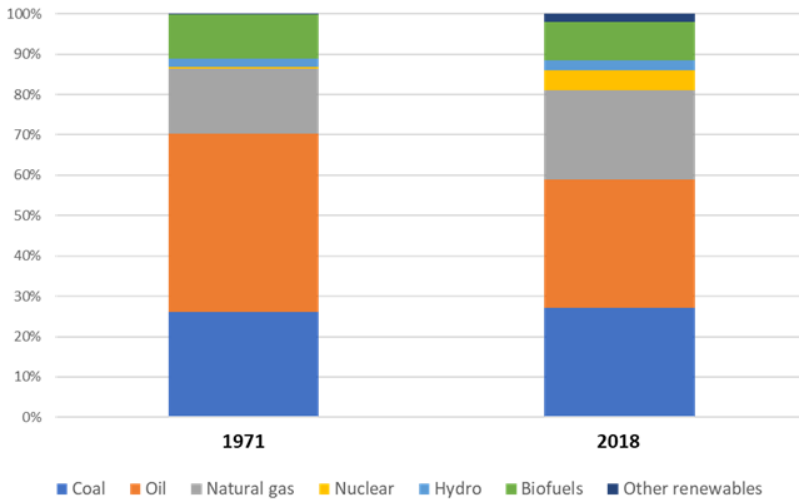

Figure 1. World total primary energy supply (TPES) in 1971 (left) and 2020 (right)[1]

However, the extensive use of these energy supplies is associated with a number of harmful consequences:

- Fossil fuels are not renewable. Their formation took millions of years, but their depletion is continuously accelerating due to the steady increase in energy demand.[2]
- Oil, coal and natural gas are not homogeneously distributed throughout the planet, which promotes international tensions and conflicts.
- Their use causes the continuous increase in CO_2 emission (Figure 2).[3]

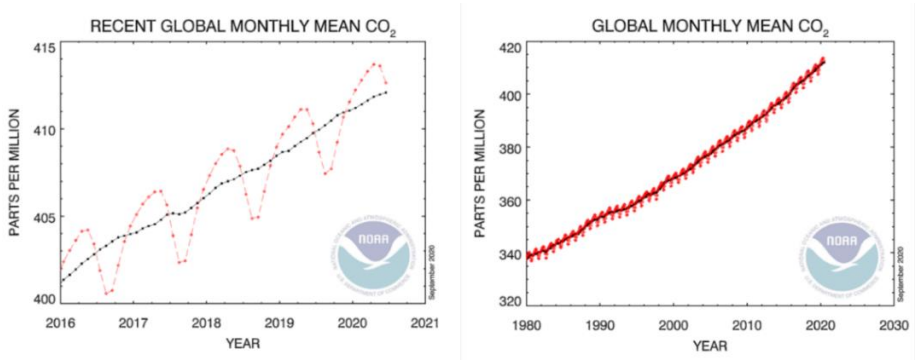

Figure 2. Monthly mean carbon dioxide emission globally averaged over marine surface sites. Last 4 years (left), last 40 years (right).[3]

This last consequence, the emission of carbon dioxide together with other greenhouse gasses is responsible for accelerating the increase in global average temperature. Since the beginning of the industrial revolution, in the 18th century, until today, the average temperature has increased by 1 °C. [4]. Even if the number looks small the actual consequences are dramatic, such as melting glaciers, diminishing snow cover, shrinking sea ice, rising sea levels, ocean acidification, and increasing atmospheric water vapor.[5]

A first international attempt to decrease the carbon dioxide emissions was the Kyoto Protocol in 1997 when 191 states and the European Union promised to reduce their annual hydrocarbon emissions for a global average of 5.2 % by 2012 and participated to the carbon credit trading. Considering that developing counties as China and India were exempted from the agreement and USA dropped out of the protocol in 2001, and that USA and China are the two biggest emitters, the prefixed aim of lowering the global emission by the 2012 failed.[6] In 2015, the Paris Climate Agreement was signed by 195 nations, with the goal of limiting the earth's temperature increase to 2 °C above the preindustrial level. In this case USA was again involved and a new framework was created to help to control and report the emissions of developing countries.[7]

The recent pandemic due to COVID-SARS-19, forced most of the countries to undergo a period of severe lockdown, with a consequent decrease in the transportation and industrial activity. The total emission of CO_2 by big developing countries like China, which is still extensively using coal as an energy

source, lowered drastically, causing a decrease in the greenhouse effect and in air-pollution.[8]

Since the idea of closing the entire industrial and transport sectors is not feasible, and neither is forcing an entire society to change drastically and abruptly its habits and its economical scheme, it is necessary to find out new sources of energy, i.e., renewables, with a low or zero carbon emission.

Several alternatives to fossil fuels have been implemented in recent years, such as wind, hydro and sun energy.[1] These energy sources respond to the parameters of renewables and carbon free, however they present important drawbacks that hinder their development. The first one is the necessity of storing the produced energy, an important point moreover when the energetic source has an ever changing nature like wind and sun. On the other hand, several fuels could be obtained by the biomass, es ethanol, methanol and formic acid but the cost of the crop and the large cultivation needed hindered the further development of this field.[9]

The most promising alternative to fossil fuels are the solar fuels, which can trap the energy given by the sun in different useful chemical as reduced products form CO_2, ammonia or hydrogen, through a process known as artificial photosynthesis, which is directly inspired nature.[10–12]

1.2 Natural photosynthesis

Photosynthesis is a process used by green plants and cyanobacteria to store the energy of sunlight in form of sugar and starches from carbon dioxide and water. The process is divided in two parts. The first one requires light and proceeds within Photosystem II (PSII) and Photosystem I (PSI) cofactor-protein complexes embedded in the thylakoid membrane. In PSII, the water is oxidized to molecular O_2, concomitantly producing reducing equivalents, which are directed to PSI[13,14] and used to form NADPH from $NADP^+$.[15] The second process occurs in the dark and utilizes the NAPDH from PSI for fixation of molecular CO_2.

The overall transformation happening in PSII and PSI can be visualized as a Z-scheme (Figure 3)[16], characteristic of a system containing two photocatalytic sites, in this case one for oxidation of water and the other for reduction of $NADP^+$.

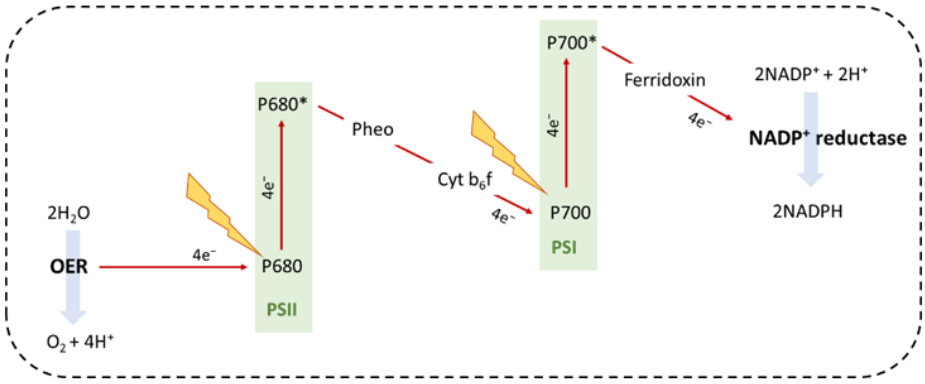

Figure 3. General representation of the Z-scheme in the natural photosynthesis.

First, the light excites the P680 chromophore in PSII. One electron is transferred form P680* to a pheophytin (Pheo) electron acceptor[13,14] initiating a chain of electron and proton transfer reactions ending in the PSI. This chain allows charge separation and avoids recombination between the oxidation and reduction products[17]. In PSI, the reduced P700 chromophore is excited by light to P700*[18] and one electron is passed to ferredoxin (Fd) bonding $NADP^+$ reductase, which is then responsible for formation of NADPH.[15]

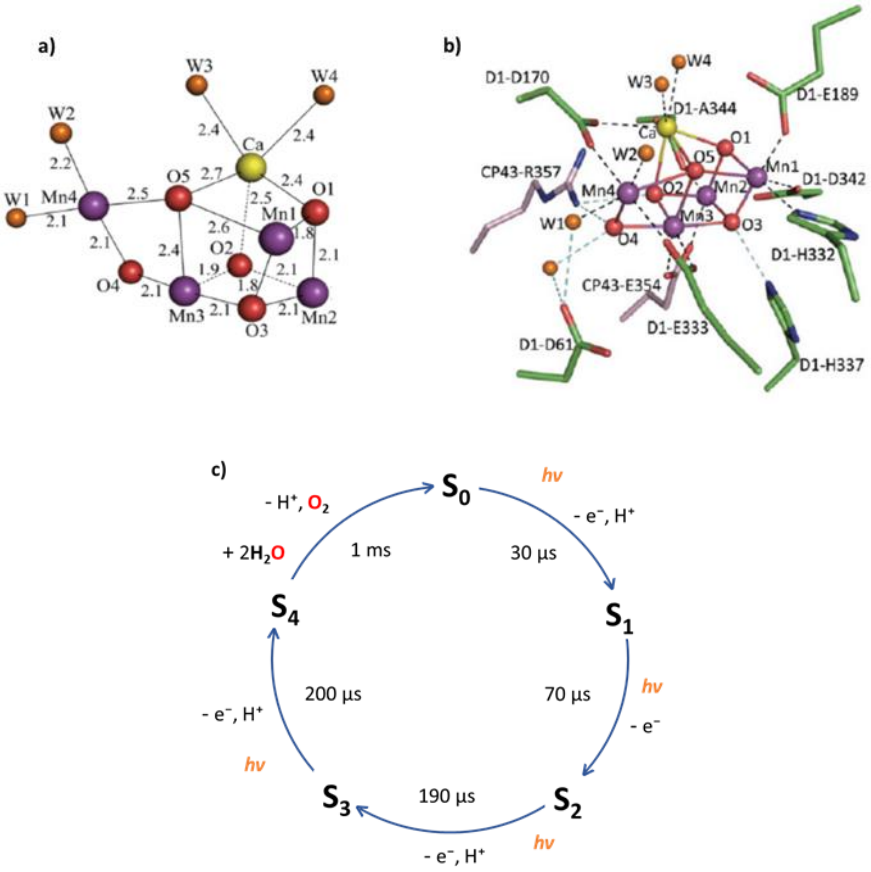

Figure 4. X-Ray structure (resolution of 1.9 Å) of the OEC without (a) and with the surrounding amino acids (b)[19]. Kok cycle (c).

The excited chromophore P680* is a strong oxidant, with a *E*° of 1.21 V vs NHE[20] and is able to carry the four consecutive one-electron oxidation reactions of OEC (oxygen evolving center), a manganese tetranuclear cluster with formula $CaMn_4O_5$.[19]

The OEC can efficiently mediate the kinetically unfavoured reaction of water oxidation and makes this process possible on the millisecond timescale[21] with a TOF of 50–400 s^{-1}.[22–24]

The catalytic cycle, named Kok cycle, is described in Figure 4c. The OEC cluster abstracts four electrons and four protons from two molecules of water. A tyrosine residue serves as an electron-transfer mediator from OEC to the P680*, and aspartates residues containing carboxylate functionalities assist the transfer

of protons. The surrounding amino acids have, in addition, the role of stabilizing the OEC at the various oxidation states.[25]

The entire reaction relies on the sequence of processes, namely light harvesting, charge separation, electron transfer, oxidation of water and utilization of the reducing equivalents for reduction of $NADP^+$.

The same principles can be used to build an artificial system, where water is the source of electrons and protons necessary for the production of molecular H_2 or reduction of CO_2 into high energy fuels.

1.3 Artificial photosynthesis

As summarized in the previous subsection, the main components of artificial photosynthetic cells are similar to the ones of the natural photosynthetic machinery:

- A light harvesting system, able to collect the energy of the sunlight.
- Catalysts, decreasing the kinetic barrier of oxidation and reduction reactions.
- A membrane, capable of dividing the products of the oxidation and reduction reactions but at the same time permeable to protons to equilibrate the pH.

These components can then be combined within one of three main architectures, which vary in simplicity of production, cost, and efficiency.

- PV-electrolyzer; a mature and commercially available technology, where a photovoltaic cell is coupled with an electrolyzer.[26]
- Mixed colloidal; this kind of cell is in theory the less complex and the cheapest, avoiding the presence of the membrane and embedding the light absorber and the two catalysts in the same compartment. This architecture is the least developed.[27]
- PEC (photoelectrochemical cell); in this case the light absorbing system is integrated in the electrodes, but the two compartments for oxidation and reduction reactions are still separated by a membrane.
  This cell is the intermediate between the feasibility of the PV-electrolyzer and the simplicity of the mixed colloidal setup. Besides the efforts in its development the costs for the PEC setup is still too high for its commercialization.[28]

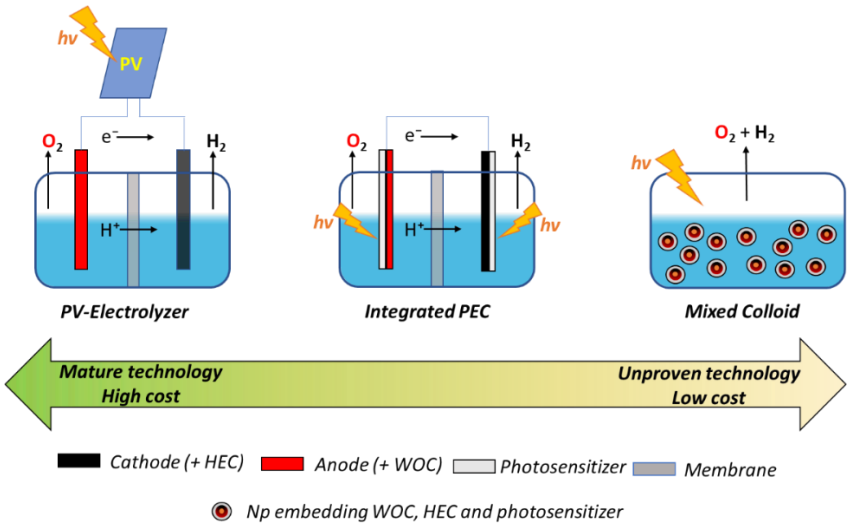

Figure 5. Schematic representation of the three current designs of artificial photosynthetic systems for hydrogen evolution.

The photosynthetic fuel cells can provide different products, depending on what kind of substrate will be reduced. From CO_2 can be formed useful carbon-based molecule as CO, HCHO, HCO_2H, $H_2C_2O_4$, CH_3OH, CH_4 (eq. 2, showing only the reduction to formaldehyde, for simplicity), from N_2 ammonia (eq. 3) or from protons hydrogen (eq. 4).In all cases, the parallel oxidation half reaction employs water as the substrate and a source of protons and electrons (eq. 1).

$$2H_2O \rightarrow O_2 + 4e^- + 4H^+ \qquad \text{eq. 1}$$

$$4e^- + 4H^+ + CO_2 \rightarrow HCHO + H_2O \qquad \text{eq. 2}$$

$$4e^- + 4H^+ + 2/3N_2 \rightarrow 4/3NH_3 \qquad \text{eq. 3}$$

$$4e^- + 4H^+ \rightarrow 2H_2 \qquad \text{eq. 4}$$

1.4 Water Oxidation Catalysts (WOCs)

The water oxidation half reaction (eq. 1) is the bottleneck in the water splitting process. The removal of 4 protons and 4 electrons from two molecules of water is thermodynamically demanding, with a standard redox potential of E° = 1.23 V at pH 0. This oxidation process occurs through a complex multistep mechanism which includes breaking of multiple OH bonds and formation of a new O–O bond, meaning a high kinetic barrier, which is manifested as overpotential. The overpotential could be defined as the extra amount of energy which should be supplied to the system to overcome this kinetic barrier. In order to decrease this extra–energy and to work at potential closer to the thermodynamic one, several water oxidation catalysts were developed during the last and this century. [29]

A good example of a WOC is the natural OEC present in the Photosystem II as described in Section 1.2. The tetranuclear cluster Mn_4O_5Ca[30,31] displays an overpotential of only 70 mV and the TOF between 50 and 400 s^{-1} [22,23], which are outstanding features. The only drawback is its instability. The cluster has to be repaired every 15-30 minutes, because of an irreversible photoinhibition.[32]

The first example of artificial WOC was a Ni-oxide reported in 1902 by Gläser and Coehn.[33] Since then, WOCs based on metal oxides experienced a fast development due to their robustness and ease of synthesis.[34,35] The lack of standard conditions for the evaluation of their activity, which is also influenced by the morphology and synthesis, is still a problem to overcome. Jaramillo and co-workers, tried to solve this issue reporting a methodology based on the evaluation of the metal oxide WOCs activity through a standard electrochemical technique, making possible a more reliable comparison.[36,37]

The first molecular complex to be tested as WOC was a Ruthenium dinuclear complex, called “the blue dimer” reported by Meyer in 1982,[38] opening the field of the molecular water oxidation catalysts. Transition metal complexes bearing organic ligands attract the interest of many research groups because of the possibility to modify the organic framework to tune the complex properties, and therefore, the catalytic performance.[39] Furthermore, molecular WOCs are considered an ideal platform for understanding the complicated mechanisms behind water oxidation, since a large number of analytical techniques are available for their study in solution.

Finally, the possibility to anchor molecular WOCs on the electrodes surface gives anodes which can be successively applied in the fuel cell. [40–44]

Thinking of its possible application in a photochemical cell for production of solar fuels a WOC should satisfy certain requirements.[28]

- Working at mild pH values.
  The water oxidation process is usually favoured in alkaline media, although those conditions in parallel with the high anodic potential enhance the corrosion of the other components of the cell. It is, thus important to find catalysts able to work at milder conditions.
- Being based on non-rare inexpensive and non-toxic metals.
  An important factor in the development of a commercially feasible WOC is its cost. For this reason, lately, the efforts of several research groups were focused on the 1st row transition metal based WOCs.

1.5 Molecular WOCs

1.5.1 Evaluation of catalytic activity of molecular WOCs

The comparison of the catalytic activity of molecular WOCs is difficult since there are no standard methods for the catalyst activation, oxygen quantification and estimation of the activity. Broadly it is possible to divide the methods used for the catalyst study as chemical or electrochemical.

The activity toward oxygen evolution of WOCs can be tested chemically using a sacrificial electron acceptor (SEA) to activate the catalyst. Several chemical oxidants are known in literature, each of them with different driving force and working pH range.[45] Examples are cerium nitrate or CAN ($(NH_4)_2[Ce^{IV}(NO_3)_6]$, $E°'$ of 1.75 V at pH 1); ruthenium(III) tris(bipyridine) ($[Ru^{III}(bpy)_3]^{3+}$, $E°'$ = 1.21 V at pH < 4); Oxone® (active component $KHSO_5$, $E°'$ = 1.82 – 0.059·pH V at pH < 5.5) and sodium periodate ($NaIO_4$, $E°'$ = 1.6 – 0.059·V at pH between 2 and 7).
Photo induced water oxidation is possible using the photosensitizer $[Ru^{II}(bpy)_3]^{2+}$ which under excitation of visible light (λ_{max} = 450 nm), forms a highly reductive species, which loses an electron taken by a sacrificial electron acceptor, typically sodium peroxodisulfite ($Na_2S_2O_8$) to generate the oxidant $[Ru^{III}(bpy)_3]^{3+}$.

The evaluation of the oxygen produced can be done though gas chromatography (GC), manometry, fluorescent probe, clarck electrode and indirectly though the bleaching of the Ce^{IV} oxidant by UV-vis absorption.
Chemical water oxidation should be considered a preliminary indication of the suitability of the molecule as WOC, since the use of an oxidant is not mimicking the real application in a photosynthetic cell.

Electrochemical tests are closer to the real application conditions of the water splitting device. In this case an electrode set at positive potential is the oxidative agent which activates the catalyst.
The oxygen evolution can be monitored with similar methods used for the chemical oxidation, to these can be added the rotating ring disk electrode (RRDE).
The activity can be calculated from the cyclic voltammetry (CV) of the system with different mathematical methodologies, it is thus important to consider this factor when comparing two catalysts studied electrochemically.
Traditionally, the used method was the one introduced by Shain,[46] which presents the drawback of evaluating the activity at the limiting catalytic current under pure kinetic conditions, which cannot be reached for the electrocatalytic water oxidation due to several side processes, such as electrode passivation and catalyst degradation.
In 2012, Savéant and co-workers elaborated the Foot Of the Wave Analysis (FOWA) [47] this methodology was then adapted by Llobet group in 2015 to evaluate kinetic of molecular based water oxidation.[48,49]
The advantage of FOWA is the possibility of analysing the WOC's activity taking in consideration the foot of the catalytic wave in the cyclic voltammogram (CV) of the catalyst, where side-phenomena as catalyst degradation or electrode consumption are not occurring. In order to properly use FOWA the system should satisfy some parameters as the Nernstian nature of all the electron transfer, the irreversibility of the involved chemical steps and the O-O bond formation as rate determining step. The number of catalysts whose activity can be valued by FOWA is thus limited.

1.5.2 Molecular water oxidation: Mechanist discoveries through Ru-based WOCs

The extensive studies on Ru-based WOCs evidenced two fundamental features, in the mechanism of water oxidation: the proton coupled electron transfer (PCET) and the mechanism of O-O bond formation.

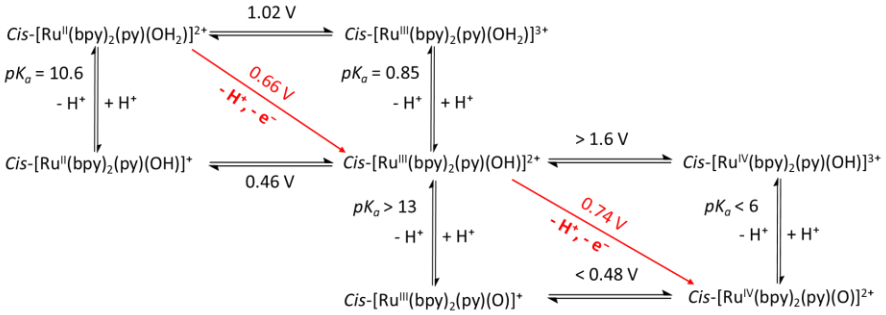

Scheme 1. Diagram for the Ru(IV/III) and Ru(III/II) redox couples of *cis*-$[Ru^{II}(bpy)_2(py)(OH_2)]^{2+}$ showing PT (proton transfer), ET (electron transfer) and PCET (proton coupled electron transfer) pathways, the last (in red) is the most energetic favourable.[50]

Meyer's group was the first to observe and study the PCET, defined as the simultaneous release of a proton and an electron.[51] The PCET decreases the energy of the catalyst oxidation avoiding the formation of unstable intermediates since the formal charge of the molecule is maintained equal during the process. In addition, the transfer of a proton from a water ligand enhances the coordinative character of the oxygen, stabilizing the whole molecule.[50,52]

The main mechanisms observed for the O-O bond formation are two: water nucleophilic attack (WNA) and inter molecular coupling (I2M).

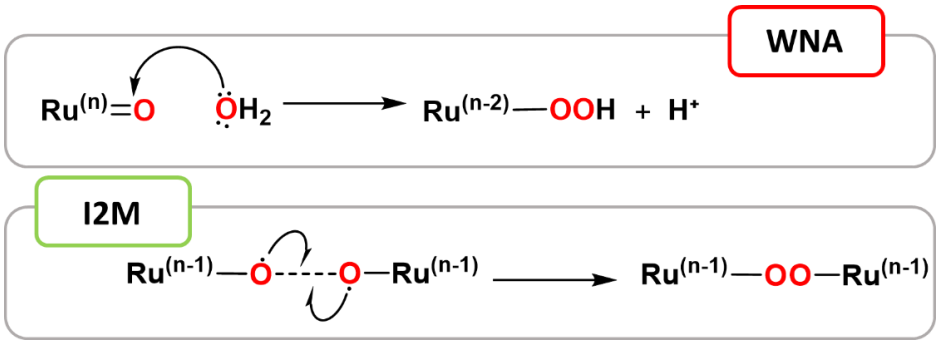

Scheme 2. Schematic representation of the two common mechanisms for the O-O bond formation through Ru-based water oxidation catalysts.

In the WNA an external water molecule attacks the partially positively charged oxygen on the high valent Ru-oxo species (Ru=O), to form a metal hydroperoxo Ru-O-O-H.
The O-O bond formation is the rate limiting step for the majority of the WOCs working through this mechanism. However, its kinetic can be enhanced when a proton is extracted from the nucleophilic water during the O-O bond formation. This can be accelerated by a base present in solution or through a pendant base present in the ligand scaffold.[53]

The I2M mechanism is observed more rarely than the previously described WNA. In this case a Ru^{IV}=O intermediate with a strong radicaloid character, which can be described as Ru^{IV}-$O^{\bullet}$, reacts with a second equal species to form a dinuclear transition state responsible for the O-O bond formation. [54,55]
The more energetic demanding event in the I2M mechanism is not the O-O formation itself but the geometrical reorganization of the dinuclear intermediate.[56] The preorganization given by a ligand scaffold which can covalently bound the two radical could decrease the overall energy of the process.[57] This strategy was not always successful, a too rigid framework as in the case of two $[Ru^{II}(bda)(pic)]^{2+}$ bounded together through a xanthene-derived axial ligand, could inhibit the catalysis.[58]
The bimolecular mechanism presents a drawback which affect the possible application of WOCs working though this pathway. In the hybrid photoanodes the molecular WOCs are forced in a fixed position which restrict their mobility.

The catalysts have, thus, to operate through a higher energetic mononuclear mechanism, which may lead to the decomposition of the complex to RuOx.[59]

1.5.3 Molecular WOCs based on Ruthenium

cis,cis-[[Ru(bpy)$_2$(H$_2$O)]$_2$(μ-O)]$^{4+}$ (**1**) or the so-called blue dimer, was the first molecular WOC studied, reported by Meyer and co-workers in 1982.[38] Even if its catalytic performances, TON = 13.2 and TOF = 0.0042 s^{-1}, at pH 1 using CAN as oxidant, are far from the real application, the blue dimer was a milestone in the WOCs history. The complete characterization, trough spectroscopic techniques, kinetic studies and DFT calculations shown, for the first time, the mechanism's features of the molecular water oxidation catalysis.[60–64]

The second example of dinuclear polypyridyl WOC was *cis,cis*-[[Ru(trpy)(H$_2$O)]$_2$(μ-bpp)]$^{3+}$ (**2**), reported by Llobet in 2004. The bpp$^-$ bridge (bis(2-pyridyl)-3,5-pyrazolate) provides a rigid scaffold, able to stabilize the complex which gives a TON of 512 and the TOF to 0.014 s^{-1}. In addition the ligand set the Ru centers in close proximity, allowing the O-O bond formation to proceed through a I2M intramolecular mechanism..[65]

In 2005, Thummel reported the first mononuclear Ru WOC [Ru^{II}(npm)(pic)$_2$(OH$_2$)]$^{2+}$ (npm is 4-t-butyl-2,6-di(1′,8′-naphthyrid-2′-yl)pyridine; pic is 4-picoline) (**3**). The activity of this new catalyst was tested chemically giving a TON of 260 and a TOF of 0.014 s^{-1} with CAN at pH 1[66] and photochemically (TON = 83, TOF = 0.12 s^{-1}, [Ru^{II}(bpy)$_3$]$^{2+}$/ $S_2O_8^{2-}$ at pH 7.0).[67] Until that moment the scientific community believed that the charge accumulation, necessary for the water oxidation process, could be held only by multinuclear complexes, as in the natural Mn cluster.

On the other side Meyer reported two mononuclear WOCs [Ru^{II}(tpy)(bpm)(OH$_2$)]$^{2+}$ (**4**) (TON of 8 and TOF of 0.02 s^{-1}, CAN pH 1) and [Ru^{II}(tpy)(bpz)(OH$_2$)]$^{2+}$. Even though the two complexes show a modest activity the mechanistic studies performed confirmed that mononuclear Ru complexes are active toward water oxidation.[68,69] Mononuclear complexes are easier to synthetize compared to dinuclear ones, so after the Thummel and Mayer reports the field of molecular WOCs expanded rapidly.
In 2009 Sun and Llobet reported a mononuclear Ru complex [Ru^{II}(bda)(pic)$_2$] (**5**) where bda is [2,2'-bipyridine]-6,6'-dicarboxylate,[70] which formed an unusual

seven coordinated Ru^{IV}-OH species under catalytic conditions. Mechanistic studies proved that this catalyst favours a bimolecular mechanism for water oxidation unlike the previous mononuclear Ru WOCs. Further modification of the apical ligand with molecules favouring the intermolecular interaction increased the WOC activity. Examples are $[Ru^{II}(bda)(isoquinoline)_2]$ (**6**) (TOF = 303 s^{-1}, CAN at pH 1).[71] and its derivatives $[Ru^{II}(bda)(6\text{-fluoroisoquinoline})_2]$ and $[Ru^{II}(bda)(6\ bromophtalazine)_2]$, with TON = 24 000 and 101 000, and TOF = 1 000 s^{-1} and 380 s^{-1} respectively using CAN at pH 1.[72]

In 2015 Llobet reported a seven coordinated Ru complex $[Ru^{IV}(OH)(tda\text{-}\kappa\text{-}N_3O)(py)_2]^+$, ($tda^{2-}$ is 2,2':6',2''-terpyridine-6,6''- dicarboxylate), this time working through a mononuclear pathway. The active species is formed through a controlled potential electrolysis (CPE) at pH 12 from the precursor $[Ru^{II}(tda)(py)_2]$ (**8**). The main advantage of this catalyst is the presence of a dangling carboxylate, providing an intramolecular base, which can easily remove a proton from water during the process of O-O bond formation. The activity was tested electrochemically giving a TOF_{max}, calculated through foot of the wave analysis (FOWA), of 8000 s^{-1}at pH 7.[48]

In 2017, Concepcion studied a modified Ru(bda) type of complex, substituting one[73] or both the carboxylic acid[74] with phosphonate groups. The complex $[(bpHc)Ru(L)_2]$ (bpH_2cH = 2,2'-bypiridine-6-phosphonic acid, L = 4-picoline or isoquinoline) was active as WOC with a TOF of 100 s^{-1} (CAN, at pH 1). The most important discovery in this work was the change in mechanism caused by the presence of the phosphonate group. The complexes studied by Concepcion are proven to follow a mononuclear pathway for the O-O bond formation, at the contrary of the previous reported R(bda) WOCs

The substitution of the carboxyl groups in the $[Ru^{II}(tda)(py)_2]^+$ with phosphonate gave the complex $[Ru^{II}(H_3tPa\text{-}\kappa\text{-}N^3O)(py)_2]^+$($H_3tPa$ = 2,2':6',2''-terpyridine-6,6''-diphosphonic acid) reported by LLobet in 2020.[75] $[Ru^{II}(H_3tPa\text{-}\kappa\text{-}N^3O)(py)_2]^+$ is the precursor for the active species $[Ru^{III}(tPaO\text{-}\kappa\text{-}N^2OPOC)(py)_2]^{2-}$ (tPaO = 3-(hydroxo- [2,2':6',2''-terpyridine]-6,6''-diyl)bis(phosphonate), obtained by further oxidation of the precursor at pH 7.7. The phenoxo-phosphonate Ru complex is generated by the intramolecular aromatic O insertion by an OH^- into the CH bond of one of the pyridyl groups. The structure of the WOC was

confirmed by X-ray and DFT studies. The activity was tested electrochemically at neutral pH to give a TOF of 16 000 s^{-1}, calculated by FOWA.

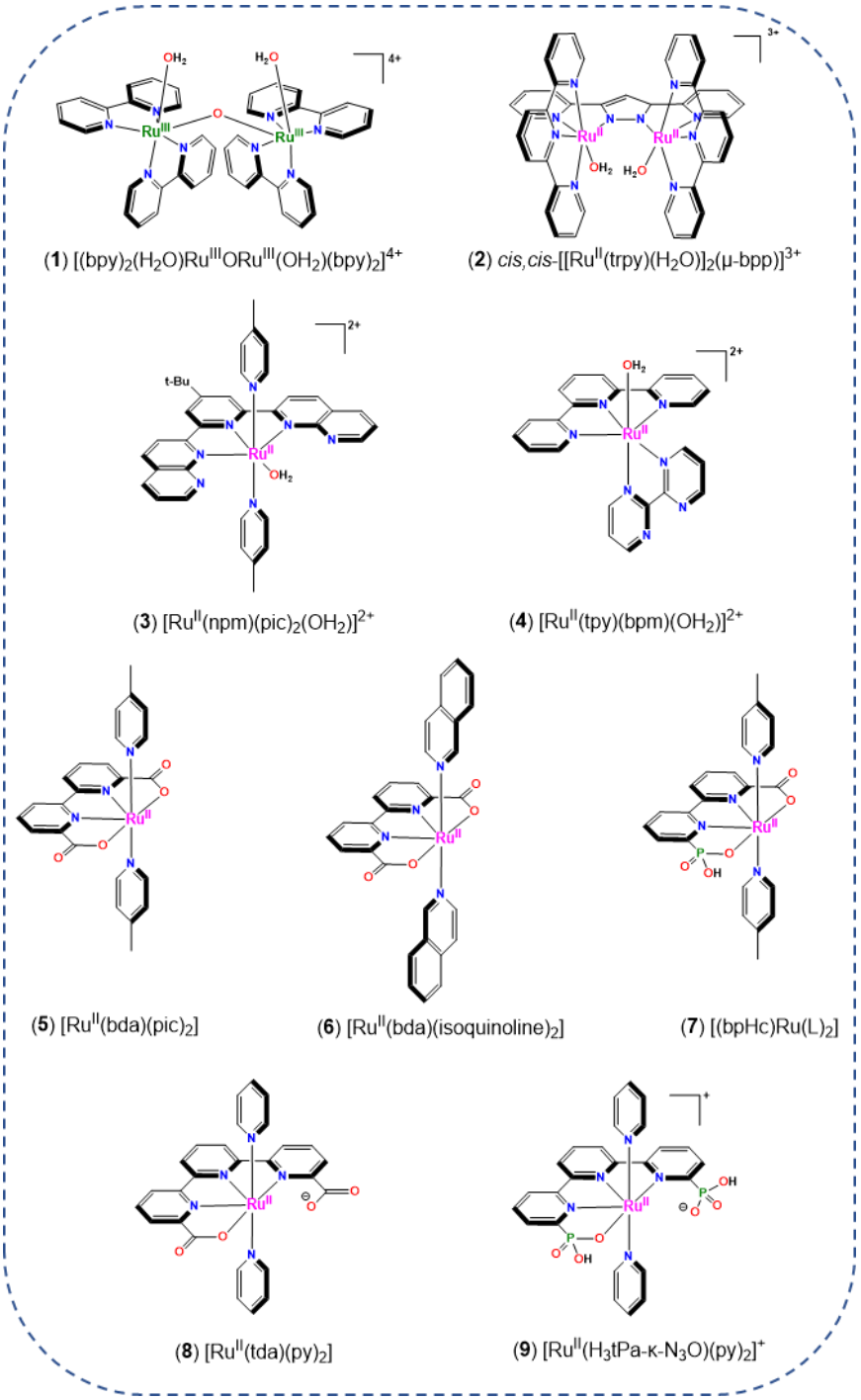

Chart 1. Structure of the cited Ru WOCs

1.6 Molecular WOCs based on 1st row transition metals

The 1st row transition metals WOCs are the cheaper alternative to 2nd or 3rd row metals. The difference in price is due to the abundancy of the element on the earth's crust, the extraction costs and the current human demand.

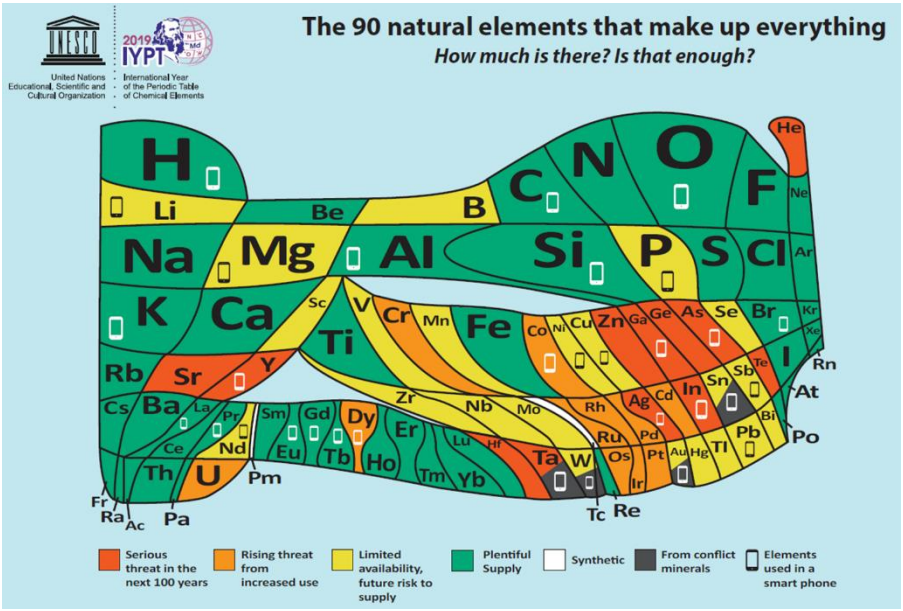

Figure 6. Periodic table adjusted for elements abundancy.[76]

Figure 6, shown above, is a new version by the European Chemical Society of the periodic table adjusted by the element abundance. It is stressed that, because of human activity, some elements, before relatively available, are going to be considered rare. It is thus important, also in the field of renewable energies to develop cheap systems, based on easily available materials. In the particular case of the water oxidation for the artificial photosynthesis, one of the aims is the generation of molecular WOCs based on first row abundant metals as Mn, Fe, Co, Ni and Cu.

The research on the field of non-noble metal molecular WOCs is expanding, even if the specific features of 1st row transition metals make their development challenging.

As well known, in early transition metals the ionization energy is higher than for the elements down the group, due to the decreased distance between the valence shell and the nucleus. In addition, the further the metal is located to the right of the period, the higher its atomic number will be, leading to a radius contraction and a more difficult oxidation. On the point of view of water oxidation, the potential which has to be applied on a WOC based on first row metals, in order to reach enough positive holes to guest the electrons derived from water, has to be quite elevated, often causing unwanted side effects as the ligand oxidation and degradation.

The electronic structure of most first row metal-based complexes, if representing an unstable configuration, make easy the ligand substitution with water, due also to the hard Lewis acid character of the metal, at the contrary of Ru complexes which are substitutionally inert.

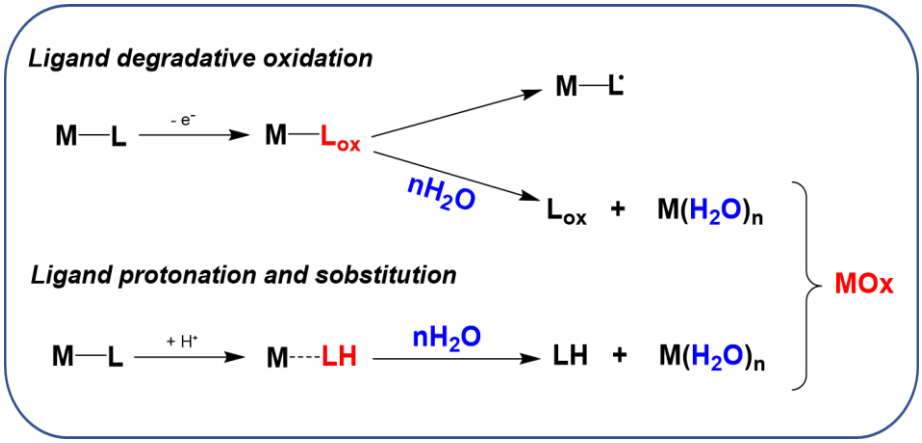

Scheme 3. Common deactivation pathways of 1st row transition metals WOCs.

The two phenomena of ligand oxidation or substitution, described above, can lead at the formation of metal oxides which could be able to perform the catalysis at the given conditions, giving misleading results. Deep analysis should thus be performed on the system after catalysis in order to avoid a wrong interpretation of the data, claiming a catalytic event as molecular when it is actually due to heterogeneous species.

On the other hand, to improve the stability of this molecular WOCs a rational design of the ligand has to be promoted. Several reported studies were often lacking a correlation between structure stability and activity of the complexes, but lately a better rationalization of the data permitted the developing of more rugged WOCs.

Below are presented some examples of molecular WOCs based on Manganese, Iron, Cobalt, Nickel and Copper.

Manganese Catalysts

Mn complexes were the first candidate as WOCs, being the natural OEC itself a Mn tetranuclear cluster.

The first molecular WOC based on Mn is a porphyrin dimer synthesized by Naruta and co. in 1994 (**10**).[77] The complex was proven to be active electrochemically in a solution of CH_3CN/H_2O containing nBu_4NOH, giving a TON value of 9.2. The monomer was inactive at the same conditions, enforcing the belief that only multinuclear systems could work as WOCs.

Crabtree Brudvig in 1999 reported a new dimer with a μ-oxo bridge connecting two molecules: $[H_2O(terpy)Mn(O)_2Mn(terpy)OH_2](NO_3)_3$ (terpy is 2,2':6,2' '-terpyridine) (**11**).[78] Tested chemically with NaClO as sacrificial acceptor, the molecule was proven to work as water oxidant with TON = 4 and TOF = 0.0033 s^{-1}, but its stability was poor. The μ-oxo bridge could easily break and MnO_4^- was identified as active species, through XAS analysis. Further, 25 % of the oxygen produced was proven to proceed form the NaClO.[79]

The stability of some Mn WOCs and the role of the oxidant were systematically studied by Styring.[80] The study proved that the most efficient oxidant was H_2O_2, followed by Oxone, TBHP and ClO^-. No O_2 evolution was detected with Ce^{IV} and $[Ru(bpy)_3]^{3+}$, until Åkermark in 2011 reported a dinuclear Mn complexes with imidazole, carboxylate and phenols groups working in water with $[Ru(bpy)_3]^{3+}$, being able to perform a photochemical catalysis.[81]

Mononuclear Mn complexes were also proven to work as water oxidants. In 2007 Sun introduced a mononuclear Mn WOC based on a corrole ligand (**12**). Its capacity to oxidize water was tested using tBuOOH and $(n\text{-}Bu)_4NOH$ electrochemically. O-O bond was formed by a molecule of water and one of base.[82]

Further examples were reported of mononuclear Mn complexes bearing an anionic ligand able to stabilize the high valent intermediate of water oxidation, Mn^{IV}/Mn^{V}=O as salen.[83] Despite some development, Mn-based molecular WOCs show in general modest activity and low stability.

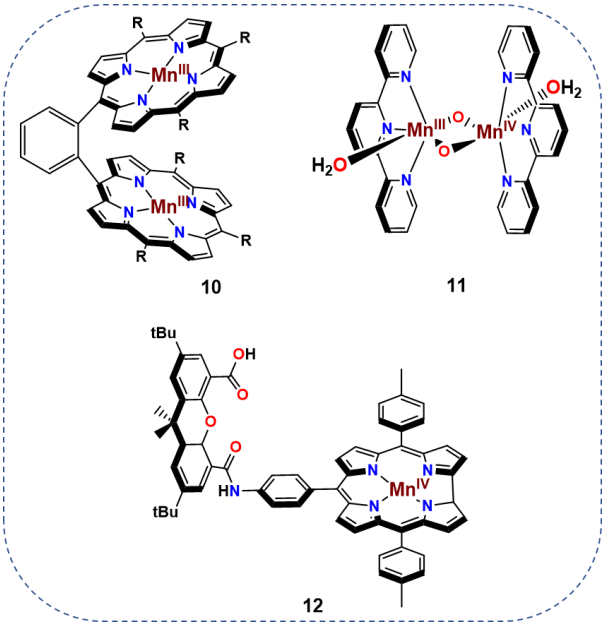

Chart 2. Structural representation of Mn-based WOCs **10**, **11**, **12**.

Iron Catalysts

Iron is one of the most abundant elements on the hearth's crust, it is not toxic and it is one of the metals most commonly used in the biological systems.
Further this atom can reach several oxidation and spin states, which can be modulated by the ligand environment.
Even if Fe could be considered a good candidate, there are few examples of molecular WOCs based on this metal.
The first attempt of Fe-based WOC was reported by Collins in 2010 with the so-called tetraamido macrocyclic ligands (TAML). This kind of ligands were already used with iron in the oxidation of organic dyes, and proved to be stable at high oxidative conditions. A family of Fe-TAML complexes were tested as WOCs with Ce^{IV}. The best results were obtained with the catalyst bearing the most electro-withdrawing ligand (**13**), reaching a TON of 16 and a TOF of 1.3 s^{-1}. The O-O bond

formation kinetic was proven to be 1st order respect to the catalyst, indicating a WNA pathway.

In 2011, Costas reported a family of Fe complexes based on commercially available tetra or penta coordinative polyamines, which were tested toward water oxidation as well, using Ce^{IV} as oxidant.[84] Two reports, introduced doubts on the stability of these molecules. Similar non-heme iron complexes were tested for photochemical water oxidation. DLS analysis of the solution after the catalysis indicated the presence of nanoparticles, whose composition was confirmed to be iron oxide by XPS.[85,86]

There are few reports of polynuclear iron WOCs. An example was given in 2016 with a pentanuclear iron complex **$[Fe_5]^{3+}$** (**14**), with bpp^- as bridging ligand. The cluster was tested as electrocatalyst for water oxidation in a mixture of 9:1 acetonitrile/water, giving a TOF of 1900 s^{-1}. Oxygen was detected at 1.42 V vs Fc/Fc^+.[87]

Two new clusters having the same structure of the first pentanuclear complex reported in 2016, but with the bpp^- ligand modified with a bromine (**[Fe_5-Br])** or a methylene (**[Fe_5-Me]**) group were described in 2019 to prove the influence of an electron-withdrawing or an electron-donor moiety on the catalytic activity.[88]

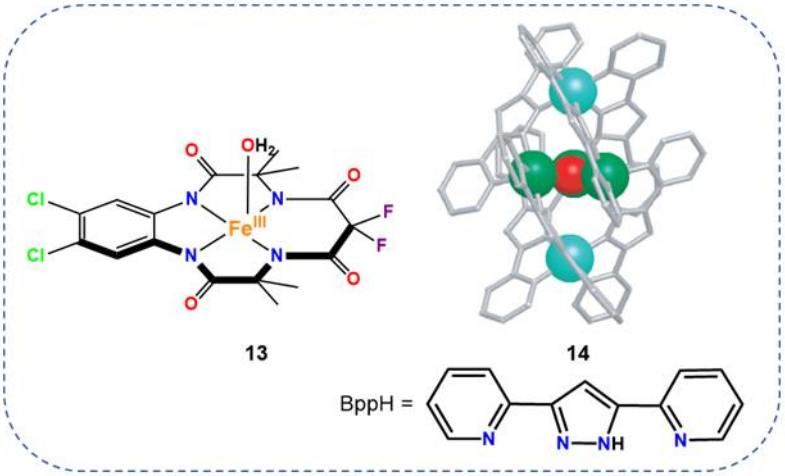

Chart 3. Structural representation of Fe-based WOCs **13**, **14**.[87]

Cobalt Catalysts

The production of water oxidation catalysts based on cobalt is mainly focused on the formation of heterogeneous catalysts, as cobalt oxides[89,90] or POMs (polyoxometallates).[91,92]

Until now, only a few examples of molecular mononuclears Co-WOCs were reported, with modest activity and stability.

One of the first studies was reported by Nocera who used hangman corroles to synthesize Co complexes with two vacant sites and a pendant base. A variant with fluoro substituents on the aryl ring (b-octafluoro complex) (**15**) was proven to drive water oxidation electrochemically.[93] The main focus of these corrole ligands was to stabilize the central metal oxidized to Co^{IV}, the species responsible for the catalysis. Recently, Gross reported a detailed study on a Co corrole, revealing the redox state participating or not to the catalysis and the beneficial in the activity of using a π-donating axial ligand.[94]

Further examples of mononuclear Co complexes bearing a porphyrine[95,96], polypiridil,[97,98] TAML[99] or salen[100] type ligands were tested as WOC, revealing modest activity. Doubts on the nature of the real active species were rising after several reports demonstrated the formation of active cobalt oxide.[101–104]

There are even less examples of dinuclear Co-WOCs. Llobet reported a bpp^- ligand based complex (**16**). The WOC was able to perform water oxidation with a modest activity at acidic pH.[105] Thapper's group tested electrochemically a dinuclear complex this time bearing the tpa ligand (tpa meaning tris(2 pyridylmethyl)amine) and a peroxo bridge. Further EDX, SEM, and XPS analysis performed on the working electrode confirmed the presence of cobalt oxide, which was considered the real active species. [96,106]

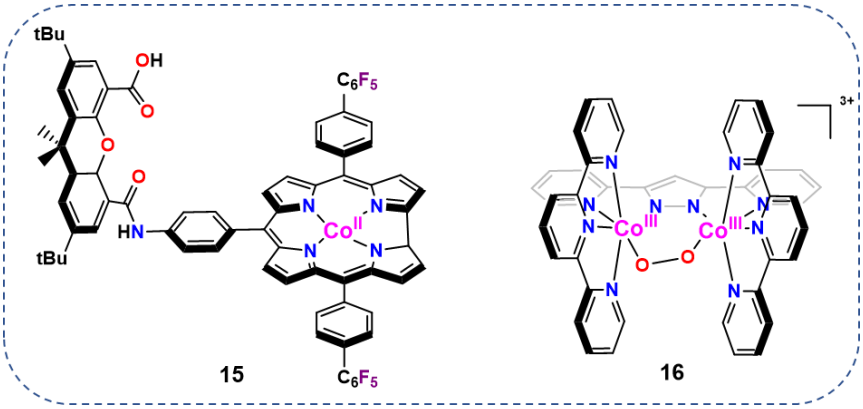

Chart 4. Structural representation of Co-based WOCs **15**, **16**.

Nickel Catalysts

Ni oxides are well known to be able to oxidize water, and several examples are reported.[107,108]

On the other hand the reported Ni-based molecular WOCs are still few, due to their high instability in water and the tendency to form NiO.

Ni porphyrins able to oxidize water at pH between 2 and 8, giving a TOF of 0.67 s^{-1} were reported by Cao in 2015 (**17**).[109] Mechanistic studies indicated the involvement of Ni^{V} in the catalysis.

Other Ni cyclam macrocycles were studied electrochemically, but the irreversibility of the Ni^{II}/Ni^{III} wave and the continuous increasing of the catalytic current over time casted doubts on the homogeneous character of the catalysis.[110–112]

The groups of Spiccia and Najafpour, through a deep analysis of the working electrode after the catalysis, confirmed the presence of active oxides.[113,114]

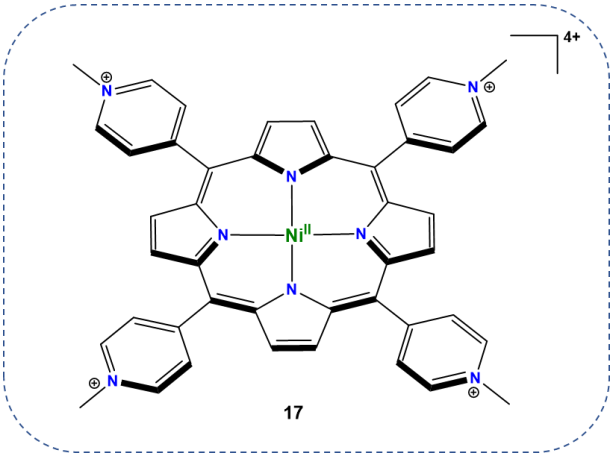

Chart 5. Structural representation of Ni-based WOC **17**.

Copper Catalysts

Copper, like iron, is a metal often used in natural enzymes as mediating oxidant in aerobic oxidation.

In contrast, only few examples of synthetic Cu-based WOCs are reported.

This can be explained by the low redox flexibility of this metal. The generation of the high oxidation states necessary to trigger the oxidation of water, can be

reached only at the cost of high energy. A solution can be the design of non-innocent ligands able to participate in the oxidation process while helping the stabilization of the oxidized metal center. This can be achieved using a ligand with a strong electron-donating character, as amines, deprotonated amides, carboxilate and alkoxides. The drawback in using this kind of functionalities is their tendency to protonate at neutral-low pH, weakening the coordination with the metal and enhancing the possibility of its leaking form the organic framework. It is thus necessary to find ligands able to stabilize the metal center, but at the same time, resistant to protonation. The examples reported below show the development in the copper-based WOCs, and the increasing importance given to the rational design of the ligand in order to build more rugged molecular water oxidation catalysts.

In 2012, Mayer reported the auto assembling complex $[Cu^{II}(bpy)(OH)_2]$ (**18**), able to perform water oxidation electrochemically at pHs between 12 and 13, with an overpotential of 750 mV and a TOF of 100 s^{-1}.[115] The high overpotential and the harsh working condition necessary for the catalyst activation were an obstacle for the further application of this WOC.

Lin modified the previous bpy ligand introducing with two hydroxides groups obtaining the 6,6-dihydroxy bipyridine ligand.[116] The Cu derivative complex (**19**) was proven to be active as water oxidation catalyst at pH between 12 and 14 with an overpotential of 640 mV, 110 mV lower than the first Cu-based WOC proposed by Mayer. This drastic change in the kinetic is due to the involvement of the ligand in the electron transfer leading to the water oxidation, as confirmed by DFT studies.

Meyer studied the activity of a Cu complex bearing a triglycyglycine ligand (**20**).[117] The ligand, bearing four negative charges, stabilizes the high oxidation state of the complex, which is able to oxidize water at pH 11 with an overpotential of 520 mV and a TOF 33 s^{-1}

In 2015, Llobet studied a series of tetraanionic tetradentate ligands N1,N1'-(1,2-phenylene)bis(N2-methyloxalamide), whose aryl moiety was modified with different substituents. The Cu complexes with the most electron-donating ligands were proved to trigger the catalysis at lower overpotential with respect to the ones with more electron-withdrawing organic scaffold (**21**). This study proved, again, the effect of the sigma donation on the stabilization of high oxidated complexes. The complex L1Cu was tested for oxygen evolution at pH

11.5 and 12.5. The TOF of the Cu WOC was calculated to be 3.6 s^{-1} (pH 11) and 12 s^{-1} (pH 12).according to FOWA.[118]

The catalytic cycle was proven by DFT calculations and a later report proposed a new mechanism for O-O bond formation, based on a SET-WNA step (single electron transfer-water nucleophilic attack) where the non-innocence of the ligand is proven. This mechanism fits well with the 1st row transition metal WOCs' reported behaviour, avoiding two simultaneous charge transfers on the metal center during the O-O bond formation, difficult for metals like copper.[119]

In 2017 the ligand N1,N1'-(1,2-phenylene)bis(N2-methyloxalamide) was modified with a pyrene at the aryl moiety. The derived complex (**22**) was tested in homogeneous phase, to give a TOF of 128 s^{-1} at an overpotential 150 mV lower than the unmodified WOC.

After heterogenization on graphene, the TOF increased of a value of 540 s^{-1} and the measured TON was 5300. These values indicate the influence of the π conjugation on the catalyst activity.[120]

In the same year Crabtree and Brudvig reported a $[(pyalk)_2Cu]$ (**23**) complex (pyalk is 2-pyridyl-2-propanoate). In this case the ligand was apparently not involved in the O-O bond formation, but stabilized the oxidated copper through its highly donating alkoxides. The catalysis occurs at pH 10, with an overpotential of 520-580 mV giving a of TOF 0.7 s^{-1} and a TON of 30.[121]

The WOCs described until now are all working at high pHs, which is considered a problem if the ideal device for generation of solar fuels should work at neutral pH. In 2015 a dimer bearing the ligand 2,7-[bis(2pyridylmethyl)aminomethyl]-1,8- naphthyridine (bpman) active at neutral pH was reported. Even if the stability and the calculated Faradaic Efficiency were good, the high overpotential hamper the possible real application of this WOC.[122]

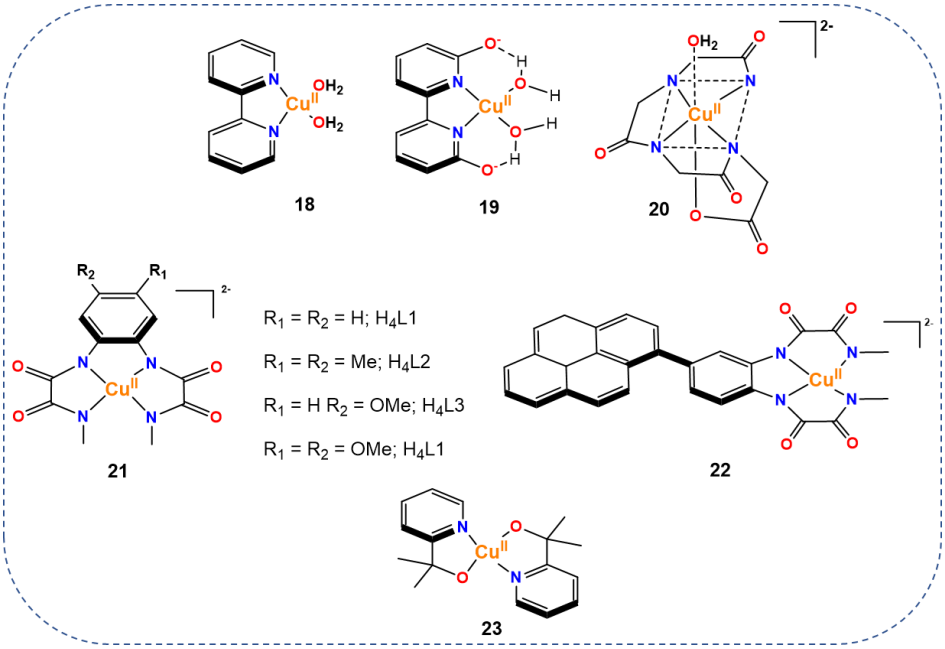

Chart 6. Structural representation of Cu-based WOCs **18**, **19**, **20**, **21**, **22**, **23**.

1.7 Molecular anodes

Photoanodes, embedding both catalyst and photosensitizer in close space, are fundamental in the development of the photochemical cell. There are different strategies for the anchoring of inorganic or organic photosensitizer and catalyst, this section will focus prevalently on the anchoring of molecular WOCs, and the formation of molecular anodes.

The formation of molecular anodes is given by the link between a conductive material and the molecular catalyst. The anchoring is provided by a functional group included in the WOC ligand, which, once attached to the electrode, has to provide a strong and conductive connection. The kind of linkages between the ligand and the support, are categorized between covalent and non-covalent and depend on the composition of the electrode. Below the main attaching strategies are described.

Anchoring on metal oxides:

The surface of metal oxides can be functionalized through covalent bonds formed between a carboxylic, phosphonic or sulfonic acid,[40,123,124] inserted in the ligand and the metal of the electrode's surface. The bond is proposed to form in a bidentate mode where two oxygens are covalently bridging two different metal centers.[125] The drawback of this method is the low stability of this bond at neutral-basic pH.[126,127] It was thus necessary to find new strategy as using hydroxamic acids or silatranes, which proved to connect stably with metal oxides also at relatively high pH values.[127–130]

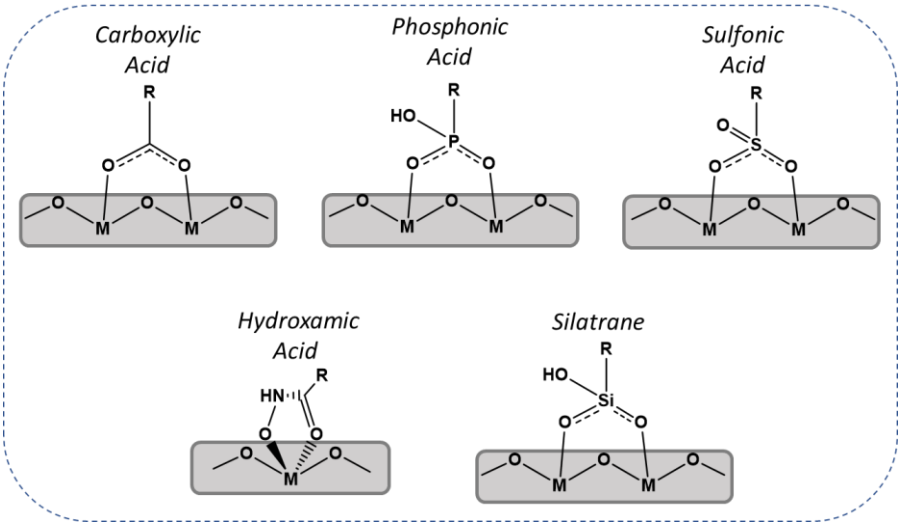

Scheme 4. Anchoring strategies on metal oxides.

Anchoring on carbon-based materials:

Carbon-based electrodes are often chosen for their low price and the good electronic conductivity. The typology of carbon-materials commercially available is also quite wide, from glassy carbon to a vast number of nanostructured materials as multi wall carbon nanotubes (MWCNT), graphene, etc. Some of the main strategies employed to anchor molecular WOCs on these surfaces are described below.[125]

- π-π stacking, which is based on physical non-covalent interactions between aromatic molecules. These interactions frequently occur through an offset arrangement, where the planes of the aromatic rings lay almost parallel one above the other, or a T-shaped arrangement, where the rings are perpendicular to each other.[131]
- Covalent bond through diazonium salts. Diazonium salts, at oxidative potentials in organic solvents, can generate an active radical, which forms a stable C-C bond with the electrode surface.
- Electropolymerization of N-substituted pyrroles or C-substituted thiophenes.

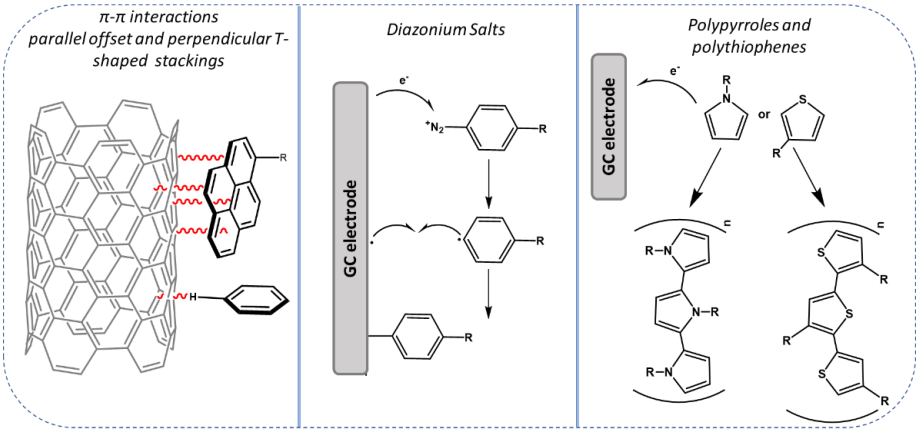

Scheme 5. Anchoring strategies on carbon-based materials.

For the anchoring of a molecular catalyst on an electrode surface some features should be taken in consideration:

- The superficial concentration of the catalyst (Γ, nmol/cm^2) which influences the current density. It is important to choose supports with a high surface area, such as MWCNT, TIO_2 nanoparticles and nano or meso-ITO.
- The mechanism is also a factor to take into consideration when choosing a catalyst to anchor on an electrode. The molecular WOCs working through I2M mechanism once attached on the electrode are forced to maintain a fixed position and thus are not able to approach a second the molecule necessary to start the catalysis. Two scenarios are possible; a change in mechanism, where the oxygen bond formation occurs through WNA, at a higher energy than the previous I2M, or the degradation of the molecule.
- The position of the linker should not create unfavourable interaction with the support, hampering the catalysis.

With all this information in mind, what follows are some examples of molecular anodes.

1.7.1 Examples of Molecular Anodes

First examples of Ruthenium catalysts anchored on metal oxide electrodes were given by the groups of Llobet and Meyer, which modified the ligand of active homogeneous catalysts with phosphonate,[137138] and carboxilate[40]acids. The chosen supports for the anchoring were TiO_2 nanoparticles, meso-ITO or FTO giving electrodes with a molecular loading (Γ) of 10, 0.5 and 0.1 nmol/cm^2 for the complexes **24**,[123] **25**[40] and **26,**[124] respectively. Complexes **25** and **26** showed an enhanced activity than in solution. At the contrary **24** was inactive once anchored on the TiO_2 nanoparticles. The two ruthenium centers were, in fact, blocked interacting with the oxo groups of the TiO_2.The anchoring group were the responsible for the complex orientation in respect to the electrode surface indicating the influence of the anchoring architecture in the retaining of the catalytic activity.[123]

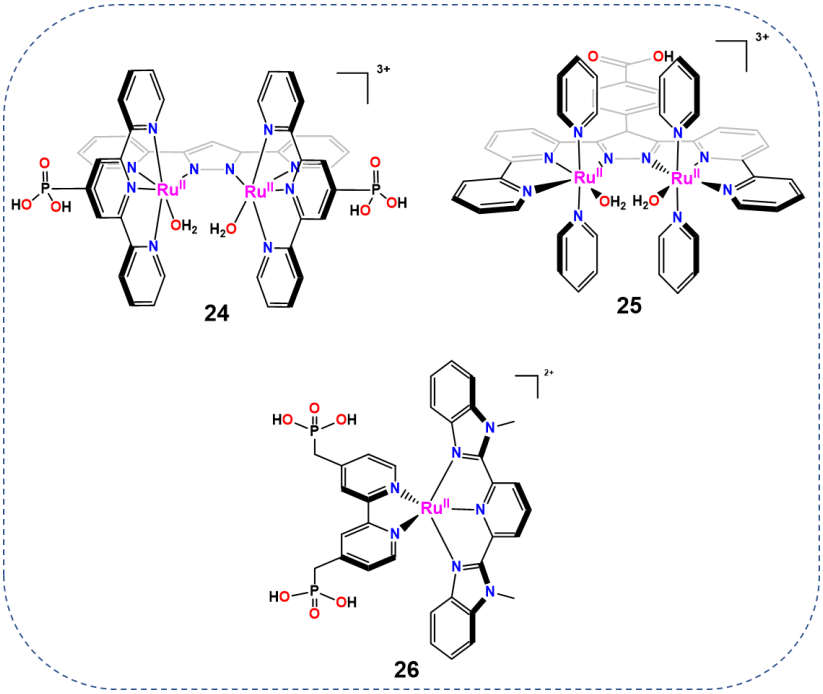

Chart 7. Structural representation of Ru-based WOCs **24**, **25**, **26**.

Sun was using MWCNT as support for a pyrene modified Ru(bda) (**27**), which was anchored on the carbon surface through non-covalent π-π stacking. The Ru(bda)

family is known to work through I2M mechanism, which explains the decreased TOF of the anchored molecule if compared with the one calculated for the species in solution (0.3 s^{-1} vs 30 s^{-1}).[41,71]

Llobet used the same strategy, anchoring though π-π stacking a pyrene modified Ru(tda) (**28**), known to work through WNA mechanism and obtaining a molecular anode giving a million TONs at pH 7 through a CPE at 1.45 V vs NHE.[132]

A further modification of Ru(tda) with a bridging ligand led to the formation of oligomers, which were anchored on MWCNT. This time the anchoring was obtained through a CH-π (T-shaped) interaction, which allowed a larger surface coverage than the one typically obtained through parallel offset arrangement. This electro anode works at neutral pH giving high values of current density.[133]

Examples of the last two anchoring strategies were given by the Sun's group, which used the diazonium salts to build a stable C-C bond between a Ru WOC and a GC electrode, maintaining the activity of the catalyst.[42]

On the other hand Llobet modified the terpyridine moieties of a dinuclear complex with pyrroles, which were electropolymerized on vitreous carbon sponge and FTO electrodes.[43]

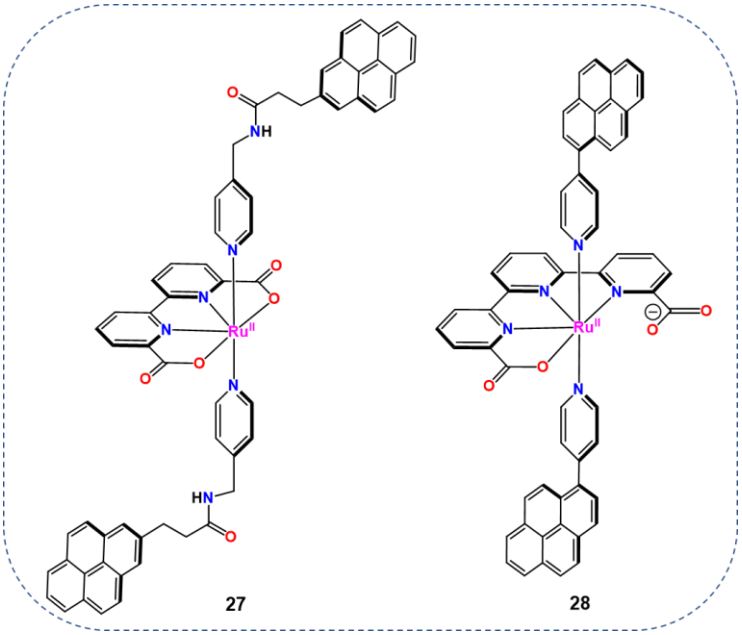

Chart 8. Structural representation of Ru-based WOCs **29**, **30**.

1.8 References

(1) IEA. https://www.iea.org/reports/world-energy-balances (accessed Oct 3, 2020).

(2) Greene, D. L.; Hopson, J. L.; Li, J. *Energy Policy* **2006**, *34*, 515–531.

(3) Dlugokencky, E.; Tans, P. No Title www.esrl.noaa.gov/gmd/ccgg/trends/ (accessed Oct 3, 2020).

(4) Morice, C. P.; Kennedy, J. J.; Rayner, N. A.; Jones, P. D. *J. Geophys. Res.* **2012**, *117*, 1–22.

(5) Climate Science Special Report: Fourth National Climate Assessment, Volume I; Wuebbles, D.J., Fahey, D.W., Hibbard, K.A., Dokken, D.J., Stewart, B.C., Maycock, T.K., Eds.; U.S. Global Change Research Program: Washington, DC, 2017. Washington DC.

(6) Kyoto Protocol to the United Nations Framework Convention On Climate Change, United Nations Framework Convention on Climate Change (UNFCCC), 1998. .

(7) Adoption of the Paris Agreement. Proposal by the President, Paris Climate Change Conference – November 2015, COP 21, Paris, France, 2015. .

(8) Quéré, C. Le; Jackson, R. B.; Jones, M. W.; Smith, A. J. P.; Abernethy, S.; Andrew, R. M.; De-gol, A. J.; Willis, D. R.; Shan, Y.; Canadell, J. G.; Friedlingstein, P.; Creutzig, F.; Peters, G. P. *Nat. Clim. Chang.* **2020**, *10*, 647–654.

(9) Luo, X.; Wang, J.; Dooner, M.; Clarke, J. *Appl. Energy* **2015**, *137*, 511–536.

(10) Lewis, N. S.; Nocera, D. G. *Proc. Nat. Acad. Sci.* **2006**, *103*, 15729–15735.

(11) Lewis, N. S. *Science (80-.).* **2016**, *351*, 353−361.

(12) Gust, D.; Moore, T. A.; Moore, A. L. *Acc. Chem. Res.* **2009**, *42*, 1890–1898.

(13) Kern, J.; Renger, G. *Photosynth Res* **2007**, *94*, 183–202.

(14) Renger, G.; Renger, T. *Photosynth Res* **2008**, *98*, 53–80.

(15) Yang, H.; Liu, J.; Wen, X.; Lu, C. *Biochim. Biophys. Acta* **2015**, *1847*, 838–848.

(16) Barber, J. *Chem. Soc. Rev.* **2009**, *38*, 185–196.

(17) Velthuys, B. R. *Annu. Rev. Plant Physiol* **1980**, *31*, 545–567.

(18) Bukhov, N.; Carpentier, R. *Photosynth Res* **2004**, *82*, 17–33.

(19) Umena, Y.; Kawakami, K.; Shen, J.; Kamiya, N. *Nature* **2011**, *473*, 55–60.

(20) Kato, Y.; Sugiura, M.; Oda, A.; Watanabe, T. *Proc. Natl. Acad. Sci.* **2009**, *106*, 17365–17370.

(21) Reus, M.; Nowaczyk, M.; Sander, J.; Ro, M. *Proc. Natl. Acad. Sci* **2006**, *103*, 6895–6900.

(22) Askerka, M.; Brudvig, G. W.; Batista, V. S. *Acc. Chem. Res.* **2017**, *50*, 41–48.

(23) Mcevoy, J. P.; Brudvig, G. W. *Chem. Rev.* **2006**, *106*, 4455–4483.

(24) McEvoy, J. P.; Brudvig, G. W. *Chem. Rev.* **2006**, *106*, 4455–4483.

(25) Yano, J.; Yachandra, V.; Division, P. B.; Berkeley, L. *Chem* **2014**, *114*, 4175–205.

(26) Schüttauf, J.-W.; Modestino, M.A.; Chinello, E.; Lambelet, D.; Delno, A.; Dominé, D.; Faes, A.; Despeisse, M.; Bailat, J.; Psaltis, D.; Moser, C.; Ballif, C. J. *Electrochem. Soc.* **2016**, *163*, F1177–F1181.

(27) Fabian, D. M.; Hu, S.; Singh, N.; Houle, F. A.; Hisatomi, T.; Domen, K.; Osterloh, F. E.; Ardo, S. *Energy Environ. Sci.* **2015**, *8*, 2825–2850.

(28) Mckone, J. R.; Lewis, N. S.; Gray, H. B. *Chem. Mat.* **2014**, *26*, 407–414.

(29) Berardi, S.; Drouet, S.; Francàs, L.; Gimbert-Suriñach, C.; Guttentag, M.; Richmond, C.; Stoll, T.; Llobet, A. *Chem. Soc. Rev.* **2014**, *43*, 7501–7519.

(30) Suga, M.; Akita, F.; Hirata, K.; Ueno, G.; Murakami, H.; Nakajima, Y.; Shimizu, T.; Yamashita, K.; Yamamoto, M.; Ago, H.; Shen, J. *Nature* **2015**, *517*, 99-103.

(31) Glo, C.; Kern, J.; Broser, M.; Zouni, A.; Yachandra, V.; Yano, J. *J. Biol. Chem.* **2013**, *288*, 22607–22620.

(32) Zavafer, A.; Koinuma, W.; Chow, W. S.; Cheah, M. H.; Mino, H. *Sci. Rep.* **2017**, *7*, 7604.

(33) Coehn, A.; Gläser, M. *Zeits. Anorg. Chem.* **1902**, *33*, 9–24.

(34) Matsumoto, Y.; Sato, E. *Mater. Chem. Phys.* **1986**, *14*, 397–426.

(35) Fujishima, A.; Honda, K. *Nature* **1972**, *238*, 37–38.

(36) McCrory, C. C. L.; Jung, S.; Ferrer, I. M.; Chatman, S. M.; Peters, J. C.; Jaramillo, T. F. *J. Am. Chem. Soc.* **2015**, *137*, 4347–4357.

(37) McCrory, C. C. L.; Jung, S.; Peters, J. C.; Jaramillo, T. F. *J. Am. Chem. Soc.* **2013**, *135*, 16977–16987.

(38) Gersten, S. W.; Samuels, G. J.; Meyer, T. J. *J. Am. Chem. Soc.* **1982**, *104*, 4029–4030.

(39) Zeng, Q.; Lewis, F. W.; Harwood, L. M.; Hartl, F. *Coord. Chem. Rev.* **2015**, *304–305*, 88–101.

(40) Odrobina, J.; Scholz, J.; Pannwitz, A.; Franca, L.; Dechert, S.; Llobet, A.; Jooss, C.; Meyer, F. *ACS Catal.* **2017**, *7*, 2116–2125.

(41) Li, F.; Zhang, B.; Li, X.; Jiang, Y.; Chen, L.; Li, Y.; Sun, L. *Andgewante Chem.* **2011**, *123*, 12484–12487.

(42) Tong, L.; Göthelid, M.; Sun, L. *Chem. Commun.* **2012**, *48*, 10025–10027.

(43) Mola, J.; Mas-marza, E.; Sala, X.; Romero, I.; Viæas, C.; Parella, T.; Llobet, A. *Angew. Chemie - Int. Ed.* **2008**, *47*, 5830–5832.

(44) Creus, J.; Matheu, R.; Peñafiel, I.; Moonshiram, D.; Blondeau, P.; Benet-Buchholz, J.; García-Antón, J.; Sala, X.; Godard, C.; Llobet, A. *Angew. Chemie* **2016**, *128*, 15608–15612.

(45) Parent, A. R.; Crabtree, R. H.; Brudvig, G. W.; Parent, A. R. *Chem. Soc. Rev.* **2013**, *42*, 2247–2252.

(46) Nicholson, R. S.; Shain, I. *Anal. Chem.* **1964**, *36*, 706–723.

(47) Costentin, C.; Savéant, J. *ChemElectroChem* **2014**, *1*, 1226–1236.

(48) Matheu, R.; Ertem, M. Z.; Benet-buchholz, J.; Coronado, E.; Batista, V. S.; Sala, X.; Llobet, A. *J. Am. Chem. Soc.* **2015**, *137*, 10786–10795.

(49) Matheu, R.; Neudeck, S.; Meyer, F.; Sala, X.; Llobet, A. *ChemSusChem* **2016**, *9*, 3361–3369.

(50) Weinberg, D. R.; Gagliardi, C. J.; Hull, J. F.; Murphy, C. F.; Kent, C. A.; Westlake, B. C.; Paul, A.; Ess, D. H.; Granville, D.; Meyer, T. J. *Chem. Rev.* **2012**, *112*, 4016–4093.

(51) Moyer, B. A.; Meyer, T. J. *J. Am. Chem. Soc.* **1978**, *100*, 3601–3603.

(52) Nagle, J. K.; Bernstein, J. S.; Young, R. C.; Meyer, T. J. *Inorg. Chem. 1981* **1981**, *20*, 1760–1764.

(53) Boyer, J. L.; Polyansky, D. E.; Szalda, D. J.; Zong, R.; Thummel, R. P.; Fujita, E. *Angew. Chem.* **2011**, *50*, 12600–12604.

(54) Moonshiram, D.; Alperovich, I.; Concepcion, J. J.; Meyer, T. J.; Pushkar, Y. *Proc. Natl. Acad. Sci.* **2013**, *110*, 3765–3770.

(55) Richmond, C. J.; Matheu, R.; Poater, A.; Falivene, L.; Benet-buchholz, J.; Sala, X.; Cavallo, L.; Llobet, A. *Chem. Eur. J.* **2014**, *20*, 17282–17286.

(56) Fan, T.; Zhan, S.; Ahlquist, S. G. *ACS Catal.* **2016**, *6*, 8308–8312.

(57) Jiang, Y.; Li, F.; Zhang, B.; Li, X.; Wang, X.; Huang, F.; Sun, L. *Angew. Chem.* **2013**, *52*, 3482–3485.

(58) Liu, Z.; Gao, Y.; Zhang, M.; Liu, J. *Inorg. Chem. Commun.* **2015**, *55*, 56–59.

(59) Matheu, R.; Franca, L.; Chernev, P.; Ertem, M. Z.; Batista, V.; Haumann, M.; Sala, X.; Llobet, A. *ACS Catal.* **2015**, *5*, 3422–3429.

(60) Hurst, J. K.; Cape, J. L.; Clark, A. E.; Das, S.; Qin, C. *Inorg. Chem.* **2008**, *47*, 1753–1764.

(61) Alperovich, I.; Smolentsev, G.; Moonshiram, D.; Jurss, J. W.; Concepcion, J. J.; Meyer, T. J.; Soldatov, A.; Pushkar, Y. *J. Am. Chem. Soc.* **2011**, *133*, 15786–15794.

(62) Jurss, J. W.; Concepcion, J. J.; Butler, J. M.; Omberg, K. M.; Baraldo, L. M.; Thompson, D. G.; Lebeau, E. L.; Hornstein, B.; Schoonover, J. R.; Jude, H.; Thompson, J. D.; Dattelbaum, D. M.; Rocha, R. C.; Templeton, J. L.; Meyer, T. J. *Inorg. Chem.* **2012**, *51*, 1345–1358.

(63) Moonshiram, D.; Jurss, J. W.; Concepcion, J. J.; Zakharova, T.; Alperovich, I.; Meyer, T. J.; Pushkar, Y. *J. Am. Chem. Soc.* **2012**, *134*, 4625–4636.

(64) Dimer, O. B.; Hurst, J. K.; Roemeling, M. D.; Lymar, S. V. *J. Phys. Chem. B* **2015**, *119*, 7749–7760.

(65) Sens, C.; Romero, I.; Llobet, A.; Parella, T. *J. Am. Chem. Soc.* **2004**, *126*, 7798–7799.

(66) Zong, R.; Thummel, R. P. *J. Am. Chem. Soc.* **2005**, *127*, 12802–12803.

(67) Lewandowska-Andralojc, A.; Polyansky, D.E.; Zong, R.; Thummel, R.P.; Fujita, E. P. *Chem. Chem. Phys.* **2013**, *15*, 14058–14068.

(68) Concepcion, J. J.; Jurss, J. W.; Templeton, J. L.; Meyer, T. J. *J. Am. Chem. Soc.* **2008**, *130*, 16462–16463.

(69) Concepcion, J. J.; Tsai, M.; Muckerman, J. T.; Meyer, T. J. *J. Am.Chem. Soc.* **2010**, *132*, 1545–1557.

(70) Duan, L.; Fischer, A.; Xu, Y.; Sun, L. *J. Am. Chem. Soc.* **2009**, *131*, 10397–10399.

(71) Duan, L.; Bozoglian, F.; Mandal, S.; Stewart, B.; Privalov, T.; Llobet, A.; Sun, L. *Nat. Chem.* **2012**, *4*, 418–423.

(72) Wang, L.; Duan, L.; Wang, Y.; Ahlquistb , M. S. G.; Sun, L. *Chem. Commun.* **2014**, *50*, 12947–12950.

(73) Sha, D. W.; Xie, Y.; Szalda, D. J.; Concepcion, J. J. *J. Am. Chem. Soc.* **2017**, *139*, 15347–15355.

(74) Xie, Y.; Shaffer, D. W.; Lewandowska-andralojc, A.; Szalda, D. J.; Concepcion, J. J. **2016**, 8067–8071.

(75) Vereshchuk, N.; Matheu, R.; Benet-buchholz, J.; Pipelier, M.; Lebreton, J.; Dubreuil, D.; Tessier, A.; Gimbert-surin, C.; Ertem, M. Z.; Llobet, A. *J. Am. Chem. Soc.* **2020**, *142*, 5068–5077.

(76) No Title https://www.euchems.eu/euchems-periodic-table/.

(77) Naruta, Y.; Sasayama, M.; Sasaki, T. *Angew. Chemie* **1994**, *33*, 1839–1841.

(78) Limburg, J.; Vrettos, J. S.; Liable-Sands, L. M.; Rheingold, A. L.; Crabtree, R. H.; Brudvig, G. W. *Science (80-.).* **1999**, *283*, 1524–1528.

(79) Najafpour, M. M.; Moghaddam, A. N.; Dau, H.; Zaharieva, I. *J. Am. Chem. Soc.* **2014**, *136*, 7245–7248.

(80) Kurz, P.; Berggren, G.; Anderlund, M. F.; Styring, S. *J. Chem. Soc. Dalt. Trans.* **2007**, No. 38, 4258–4261.

(81) Karlsson, E. A.; Lee, B. L.; Åkermark, T.; Johnston, E. V.; Kärkäs, M. D.; Sun, J.; Hansson, Ö.; Bäckvall, J. E.; Åkermark, B. *Angew. Chemie - Int. Ed.* **2011**, *50*, 11715–11718.

(82) Gao, Y.; Liu, J.; Wang, M.; Na, Y.; Åkermark, B.; Sun, L. *Tetrahedron* **2007**, *63*, 1987–1994.

(83) Mcauliffe, C. A.; Parish, R. V. D.; Tames, J. *Dalt. Trans.* **1985**, *7*, 1391–1397.

(84) Fillol, J. L.; Codolà, Z.; Garcia-Bosch, I.; Gàmez, L.; Pla, J. J.; Costas, M. *Nat. Chem.* **2011**, *3*, 807–813.

(85) Hong, D.; Mandal, S.; Yamada, Y.; Lee, Y. M.; Nam, W.; Llobet, A.; Fukuzumi, S. *Inorg. Chem.* **2013**, *52*, 9522–9531.

(86) Chen, G.; Chen, L.; Ng, S.; Man, W.; Lau, T. *Angew. Chem.* **2013**, *4*, 1789–1791.

(87) Okamura, M.; Kondo, M.; Kuga, R.; Kurashige, Y.; Yanai, T.; Hayami, S.; Praneeth, V. K. K.; Yoshida, M.; Yoneda, K.; Kawata, S.; Masaoka, S. *Nature* **2016**, *530*, 465–468.

(88) Praneeth, V. K. K.; Kondo, M.; Okamura, M.; Akai, T.; Izu, H.; Masaoka, S. *Chem. Sci.* **2019**, *10*, 4628–4639.

(89) Kanan, M. W.; Nocera, D. G. *Science (80-.).* **2008**, *321*, 1072–1076.

(90) Lutterman, D. A.; Surendranath, Y.; Nocera, D. G. *J. Am. Chem. Soc.* **2009**, *131*, 3838–3839.

(91) Yin, Q.; Tan, J. M.; Besson, C.; Geletii, Y. V; Musaev, D. G.; Kuznetsov, A. E.; Luo, Z.; Hardcastle, K. I.; Hill, C. L. *Science (80-.).* **2010**, *328*, 342–346.

(92) Wang, S.; Yang, G. *Cemical Rev.* **2015**, *115*, 4893–4962.

(93) Dogutan, D. K.; McGuire, R.; Nocera, D. G. *J. Am. Chem. Soc.* **2011**, *133*, 9178–9180.

(94) Sinha, W.; Mizrahi, A.; Mahammed, A.; Tumanskii, B.; Gross, Z. *Inorg. Chem.* **2018**, *57*, 478–485.

(95) Nakazono, T.; Parent, A. R.; Sakai, K. *Chem. Commun.* **2013**, *49*, 6325–6327.

(96) Wang, H.; Mijangos, E.; Ott, S.; Thapper, A. *Andgewante Chem.* **2014**, *53*, 14499–14502.

(97) Leung, C.-F.; Ng, S.-M.; Ko, C.-C.; Man, W.-L.; Wu, J.; Chen, L.; Tai-Chu, L. *Energy Environ. Sci.* **2012**, *5*, 7903–7907.

(98) Wang, H.; Lu, Y.; Mijangos, E.; Thapper, A. *Chin. J. Chem.* **2014**, *32*, 467–473.

(99) Du, H.-Y.; Chen, S.-C.; Su, X.-J.; Jiao, L.; Zhang, M.-T. *J. Am. Chem. Soc.* **2018**, *140*, 1557−1565.

(100) Pizzolato, E.; Natali, M.; Posocco, B.; Galloni, P.; Bazzan, I.; Di Valentin, M.; Galloni, P.; Conte, V.; Bonchio, M.; Scandola, F.; Sartorel, A. *Chem. Commun.*

2013, *49*, 9941–9943.

(101) Hong, D.; Jung, J.; Park, J.; Yamada, Y.; Suenobu, T.; Lee, Y.; Nam, W.; Fukuzumi, S. *Environ. Energy* **2012**, *5*, 7606–7616.

(102) Wu, X.; Li, F.; Zhang, B.; Sun, L. *J. Photochem. Photobiol. C Photochem. Rev.* **2015**, *25*, 71–89.

(103) Najafpour, M. M.; Feizi, H. *Catal. Sci. Technol.* **2018**, *8*, 1840–1848.

(104) Wang, J.; Sahoo, P.; Lu, T. *ACS Catal.* **2016**, No. 6, 5062−5068.

(105) Rigsby, M. L.; Mandal, S.; Nam, W.; Spencer, L. C.; Stahl, S. S. *Chem. Sci.* **2012**, *3*, 3058–3062.

(106) Wang, J.; Sahoo, P.; Lu, T. *ACS Catal.* **2016**, *6*, 5062–5068.

(107) Wang, X.; Luo, H.; Yang, H.; Sebastian, P. J.; Gamboa, S. A. *Int. J. Hydrogen Energy* **2004**, *29*, 967–972.

(108) Sun, K.; Park, N.; Sun, Z.; Zhou, J.; Wang, J.; Pang, X.; Shen, S.; Noh, S. Y.; Jing, Y.; Jin, S.; Yu, P. K. L.; Wang, D. *Energy Environ. Sci.* **2012**, *5*, 7872–7877.

(109) Han, Y.; Wu, Y.; Lai, W.; Cao, R. *Inorg. Chem.* **2015**, *54*, 5604−5613.

(110) Wang, J. W.; Hou, C.; Huang, H. H.; Liu, W. J.; Ke, Z. F.; Lu, T. B. *Catal. Sci. Technol.* **2017**, *7*, 5585–5593.

(111) Luo, G. Y.; Huang, H. H.; Wang, J. W.; Lu, T. B. *ChemSusChem* **2016**, *9*, 485–491.

(112) Zhang, M.; Zhang, M.-T.; Hou, C.; Ke, Z.-F.; Lu, T.-B. *Angew. Chemie* **2014**, *126*, 13258–13264.

(113) Singh, A.; Chang, S. L. Y.; Hocking, R. K.; Bach, U.; Spiccia, L. *Catal. Sci. Technol.* **2013**, *3*, 1725–1732.

(114) Najafpour, M. M.; Feizi, H. *Dalt. Trans.* **2018**, *47*, 6519–6527.

(115) Barnett, S. M.; Goldberg, K. I.; Mayer, J. M. *Nat. Chem.* **2012**, *4*, 498–502.

(116) Zhang, T.; Wang, C.; Liu, S.; Wang, J. L.; Lin, W. *J. Am. Chem. Soc.* **2014**, *136*, 273–281.

(117) Zhang, M.; Chen, Z.; Kang, P.; Meyer, T. J. **2013**, No. Ii, 2–5.

(118) Garrido-Barros, P.; Funes-Ardoiz, I.; Drouet, S. . B.-; Buchholz, J.; Maseras, F.;

Llobet, A. *J. Am. Chem. Soc.* **2015**, *137*, 6758–6761.

(119) Funes-ardoiz, I.; Garrido-barros, P.; Llobet, A.; Maseras, F. *ACS Catal.* **2017**, *7*, 1712–1719.

(120) Garrido-Barros, P.; Gimbert-Surinifach, C.; Moonshiram, D.; Picón, A.; Monge, P.; Batista, V. S.; Llobet, A. *J. Am. Chem. Soc.* **2017**, *139*, 12907–12910.

(121) Fisher, K. J.; Materna, K. L.; Mercado, B. Q.; Crabtree, R. H.; Brudvig, G. W. *ACS Catal.* **2017**, *7*, 3384–3387.

(122) Su, X.-J.; Gao, M.; Jiao, L.; Liao, R.-Z.; Siegbahn, P. E. M. .; Cheng, J.-P.; Zhang, M.-T. *Angew. Chem.* **2015**, *883*, 4909–4914.

(123) Francàs, L.; Richmond, C.; Garrido-barros, P.; Planas, N.; Roeser, S.; Benet-buchholz, J.; Escriche, L.; Sala, X.; Llobet, A. *Chem. Eur. J.* **2016**, *22*, 5261–5268.

(124) Chen, Z.; Concepcion, J. J.; Jurss, J. W.; Meyer, T. J. *J. Am. Chem. Soc.* **2009**, *131*, 15580–15581.

(125) Bullock, R. M.; Das, A. K.; Appel, A. M. *Chem. Eur. J.* **2017**, *23*, 7626–7641.

(126) Guerrero, G.; Mutin, P. H.; Vioux, A. *Chem. Mater.* **2001**, *13*, 4367–4373.

(127) Materna, K. L.; Crabtree, R. H.; Brudvig, G. W. *Chem. Soc. Rev.* **2017**, *46*, 6099–6110.

(128) Brennan, B. J.; Llansola Portolés, M. J.; Liddell, P. A.; Moore, T. A.; Moore, A. L.; Gust, D. *Phys. Chem. Chem. Phys.* **2013**, *15*, 16605–16614.

(129) Materna, K. L.; Rudshteyn, B.; Brennan, B. J.; Kane, M. H.; Bloom, A. J.; Huang, D. L.; Shopov, D. Y.; Batista, V. S.; Crabtree, R. H.; Brudvig, G. W. *ACS Catal.* **2016**, *6*, 5371–5377.

(130) Materna, K. L.; Brennan, B. J.; Brudvig, G. W. *Dalt. Trans.* **2015**, *44*, 20312–20315.

(131) Martinez, C. R.; Iverson, B. L. *Chem. Sci.* **2012**, *3*, 2191–2201.

(132) Creus, J.; Matheu, R.; Peñafiel, I.; Moonshiram, D.; Blondeau, P.; Benet-Buchholz, J.; García-Antón, J.; Sala, X.; Godard, C.; Llobet, A. *Angew. Chemie - Int. Ed.* **2016**, *55*, 15382–15386.

(133) Hoque, A.; Gil-sepulcre, M.; Aguirre, A. De; Elemans, J. A. A. W.; Moonshiram, D.; Matheu, R.; Shi, Y.; Benet-buchholz, J.; Sala, X.; Malfois, M.; Solano, E.; Lim, J.; Garzón-manjón, A.; Scheu, C.; Lanza, M.; Maseras, F.; Gimbert-suriñach, C.; Llobet, A. *Nat. Chem.* **2020**, *12*, 1060–1066.

Chapter 2

Objectives

The following section contains the objectives of this thesis, which pursue the challenges still remaining in the development and application of rugged water oxidation catalysts based on first row transition metals

The use of first row transition metals in the creation of molecular water oxidation catalysts is considered advantageous for their low toxicity, abundancy and moderate price.

Some examples of non-noble metal WOCs are available nowadays, but their ligand substitution lability, increased at neutral and acidic pH, and the necessity of high potential to perform catalysis are the drawbacks which made their study more difficult than for ruthenium based WOCs. The consequent lack of mechanistic knowledge about the pathways taken in the water oxidation and the involved active species is the factor which is further slowing down the development in this field. It is thus necessary to rationally design rugged WOCs, and this can be accomplished through the synthesis and the study of non-innocent ligands, able to participate in the catalysis while stabilizing the metal center. The further modification of the ligand with the appropriate functionalities can lead to the anchoring of the WOCs on electrodes, creating robust molecular anodes.

Therefore, the main objectives of this thesis are the generation non-innocent ligands, able to form rugged first row transition metal WOCs, which, after ligand modification, can be anchored into electrode surfaces, to obtain molecular anodes. From these general aims, specific objectives have been pursued during the development of the thesis.

Objective 1: Synthesis and characterization of rationally designed WOCs bearing redox non-innocent ligands. In chapter 3, the influence of different tetra-amidate macrocycle ligands (TAML) on the activity and stability of Cu-based WOCs will be studied.

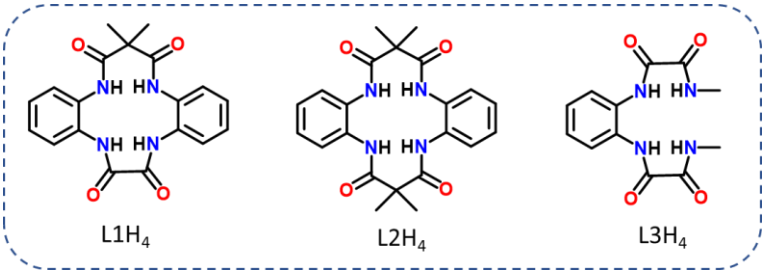

Objective 2. Synthesis of polymeric Cu-based molecular anodes. The ligand of a Cu-based WOC, will be conveniently modified with pyrene, which can be electropolymerized on the surface of electrodes, creating novel molecular anodes. The activity of the new materials will be tested at neutral and basic pH.

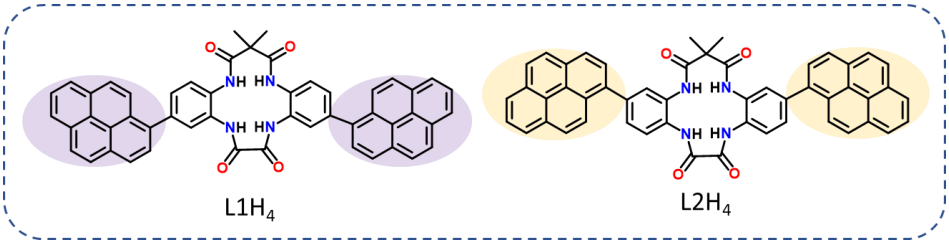

Objective 3. Unrevealing the true catalyst. The last objective will be pursued through a deep reinvestigation of a pentanuclear iron complex, considered as homogenous WOC. Several techniques as electrochemistry, and X-ray absorption spectroscopy (XAS), will be employed to understand if the catalysis is trigged by the complex or if it is just the precursor for active metal oxides

Chapter 3

Redox Metal–Ligand Cooperativity Enables Robust and Efficient Water Oxidation Catalysis at Neutral pH with Macrocyclic Copper Complexes

Chapter 3 shows the importance of the rational design of the ligand in the development of molecular WOCs based on first row transition metals. One Cu-based complex with a π delocalized tetraamido macrocycle ligand (TAML) was studied as a WOC and compared with other similar systems featuring a lower delocalization. The first complex showed a large activity and stability due to the metal-ligand cooperativity in the formation of the positive holes necessary to guest the electrons from water, which did not occur in the other two complexes, leading to lower performances or even decomposition. Further, the macrocycle effect could be appreciated when the catalyst, bearing a macrocycle as ligand, proved to be stable at neutral pH while an acyclic complex was decomposing.

Chapter 3

Project A. Redox Metal–Ligand Cooperativity Enables Robust and Efficient Water Oxidation Catalysis at Neutral pH with Macrocyclic Copper Complexes

Garrido-Barros, P.; Moonshiram, D.; Gil-Sepulcre, M.; Pelosin, P.; Gimbert-Suriñach, C.; Benet-Buchholz, J.; Llobet, A. J. Am. Chem. Soc. **2020**, *142*, 41, 17434–17446.

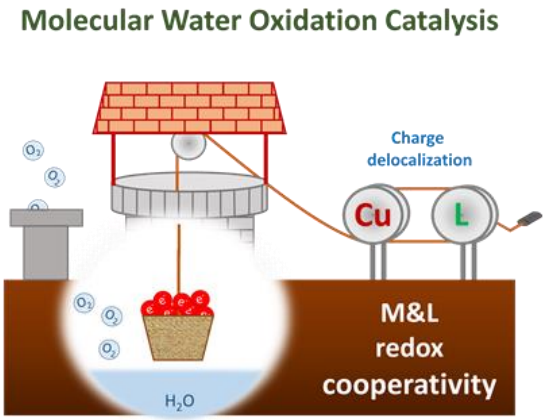

Abstract

Water oxidation catalysis stands out as one of the most important reactions to design practical devices for artificial photosynthesis. Use of late first-row transition metal (TM) complexes provides an excellent platform for the development of inexpensive catalysts with exquisite control on their electronic and structural features via ligand design. However, the difficult access to their high oxidation states and the general labile character of their metal–ligand bonds pose important challenges. Herein, we explore a copper complex ($\mathbf{1}^{2-}$) featuring an extended, π-delocalized, tetra-amidate macrocyclic ligand (TAML) as water oxidation catalyst and compare its activity to analogous systems with lower π-delocalization ($\mathbf{2}^{2-}$ and $\mathbf{3}^{2-}$). Their characterization evidences a special metal–ligand cooperativity in accommodating the required oxidative equivalents using $\mathbf{1}^{2-}$ that is absent in $\mathbf{2}^{2-}$ and $\mathbf{3}^{2-}$. This consists of charge delocalization promoted by easy access to different electronic states at a narrow energy range, corresponding to either metal-centered or ligand-centered oxidations, which we identify as an essential factor to stabilize the accumulated oxidative charges. This translates into a significant improvement in the catalytic

performance of $\mathbf{1}^{2-}$ compared to $\mathbf{2}^{2-}$ and $\mathbf{3}^{2-}$ and leads to one of the most active and robust molecular complexes for water oxidation at neutral pH with a k_{obs} of 140 s^{-1} at an overpotential of only 200 mV. In contrast, $\mathbf{2}^{2-}$ degrades under oxidative conditions, which we associate to the impossibility of efficiently stabilizing several oxidative equivalents via charge delocalization, resulting in a highly reactive oxidized ligand. Finally, the acyclic structure of $\mathbf{3}^{2-}$ prevents its use at neutral pH due to acidic demetalation, highlighting the importance of the macrocyclic stabilization.

Contributions

All authors have given approval to the final version of the manuscript.

A.1 Introduction

The need to replace fossil fuels by a renewable and clean source of energy is increasingly urgent as a consequence of global warming becoming more significant and irreversible.[1,2] Besides the scientific community that has been actively working to come up with a solution during recent decades, policy makers and society in general are starting to mobilize in the search for clean and sustainable energy vectors[3–5]. Artificial photosynthesis to produce solar fuels from water and sunlight is nowadays one of the most promising short-term strategies.[6–10] A common step in all of the proposed photosynthetic schemes, both natural or artificial, is the catalytic oxidation of water to molecular oxygen (eq 1) in order to produce electrons and protons for the further reduction of protons to hydrogen (eq 2) or the reduction of other interesting substrates such as CO_2.[11–14] This oxidative half reaction has attracted the attention of researchers over the years since overcoming its high kinetic barrier would largely solve the efficiency problems for practical application.[15–17]

$$2H_2O \rightarrow O_2 + 4H^+ + 4e^- \qquad E^0 = 1.23 \text{ vs. NHE at pH 0} \qquad \text{(eq. 1)}$$

$$2H^+ + 2e^- \rightarrow H_2 \qquad E^0 = 0.0 \text{ vs. NHE at pH 0} \qquad \text{(eq. 2)}$$

Molecular complexes offer a great platform to drive this reaction catalytically as their electronic and structural properties can relatively easily be fine tuned by ligand modification in order to improve the catalytic efficiencies.[18,19] Ultimately, molecular catalysts can be incorporated on electrodes and photoelectrodes

leading to active molecular heterogeneous catalysts with exquisite control over their properties.[20–23] However, the design of improved molecular catalysts relies on our understanding of the mechanistic pathways for water oxidation and the structure–activity relationships.[18] Although significant advances have been achieved in ruthenium catalysts,[24] knowledge regarding first-row transition metals (TMs) is still scarce and detailed understanding at a molecular level is generally lacking.[25,26] Rationalization of their design rules is indispensable in order to take advantage of their favourable properties including high abundance and nontoxicity.

Two important challenges for first-row TM complexes are the ligand substitution lability and the accessibility to multiple oxidation states at relatively low potentials, and those are the main factors responsible for the catalyst degradation pathways (Figure 1a). Moreover, the requirement of using water as a substrate and ideally as solvent poses ligand protonation and subsequent metal decoordination as competing processes. Those phenomena are in sharp contrast with Ru complexes that are generally substitutionally inert and have access to high oxidation states within a narrow potential range via proton coupled electron transfer. For abundant first-row TMs in general, generation of high oxidation states resulting in active metal–oxo (M–O)[27] units is limited by the large potentials separating the different redox couples, which could favor alternative ligand oxidative degradation and/or metal oxide formation (Figure 1a). In particular, Cu complexes at oxidation state III can only be obtained with strongly electron-donating ligands.[28–30]

Thus, to further facilitate access to formally high oxidation states, we[31] and others[32–36] have described the use of redox-active ligands that are oxidized in a reversible manner. Storage of oxidative equivalents (holes) by both the metal center and the ligand helps the four-electron removal needed for the water oxidation reaction and thus widens the scope of useful molecular water oxidation catalysts (WOCs).[20] Today the use of well-defined and rugged Cu WOCs is still limited to basic pH[31,32,37–42] with very few examples reported at neutral pH featuring high overpotentials, slow kinetics, and/ or limited information about the long-term stability.[43–45] Further, a detailed analysis at the molecular level is frequently lacking, which is important to understand the structure–activity

relationships and the possible formation of copper oxide materials as the active catalytic species.[46–49]

In order to address the low acidic and oxidative stabilities without compromising the overpotential and catalytic rates, we focused our attention on the use of tetra-amidate macrocyclic ligands (TAML). Macrocyclic ligands are expected to provide additional stability to the Cu center with regard to related acyclic ligands such as H_4L3[31] (N1,N1'-(1,2-phenylene)bis-(N2-methyloxalamide)) depicted in Figure 1b via the "macrocyclic effect".[50–55] This should enhance the pH range of stability of the catalysts at the desired lower pH values. While those ligands also help to stabilize high oxidation states in the metal centers,[56] we consider their redox non−innocent character, which relies on oxidation of the phenyl-bisamidate bridge similar to the corresponding acyclic analogues (see Figure 1c).[57] While those units can accumulate up to two oxidative equivalents, the redox potentials for both oxidations are separated by more than 500 mV, evidencing the relatively difficult access to the second oxidation event and thus precluding their multiredox non−innocent character (accumulation of more than one oxidative equivalent). Moreover, although the redox non−innocence of these types of ligands during water oxidation has been invoked, still high-valent $M^{IV/V}$−O groups are required for initiating the catalytic process as experimentally evidenced, thus controlling the overall overpotential.[56,58–63]

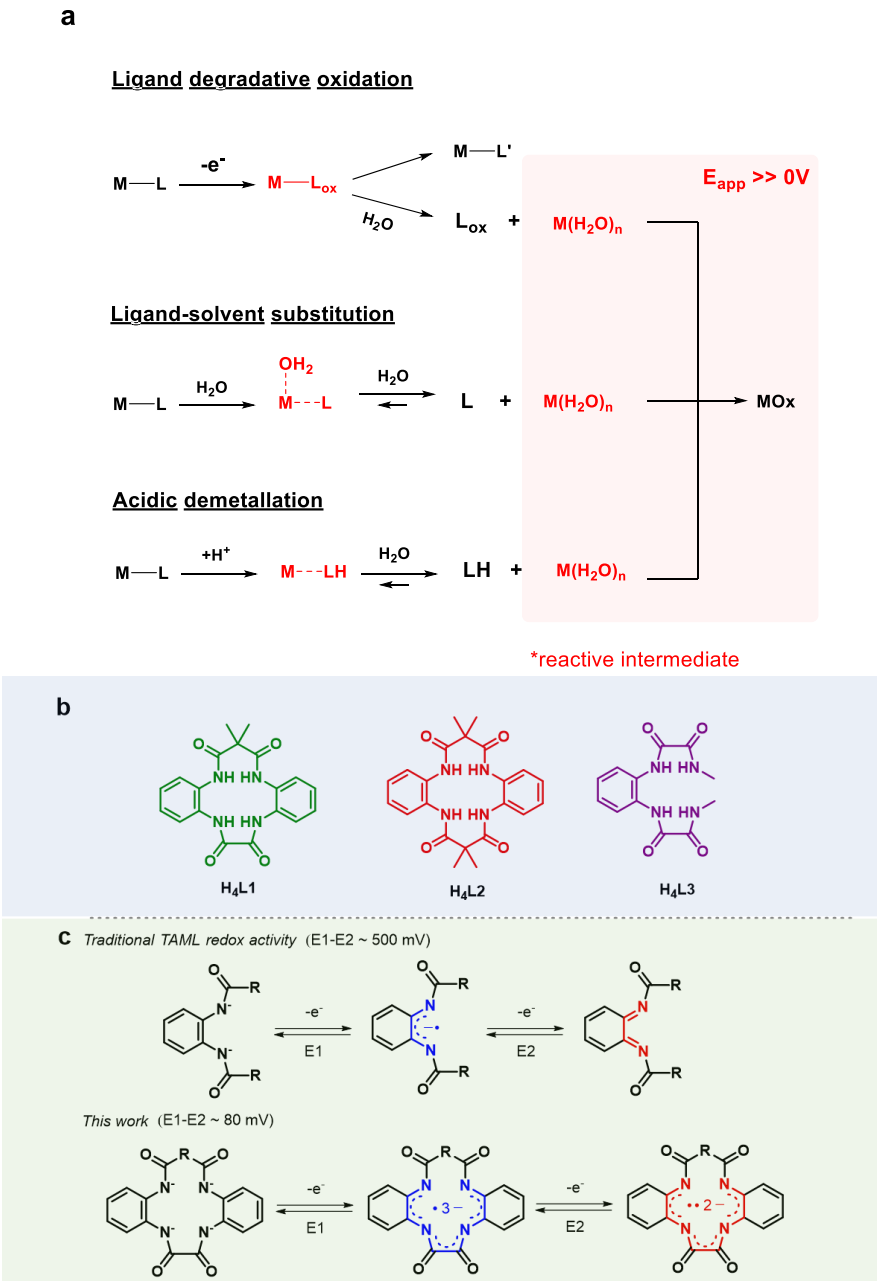

Figure 1. (a) Schematic representation of the main pathways for catalyst degradation under conditions used in water oxidation leading to the formation of metal-aquo complexes and free ligand. (b) Structure of the three tetraamidate ligands, including both macrocyclic and acyclic alternatives, discussed in this work. (c) Redox non-innocence TAML ligand *vs*. high π-delocalized $L1^{4-}$.

We envision that the use of highly π-extended TAML with two phenyl-bisamidate units will allow access to several oxidations in the ligand at a lower potential range due to greater stabilization of the resulting radicals, rendering multiredox active character (Figure 1c). Importantly, this will be key for accessing multiple oxidations with late transition metals such as copper given the limited access to their higher oxidation states. We focused our attention on the macrocyclic ligands depicted in Figure 1b, H_4L1 (15,15-dimethyl-8,13-dihydro-5H-dibenzo[b,h][1,4,7,10]tetraazacyclotridecine- 6,7,14,16(15H,17H)-tetraone)[64] and H_4L2 (7,7,16,16-tetramethyl-5,9,14,18-tetrahydrodibenzo[b,i][1,4,8,11]-tetraazacyclotetradecine-6,8,15,17(7H,16H)-tetraone).[65] We anticipate that the use of such ligands with copper will also foster a larger metal–ligand electronic interaction due to the usually higher covalency promoted by the more electronegative late transition metals. In this context, we report the synthesis, spectroscopic, and electrochemical characterization of two new Cu complexes $[(L1)Cu^{II}]^{2-}$, $\mathbf{1}^{2-}$, and $[(L2)Cu^{II}]^{2-}$, $\mathbf{2}^{2-}$, together with their performance as catalysts for the water oxidation reaction. We compare those new complexes with previously reported acyclic analogue $\mathbf{3}^{2-}$.[31]

A.2 Results

Synthesis, Structural, and Electronic Properties of Cu(II) Amidate Complexes.

Synthesis of the macrocyclic ligands H_4L1 and H_4L2 is reported in the Supporting Information together with the corresponding characterization (Figures S1–S7). Synthesis of the Cu(II) complexes is straightforward and consists of mixing methanolic solutions of the deprotonated macrocyclic ligand and $Cu(ClO_4)_2$ as a metal precursor leading to the corresponding complexes in relatively good yields. The anionic Cu(II) complexes $\mathbf{1}^{2-}$ and $\mathbf{2}^{2-}$ obtained in this manner were characterized by elemental analysis, spectroscopic and electrochemical techniques, and Xray diffraction analysis.

Figure 2 shows the side views of the ORTEP plot for the anionic complexes $\mathbf{1}^{2-}$and $\mathbf{2}^{2-}$ (top views in Figure S8). Both feature a square-planar coordination environment similar to the analogous acyclic complex $[(L3)Cu^{II}]^{2-}$, $\mathbf{3}^{2-}$, and its family of related substituted complexes.[31] The strong σ-donor character of the amidate groups compensates for the electron-deficient configuration of the 17

e^- complexes and ensures strong metal–ligand bonds reflected in the short Cu–N distances and high stabilization of the d^9 Cu(II) ion as a square-planar, four-coordinated metal center. In the case of complex $\mathbf{1}^{2-}$ bearing the 13-membered ring ligand $L1^{4-}$, those distances are in the range of 1.895(7)–1.928(8) Å, significantly shorter than those formed by the 14-membered ring ligand in $\mathbf{2}^{2-}$ (1.922(6)–1.941(6) Å) due to the larger size and rigidity of the macrocyclic ligand $L2^{4-}$. In both cases, the metal–ligand distances are shorter than those found for the family of analogous Cu(II) complexes bearing the acyclic tetraamidate ligand $L3^{4-}$ (1.938–1.953 Å),[31,66] evidencing the stronger Cu–N bond interactions in the case of the macrocyclic complexes.

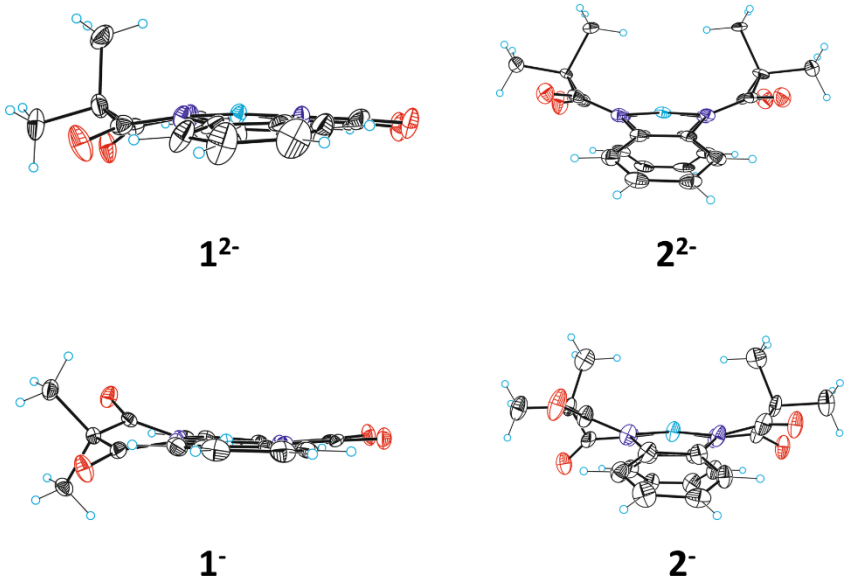

Figure 2. ORTEP drawing (thermal ellipsoids drawn at a 50 % probability level) showing side views of the cationic structure of $\mathbf{1}^{2-}$, $\mathbf{1}^{-}$, $\mathbf{2}^{2-}$, and $\mathbf{2}^{-}$. Colour code: C, black; N, blue; O, red; Cu, light blue.

The short Cu–N bond lengths obtained for the macrocyclic complexes $\mathbf{1}^{2-}$ and $\mathbf{2}^{2-}$ together with the lower basicity of the phenyl-bisamidate ligands than alkyl amidates is reflected in their relative stability in aqueous solutions as compared to the acyclic $\mathbf{3}^{2-}$. While the latter decoordinates at pH lower than 10, the former are stable all the way down to pH 7 (Figures S13–S15), which is highly desirable for their potential application as molecular electroanodes.[67,68]

X-ray absorption near-edge and extended X-ray absorption fine structure spectroscopies (XANES and EXAFS, respectively) were further used to characterize the electronic and structural properties of complex $\mathbf{1}^{2-}$, and the results are shown in Figure 3 and Figure S9. The EXAFS simulation carried out for $\mathbf{1}^{2-}$ shows a remarkable agreement between the simulated Cu−N bonding distances and those obtained by X-ray diffraction (XRD) (Table S1). In addition, the XANES spectrum of $\mathbf{1}^{2-}$ further shows a noticeable pre-edge feature at low photon energies, 8979.1 eV, corresponding to the 1s → 3d electronic transition[69–71] as well as a main peak along the rising edge region at ∼8987 eV commonly observed in Cu(II) square-planar complexes (Figure 3a).[20,72] This transition is assigned to a metal localized 1s → 4p transition with "shakedown" contribution arising from a coupled ligand to metal charge transfer (LMCT) transition.[73] The extended π-delocalization over the two phenyl groups and the oxamide bridge in ligand $L1^{4-}$ is responsible for the nearly flat geometry of complex $\mathbf{1}^{2-}$ in contrast to complex $\mathbf{2}^{2-}$, where the presence of two dimethylmalonamide bridges with sp^3 quaternary carbons breaks the π-conjugation between both phenyl groups. This results in a distorted structure where the two phenyl groups lie below the plane formed by the four N atoms bonded to the Cu center (the angle formed by the two phenyl rings is 50.1°) as can be observed in Figure 2 for $\mathbf{2}^{2-}$.

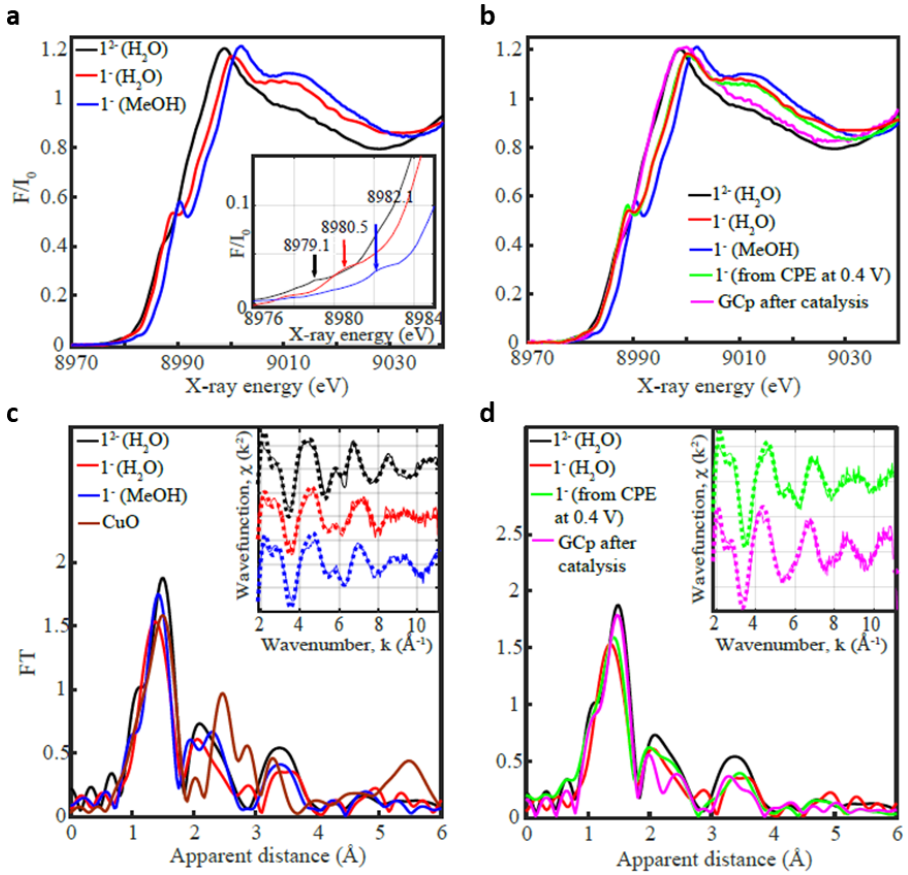

Figure 3. (a) Normalized Cu K-edge XANES of complex $\mathbf{1}^{2-}$ (1 mM) in water (black) and its oxidized analogous $\mathbf{1}^{-}$ (1 mM) in water (red) and methanol (blue) prepared by chemical oxidation with I_2. (Inset). Zoom in of the pre-edge regions. (b) Same as in a for 1 mM $\mathbf{1}^{2-}$ (black), chemically synthesized $\mathbf{1}^{-}$ (red and blue), electrochemically synthesized $\mathbf{1}^{-}$ (green), and a GC plate electrode used for a CPE (magenta) of 1 mM $\mathbf{1}^{2-}$at pH 7 with E_{app} = 1.25 V (magenta). (c) Experimental Fourier transforms of k^2-weighted EXAFS spectra for complex $\mathbf{1}^{2-}$ (1 mM) in water (black), chemically synthesized $\mathbf{1}^{-}$ (1 mM) in water (red) and methanol (blue), and solid CuOx (brown). (Inset) Corresponding back Fourier transforms. (d) Same as in c for 1 mM $\mathbf{1}^{2-}$ (black), its chemically oxidized analogous $\mathbf{1}^{-}$ (red), electrochemically synthesized $\mathbf{1}^{-}$ (green), and a GC plate electrode after CPE of a 1 mM $\mathbf{1}^{2-}$ at pH 7 with E_{app} = 1.25 V. (Inset) Back Fourier-transformed experimental (solid lines) and fitted (dashed lines) $k^2[\chi(k)]$. See the SI for additional experimental details.

The delocalization phenomenon is also manifested in the UV–vis spectra of $\mathbf{1}^{2-}$and $\mathbf{2}^{2-}$ in organic solvents and in water, where complex $\mathbf{1}^{2-}$ presents two new bands at 390 and 550 nm that can be tentatively assigned to low-energy ligand-to-metal or ligand-to-ligand charge transfer as a consequence of the smaller difference in the energy levels (Figures S10–S12).[74] In contrast, these transitions

occur at significantly higher energy (280–310 nm) in the case of $\mathbf{2}^{2-}$ due to the lower delocalization. Time-dependent density functional theory (TD-DFT) simulations of the UV–vis spectra performed on complexes $\mathbf{1}^{2-}$ and $\mathbf{2}^{2-}$ fully support these assignments (Figures S66–S69). Similarly, in the case of $\mathbf{3}^{2-}$, those transitions also feature higher energy (500 and 340 nm)[75] than in $\mathbf{1}^{2-}$ but lower than $\mathbf{2}^{2-}$, probably due to higher electronic delocalization through the (bis)amidate bridges compared to the dimethylmalonamide bridges in complex $\mathbf{2}^{2-}$.

High Oxidation States of Cu Amidate Complexes in Organic Solvents.

The one-electron-oxidized Cu(III) species, $\mathbf{1}^{-}$ and $\mathbf{2}^{-}$, can be obtained electrochemically or chemically using iodine as oxidant (see Supporting Information for detailed synthesis). Crystal structures of both complexes were obtained, and their ORTEP views are presented in Figure 2 and Figure S8. It can be appreciated that the Cu centers have the typical square-planar D_{4h} type of geometry expected for d^8 ions. In the case of $\mathbf{1}^{-}$, the Cu–N distances are on average around 0.18 Å reduced as compared with its Cu(II) homologue which reflects the relative flexibility of the ligand adopting a more constrained conformation at oxidation state III. Similar results can be extracted from the X-ray structure of $\mathbf{2}^{-}$ whose ORTEP drawing is also shown in Figure 2. The Cu–N distances extracted from the simulation of EXAFS spectrum of $\mathbf{1}^{-}$ in the solid state are also in very good agreement with the contraction observed in the X-ray data (Figure S9 and Table S1). In addition, the XANES spectrum shows a pre-edge at 8982.1 eV for the Cu(III) complex $\mathbf{1}^{-}$ that is 3.0 eV higher than that for the Cu(II) $\mathbf{1}^{2-}$, in agreement with related complexes previously described in the literature.[20,76–78]

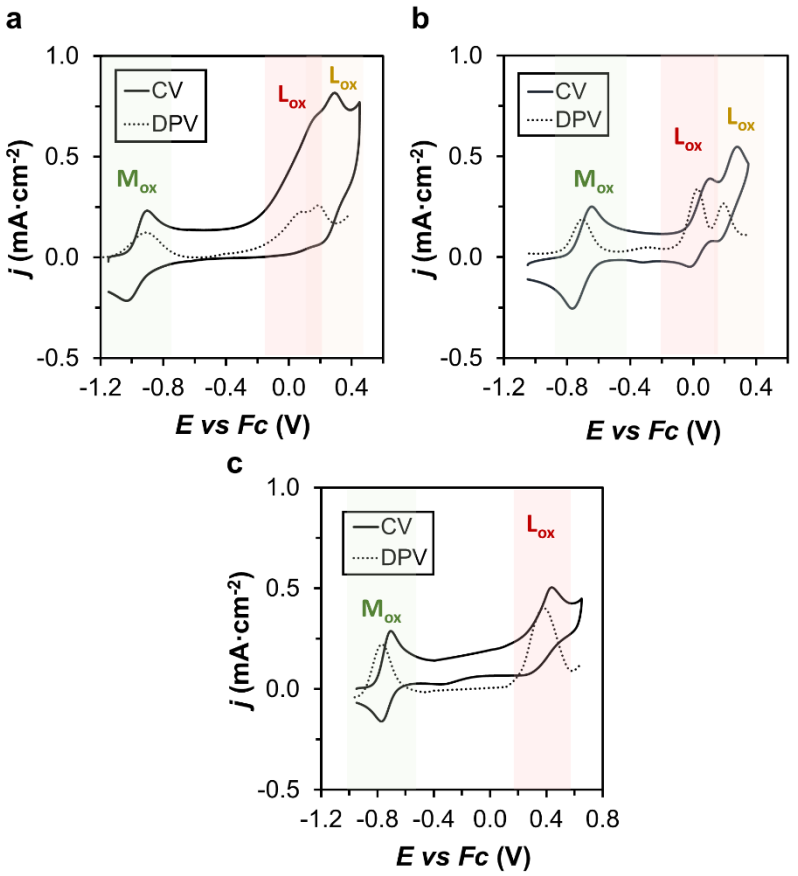

Figure 4. CV and DPV of a 1 mM MeCN solution of (a) $\mathbf{1}^{2-}$, (b) $\mathbf{2}^{2-}$, and (c) $\mathbf{3}^{2-}$ using 0.1 M $TBAPF_6$ as supporting electrolyte and glassy carbon as the working electrode.

The redox properties of these Cu complexes were investigated by means of cyclic voltammetry (CV) and differential pulse voltammetry (DPV) techniques in MeCN. CV and DPV of $\mathbf{1}^{2-}$, $\mathbf{2}^{2-}$, and $\mathbf{3}^{2-}$ are presented in Figure 4 and Figure S16. CV shows a chemically reversible wave associated with the Cu(III)/Cu(II) redox couple at $E_{1/2}$ = −0.90 and −0.70 V vs ferrocene (Fc) for macrocyclic complexes $\mathbf{1}^{2-}$ and $\mathbf{2}^{2-}$, respectively, and $E_{1/2}$ = −0.75 V for $\mathbf{3}^{2-}$ consistent with previous results.[31] Those low redox potentials evidence the high stability of the generated Cu(III) species due to the tetraanionic character of the ligand that forces a square-planar geometry typical for d^8 Cu(III) complexes.[30] The 200 mV lower potential for $\mathbf{1}^{2-}$ is associated with the stronger bonds and shorter Cu–N

distances as indicated in the previous section and reflects a strong sigma-donation capacity due to the reduced size of the 13-membered ring macrocycle as opposed to the 14-membered ring of $L2^{4-}$. In the case of $\mathbf{3}^{2-}$, the more flexible ligand backbone might be responsible for a greater stabilization of the Cu(III) center as compared to complex $\mathbf{2}^{2-}$, leading to a slightly lower redox potential despite their close Cu–N distances in the Cu(II) state. DFT calculations of the first redox process for these complexes are in good agreement with the observed potentials and satisfactorily reproduce the mentioned difference between them (Figures S70 and S71 and ref 31).

Interestingly, at higher anodic potentials the CV of $\mathbf{1}^{2-}$ and $\mathbf{2}^{2-}$ show the presence of two more redox processes that are associated with ligand-based π-electron oxidations. Whereas for $\mathbf{2}^{2-}$ they are chemically reversible, for $\mathbf{1}^{2-}$ they appear as chemically quasi-reversible. The separation in both ligand centered waves is around 80 and 180 mV for $\mathbf{1}^{2-}$ and $\mathbf{2}^{2-}$, respectively, which contrasts with the oxidation at TAML ligands containing only one phenyl-bisamidate group where both waves are separated by more than 500 mV.[57] This is also consistent with the CV of complex $\mathbf{3}^{2-}$, which features only one ligand-based oxidation in the same potential range (Figure 4c). These results put forward the easier access to higher oxidation states at the ligand when using $L1^{4-}$ and $L2^{4-}$ vs $L3^{4-}$ or the previously reported TAML ligand. Further, the 80 mV difference between the two ligand-based redox couples in $L1^{4-}$ might be explained due to high delocalization of the generated radical. Density functional theory (DFT) calculations in organic solvents of new macrocyclic complexes show the ligand-centered SOMO corresponding to ligand-based oxidations (Figures S70 and S71). The different degree of π- delocalization is evidenced comparing the SOMO of oxidized complex **1**, which is extended to both phenyl-bisamidate units, with that of complex **2**, featuring less contribution of the second phenyl-bisamidate unit.

High Oxidation States of Cu Amidate Complexes in Aqueous Solutions.

Figure 5 shows the CV of complexes $\mathbf{1}^{2-}$, $\mathbf{2}^{2-}$, and $\mathbf{3}^{2-}$ at pH 12 and 7 (further CV and DPV in Figures S17 and S18). All of the redox potentials in aqueous solution are versus NHE. At both pH values, $\mathbf{1}^{2-}$ and $\mathbf{2}^{2-}$ show the presence of a one-electron wave followed by a second catalytic wave at higher potentials, similar

to what was found for complex $\mathbf{3}^{2-}$ at pH 12. To elucidate the nature of these redox transitions in aqueous solutions, a series of spectroscopic experiments were carried as described below. The structural properties of complex $\mathbf{1}^{2-}$ and its one electron-oxidized species $\mathbf{1}^{-}$ (obtained by chemical oxidation, see SI) in aqueous solution were studied by X-ray absorption spectroscopy (XAS), nuclear magnetic resonance (NMR), and electron paramagnetic resonance (EPR). Complex $\mathbf{1}^{-}$ was also prepared via controlled potential electrolysis (CPE) at 0.4 V vs NHE for comparative XAS study (see SI for further details). Surprisingly, the XANES spectrum for $\mathbf{1}^{-}$ in pH 7 solution shows a pre-edge at 8990.5 eV that is between the expected value for Cu(II) and Cu(III), suggesting that in aqueous solution the first oxidation process is not entirely metal based in contrast to MeOH solution. This is in agreement with the 1H NMR spectroscopy of $\mathbf{1}^{-}$, which in MeOH (Figure S27) displayed the typical diamagnetic behaviour expected for a D_{4h} symmetry d^8 ion, but in D_2O, it showed no resonances in the 0–10 ppm range in agreement with a paramagnetic behaviour. These observations indicate a ligand-centered oxidation in water solution, which is further supported by EPR spectroscopy of $\mathbf{1}^{-}$, which is silent in MeOH, whereas in H_2O there is an EPR signal, consistent with paramagnetic behaviour derived from a ligand-centered oxidation (Figures 5d and S29).

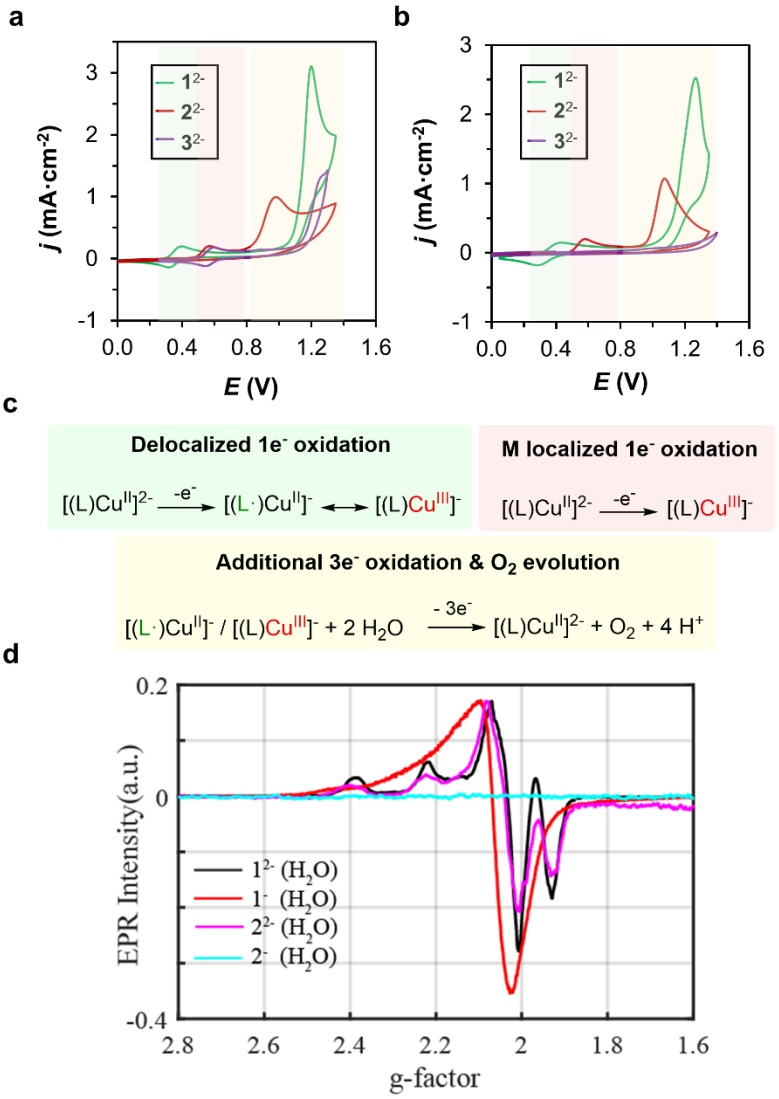

Figure 5. (a) CV of 1 mM $\mathbf{1}^{2-}$ (green), $\mathbf{2}^{2-}$ (red), and $\mathbf{3}^{2-}$ (purple) in aqueous solution using phosphate buffer at pH 12 with an ionic strength of 0.1 M. BDD electrode was employed as the working electrode, and scan rate was set to 100 mV·s^{-1}. (b) CV of 1 mM $\mathbf{1}^{2-}$ (green), $\mathbf{2}^{2-}$ (red), and $\mathbf{3}^{2-}$ (purple) in aqueous solution using phosphate buffer at pH 7 with an ionic strength of 0.1 M. Similar experimental set up was used as in a. (c) Schematic representation of the different oxidation events taking place in the CVs of complexes $\mathbf{1}^{2-}$ –$\mathbf{3}^{2-}$. (d) X-band EPR spectra (20 K) of $\mathbf{1}^{2-}$, $\mathbf{1}^{-}$, $\mathbf{2}^{2-}$ and $\mathbf{2}^{-}$ in H_2O (0.1 mM). Color code: Shading colors in a and b of the redox events refers to the redox processes indicated in c.

Therefore, we described $\mathbf{1}^-$ in water as a triplet ground state (S = 1) with ferromagnetic coupling between the S = 1/2 d^9 Cu(II) center and the S = 1/2 radical ligand $L1^{3-}$. The low zero-field splitting (ZFS) allows for EPR transitions using a standard X-band microwave source. EPR characterization is supported by analogous square-planar Cu(II) complexes bearing phenoxyl radical ligands previously reported.[79–81] Alternative metal-centered oxidation or antiferromagnetic coupling of metal and ligand radicals is discarded since they would generate EPR-silent signals. The ferromagnetic behaviour in $\mathbf{1}^-$ is explained by the absence of overlap between the orbitals hosting the unpaired electrons since the d_{x2-y2} orbitals of the metal center are orthogonal to the π-system of the ligand (Figure S73).[82] The electronic delocalization in this triplet species is responsible for the broadening of the EPR signal and prevents hyperfine coupling resolution.[83–85] This contrasts with the hyperfine splitting observed in the S = 1/2 species $\mathbf{1}^{2-}$ with a localized unpaired electron in the metal center. In agreement, the EPR simulation of $\mathbf{1}^{2-}$ and $\mathbf{1}^-$ in H_2O shows clearly different g factors and hyperfine splitting (Figure 5), illustrating the different electronic environments. G values, g_{xx} of 2.138, g_{yy} of 2.045, and g_{zz} of 1.940, with A_{xx} of 215 G could be extracted from the EPR simulation of $\mathbf{1}^{2-}$ in H_2O (Figure S30), whereas simulation of $\mathbf{1}^-$ assuming a triplet ground state yielded g_{xx}, g_{yy}, and g_{zz} values of 2.230, 2.050, and 2.050, respectively, together with zero-field splitting parameters of D and E to be 40 and 5 G, respectively (Figure S30).

This description was further supported by DFT, where it is found that the low-energy triplet structure for $\mathbf{1}^-$ has a SOMO centered in the ligand with π-character and spin density entirely delocalized between the metal center and the π-system of $L1^{4-}$ (Figure S73). The alternative calculated singlet structure corresponding to metal oxidation centered in the d orbitals has a similar energy with only a 0.7 kcal·mol^{-1} difference. The spin crossover phenomenon clearly demonstrates the close proximity between the two different electronic states corresponding to accommodation of the oxidative equivalent in either metal d orbitals or ligand π-delocalized orbitals, respectively.

Furthermore, UV–vis analysis of the oxidized species by spectroelectrochemistry in aqueous solution shows a distinguishable decrease of the bands in the UV region (at around 300 nm), which is again consistent with the generation of partial radical character in the π-system of the ligand, weakening the π–π * transitions (Figures S36 and S37).[20,86] The fact that the spin state and thus the

specific electronic structure of complex $\mathbf{1}^{-}$ is dependent on the solvation effects further evidences the existence of a large degree of degeneration in its frontier orbitals. This reflects a close energy match between the metal d orbitals and the ligand π-system that is absent in previous Fe or Co TAML complexes.[56–60] In sharp contrast, the 1H NMR spectra for $\mathbf{2}^{-}$in MeOH and D_2O are basically identical, thus indicating that the first oxidation is metal based and that the spin crossover phenomena just described for $\mathbf{1}^{-}$ does not occur in $\mathbf{2}^{-}$ (Figure S28). In addition, $\mathbf{2}^{2-}$in H_2O shows similar features to $\mathbf{1}^{2-}$, with G values g_{xx} of 2.150, g_{yy} of 2.060, and g_{zz} of 1.940 with A_{xx} of 215 G (Figure S30), while complex $\mathbf{2}^{-}$ is EPR silent, consistent with the assignment of a Cu(III) species. Those differences with $\mathbf{1}^{2-}$ reflect the importance of the relative energy of the molecular orbitals generated by π-delocalization.

Water Oxidation Catalysis by Cu Amidate Complexes.

The CV in Figure 5 at pH 12 shows the presence of a second wave that is catalytic in nature at high anodic potentials. Complex $\mathbf{1}^{2-}$ has the largest catalytic wave with its foot situated at approximately 1.0 V, which is about 100 mV lower than that of the acyclic complex $\mathbf{3}^{2-}$. For $\mathbf{2}^{-}$ the foot of the catalytic wave starts at approximately 0.8 V but the III/II wave disappears after catalysis, importantly indicating the disappearance of the initial molecular complex from the double layer. At pH 7, the acyclic complex decomposes, and thus, there is no electroactivity associated with $\mathbf{3}^{2-}$, in sharp contrast with the stability displayed by $\mathbf{1}^{2-}$ and $\mathbf{2}^{2-}$.

At pH 7, the foot of the catalytic wave for $\mathbf{1}^{2-}$ starts at approximately 1.0 V, which represents an overpotential of ca. 200 mV, whereas for $\mathbf{2}^{2-}$ the foot of the catalytic wave starts at approximately 0.9 V and represents an overpotential of only 100 mV. However, while for $\mathbf{1}^{2-}$ the III/II wave is fully reversible after catalysis, the reversibility is lost for $\mathbf{2}^{2-}$, indicating again the poor performance of the latter as a water oxidation catalyst. These data manifest how small variations on the ligand structure have an extraordinary impact in the catalyst performance in terms of catalytic current, overpotential, and stability. Here, the right size and electronic structure of the 13-membered ring macrocycle satisfactorily fit the geometrical and electronic demands of both Cu(II) and Cu(III) and thus generate a very rugged catalyst. Enlarging the cavity by one more unit

generating a 14-membered ring with reduced π-delocalization has a catastrophic effect on the stability of the catalyst.

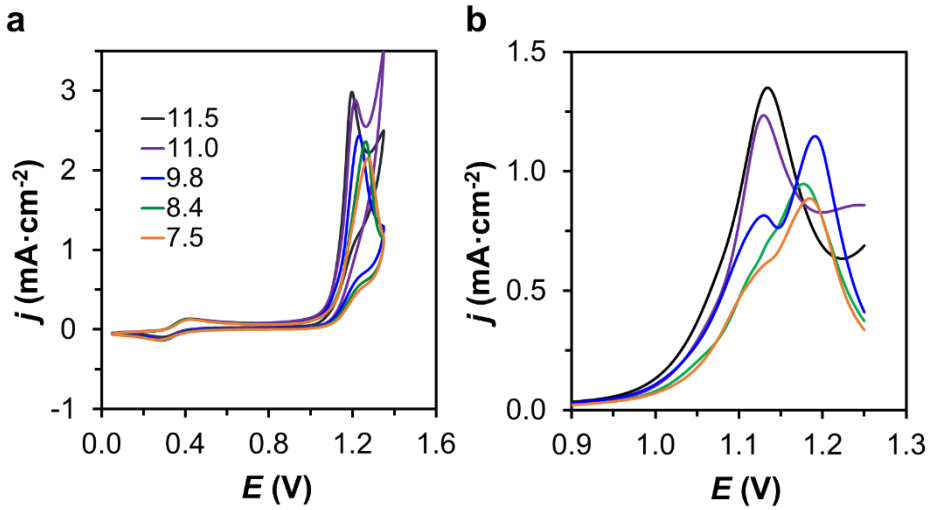

Figure 6. (a) CV of aqueous solutions at different pH containing 1 mM complex $\mathbf{1}^{2-}$ in a 0.1 M phosphate buffer solution. BDD electrode was employed as the working electrode, and scan rate was set to 100 $mV \cdot s^{-1}$. (b) DPV of aqueous solutions at different pHs containing 1 mM complex $\mathbf{1}^{2-}$ in the same conditions as in a.

The redox properties of $\mathbf{1}^{2-}$ and $\mathbf{2}^{2-}$ were further investigated as a function of pH by CV and DPV as shown in Figure 6 and Figures S32–S34. It is interesting to realize that at the 7–10 pH range there are two different oxidation events under catalysis for $\mathbf{1}^{2-}$ that can be easily identified in the DPV experiment, which implies an additional oxidation process. At the pH range 11–12, there is a single electrocatalytic process in the potential range studied. This suggests that at high pH (for instance, at pH 11) after removal of two electrons from $\mathbf{1}^{2-}$ and a further hydroxido coordination the new species [**1**(**OH**)]$^{-}$ generated is very active toward O–O bond formation and O_2 release, similar to previous observations with catalyst $\mathbf{3}^{2-}$. However, at pH 7, the kinetics of O–O bond formation will be slower because the [OH^{-}] is 4 orders of magnitude lower. Access to an additional electron removal generating the neutral species [**1**(**OH**)] will generate a much more electrophilic oxygen at the Cu–OH group that can also be responsible for the water oxidation catalysis at neutral pH.

These reaction pathways are supported by DFT calculations (vide infra). Spectroelectrochemistry performed in an optically transparent thin layer electrochemical (OTTLE) cell reveals the UV–vis spectra corresponding to the different redox processes observed in the CV (Figures S36 and S37). At redox potentials above 0.4 V the UV–vis spectrum for $\mathbf{1}^{-}$ is obtained showing small changes in the UV region with regard to that of $\mathbf{1}^{2-}$, consistent with the proposed ligand oxidation. Scanning to catalytic potentials and returning to the initial values, the UV–vis spectrum remains constant and is consistent with the high stability of the catalyst. Under catalytic potentials, similar features to those corresponding to $\mathbf{1}^{-}$ are obtained with slightly lower absorbance in the UV region probably due to the further oxidation of the ligand in the resting state.

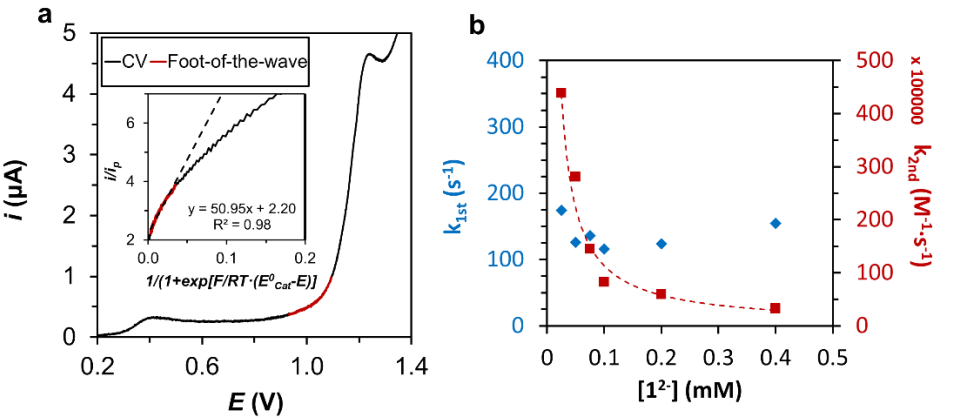

Figure 7. (a) Linear sweep voltammetry of an aqueous solution at pH 7 containing 0.1 mM complex $\mathbf{1}^{2-}$ with 0.1 M phosphate buffer. BDD was employed as the working electrode at a scan rate of 100 mV·s^{-1}. Red trace represents the data used for the foot-of-the-wave analysis (FOWA). (Inset) FOWA under these conditions, where the red trace represents again the data used for the linear fit derived from FOWA equations. Black dashed line represents the ideal response of the system. (b) Plot of the observed kinetic constant calculated with FOWA assuming a first-order mechanism (blue trace) or a second order mechanism (red trace) in catalyst.

To extract more information about this system kinetic analysis was also carried out for $\mathbf{1}^{2-}$ based on foot of the wave analysis (FOWA).[87] It has been performed at pH 7 and 12 within the concentration range of 10–400 μM, and the results are reported in Figure 7 and Figure S35. A value of 200 s^{-1} for the k_{obs} (TOF_{max}) is obtained at pH 12, which is around 2 orders of magnitude higher than that obtained for $\mathbf{3}^{2-}$. At pH 7, a k_{obs} of 140 s^{-1} is obtained, which is among the highest

reported for first-row transition metals at pH 7 (vide infra).[26] Further, a plot of the observed k_{obs} vs the catalyst concentration indicates a first-order behavior with regard to $\mathbf{1}^{2-}$ and thus suggests that the O−O bond formation occurs via a water nucleophilic attack (WNA) pathway.[88]

DFT Characterization of Water Oxidation.

With all these data in hand, we additionally performed DFT calculations for complex $\mathbf{1}^{2-}$ (Figures S72−S78) in order to characterize the electronic states and coordination environments of the oxidized species responsible for catalytic activity.

A summary of the results is shown in Figure 8 and Schemes S1 and S2. As already discussed, in aqueous solution the first one electron oxidation leads to a triplet $\mathbf{1}^{-}$ species where the unpaired electrons are mainly delocalized all over the complex (Figure S73). Analysis of the SOMO clearly shows the oxidation being centered in the π-orbitals of the ligand with a low contribution of d_{xz} and d_{yz} orbitals of the metal due to π-type interactions. This species is very close in energy to the singlet species corresponding to an oxidation centered in the metal d orbitals as discussed previously. This small energy difference could promote stabilization of the oxidative equivalents by easy access to both electronic structures, giving rise to charge delocalization (Figure 8b, Figure S73).The coordination of a water or OH^{-} ligand to $\mathbf{1}^{-}$ is energetically unfavoured.

A second one-electron removal to generate **1** yields a quartet species with SOMOs centered on the π-orbitals of the ligand (Figure S74). Once again, the alternative doublet species, where the second oxidation is mainly accommodated in the metal d orbitals, is very close in energy (2.1 kcal·mol^{-1}), suggesting high degeneration in the different electronic structures. The coordination of a hydroxido ligand is now favoured by ΔG^{o} = −1.1 kcal·mol^{-1}, leading to [**1**(**OH**)]$^{-}$ with a quartet multiplicity. This species has similar spin distribution and SOMOs as in **1** with partial contribution of the hydroxocentered orbitals (see Figure S75).

At pH 12, the [**1**(**OH**)]$^{-}$ species is responsible for the O−O bond formation that leads to oxygen release and regenerates the initial Cu complex. This step has also been calculated, and a mechanism based on single electron transfer-water

nucleophilic attack (SET-WNA) was found operative for O–O bond formation in a similar manner as proposed recently for several copper complexes including $\mathbf{3}^{2-}$ (Scheme S2).[31,89] In this mechanism, a first single electron transfer (SET) from an external hydroxide molecule leads to formation of a 2 center-3 electron (2c-3e) intermediate where the ligand has been reduced by one electron (Figure S77). Further shortening of the O–O bond led to a second SET to form a hydroperoxo species with concomitant ligand reduction to its initial oxidation state (Figure S78). Electron and proton removal from this species via proton-coupled electron transfer (PCET) eventually results in formation of oxygen and recovery of initial complex $\mathbf{1}^{2-}$.

However, at neutral pH, a third oxidation is observed under catalytic conditions that is consistent with an additional oxidized species. DFT proposes formation of a triplet species **1**(**OH**) that would be responsible for the O–O bond formation at pH 7 (Figure S76). Here, one-electron removal from the ligand leads to a spin density delocalized among the metal center, the OH^- ligand, and one of the phenyl rings of the $L1^{4-}$ ligand. The LUMO and SOMO are thus centered on the ligand π-system, where two electrons alfa and one electron beta have been removed, leading to only one unpaired electron in the ligand. In this case, calculation of the alternative electronic structure corresponding to a metal center oxidation and two unpaired electrons in the ligand remained elusive since in both cases the resulting electronic structure would also correspond to a triplet state with small differences in energy.

Instead, a singlet state could be optimized, also associated with a Cu(III) complex with no unpaired electrons in the ligand (alfa and beta electrons were removed corresponding to a closed-shell configuration). This singlet state is still close in energy (ΔG = 6.3 kcal·mol^{-1}) and potentially represents a higher limit for the energy of the alternative metal/ligand oxidized triplet species that we were not able to find. Once again, a SET-WNA mechanism could operate to promote O–O bond formation with generation of the 2c-3e intermediate and further formation of a hydroperoxo species (Scheme S2 and Figures S77 and S78).

When the similar triply oxidized species is investigated for catalyst $\mathbf{2}^{2-}$ ($\mathbf{2}^{+}$, before OH^- coordination), a singlet species results as the most stable electronic structure where one oxidative equivalent is accumulated in the metal center and

two in the ligand (corresponding to removal of an alfa and a beta electron). In this species, the LUMO is mainly centered in one of the phenyl rings (Figure S79). Addition of a hydroxide ligand to the apical position of the metal center in $\mathbf{2}^{+}$ leads to the exothermic hydroxo attack to a carbon atom in the oxidized phenyl ring forming a C–O bond (Figure S8). This evidences the potential oxidative degradation pathways of this complex and is in good agreement with its poor performance as a water oxidation catalyst.

As previously reported via experiments and DFT,[31,89] catalyst $\mathbf{3}^{2-}$ performs water oxidation at basic pH via a first oxidation in the metal and a second oxidation in the ligand, which generates the active intermediate toward O–O bond formation. Here, the acyclic tetra amidate ligand can only accommodate one oxidative equivalent in the studied potential range. This prevents further oxidation and generation of reactive species with an oxidized ligand as in complex $\mathbf{2}^{2-}$, which was identified as being responsible for the oxidative degradation process.

Redox Metal–Ligand Cooperativity Enables Robust and Efficient Water Oxidation Catalysis at Neutral pH with Macrocyclic Copper Complexes

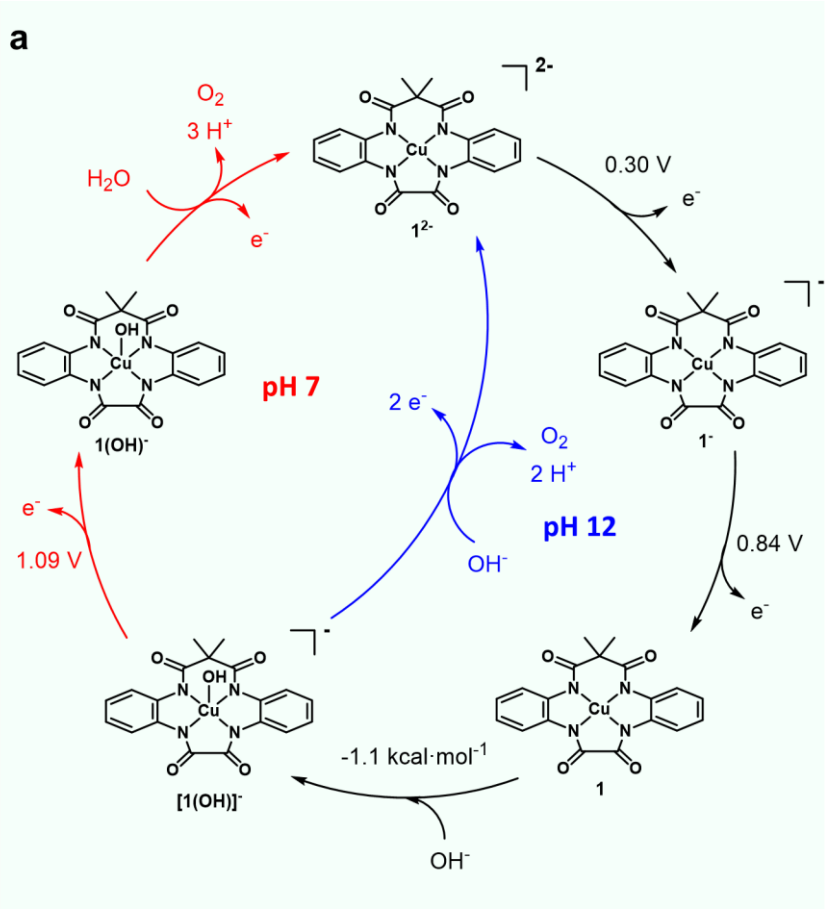

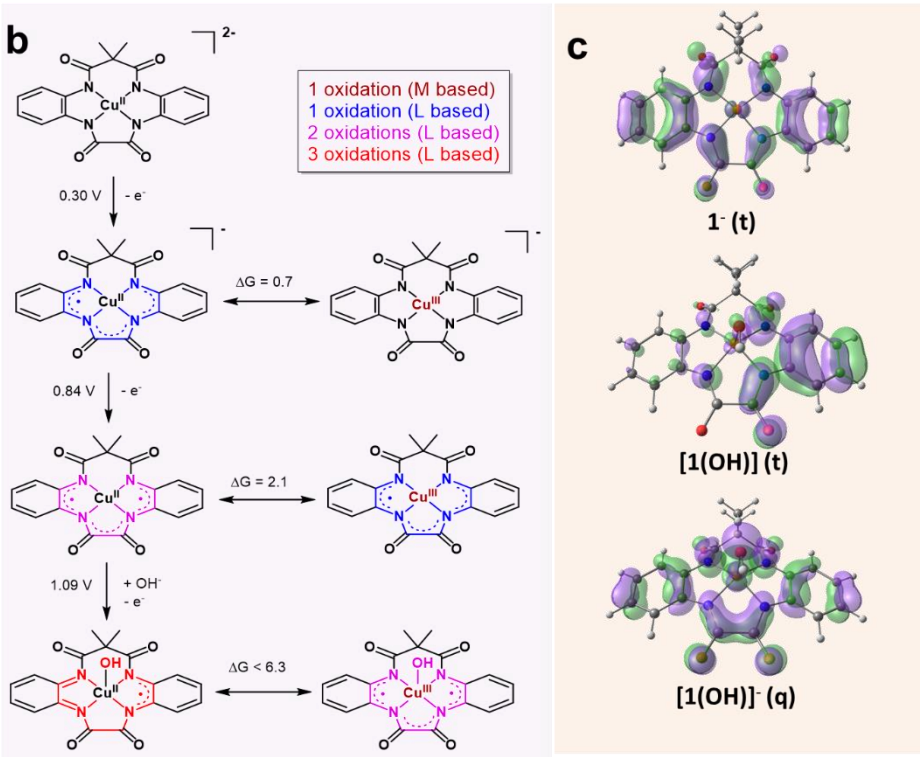

Figure 8. (a) Schematic representation of the proposed catalytic cycle for water oxidation by complex $\mathbf{1}^{2-}$ at neutral and basic pH. Energies in the diagram are calculated free energies, and potentials are the calculated values referenced to NHE. Oxidation events at 0.30, 0.84, and 1.09 V leading to, respectively, species $\mathbf{1}^{-}$, $[\mathbf{1}(\mathbf{OH})]^{-}$, and $[\mathbf{1}(\mathbf{OH})]$ are associated with the observed waves in the CV and DPV of Figure 6. (b) Schematic representation of the electronic states corresponding to each oxidation state of complex $\mathbf{1}^{2-}$ with the calculated redox potential and the energy difference between the different multiplicities. (c) Optimized structures and SOMO (represented in green and purple) of the intermediates relevant for O–O bond formation. Color code for atoms: orange is copper, blue is nitrogen, red is oxygen, gray is carbon, and white is hydrogen.

Stability Tests and Oxygen Measurements.

The long-term stability of the water oxidation catalysts $\mathbf{1}^{2-}$ and $\mathbf{2}^{2-}$ was investigated based on repetitive cyclic voltametric experiments and CPE coupled to O_2 detection analysis. The electrodes after catalysis were further analyzed by CV, scanning electron microscopy (SEM), energy-dispersive X-ray spectroscopy (EDX), XANES, and EXAFS (Supporting Information).

Repetitive cyclic voltammetry experiments of complex $\mathbf{2}^{2-}$show a decrease of about 80% of the initial current density at the catalytic wave in the second cycle

and thus clearly indicates the low stability against oxidative degradation of this catalyst.

In sharp contrast, catalyst $\mathbf{1}^{2-}$ shows a very high oxidative stability even after 100 consecutive cycles in the range from −0.15 to 1.3 V as displayed in Figure S40. Here, however, an adsorption phenomenon is observed as described in the SI (section 6), which slightly shifts the potentials of the first redox couple and decreases the catalytic current densities due to a low conductivity of the aggregate generated (Figure S20). At higher concentrations of 2 mM, this adsorption and subsequent passivation of the electrode is more drastic (Figure S38). The nature of the adsorbed layer was analyzed after catalysis by XAS, showing that the local structural conformation of complex $\mathbf{1}^{2-}$ remains unchanged, as evidenced by similar XANES spectra and K-edge energies and the same Cu−N bond distances of 1.92 Å observed both before and after catalysis by EXAFS. Importantly, no EXAFS spectral features corresponding to CuOx were observed after catalysis (Figure 3). Moreover, rinse test experiments clearly show the absence of catalytic activity of this adsorbed layer (Figures S21, S39, and S41).

A CPE experiment coupled to O_2 detection using a Clark-type sensor was carried out, and the results are presented in Figures S45−S53. In these experiments, the concentration of the catalyst was kept at a low value of 0.1 mM in order to minimize the adsorption process. Using a high surface GC plate electrode (1.0 cm^2) for the CPE experiment for 11 h at an applied potential (E_{app}) of 1.2 V afforded 79 TONs (using the total amount of catalyst in solution) and a faradaic efficiency (FE) of 50%. The low value for the FE might be related to the oxidative degradation of the carbon electrodes. Indeed, when a similar experiment was performed in a BDD (0.5 cm^2) for 11 h, 34 TONs were obtained in the same time scale with a FE close to 100% as expected for the more oxidatively robust BDD electrode. Using Savéant's formula[32,87] that takes into consideration the concentration of the electroactive catalyst within the double layer, it results in a value of approximately 6 million TONs.

Rinse tests (Figures S48 and S53) of the electrodes after the CPE discard the presence of active CuOx at the surface of the electrodes due to the lack of electroactivity. This agrees with XAS (Figure 3) and microscopy analyses (Figures

S58–S65) of the same electrodes, where the spectroscopic features of copper oxide are absent. Control experiments in the absence of catalyst and using $Cu(NO_3)^2$ as the copper source confirm the catalytic activity arising from the molecular catalyst (Figures S54–S57).

Entry	Catalyst[h]	pH	Conditions	η(mV)	TOF_{max} (s^{-1})	TONs	Ref
1	$[(bpy)Cu(OH)_2]$	12.5	0.1 M NaOH/NaOAc	750	100[c]	0.45[a]	37
2	$[(dhbp)Cu(OH_2)$	12.4	0.1 M NaOH/NaOAc	540	0.4[c]	1[a] (400)[b]	32
3	$[Cu(pyalk)_2]$	13.3	0.1 M KOH	520	0.7[c]	30[a]	40
4	3^{2-}	11.5	0.1 M phbf[f]	700[j]	3.6[b]	0.5[a] (1.9 x10^3)[b]	31
5	1^{2-}	7	0.1 M phbf[f]	200[j]	140[b],(162[i])	79[a] (6x10^6)[b]	tw[e]
6	2^{2-}	7	0.1 M phbf[f]	100[j]	--	NR[g]	tw[e]
7	$[(Py_3P)Cu(OH)]^-$	8	0.1 M phbf[f]	500	20[c]	19[a]	41
8	$[Cu_2(BPMAN)(\mu\text{-}OH)]^{3+}$	7	0.1 M phbf[f]	800	0.6[c]	NR[g]	43
9	[Cu(Porf)]	7	0.1 M phbf[f]	310	30[b]	5[a]	45
10	$\{[(MeOH)Fe(HL5)]_2(\mu\text{-}O)\}^{4+}$	7	0.1 M Na_2SO_4	300	1.2[c]	NR[g]	96
11	[Ni(Porf)]	7	0.1 M phbf[f]	183	0.67[c]	NR[g]	97
12	$[Co(Py5)(OH_2)]^{2+}$	7.6	0.1 M phbf[f]	500	79[c]	NR[g]	98

Table 1. Summary of the catalytic performance of different relevant complexes used for water oxidation electrocatalysis containing Cu, Fe[90], Ni[91] and Co[92]

[a] Calculated from bulk. [b] Calculated from Savéant's FOWA[87]. [c] Calculated from the maximum catalytic current assuming ideal S-shape response of the CV[93] [d] Mixtures of water and propylene carbonate as solvent. [e] tw stands for this work. [f] phbf is phosphate buffer. [g] NR stands for not reported. [h] ligands abbreviation used: bpy is 2,2'-bpy; dhbp is 6,6'-dihydroxy-2,2'-bpy; pyalk is 2-pyridyl-2-propanoate; Py_3P is N,N-bis(2-(2-pyridyl)ethyl)pyridine-2,6-dicarboxamidate; BPMAN is 2,7-[bis(2-pyridylmethyl)aminomethyl]-1,8-naphthyridine; Me_4Cyclam is 1,4,8,11-Tetramethyl-1,4,8,11-tetraazacyclotetradecane, Porf is tetrakis(4-*N*-methylpyridyl)porphyrin; dpaq is 2-[bis(pyridin-2-ylmethyl)]amino-*N*-quinolin-8-yl-acetamidate; HL5 (Hbbpya) is *N,N*-bis(2,2'-bipyrid-6-yl)amine; $H^{\beta F}$CX-CO_2H is 2,3,7,8,12,13,17,18-Octafluoro-10-(4-(5-Hydroxycarbonyl-2,7-di-tert-butyl-9,9-dimethyl-xanthene))-5,15-bis(pentafluorophenyl)corrole; Py5 is 2,6-(bis(bis-2-pyridyl)methoxymethane)pyridine. The value of the kinetic constant k_{obs} and thus TOF_{max} for this

system has also been calculated with the approximate method assuming S-shape response of the CV. The overpotential has been calculated from the DPV experiment as the potential where the maximum peak corresponding to the catalytic process appears.

A.3 Discussion and Conclusions

One of the key issues for the design of a molecular water oxidation catalyst is the strategy that a molecule will follow to store the four positive charges (or holes) so that they can be progressively transferred to two water molecules for their oxidation to form dioxygen.[94] The presence of redox-active ancillary ligands that can be reversibly oxidized allows it to have an additional site of oxidative equivalent storage and thus increases the versatility for catalyst design that in turn can lead to better control of overpotentials as well as turnover frequencies.

This is particularly important for first-row TMs where the energy differences from successive oxidation states is much larger than that in Ru complexes as manifested by their K-edge energies (0.8 eV per oxidation state for Ru;[95] 2.8–3.3 eV for Cr, Mn, Co;[96–98] and 3.1 eV for Cu (this work)). Ligand design is also important with regard to the stability of these complexes at low pH. To take advantage of this, it is of paramount importance to understand the behaviour of the redox-active ligands combined with transition metals, that is the interplay between the two of them when electrons are removed from the complex. For this purpose, it is useful to elucidate the main site of electron removal in the different formal oxidation states of the complex.

In this context, it is interesting to see that in organic solvents the first oxidation occurs at the metal site for both $\mathbf{1}^{2-}$ and $\mathbf{2}^{2-}$, generating a diamagnetic d^8 Cu(III) ion complex. Then the second and third oxidations occur mainly at the phenylbisamidate units of the ligands, and their redox potentials are relatively close. However, in aqueous solution it is striking to realize that for $\mathbf{2}^{2-}$ the oxidation sequence is similar as in organic solvents, but for $\mathbf{1}^{2-}$ oxidation leads to a paramagnetic species where electron density has also been removed from the π-system of the ligand. The change in the electronic structure, or valence tautomerism, exerted by the solvent interaction evidences the energetic near degeneration in the frontier orbitals and the subsequent easy access to the different electronic states, corresponding to metal-centered, d-orbital oxidation or ligand centered, π-orbital oxidation. This behaviour determines an important

redox metal–ligand cooperativity in complex $\mathbf{1}^{2-}$ upon electron removal that is absent in complex $\mathbf{2}^{2-}$, which features lower degeneration of the frontier orbitals due to the lower π-delocalization. It is impressive here how small variations on the ligands and their π-system can affect the stability of the different spin states of the complex at the different oxidation states and also can have radical changes on catalyst performance. While complex $\mathbf{2}^{2-}$ suffers decomposition during catalysis, $\mathbf{1}^{2-}$ remains stable and highly active thanks to the evidenced redox cooperativity between the metal and the ligand upon subsequent oxidations, which leads to stabilization of the accumulated oxidative equivalents by charge delocalization. Importantly, this phenomenon avoids the high-energy oxidized species centered at the ligand that can undergo oxidative degradation and high-valent metal centers that require large potentials and are frequently involved in formation of metal oxides. The larger macrocycle size and more limited electronic π-delocalization in complex $\mathbf{2}^{2-}$prevents such productive metal–ligand cooperation and leads to poor stability under oxidative conditions. Consistent with previous analysis, this could be attributed to the higher reactivity of the oxidized ligand that undergo fast degradation.

In addition, the stabilization against acidic demetalation and the two accessible and close ligand-based oxidations are essential characteristics of the macrocyclic ligands to enable water oxidation at neutral pH, where an extra oxidation is required to generate a more active Cu complex. In the case of catalyst $\mathbf{3}^{2-}$, which also features more limited electronic delocalization, water oxidation at pH 12 proceeds via a similar initial sequence as in $\mathbf{2}^{2-}$ with first metal oxidation and second ligand oxidation. However, the acyclic ligand in this case determines a more labile character of the complex, which undergoes acidic demetalation below pH 10 and prevents its application in water oxidation at neutral pH.
Moreover, this complex only features one phenyl ring and thus can only accumulate one oxidative equivalent at the accessed potential. This prevents the generation of more active Cu intermediates and thus would limit its application in water oxidation at pH 7 according to previous findings using catalyst $\mathbf{1}^{2-}$.

We envision the cooperative approach reported here for oxidative equivalent accumulation as a powerful tool for the design of more stable and efficient molecular catalyst for redox reactions. Elucidating the nature of the oxidative processes is thus essential to understanding and promoting productive

mechanisms toward water oxidation. In this context, the frequent lack of analysis regarding the irreversible precatalytic waves hinders establishing relevant design criteria. That behaviour is indicative of substantial changes in the nature of the initial molecular complexes upon oxidation, which usually leads to degradation as in the case of complex $\mathbf{2}^{2-}$. A few of the most illustrative examples of first-row TM complexes used in water oxidation are presented in Table 1, which helps to contextualize the current achievements. As evidenced from these data, the general performance of the first-row TMs at neutral pH is limited in terms of TOF and TONs. Moreover, the scarce mechanistic information available precludes analysis of the structure–activity relationships.

In the present work we show that by using the redox-active ligand strategy and properly using the molecular coordination chemistry toolkit we managed to generate an extremely robust and fast water oxidation catalyst with a TOF_{max} of 140 s^{-1} that works even at neutral pH at very low overpotentials of 200 mV. This kinetics is also relevant compared to the fastest Ru catalysts at pH 7 when similar low overpotential values are considered via the Tafel plot, which feature TOF on the order of 10^{-2}–10.[24] In addition, we achieve an unprecedented electrochemical and spectroscopic characterization of the species involved in the catalytic cycle for first-row TM complexes that has been supported by DFT calculations. Those studies have revealed an alternative cooperative mechanism in the accumulation of oxidative equivalents to promote water oxidation, in contrast with traditional pure metal oxidations. We expect this work will contribute to open new avenues for the design of redox non-innocent ligands for catalytic oxidations.

A.4 Aknowledgments

Support from MINECO, FEDER, and AGAUR is gratefully acknowledged (CTQ2016-80058-R, SEV-2013-0319, ENE2016-82025-REDT, CTQ2016-81923-REDC, and 2017-SGR-1631). P.G.-B acknowledges the “La Caixa” Foundation” for the Ph.D. grant. D.M. acknowledges support from the Severo Ochoa Excellence program (SEV-2016-0686) from the Instituto IMDEA Nanociencia Acciones de Dinamization Europa Investigacion grant (EIN2019-103399), and the “Ministerio de Ciencia, Innovacion y Universidades Grant” (PID2019-111086RA-I00). XAS experiments were performed at the CLAESS beamline at ALBA Synchrotron with

the beamline support of the ALBA staff under proposal no. 2016091818 and additionally used resources of sector 20 beamline at the Advanced Photon Source (APS) at Argonne National Laboratory. Sector 20 beamline at APS is operated by the U.S DOE, under contract no. DE-AC02-06CH11357 and the Canadian Light Source.

A.5 References

.(1) Steffen, W.; Rockström, J.; Richardson, K.; Lenton, T. M.; Folke, C.; Liverman, D.; Summerhayes, C. P.; Barnosky, A. D.; Cornell, S. E.; Crucifix, M.; Donges, J. F.; Fetzer, I.; Lade, S. J.; Scheffer, M.; Winkelmann, R.; Schellnhuber, H. J. *Proc. Natl. Acad. Sci.* **2018**, *115* (33), 8252–8259. https://doi.org/10.1073/pnas.1810141115.

(2) Balmaseda, M. A., Trenberth, K. E.; Källén,. W. *Geophys. Res. Let.* **2013**, *40*, 1754–1759.

(3) The Intergovernmental Panel on Climate Change (IPCC). Climate Change 2014: Mitigation of Climate Change; Edenhofer, O. et al., Eds.; Cambridge University Press, 2014.

(4) United Nations. Adoption of the Paris Agreement: Proposal by the President; UNFCCC, 2015; https://unfccc.int/resource/docs/2015/cop21/eng/l09.pdf.

(5) Stahel, W. R. *Nature* **2016**, *531*, 435–438.

(6) Grätzel, M. *Acc. Chem. Res.* **1981**, *14* (i), 376–384.

(7) Lewis, N. S. *Science* **2016**, *351*, 353−361.

(8) Nocera, D. G. *Acc. Chem. Res.* **2017**, *50*, 616−619.

(9) Melis, A. *Environ. Sci.* **2012**, *5*, 5531–5539.

(10) Garrido-Barros, P.; Funes-Ardoiz, I.; Farrás, P.; Gimbert-Suriñach, C.; Maseras, F.; Llobet, A. In Science of Synthesis: Catalytic Oxidations in Organic Synthesis; Muniz, K., Ed.; Georg Thieme Verlag,. **2018**.

(11) McEvoy, J. P.; Brudvig, G. W. *Chem. Rev.* **2006**, *106* (11), 4455–4483.

(12) Cox, N.; Pantazis, D. A.; Neese, F.; Lubitz, W. *Acc. Chem. Res.* **2013**, *46*, 1588−1596.

(13) Nelson, N.; Ben-Shem, A. *Nat. Rev. Mol. Cell Biol.* **2004**, *5* (12), 971–982.

(14) Berardi, S.; Drouet, S.; Francàs, L.; Gimbert-Suriñach, C.; Guttentag, M.; Richmond, C.; Stoll, T.; Llobet, A. *Chem. Soc. Rev.* **2014**, *43* (22), 7501–7519.

(15) Godwin, I.; Rovetta, A.; Lyons, M.; Coleman, J. *Curr. Opin. Electrochem.* **2018**, *7*, 31–35.

(16) Blakemore, J. D., Crabtree, R. H. & Brudvig, G. W. *Chem. Rev.* **2015**, *115*, 12974–13005.

(17) McCrory, C. C. L.; Jung, S.; Ferrer, I. M.; Chatman, S. M.; Peters, J. C.; Jaramillo, T. F. *J. Am. Chem. Soc.* **2015**, *137* (13), 4347–4357.

(18) Garrido-Barros, P.; Gimbert-Suriñach, C.; Matheu, R.; Sala, X.; Llobet, A. *Chem. Soc. Rev.* **2017**, *46* (20), 6088–6098.

(19) Matheu, R.; Garrido-Barros, P.; Gil-Sepulcre, M.; Ertem, M. Z. .; Sala, X.; Gimbert-Suriñach, C. . *Nat. Rev. Chem.* **2019**, *3*, 331–341.

(20) Garrido-Barros, P.; Gimbert-Surinifach, C.; Moonshiram, D.; Picón, A.; Monge, P.; Batista, V. S.; Llobet, A. *J. Am. Chem. Soc.* **2017**, *139* (37), 12907–12910.

(21) Alibabaei, L.; Sherman, B. D.; Norris, M. R.; Brennaman, M. K.; Meyer, T. J. *Proc. Natl. Acad. Sci. U. S. A.* **2015**, *112*, 5899−5902.

(22) Matheu, R.; Moreno-Hernandez, I. A.; Sala, X.; Gray, H. B.; Brunschwig, B. S.; Llobet, A.; Lewis, N. S. *J. Am. Chem. Soc.* **2017**, *139*, 11345− 11348.

(23) Ezhov, R.; Karbakhsh Ravari, A.; Page, A.; Pushkar, Y. ACS Catal. 2020, 10,. *ACS Catal.* **2020**, *10*, 5299−5308.

(24) Matheu, R., Ertem, Z. M., Gimbert-Suriñach, C., Sala, X., and Llobet, A. *Chem. Rev.* **2019**, *119*, 3453–3471.

(25) Roger, I., Shipman, M. A. & Symes, M. D. *Nat. Rev. Chem.* **2017**, *1*, 301–313.

(26) Kärkäs, M. D.; Åkermark, B. *Dalt. Trans.* **2016**, *45*, 14421−14461.

(27) Ezhov, R.; Ravari, A. K.; Pushkar, Y. *Angew. Chem.* **2020**, *132*, 13604–13607.

(28) Storr, T.; Verma, P.; Pratt, R. C.; Wasinger, E. C.; Shimazaki, Y.; Stack, T. D. P. *J. Am. Chem. Soc.* **2008**, *130* (46), 15448–15459.

(29) Gary, J. B.; Citek, C.; Brown, T. A.; Zare, R. N.; Wasinger, E. C.; Stack, T. D. P. *J. Am. Chem. Soc.* **2016**, *138*, 9986–9995.

(30) Anson, F. C.; Collins, T. J.; Richmond, T. G.; Santarsiero, B. D.; Toth, J. E.; Treco, B. G. T.. *J. Am. Chem. Soc.* **1987**, *109*, 2974–2979.

(31) Garrido-Barros, P.; Funes-Ardoiz, I.; Drouet, S. . B.-; Buchholz, J.; Maseras, F.; Llobet,. *J. Am. Chem. Soc.* **2015**, *137*, 6758−6761.

(32) Zhang, T.; Wang, C.; Liu, S.; Wang, J.-L.; Lin, W. A. *J. Am. Chem. Soc.* **2014**, *136*,

273−281.

(33) Muckerman, J. T.; Polyansky, D. E.; Wada, T.; Tanaka, K.; Fujita, E. *Inorg. Chem.* **2008**, *47*, 1787–1802.

(34) Boyer, J. L.; Rochford, J.; Tsai, M.-K.; Muckerman, J. T.; Fujita, E. *Coord. Chem.* **2010**, *254*, 309–330.

(35) Shi, J.; Guo, Y.-H.; Xie, F.; Chen, Q.-F.; Zhang, M. T. *Angew. Chem.* **2019**, *59*, 4000–4008.

(36) Ravari, A. K.; Zhu, G.; Ezhov, R.; Pineda-galvan, Y.; Page, A.; Weinschenk, W.; Yan, L.; Pushkar, Y. **2020**, *142*, 884−893.

(37) Barnett, S. M.; Goldberg, K. I.; Mayer, J. M. *Nat. Chem.* **2012**, *4*, 498–502.

(38) Zhang, M. T.; Chen, Z.; Kang, P.; Meyer, T. J. *J. Am. Chem. Soc.* **2013**, *135* (6), 2048–2051.

(39) Gerlach, D. L.; Bhagan, S.; Cruce, A. A.; Burks, D. B.; Nieto, I.; Truong, H. T.; Kelley, S. P.; Herbst-gervasoni, C. J.; Jernigan, K. L.; Bowman, M. K.; Pan, S.; Zeller, M.; Papish, E. T. S. *Inorg. Chem.* **2014**, *53*, 12689−12698.

(40) Fisher, K. J.; Materna, K. L.; Mercado, B. Q.; Crabtree, R. H.; Brudvig, G. W. *ACS Catal.* **2017**, *7*, 3384− 3387.

(41) Coggins, M. K.; Zhang, M.-T.; Chen, Z. F.; Song, N.; Meyer, T. *Angew. Chem.* **2014**, *53*, 12226–12230.

(42) Chen, F.; Wang, N.; Lei, H.; Guo, D.; Liu, H.; Zhang, Z. .; Zhang, Z.; Lai, W.; Cao, R. *Inorg. Chem.* **2017**, *56*, 13368–13375.

(43) Su, X.-J.; Gao, M.; Jiao, L.; Liao, R.-Z.; Siegbahn, P. E. M. .; Cheng, J.-P.; Zhang, M.-T. *Angew. Chem.* **2015**, *883*, 4909–4914.

(44) Prevedello, A.; Bazzan, I.; Carbonare, D.; Giuliani, A.; Bhardwaj, S.; Africh, C.; Cepek, C.; Argazzi, R.; Bonchio, M.; Caramori, S.; Robert, M.; Sartorel, A. *Chem. Asian J.* **2016**,*11*, 1281−1287.

(45) Liu, Y.; Han, Y.; Zhang, Z.; Zhang, W.; Lai, W.; Cao, R. *Chem. Sci.* **2019**, *10*, 2613–2622.

(46) Chen, Z.; Meyer, T. J. *Angew. Chem.* **2013**, *52*, 700–703.

(47) Yu, F.; Li, F.; Zhang, B.; Li, H.; Sun, L. *ACS Catal.* **2015**, *5*, 627−630.

(48) Liu, X.; Jia, H.; Sun, Z.; Chen, H.; Xu, P.; Du, P. *Electrochem. commun.* **2014**, *46*, 1–4.

(49) Li, T.-T.; Cao, S.; Yang, C.; Chen, Y.; Lv, X.-J.; Fu, W.-F. *Inorg. Chem.* **2015**, *54*, 3061−3067.

(50) Cabbiness, D. K.; Margerum, D. W. J. Am. Chem. Soc. 1969, 91,. *J. Am. Chem. Soc.* **1969**, *91*, 6540–6541.

(51) Cabbiness, D. K.; Margerum, D. W. *J. Am. Chem. Soc.* **1970**, *92*, 2151–2153.

(52) Hancock, R. D.; McDougall, G. J. *J. Am. Chem. Soc.* **1980**, *102* (11), 6551–6553.

(53) Kodama, M.; Kimura, E. *J. Chem. Soc., Chem. Commun.* **1975,** 891−892.

(54) Lam, B. M. T.; Halfen, J. A.; Young, V. G.; Hagadorn, J. R. .; Holland, P. L.; Lledos, A.; Cucurull-Sanchez, L.; Novoa, J. J. . Alvarez, S.; Tolman, W. B. *Inorg. Chem.* **2000**, *39* (3), 4059–4072.

(55) Lindoy, L. F. The Chemistry of Macrocyclic Ligand Complexes; Cambridge University Press,. **2009**.

(56) Ellis, W. C.; McDaniel, N. D.; Bernhard, S.; Collins, T. J. *J. Am. Chem. Soc.* **2010**, *132* (32), 10990–10991.

(57) Van Leest, N. P.; Tepaske, M. A.; Oudsen, J.-P. H.; Venderbosch, B.; Rietdijk, N. R.; Siegler, M. A.; Tromp, M.; van der Vlugt, J. I.; de Bruin, B. *J. Am. Chem. Soc.* **2020**, *142*, 552−563.

(58) Du, H.-Y.; Chen, S.-C.; Su, X.-J.; Jiao, L.; Zhang, M.-T. **2018**, *140*, 1557−1565.

(59) Panda, C.; Debgupta, J.; Diaz Diaz, D.; Singh, K. K.; Sen Gupta, S.; Dhar, B. B. *J. Am. Chem. Soc.* **2014**, *136*, 12273−12282.

(60) Das, D.; Pattanayak, S.; Singh, K. K.; Garai, B.; Gupta, S. *Chem. Commun.* **2016**, *52*, 11787–11790.

(61) Ertem, M. Z.; Gagliardi, L.; Cramer, C. J. *Chem. Sci.* **2012**, *3*, 1293–1299.

(62) Liao, R.-Z.; Li, X.-C.; Siegbahn, P. E. M. Liao, R.-Z.; Li, X.-C.; Siegbahn, P. E. M. *Eur. J. Inorg. Chem.* **2014**, *2014*, 728–741.

(63) Lee, H.; Wu, X.; Sun, L. Lee, H.; Wu, X.; Sun, L. *ChemSusChem* **2020**, *13*, 3277–3282.

(64) Ellis, W. C.; Tran, C. T.; Roy, R.; Rusten, M.; Fischer, A.; Ryabov, A. D.; Blumberg, B.; Collins, T. J. R *J. Am. Chem. Soc.* **2010**, No. 7, 9774–9781.

(65) Kojima, T.; Ogishima, F.; Nishibu, T.; Kotani, H.; Ishizuka, T. .; Okajima, T.; Nozawa, S.; Shiota, Y.; Yoshizawa, k.; Ohtsu, H. .; Kawano, M.; Shiga, T.; Oshio, H. *Inorg. Chem.* **2018**, *57*, 15448−15459.

(66) Abdulmalic, M. A.; Aliabadi, A.; Petr, A.; Krupskaya, Y.; Kataev, V.; Zaripov, R.; Vavilova, E.; Voronkova, V.; Salikov, K.; Hahn, T.; Kortus, J.; Schaarschmidt, D. *Dalt. Trans.* **2015**, *44*, 8062–8079.

(67) Zahran, Z. N.; Tsubonouchi, Y.; Mohamed, E. A.; Yagi, M. *ChemSusChem* **2019**, *12*, 1775–1793.

(68) Garrido-barros, P.; Matheu, R.; Gimbert-suriñach, C.; Llobet, A. *Curr. Opin. Electrochem.* **2019**, *15*, 140–147.

(69) Baker, M. L.; Mara, M. W.; Yan, J. J.; Hodgson, K. O.; Hedman, B.; Solomon, E. I. *Coord. Chem. Rev.* **2017**, *345*, 182–208.

(70) Smith, T. A.; Penner-hahn, J. E.; Herding, M. A.; Doniach, S.; Hodgson, K. O. *J. Am. Chem. Soc.* **1985**, *107*, 5945–5955.

(71) Tomson, N. C.; Williams, K. D.; Dai, X.; Sproules, S. *Chem. Sci.* **2015**, *6*, 2474–2487.

(72) Gaur, A; Klysubun, W; Joshi, S K; Soni, B.; Shrivastava, B. D.; Prasad, J. *J. Phys. Conf. Ser.* **2016**, *712* (No. 012084.).

(73) Debeer, S.; Randall, D. W.; Nersissian, A. M.; Valentine, J. S.; Hedman, B.; Hodgson, K. O.; Solomon, E. I.; April, R. V; Final, I.; June, F. *J. Phys. Chem. B* **2000**, *104*, 10814–10819.

(74) Hunt, C.; Peterson, M.; Anderson, C.; Chang, T.; Wu, G.; Scheiner, S. Switchable *J. Am. Chem. Soc.* **2019**, *141*, 2604−2613.

(75) Ruiz, R.; Surville-barland, C.; Aukauloo, A.; Anxolabehere-mallart, E.; Journaux, Y.; Muñoz, M. C. *J. Chem. Soc., Dalt. Trans.* **1997**, 745–751.

(76) Solomon, E. I.; Heppner, D. E.; Johnston, E. M.; Ginsbach, J. W.; Cirera, J.; Qayyum, M.; Kieber-emmons, M. T.; Kjaergaard, C. H.; Hadt, R. G.; Tian, L. *Chem. Rev.* **2014**, *114*, 3659–3853.

(77) Dubois, J. L.; Mukherjee, P.; Collier, A. M.; Mayer, J. M.; Solomon, E. I.; Hedman, B.; Stack, T. D. P.; Hodgson, K. O. *J. Am. Chem. Soc.* **1997**, *119*, 8578–8579.

(78) Dubois, J. L.; Mukherjee, P.; Stack, T. D. P.; Hedman, B.; Solomon, E. I.; Hodgson, K. O.; *J. Am. Chem. Soc.* **2000**, *122*, 5775–5787.

(79) Wang, Y.; Stack, T. D. P. **1996**, *7863* (14), 13097–13098.

(80) Verma, P.; Pratt, R. C.; Storr, T.; Wasinger, E. C.; Stack, T. D. P. *Proc. Natl. Acad. Sci. U. S. A.* **2011**, *108*, 18600−18605.

(81) Orio, M.; Jarjayes, O.; Kanso, H.; Philouze, C.; Neese, F.; Thomas, F. *Angew. Chem., Int. Ed.* **2010**, *49*, 4989–4992.

(82) Demir, S.; Jeon, I.; Long, J. R.; Harris, T. D. *Coord. Chem. Rev.* **2015**, *289–290*, 149–176.

(83) Peeks, M. D.; Tait, C. E.; Neuhaus, P.; Fischer, G. M.; Ho, M.; Cnossen, A.; Harmer, R.; Timmel, C. R.; Anderson, H. L. *J. Am. Chem. Soc.* **2017**, *139*, 10461−10471.

(84) Richert, S.; Tait, C. E.; Timmel, C. R. *J. Magn. Reson.* **2017**, *280*, 103–116.

(85) Chłopek, K.; Bothe, E.; Neese, F.; Weyhermu, T.; Wieghardt, K. *Inorg. Chem.* **2006**, *45*, 6298–

(86) Naqvi, K. R.; Melø, T. B. *Chem. Phys. Lett.* **2006**, *428*, 83–87.

(87) Costentin, C.; Drouet, S.; Robert, M.; Savèant, J. *J. Am. Chem. Soc* **2012**, *134*, 11235–11242.

(88) Matheu, R.; Neudeck, S.; Meyer, F.; Sala, X.; Llobet, A. *ChemSusChem* **2016**, *9*, 3361–3369.

(89) Funes-ardoiz, I.; Garrido-barros, P.; Llobet, A.; Maseras, F. *ACS Catal.* **2017**, *7*, 1712−1719.

(90) Kottrup, K. G.; Agostini, S. D.; Langevelde, P. H. Van; Siegler, M. A.; Hetterscheid, D. G. *ACS Catal.* **2018**, *8*, 1052−1061.

(91) Han, Y.; Wu, Y.; Lai, W.; Cao, R. *Inorg. Chem.* **2015**, *54*, 5604−5613.

(92) Wasylenko, D. J.; Ganesamoorthy, C.; Borau-garcia, J.; Berlinguette, C. P. *Chem. Commun.* **2011**, *47*, 4249–4251.

(93) Costentin, C.; Savèant, J. *ChemElectroChem* **2014**, *1*, 1226–1236.

(94) Romain, S.; Vigara, L.; Llobet, A. *Acc. Chem. Res.* **2009**, *42*, 1944−1953.

(95) Planas, N.; Vigara, L.; Cady, C.; Mir, P.; Huang, P.; Hammarstr, L.; Leidel, N.; Dau, H.; Haumann, M.; Gagliardi, L.; Cramer, C. J.; Llobet, A. *Inorg. Chem.* **2011**, *50*, 11134–11142.

(96) Schrapers, P.; Mebs, S.; Goetzl, S.; Hennig, S. E.; Dau, H. *PLoS One* **2016**, *11* (7), No. e0158681.

(97) Karel, J.; Bernardi, F.; Wang, C.; Stinshoff, R.; Born, N.; Ouardi, S.; Burkhardt, U.; Fecher, G. H.; Felser, C. *Phys. Chem. Chem. Phys.* **2015**, *17*, 31707–31714.

(98) Arčon, I.; Mirtič, B.; Kodre, A. *J. Am. Ceram. Soc.* **1998**, *81*, 222–224.
.

A.6 Supporting information

1. Experimental Section

Materials

All the chemicals used in this work were provided by Sigma Aldrich Chemical Co and they have been used without further purification. The solvents were selected to be HPLC grade and the deionized water was obtained with high purity by passing through a nanopore Milli-Q water purification system. Aqueous basic buffer solutions at pH 12 and 7 were prepared using the necessary amount of NaH_2PO_4, Na_2HPO_4 and Na_3PO_4 salts and adjusting the pH to the desired value so that the final ionic strength was 0.1 M. Complex $[(L3)Cu](NMe_4)_2$ was prepared according to previously described procedures.[1–3]

GC plate electrodes were purchased from HTW, Germany, and are made of glassy carbon SIGRADUR® with the dimensions 20x10x0.18 mm. BDD electrode was purchased from Fraunhofer Center for Coatings and Diamond Technologies with the dimensions of 10x10x0.5 mm.

Spectroscopic Techniques

NMR spectroscopy was carried out in a 400 MHz Bruker Advance II spectrometer and a Bruker Advance 500 MHz. All the measurements were done at room temperature in deuterated solvents using residual protons as internal references. UV-vis spectroscopy was performed using a Cary 50 (Varian) UV-vis spectrophotometer with 1 cm and 2 mm quartz cuvettes.

Electron Paramagnetic Resonance

Electron Paramagnetic Resonance was performed in an EMX Micro X-band EPR spectrometer (Bruker) at 20 K using a liquid He cryostat (Oxford Instruments). Data acquisition: perpendicular mode, modulation frequency of 100 KHz, microwave frequency of 9.36 GHz, modulation amplitude of 10 G, a 10.24 ms time constant and 19.02 ms conversion time with a microwave power of 0.1851 mW. Spectra were simulated using the NHFML software package.

EPR simulations were done with NHFML software (Figure S30). G_{xx} = 2.138, g_{yy} = 2.045 and g_{zz} = 1.904 with A_{xx} = 215 G are clearly resolved in $\mathbf{1}^{2-}$ in H_2O. The simulation of $\mathbf{1}^{2-}$ in H_2O was carried out with line width of 35 G, 10 G and 5 G at

g_{xx}, g_{yy} and g_{zz}. Hyperfine couplings with the four N with I = 1 nuclear spin were also added with A_{yy} = 20 G and A_{zz} = 13 G in the simulation of $\mathbf{1}^{2-}$ in H_2O. By contrast, G_{xx} = 2.15 g_{yy} = 2.06 and g_{zz} = 1.937 with A_{xx} = 215 G are clearly resolved in $\mathbf{2}^{2-}$ in H_2OThe simulation of $\mathbf{2}^{2-}$ in H_2O was carried out with line width of 31 G, 8 G and 5 G at g_{xx}, g_{yy} and $g_{zz.}$ Hyperfine couplings with the four N with I = 1 nuclear spin were also added with A_{yy} = 20 G and A_{zz} = 13 G in the simulation of $\mathbf{2}^{2-}$ in H_2O. Lastly, the simulation of 1^- in H_2O assuming a triplet was carried out with linewidths of 130 G, 38 G and 45 G at g_{xx}, g_{yy} and g_{zz} respectively. G_{xx} = 2.23, g_{yy} = 2.05 and g_{zz} = 2.05 were clearly resolved in the simulation of 1^- in H_2O. The simulated zero field splitting parameters for 1^- in H_2O further yielded D and E to be 40 and 5 G respectively.

Elemental Analysis and Mass Spectrometry

Elemental Analysis of the samples was carried out in a Thermo Finnigan elemental analyzer Flash 1112 model.

Exact mass analyses were performed with a micrOTOF mass spectrometer (from Bruker company) using Electrospray ionization technique in methanol by direct injection and detecting with positive polarity.

X-ray Absorption Spectroscopy (XAS) Methods

X-ray absorption spectra were collected at the Advanced Photon Source (APS) at Argonne National Laboratory on bending magnet beamline 20 at electron energy 9.0 KeV and average current of 100 mA and at the CLAESS beamline at ALBA synchrotron light source[4]The radiation at APS was monochromatized by a Si (110) crystal monochromator. The intensity of the X-rays were monitored by three ion chambers (I_0, I_1 and I_2) filled with 80% nitrogen and 20% helium and placed before the sample (I_0) and after the sample (I_1 and I_2). Cu metal was placed between ion chambers I_1 and I_2 and its absorption was recorded with each scan for energy calibration. The samples were kept at 20 K in a He atmosphere at ambient pressure. Hybrid materials on glassy carbon surfaces were recorded as fluorescence excitation spectra using a 13-element energy-resolving detector. All samples were measured in a continuous helium flow cryostat in fluorescence mode with a 13-element Germanium detector. Around 15-20 XAS spectra were collected for each solution sample. No more than 5

scans were taken at each sample position at any condition. Two glassy carbon sheets with sub-monolayer coverage of the hybrid materials were on the other hand stacked on top on each other and wrapped in kapton tape. Around 30 XAS spectra of each hybrid sample were collected. Care was again taken to measure at several sample positions on each sample and no more than 5 scans were taken at each sample position. In order to reduce the risk of sample damage by x-ray radiation, 80% flux was used in the defocused mode (beam size 5500 µm (Horizontal) x 600 µm (Vertical)) and no damage was observed scan after scan to any samples. All samples were also protected from the x-ray beam during spectrometer movements by a shutter synchronized with the scan program. Cu XAS energy was calibrated by the first maxima in the second derivative of the copper metal X-ray Absorption Near Edge Structure (XANES) spectrum. The CuO reference compound diluted with Boron Nitride (BN) and the Cu complexes in solution and upon deposition electrode surfaces were additionally measured on the CLAESS wiggler beamline at the ALBA synchrotron light source whereby the radiation was monochromatized using a pair Si (111) crystals. Similarly, two glassy carbon sheets wrapped in kapton tape were mounted between PEEK sample holders and measured with a circular beam spot size of around 15 µm using a liquid nitrogen cryostat cooled down to 77 K. Fluorescence absorption measurements were carried out on hybrid materials at ALBA with an Amptek silicon drift solid state detector (XR-100 SDD)[4Error! Bookmark not defined.] placed at 90 degrees to the incoming beam. The silicon drift detector was placed on a motorized stage allowing the sample-detector distance to be easily changed between 30-110 mm.[5] Solid CuO diluted with BN powder was pressed between polypropylene and mylar tape, and measured in the cryostat in transmission mode. Around 3 scans were collected on CuO and around 20-25 scans were collected on the solution samples and hybrid materials. Care was once again taken to measure at both solution and hybrid samples to minimize radiation damage. No more than 2 scans were taken in this instance on each spot on the solution samples.

Extended X-ray Absorption Fine Structure (EXAFS) Analysis

Athena software[6] was used for data processing. The energy scale for each scan was normalized using copper metal standard. Data in energy space were pre-edge corrected, normalized, deglitched (if necessary), and background corrected. The processed data were next converted to the photoelectron wave

vector (k) space and weighted by k^2. The electron wave number is defined as $k = [2m(E - E_0)/\hbar^2]^{1/2}$, E_0 is the energy origin or the threshold energy. K-space data were truncated near the zero crossings k = 1.839 to 11.1 Å^{-1} for the solution and the hybrid materials, in Cu EXAFS before Fourier transformation. The k-space data were transferred into the Artemis Software for curve fitting. In order to fit the data, the Fourier peaks were isolated separately, grouped together, or the entire (unfiltered) spectrum was used. The individual Fourier peaks were isolated by applying a Hanning window to the first and last 15% of the chosen range, leaving the middle 70% untouched. Curve fitting was performed using *ab initio*-calculated phases and amplitudes from the FEFF8[7] program from the University of Washington. *Ab initio*-calculated phases and amplitudes were used in the EXAFS equation

$$\chi(k) = S_0^2 \sum_j \frac{N_j}{kR_j^2} f_{eff_j}(\pi, k, R_j) e^{-2\sigma_j^2 k^2} e^{\frac{-2R_j}{\lambda_j(k)}} \sin(2kR_j + \phi_{ij}(k)) \qquad (1)$$

where N_j is the number of atoms in the j^{th} shell; R_j the mean distance between the absorbing atom and the atoms in the j^{th} shell; f_{eff_j} (π,*k*, R_j) is the *ab initio* amplitude function for shell *j*, and the Debye-Waller term $e^{-2\sigma_j^2 k^2}$ accounts for damping due to static and thermal disorder in absorber-backscatterer distances. The mean free path term $e^{\frac{-2R_j}{\lambda_j(k)}}$ reflects losses due to inelastic scattering, where $\lambda_j(k)$, is the electron mean free path. The oscillations in the EXAFS spectrum are reflected in the sinusoidal term $\sin(2kR_j + \phi_{ij}(k))$, where $\phi_{ij}(k)$ is the *ab initio* phase function for shell *j*. This sinusoidal term shows the direct relation between the frequency of the EXAFS oscillations in k-space and the absorber-backscatterer distance. S_0^2 is an amplitude reduction factor.

The EXAFS equation[8] (equation 2) was used to fit the experimental Fourier isolated data (q-space) as well as unfiltered data (k-space) and Fourier transformed data (R-space) using *N*, S_0^2, E_0, *R,* and σ^2 as variable parameters (Table S1). *N* refers to the number of coordination atoms surrounding Cu for each shell. The quality of fit was evaluated by R-factor and the reduced Chi^2 value. The deviation in E_0 ought to be less than or equal to 10 eV. R-factor less than 2% denotes that the fit is good enough.**Error! Bookmark not defined.**

whereas R-factor between 2 and 5% denotes that the fit is correct within a consistently broad model. The reduced Chi^2 value is used to compare fits as more absorber-backscatter shells are included to fit the data. A smaller reduced Chi^2 value implies a better fit. Similar results were obtained from fits done in k, q, and R-spaces.

General electrochemistry

Cyclic Voltammetry (CV), Linear Sweep Voltammetry (LSV), and Differential Pulse Voltammetry (DPV) and Controlled Potential Electrolysis (CPE) experiments were carried out on an IJ-Cambria CHI-660 potentiostat. We used a one-compartment three-electrode cell for these measurements except the CPE, for which a two-compartment three-electrode configuration was employed. Glassy Carbon (GC) or boron doped diamond (BDD) disk electrodes (3 mm of diameter) were used as working electrodes, Pt wire (unless indicated) as counter electrode, Mercury/Mercurous sulfate (K_2SO_4 sat.), MSE, as reference electrode for CV, LSV and DPV. For CPE, Silver/Silver Chloride (KCl sat.) was used as reference and either BDD plate (BDDp) disk or GC plate (GCp) as working electrode. All redox potentials in aqueous solutions are reported versus NHE by adding 0.65 V or 0.2 V to the measured potential, depending on whether MSE or Silver/Silver Chloride electrodes were employed respectively. In organic solvent, the potential was reported versus the Fc/Fc^+ couple that was independently measured in the same conditions.

GC disk working electrode pretreatment for homogeneous phase analysis consisted in polishing with 1, 0.3 and 0.05 μm alumina paste whereas BDD disk electrode was polished using diamond paste. After polishing, the electrodes were rinsed with water and acetone and blow-dried finally.

CVs and LSVs were collected at 50 $mV \cdot s^{-1}$ except other specification. DPV were obtained with the following parameters: amplitude= 50 mV, step height=4 mV, pulse width= 0.05 s, pulse period= 0.5 s and sampling width= 0.0167 s. $E_{1/2}$ values for the reversible waves were obtained from the half potential between the oxidative and reductive peaks, and the one for irreversible processes are estimated according to the potential at the I_{max} in DPV measurements. All the measurements were done applying IR compensation.

When acetonitrile was used as organic solvent, tetrabutylammonium hexafluorophosphate ($[NBu_4]PF_6$) was added in a concentration of 0.1 M as supporting electrolyte.

Oxygen quantification

For the CPE experiments coupled to Oxygen detection, one of the two compartments was loaded with the catalyst solution (4 ml) and the other compartment was loaded with buffer solution (4 ml). The working and reference electrodes were placed in the catalyst compartment whereas the counter was placed in the other. Both compartments were closed with septa, through which the electrodes were connected to the potentiostat. The Clark sensor was then connected through the septum to the catalyst compartment. Then, the cell was bubbled with nitrogen during 30 min until the Clark signal indicates the absence of oxygen, after which the nitrogen flow was removed and the Clark signal was allowed to stabilize during 10 more min to check for possible leaks. Finally, the CPE experiment was started by setting up the potential. After the corresponding time, the CPE was stopped and the signal of the Clark was again left to stabilize until a plateau was observed indicating that no more oxygen is being detected. The oxygen produced was quantified upon calibration of the Clark sensor in the same experimental set up by adding known amounts of pure oxygen. The Faradaic Efficiency (FE) was calculated taking into account the total charge passed during the CPE (Q), the number of electrons involved in the water oxidation process ($n_e = 4$), the Faraday constant (F) and the amount of oxygen produced (N_{O2}), following the next equation:

$$FE = \frac{N_{O2}}{\frac{Q}{n_e F}}$$

TONs calculation based on electroactive catalyst

In order to calculate the turnover number of the oxygen evolution experiment, we started considering the amount of catalyst in the bulk solution and the amount of oxygen generated after the CPE yielding a TON of 34 using the BDD electrode.

However, for a stable catalyst that remains active after the CPE, this calculation underestimates the real TON value since only the catalyst in the electroactive layer of the solution in contact with the electrode is involved in the water oxidation. Savéant and co-workers[9] developed a methodology considering this fact in electrocatalytic process. In addition, Lin and co-workers adapted this formula to the water oxidation reaction:[10]

$$TON = \frac{k_{obs}t}{1 + \exp\left[\frac{F}{R \cdot T}(E^0_{cat} - E)\right]} \quad (2)$$

The calculated TON considering the catalytic amount around the electrode is 6045490 for the bulk performed at 1.2 V during 12 h in pH 7 aqueous solution.

Foot-of-the-wave analysis

Due to the complicated analysis of a 4 electrons 4 protons catalytic process, Foot of the wave analysis was performed by using the equations deducted for a simplified EC_{cat} process where E means electron transfer step and C_{cat} means catalytic chemical step.[11,12] The kinetic constant obtained in this way represent and observed kinetic constant (k_{obs}) for the overall catalytic mechanism. The equation derived from this analysis depends on the assumption of the order of reaction in catalyst in the rate determining step, giving different expressions for a first order (equation 3) and second order (equation 4).

$$\frac{i}{i_p} = \frac{n_e \cdot 2.24 \cdot \sqrt{\frac{R \cdot T}{F \cdot v} \cdot k_{1st}}}{1 + \exp\left[\frac{F}{R \cdot T}(E^0_{cat} - E)\right]} \quad (3)$$

$$\frac{i}{i_p} = \frac{n_e \cdot 2.24 \cdot \sqrt{\frac{R \cdot T}{3 \cdot F \cdot v} \cdot k_{2nd} \cdot C^0_{cat}}}{\left(1 + \exp\left[\frac{F}{R \cdot T}(E^0_{cat} - E)\right]\right)^{3/2}} \quad (4)$$

Where k_{1st} is the observed rate constant assuming a first order mechanism in catalyst, k_{2nd} is the observed rate constant assuming a second order mechanism in catalyst, F is the Faraday constant, R is the gas constant, T is the temperature, *v* is the scan rate. In this case, n_e = 4 due to the 4 electrons involved in the

catalytic water oxidation to dioxygen. The intensity of the one-electron wave (i_p) has been estimated from the one-electron precatalytic wave. E^0_{cat} has been determined as the potential of the catalytic process obtained from DPV experiments. For each catalyst concentration, the FOWA has been performed in similar regions of the potential range, selected as the foot of the wave region where the plot of i/i_p versus $1/(1+\exp[F/(RT)(E^0_{cat}-E)])$ behaves linearly ($R^2 > 0.85$). In any case, k_{obs} obtained from the slope of that plot should be constant with the catalyst concentration if the assumption of the order of reaction and thus the equation used are correct.

Computational chemistry

We have performed all the calculations with the Gaussian09 program package[13] using Density Functional Theory. We employed B3LYP functional including empirical dispersion correction proposed by Grimme (B3LYP-D3).[14,15] The basis set was divided into 6-31+G(d) for C, N, S, O and H atoms,[16–18] and LANL2TZ(f) for Cu.[19–21] Implicit solvation was introduced through the SMD model,[22] with methanol, acetonitrile or water as the solvent. All geometry optimizations were computed in solution without symmetry restrictions. We confirmed the nature of all computed stationary points as minima through vibrational frequency calculations. Free energy corrections were calculated at 298.15 K and 105 Pa pressure, including zero point energy corrections (ZPE). In addition, a correction term of 1.9 kcal/mol (at 298 K) was added when necessary to account for the standard state concentration of 1 M, except for water whose considered concentration was 55.6 M and the correction term 4.3 kcal/mol. Unless otherwise mentioned, all reported energy values are free energies in solution.

In the transformation from free energies to electrochemical magnitudes we took from the literature the values of 4.28 V for the absolute potential of the standard hydrogen electrode[23] and-11.72 eV for the free energy of the proton in aqueous solution at pH=1.[24] The value for the free energy of the proton was translated to the experimental pH value by adding a correction term of -0.059*pH, following the same procedure as other authors.[25]

The functional for the DFT calculations was B3LYP-D3 based on the calibration carried out in a previous work on related systems,[2] where its performance was

compared with that of M06, M06-D3, M06L, M06-2X, ωB97xD and B97D. In order to validate this DFT methodology again, we compare the calculated redox potential with respect to the experimental values of the Cu(III)/Cu(II) redox couple for both catalysts in water and organic solutions, finding an good agreement.

2. Synthetic details of new macrocyclic complexes

H_4L1, H_4L2

The macrocyclic ligand H_4L1 was prepared and characterized following the procedures already described in the literature.[26]

H_4L1: **Yield** 63%. Elemental Analysis calc.(%) for $C_{19}H_{18}N_4O_4 \cdot 2\ H_2O$: C 55.96, H 5.59, N 13.74, found (%): C 56.36, H 5.38, N 13.07. HR-MS (ESI negative mode, CH_2Cl_2): m/z $[M]^-$ = 365.1260 (Expected: 365.1255). ^{1}H-NMR (DMSO-d_6): δ [ppm]= 9.66 (N-H1, s, 2H), 9.55 (N-H2, s, 2H), 7.62 (Ph-H, m, 2H), 7.35 (Ph-H, m, 6H), 1.54 (Me-H, s, 6H).

H_4L2 has been synthetized following similar procedures as previously employed for H_4L1,[26] using dimethylmalonyl dichloride instead of oxalyl chloride in order to get the 14-member ring ligand: to a solution of 100 mg (0.32 mmol) of N^1,N^3-bis(2-aminophenyl)-2,2-dimethylmalonamide synthetized as previously described[26] in THF (100 ml) was added 2 ml of pyridine and subsequently a solution of dimethylmalonyl dichloride (0.32 mmol) dissolved in 50 ml of THF dropwise. The reaction was allowed to stir for 12 h, time after which a pale pink precipitate is formed. The precipitate (pyridinium chloride) was filtered off and the solution is evaporated until dryness by rotatory evaporation. The remaining white solid is further purified by sonication in hexane affording pure H_4L2.

H_4L2: **Yield** 75 %. Elemental Analysis calc. (%) for $C_{22}H_{24}N_4O_4 \cdot 0.5\ H_2O$: C 63.30, H 6.04, N 13.42, found (%): C 63.60, H 5.58, N 13.20. HR-MS (ESI negative mode, CH_2Cl_2): m/z $[M]^-$ = 407.1743 (Expected: 407.1725). ^{1}H-NMR (DMSO-d_6): δ [ppm]= 9.32 (N-H, s, 4H), 7.41 (H2, m, 4H), 7.21 (H1, m, 4H), 1.53 (Me-H, s, 12H). ^{13}C-NMR (DMSO-d_6): δ [ppm]= 171.96 (C4, 4C), 131.16 (C3, 4C), 126.36 (C2, 4C), 126.04 (C1, 4C), 51.23 (C5, 4C), 24.05 (C_{me}, 4C).

$[(L1)Cu](NMe_4)_2$ and $[[(L2)Cu](NMe_4)_2$

These copper complexes have been synthesized following similar procedure as described in the literature:[2,3] 0.5 mmol of the corresponding ligand (H_4L1 and H_4L2) was suspended in methanol (mL) and the mixture was sonicated until homogeneous suspension. To this mixture, 1.05 ml of a tetramethylammonium hydroxide (25% wt. methanolic solution, 2mmol) was added and then heated at 70 ºC with vigorous stirring until reaching a clear solution. Afterward, Copper (II) perchlorate hexahydrate was added dropwise in a methanolic solution (0.5 mmol in 5 mL). After 30 min of reaction, the appearing precipitate was filtered off and the filtrate was concentrated down to about 1 ml. Adding 1 ml of acetonitrile lead to the precipitation of more solid that was removed again by filtration. The remaining copper complex ($[(LY)Cu](NMe_4)_2$) in solution was precipitated using equal volume of ether and acetone. This product was filtered, washed with acetone and ether, and dried under vacuum. Slow diffusion of ether into concentrated methanolic solution of the complexes afforded single crystal suitable for X-Ray diffraction analysis.

$[(L1)Cu](NMe_4)_2$: **Yield** 89 %. Elemental Analysis calc. (%) for $C_{27}H_{38}CuN_6O_4 \cdot 5.5\ H_2O$: C 48.17, H 7.34, N 12.48, found (%): C 48.14, H 7.70, N 12.14.

$[(L2)Cu](NMe_4)_2$: **Yield** 92 %. Elemental Analysis calc.(%) for $C_{30}H_{44}CuN_6O_4$: C 58.47, H 7.20, N 13.64, found (%): C 58.09, H 7.13, N 13.85.

$[(L1)Cu](NMe_4)$ and $[[(L2)Cu](NMe_4)$

These copper (III) complexes have been synthesized following similar procedure as described in the literature by chemical oxidation with iodine:[3] 0.174 mmol of the corresponding copper (II) complex ($[(L1)Cu](NMe_4)_2$ and $[[(L2)Cu](NMe_4)_2$)was dissolved in 10 ml of methanol and then 5 ml of a methanolic solution containing a slight excess of I_2 (0.09 mmol) and the solution was warmed to 50 ºC for 30 min. Afterward, the appearing solid was filtered off and the solution was evaporated until a dry solid was obtained. The solid was further purified by recrystallization with ether from a methanol solution.

$[(L1)Cu](NMe_4)$: **Yield** 93 %. Elemental Analysis calc. (%) for $C_{23}H_{26}CuN_5O_4$: C 55.25, H 5.24, N 14.01, found (%): C 55.62, H 5.61, N 14.48.

[(L2)Cu](NMe$_4$): **Yield** 95 %. Elemental Analysis calc. (%) for $C_{26}H_{32}CuN_5O_4$: C 57.60, H 5.95, N 12.92, found (%): C 57.42, H 5.81, N 13.24.

[(L1)Cu](NMe$_4$) has also been synthetized electrochemically by performing controlled potential electrolysis at 0.4 V in an aqueous solution containing 3 mL of 0.1 mM $\mathbf{1}^{2-}$ at pH 7 (0.1 ionic strength of phosphate buffer) using a GC plate (1 cm^2) as working electrode until the charge correspond to one electron oxidation of all the complex in solution (29 mC), reaching a background current density of 0.05 mA·cm^{-2}.

[(L1)Zn]Na$_2$

This complex was synthesized by a different procedure than in the case of Cu complex.50.02 mmols of the precursor ligand were weighted and dispersed in 1 mL of water/MeOHmixture (1:1) using a sonicator for 15 minutes. The mixture was brought to 80 ºC and 0.1 ml of a solution containing 1mmol/ml of NaOH in water was added, stirring after at 80ºC for 30 minutes. A Zn(OTf)$_2$ solution of 0.02 mmols in 0.2 mL of water was added to the mixture drop wise. After 1 day at the same temperature, the solids are removed by filtration and the solvent is totally evaporated. The obtained solid was dissolved in MeOH to remove unreacted ligand by filtration and solvent is again evaporated. Finally, the remaining solid was washed with ether and vacuum dried. Yield 53%.

3. Structure and Spectroscopic Characterization

NMR Spectroscopy

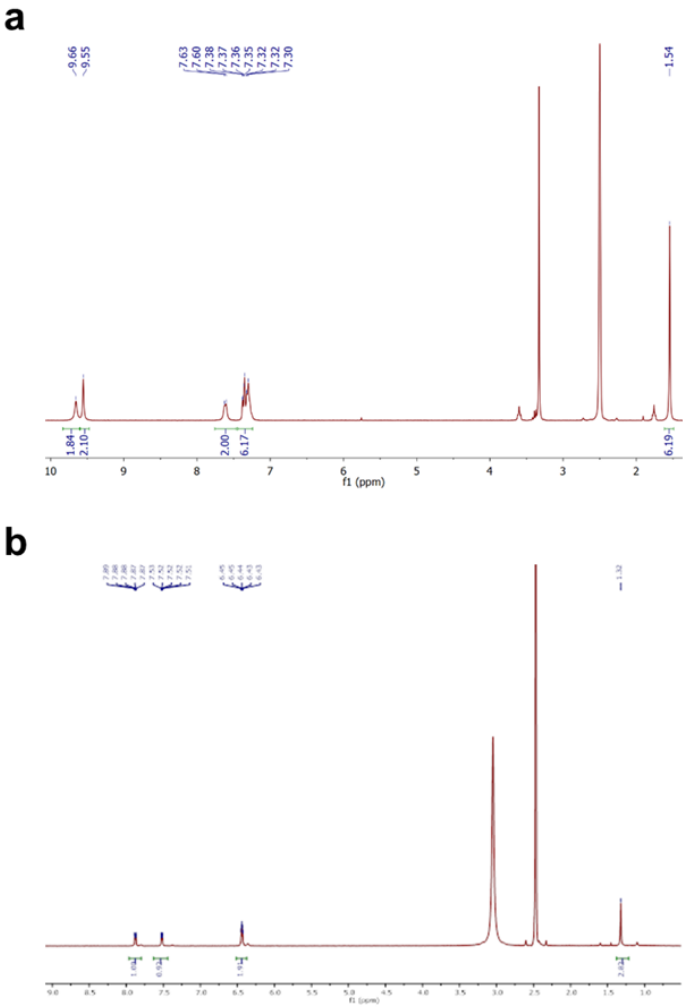

Figure S1. ^{1}H-NMR spectrum of (a) ligand H_4L1 and (b) $[(L1)Zn]Na_2$ in d_6-DMSO (400 MHz).

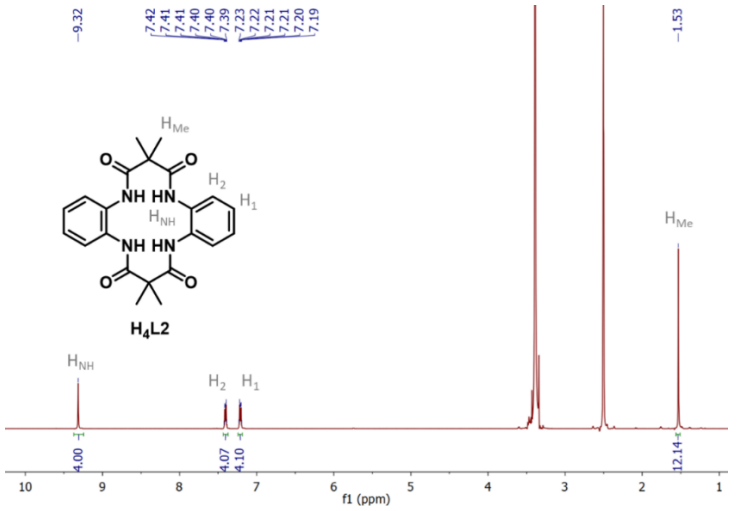

Figure S2. ^{1}H-NMR spectrum of ligand H_4L2 in d_6-DMSO (400 MHz).

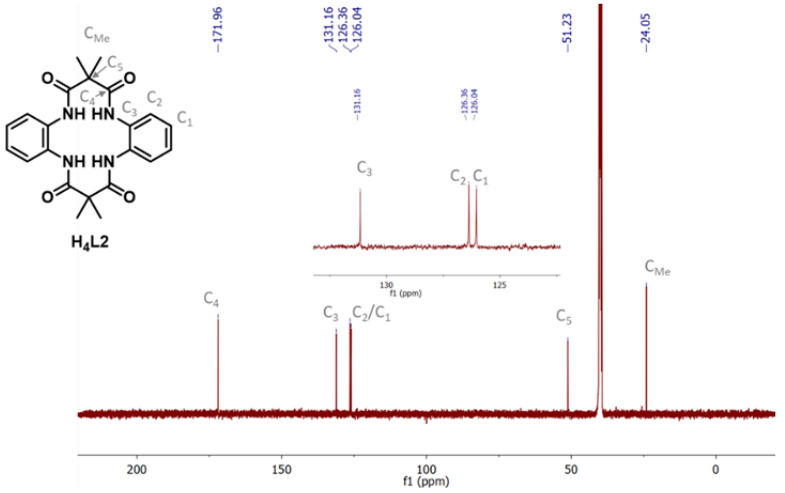

Figure S3. ^{13}C-NMR spectrum of ligand H_4L2 in d_6-DMSO (400 MHz).

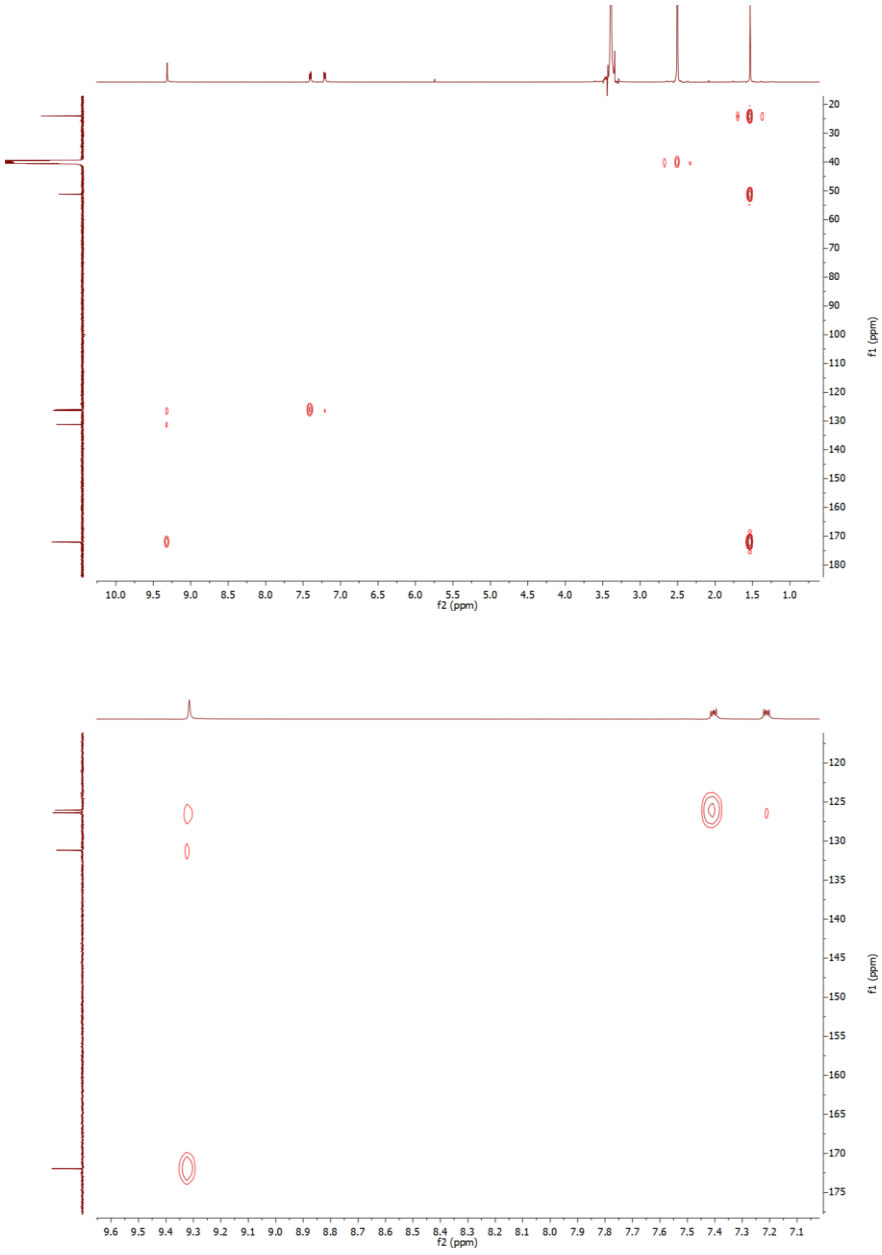

Figure S4. HMBC spectrum of ligand H_4L2 in d_6-DMSO (400 MHz).

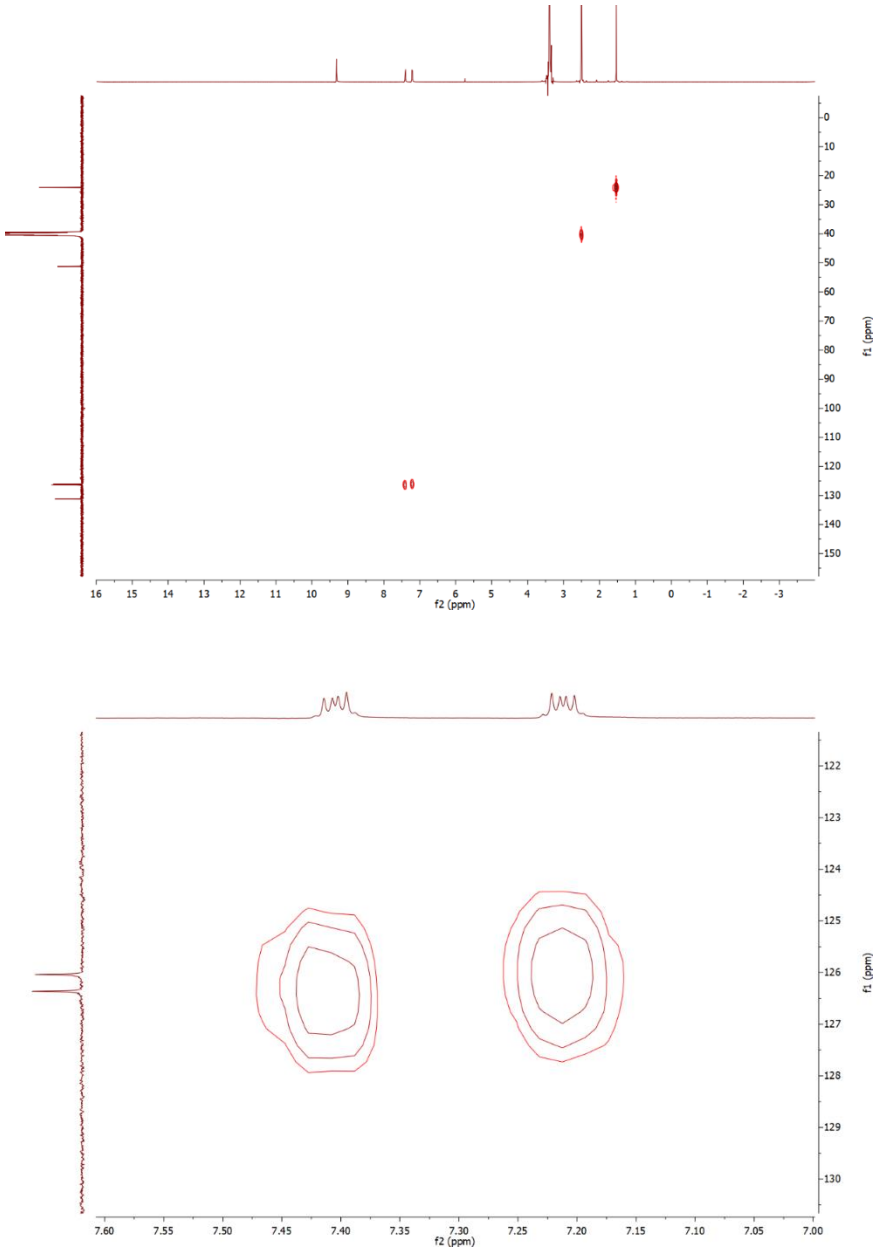

Figure S5. HMQC spectrum of ligand H_4L2 in d_6-DMSO (400 MHz).

ESI-MS Spectrometry:

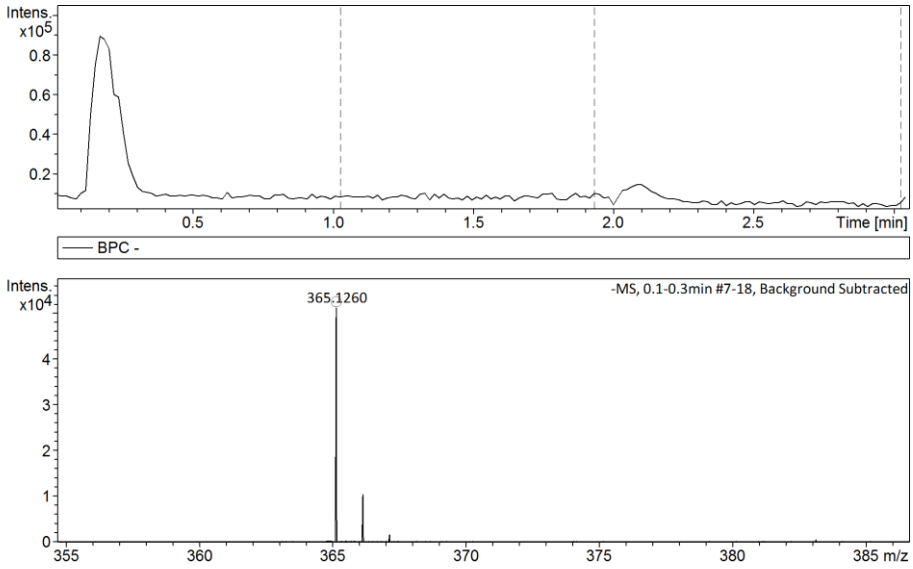

Figure S6. ESI-MS spectrum (negative mode) of ligand H_4L1 ligand in MeOH solution.

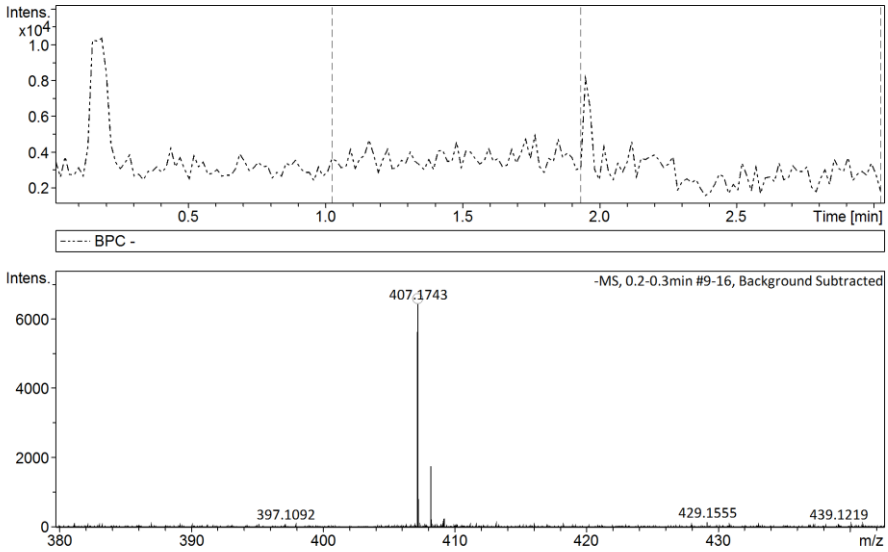

Figure S7. ESI-MS spectrum (negative mode) of ligand H_4L2 ligand in MeOH solution.

X-Ray Crystallography

Crystal preparation: Crystals of $\mathbf{1}^{2-}$, $\mathbf{2}^{2-}$, $\mathbf{1}^{-}$ and $\mathbf{2}^{-}$ were grown by slow diffusion of diethyl ether into an acetonitrile solution of the corresponding complex. The crystals for these samples were selected using a Zeiss stereomicroscope using polarized light and prepared under inert conditions immersed in perfluoropolyether as protecting oil for manipulation.

Data collection: Crystal structure determinations for samples $\mathbf{1}^{2-}$, $\mathbf{2}^{2-}$, $\mathbf{1}^{-}$ and $\mathbf{2}^{-}$ were carried out using a Apex DUO Kappa 4-axis goniometer equipped with an APPEX 2 4K CCD area detector, a Microfocus Source E025 IuS using MoK_α radiation, Quazar MX multilayer Optics as monochromator and an Oxford Cryosystems low temperature device Cryostream 700 plus (T = -173 ˚C). *Programs used:* Bruker Device: Data collection APEX-2[27], data reduction Bruker Saint[28] V/.60A and absorption correction SADABS[29] or TWINABS[30].

Structure Solution and Refinement: Crystal structure solution was achieved using the computer program SHELXT[31]. Visualization was performed with the program SHELXle[32]. Missing atoms were subsequently located from difference Fourier synthesis and added to the atom list. Least-squares refinement on F^2 using all measured intensities was carried out using the program SHELXL 2015[33]. All non-hydrogen atoms were refined including anisotropic displacement parameters. **Comments to the structures:** Sample $\mathbf{1}^{2-}$: The asymmetric unit contains four molecules of the Cu metal-complex, eight tetramethyl ammonium cations and sixteen water molecules. Two of the tetramethyl ammonium cations are disordered in two orientations (ratios 65:35 and 75:25). The compound crystallizes in the chiral space group $P2_1$ as a racemic twin (ratio twinning 52:48). Sample $\mathbf{1}^{-}$**:** The asymmetric unit contains one molecule of the Cu metal-complex, one tetramethyl ammonium cation and one acetonitrile molecule. Sample $\mathbf{2}^{2-}$: The asymmetric unit contains one molecule of the Cu metal-complex and two tetramethyl ammonium cations. The sample measured was multicomponent crystal (Probably more than five crystals) of very low diffraction power, reaching only low resolution (Commented B-alert in the CIF-file related to the low resolution). Two crystals could be identified (ratio 74:26) which were processed with TWINABS taking in account overlapping reflections. Sample $\mathbf{2}^{-}$: The asymmetric unit contains a half molecule of the Cu metal-complex, a half

tetramethyl ammonium cation and a half acetonitrile molecule. The complete molecule is generated by a mirror plane operation. The main molecule is disordered in to positions (ratio 50:50) showing a shift of 0.6 Å for both positions. The acetonitrile molecule is disordered in two orientations with a ratio of 50:50.

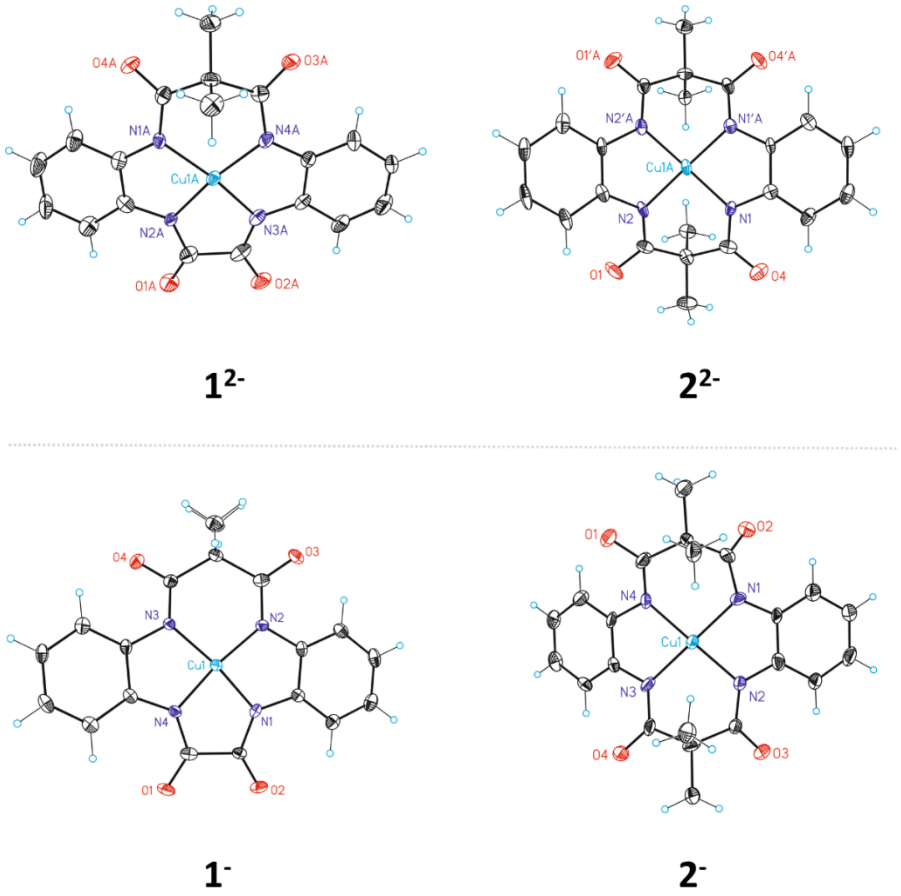

1^{2-} **2^{2-}**

1^{-} **2^{-}**

Figure S8. ORTEP drawing (thermal ellipsoids drawn at a 50 % probability level) showing the top view of the structure of **1^{2-}**, **2^{2-}**, **1^{-}** and **2^{-}**. Tetramethyl ammonium cations and solvent molecules have been omitted in the sake of clarity. Colour code: C, black; N, blue; O, red; Cu, light blue.

X-Ray absorption Spectroscopy

Table S1. EXAFS Fits parameters

Sample	Fit	Region	Shell,N	R, Å	E_0	ss.^{2} (10^{-3})	R-factor	Reduced Chi-square
1^{2-} powder	1	1	Cu-N,4	1.91	4.7	5.4	0.0009	372
	2	I,II	Cu-N,4	1.89	0.4	4.6	0.0393	3635
			Cu-C,8	2.78				
	3	all	Cu-N,4	1.89	2.0	4.8	0.0151	2194
			Cu-C,8	2.81		11.9		
			Cu-C,17	3.39		47.3		
	4	**all**	**Cu-N,4**	**1.90**	**2.8**	**5.0**	**0.0117**	**810**
			Cu-C,8	**2.82**		**10.4**		
			Cu-C,17	**3.29**		**26.0**		
			Cu-C,13	**3.66**		**19.7**		
			Cu-N,8	**3.85**		**8.4**		
1^{-} powder	5	1	Cu-N,4	1.83	4.9	5.7	0.0002	79
	6	I,II	Cu-N,4	1.82	1.5	5.7		
			Cu-C,8	2.72		23.2		
	7	all	Cu-N,4	1.82	2.1	5.7	0.0125	1495
			Cu-C,8	2.76		13.3		
			Cu-C,17	3.35		47.4		
	8	**all**	**Cu-N,4**	**1.82**	**2.7**	**5.8**	**0.0078**	**460**
			Cu-C,8	**2.78**		**11.5**		
			Cu-C,17	**3.26**		**24.2**		
			Cu-C,13	**3.63**		**17.7**		
			Cu-N,8	**3.83**		**7.1**		
1^{2-} in H_2O	9	1	Cu-N,4	1.93	6.6	3.9	0.0012	1428
	10	I,II	Cu-N,4	1.92	2.4	3.2	0.0261	5535
			Cu-C,8	2.75		18.8		
	11	all	Cu-N,4	1.92	3.5	3.3	0.0115	5220
			Cu-C,8	2.79		13.2		
			Cu-C,17	3.41		38.1		
	12	**all**	**Cu-N,4**	**1.92**	**3.1**	**3.6**	**0.0130**	**2087**
			Cu-C,8	**2.80**		**10.8**		
			Cu-C,17	**3.29**		**26.6**		

1^{-} in CH_3OH	13	1	Cu-N,4	1.84	4.2	5.6	0.0036	292
	14	I,II	Cu-N,4 Cu-C,8	1.83 2.67	1.3	5.5 39.3	0.0249	612
	15	all	Cu-N,4 Cu-C,8 Cu-C,17	1.83 2.74 3.34	1.6	5.3 16.4 46.5	0.0184	489
	16	**all**	**Cu-N,4** **Cu-C,8** **Cu-C,17** **Cu-C,13** **Cu-N,8**	**1.83** **2.77** **3.24** **3.59** **3.77**	**2.5**	**5.5** **12.9** **25.6** **23.0** **11.6**	**0.0134**	**169**
1^{-} in H_2O	17	1	Cu-N,4	1.85	2.9	6.1	0.0005	11
	18	I,II	Cu-N,4 Cu-C,8	1.84 2.65	-0.1	6.1 34.1	0.0188	153
	19	all	Cu-N,4 Cu-C,8 Cu-C,17	1.83 2.70 3.32	0.3	5.7 20.0 68.3	0.0151	172
	20	**all**	**Cu-N,4** **Cu-C,8** **Cu-C,17** **Cu-C,13** **Cu-N,8**	**1.84** **2.73** **3.19** **3.52** **3.78**	**1.4**	**5.7** **13.6** **27.9** **13.6** **8.3**	**0.0101**	**48**
1^{2-} generated electrochemically	21	1	Cu-N,4	1.86	4.4	7.8	0.0008	42
	22	I,II	Cu-N,4 Cu-C,8	1.86 2.73	2.5	6.6 38.8	0.0157	190
	23	all	Cu-N,4	1.85	2.9	6.9	0.01	178

GCp after bulk catalysis in ph 7 solution with 1 mM $\mathbf{1}^{2-}$	29	1	Cu-N,4	1.93	4.9	5.1	0.0006	43
	30	I,II	Cu-N,4 Cu-C,8	1.93 2.77	5.1	4.5 77.6	0.0058	90
	31	all	Cu-N,4 Cu-C,8 Cu-C,17	1.92 2.83 3.52	2.9	4.9 37.3 55.4	0.0028	74
	32	**all**	**Cu-N,4** **Cu-C,8** **Cu-C,17** **Cu-C,13** **Cu-N,8**	**1.92** **2.86** **3.42** **3.81** **4.02**	**3.8**	**5.0** **29.5** **36.0** **17.5** **25.7**	**0.0021**	**60**

- The amplitude reduction factor, S_0^2 was fixed to 1.

Region I refers to the region between 1 to 1.9 Å, II to 1- 2,8/2.9 Å, all to 1 to 3.8/4 Å.

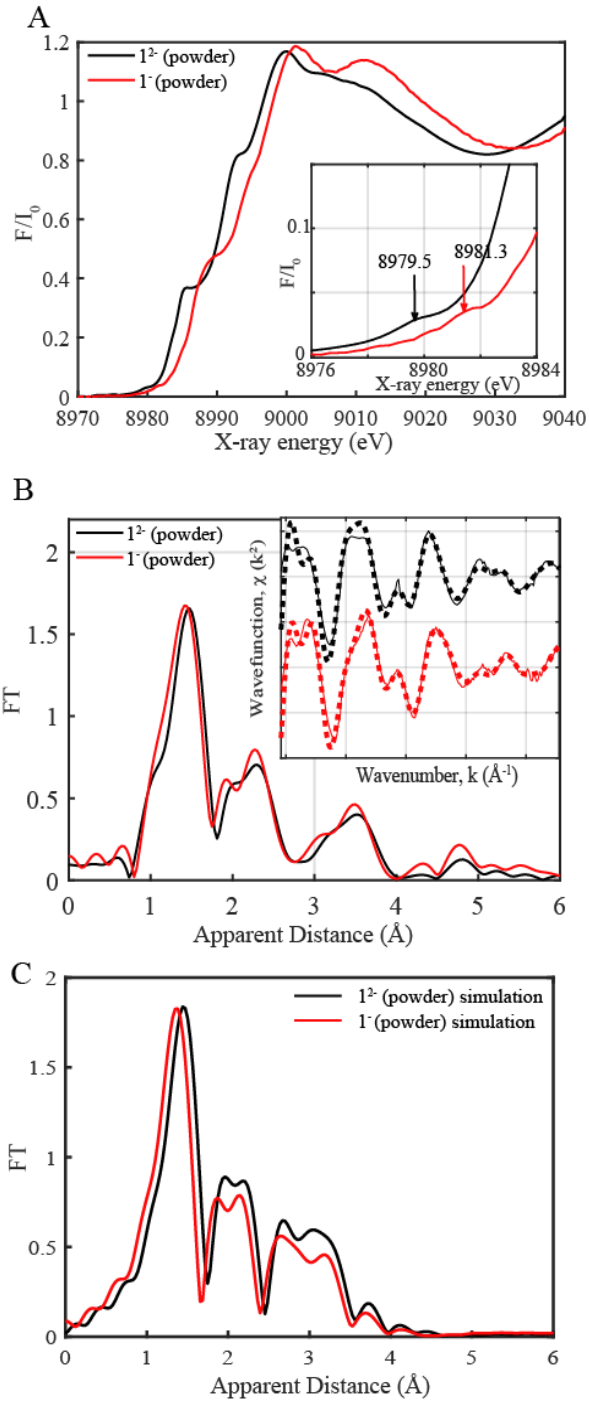
A
1²⁻ (powder)
1⁻ (powder)
F/I0
X-ray energy (eV)
8979.5
8981.3
B
1²⁻ (powder)
1⁻ (powder)
FT
Wavefunction, χ (k²)
Wavenumber, k (Å⁻¹)
Apparent Distance (Å)
C
1²⁻ (powder) simulation
1⁻ (powder) simulation
FT
Apparent Distance (Å)

Figure S9. A. Normalized Cu K-edge XANES of $\mathbf{1}^{2-}$ and $\mathbf{1}^{-}$ as powders. **Inset**. Zoom in of the pre-edge regions. **B**. Experimental Fourier transforms of k^2-weighted Cu EXAFS of $\mathbf{1}^{2-}$ and $\mathbf{1}^{-}$ in powder form **C.** Simulated Fourier transforms of k^2-weighted Cu EXAFS using DFT optimized coordinates as input.

UV-vis Spectroscopy

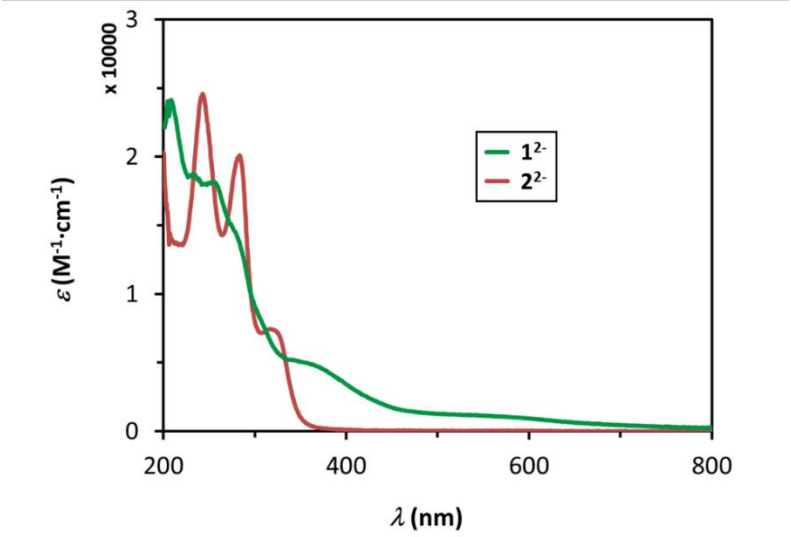

Figure S10. UV-vis spectra of a MeCN solution containing 1 mM of either $\mathbf{1}^{2-}$ (green trace) or $\mathbf{2}^{2-}$ (red trace).

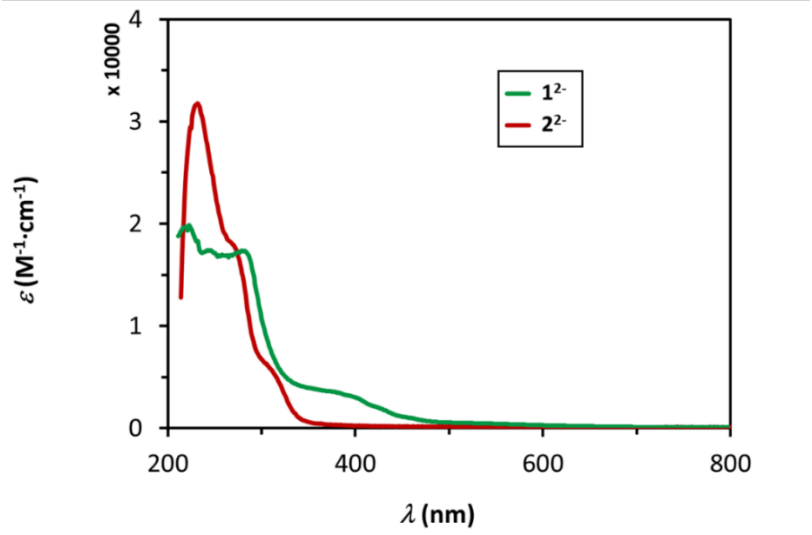

Figure S12. UV-vis spectra of a pH 7 aqueous solution containing 1 mM of either $\mathbf{1}^{2-}$ (green trace) or $\mathbf{2}^{2-}$ (red trace).

4. Stability of copper complexes against acidic demetallation:

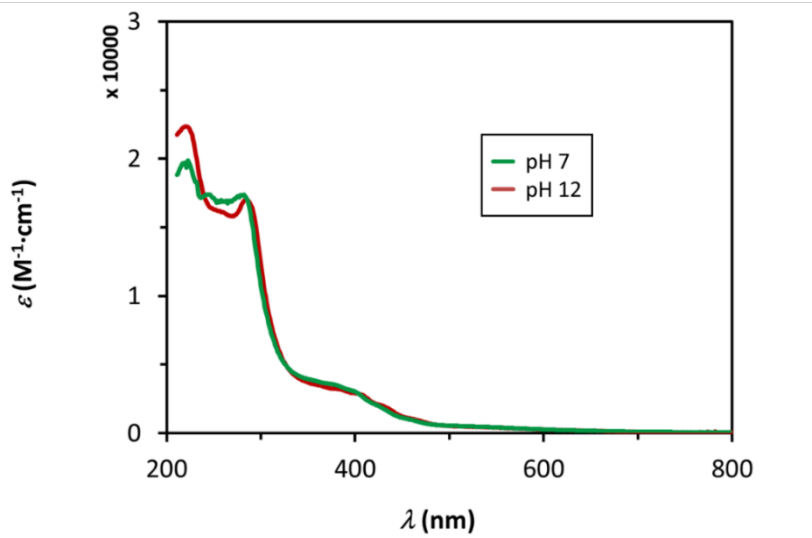

Figure S13. UV-vis spectra of a solution with 1 mM $\mathbf{1}^{2-}$ in aqueous solution at pH 7 (green trace) and 12 (red trace).

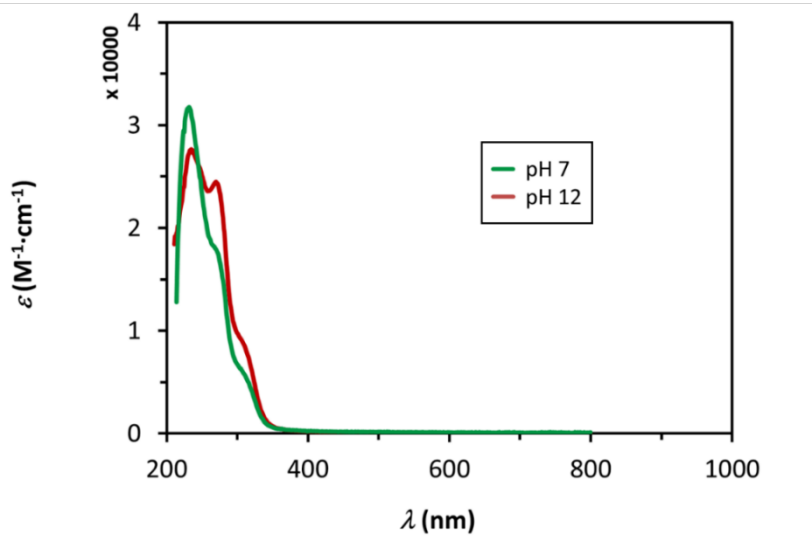

Figure S14. UV-vis spectra of a solution with 1 mM $\mathbf{2}^{2-}$ in aqueous solution at pH 7 (green trace) and 12 (red trace).

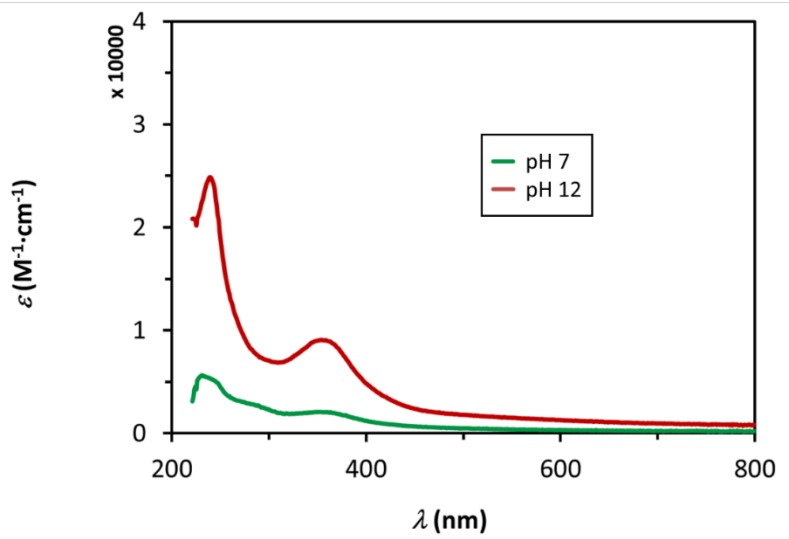

Figure S15. UV-vis spectra of a solution with 1 mM $\mathbf{3}^{2-}$ in aqueous solution at pH 7 (green trace) and 12 (red trace).

5. Electrochemistry of 1^{2-} and 2^{2-} in organic solvents

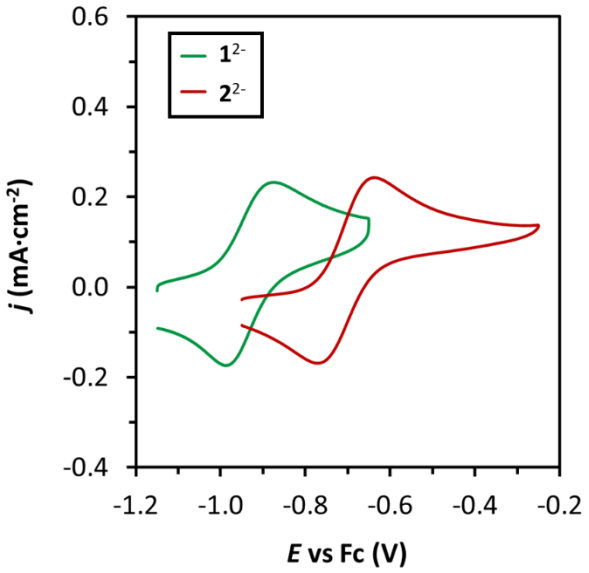

Figure S16. CV of 1 mM $\mathbf{1}^{2-}$ (green) and $\mathbf{2}^{2-}$ (red) in MeCN solutions containing 0.1 M $TBAPF_6$ as electrolyte. BDD disk working electrode was used and the scan rate was set to 100 $mV \cdot s^{-1}$.

Table S2. Redox potentials (*V*) of relevant species

Catalyst	*E1*	E2	E3
$\mathbf{1}^{2-}$ (MeCN)	-0.90 vs Fc	0.09 vs Fc	0.17 vs Fc
$\mathbf{2}^{2-}$ (MeCN)	-0.70 vs Fc	0.04 vs Fc	0.21 vs Fc
$\mathbf{3}^{2-}$ (MeCN)	-0.75 vs Fc	0.38 vs Fc	-

6. Electrochemistry of 1^{2-} and 2^{2-} in aqueous solutions

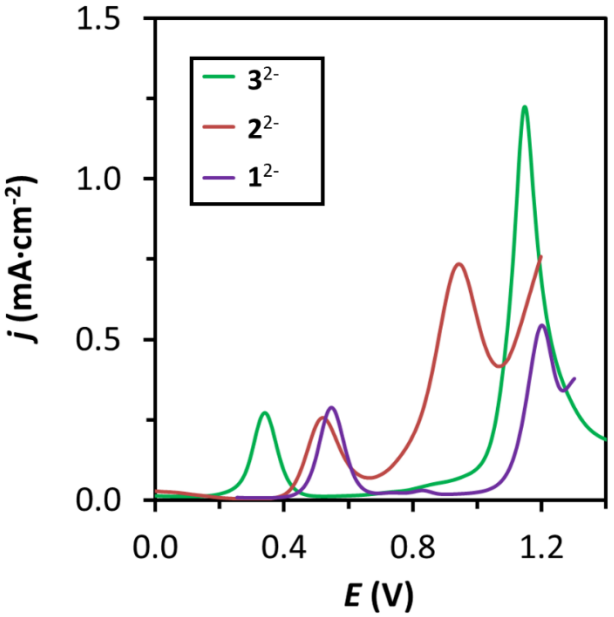

Figure S17. DPV of pH 12 solutions containing 1 mM $\mathbf{1}^{2-}$ (green), $\mathbf{2}^{2-}$ (red) and $\mathbf{3}^{2-}$ (purple) using BDD as a working electrode.

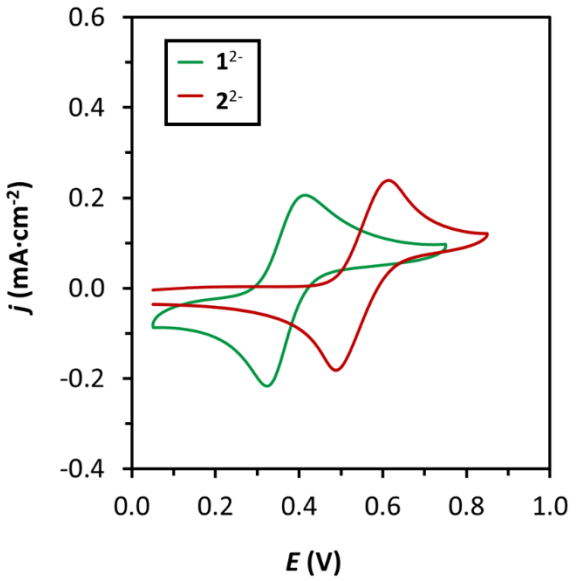

Figure S18. CV of 1 mM $\mathbf{1}^{2-}$ (green) and $\mathbf{2}^{2-}$ (red) in aqueous solution at pH 7 containing 0.1 M phosphate buffer. BDD disk working electrode was used and the scan rate was set to 100 mV·s^{-1}.

Table S3. Redox potentials (*V*) of relevant species

Catalyst	*E1*	E2	E3
$\mathbf{1}^{2-}$ (pH 12)	0.35 vs NHE	1.11 vs NHE	-
$\mathbf{2}^{2-}$ (pH 12)	0.55 vs NHE	0.91 vs NHE	-
$\mathbf{3}^{2-}$ (pH 12)	0.56 vs NHE	1.25 vs NHE	-
$\mathbf{1}^{2-}$ (pH 7)	0.35 vs NHE	1.11 vs NHE	1.18 vs NHE
$\mathbf{2}^{2-}$ (pH 7)	0.55 vs NHE	0.91 vs NHE	-
$\mathbf{3}^{2-}$ (pH 7)	-	-	-
$[(L1)Zn]^{2-}$ (pH7)	1.21 vs NHE	-	-
L1 (pH 7)	1.25 vs NHE	-	-

*Adsorption process during electrochemical oxidation of **1**$^{2-}$ to **1**$^{-}$*

An interesting side phenomenon associated with **1**$^{-}$ is the capacity to adsorb into electrode surfaces most likely via π-interactions given the planarity of this molecule. This phenomenon was monitored by CPE and CV (Figures S19-S26) using glassy carbon and boron doped diamond (BDD) electrodes and shows that it mainly occurs for concentrations of **1**$^{-}$ above 1 mM. As evidenced by the CV data (Figure S24-26), the copper complex **1**$^{2-}$ is physically adsorbed upon oxidation to **1**$^{-}$. The reverse scan shows a typical desorption wave featuring larger charge compared to the oxidative wave. The adsorbed layer was characterized by XANES and EXAFS (Figure S31) and interestingly, it features similar spectra to that of the molecular complex **1**$^{2-}$, suggesting a potential population of the SOMO π-orbital of the Cu complex by the electron density of the electrode surface. Electrochemical experiments (Figures S24-S26) and XPS (Figure S61) show that this complex desorbs from the surface of the electrode upon returning to the potentials corresponding to the Cu(II) oxidation state.

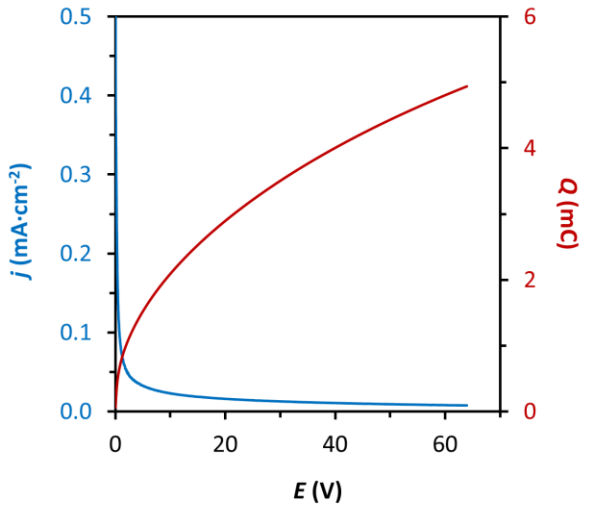

Figure S19. CPE at 0.3 V in an aqueous solution containing 1 mL of an aqueous solution with 1 mM $\mathbf{1}^{2-}$ at pH 7 using a GC disk (0.07 cm^2) as working electrode. The charge passed corresponds to 0.052 µmols of electrons, that is around the 5 % of the total charge expected for one mole of electrons (97 mC).

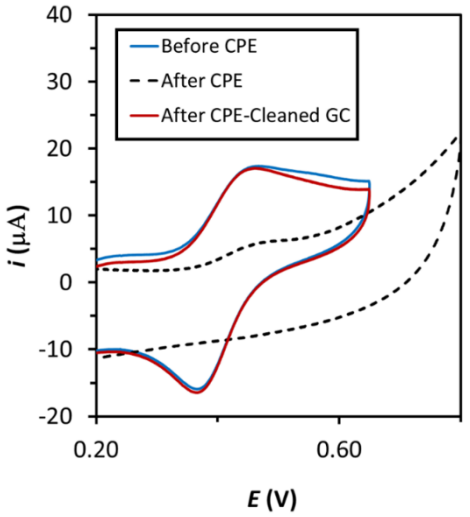

Figure S20. CV of an aqueous solution containing 1 mM of complex $\mathbf{1}^{2-}$ at pH 7 before and after CPE at 0.3 V (Figure S19) using the same GC disk electrode employed for the CPE experiment (blue and dashed black lines). CV of the same solution using the GC disk electrode after cleaning and polishing (red trace).

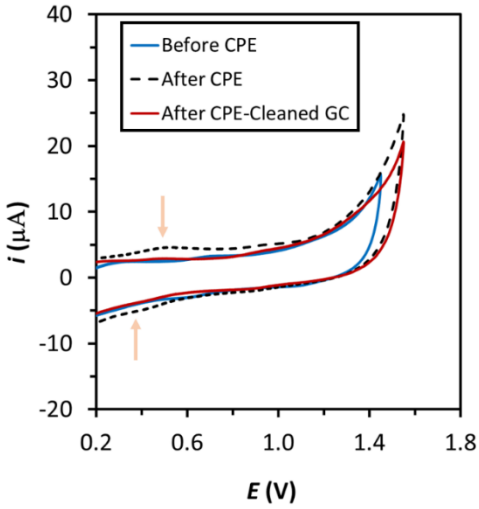

Figure S21. Rinse test after CPE at 0.3 V using 1 mM of complex $\mathbf{1}^{2-}$ (Figure S19): CV in a fresh pH 7 buffer solution of the GC disk electrode before (blue line) and after (black dashed line) the CPE (Figure S19) and CV of the same electrode after polishing (red line). Yellow arrows point to the appearance of the redox wave corresponding to complex $\mathbf{1}^{2-}$ adsorbed upon oxidation.

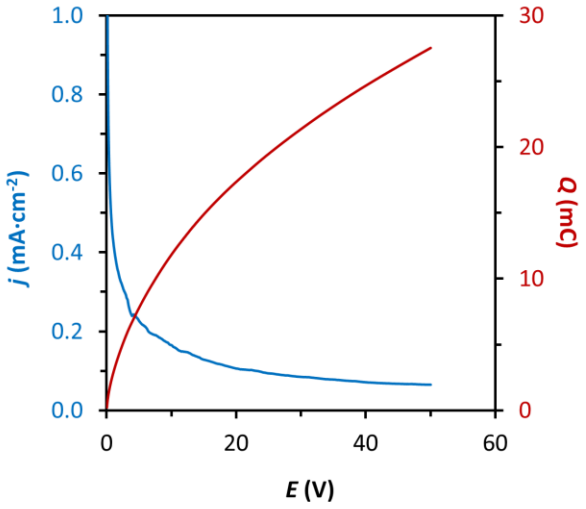

Figure S22. CPE at 0.3 V in an aqueous solution containing 1 mL of 1 mM $\mathbf{1}^{2-}$ at pH 7 using a GC plate (1 cm^2) as working electrode. The charge passed corresponds to 0.29 µmols of electrons, that is around the 29 % of the total charge expected for the 1 mM complex solution.

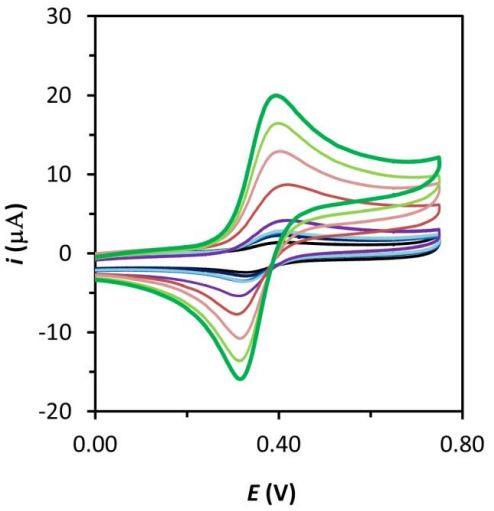

Figure S23. CV of an aqueous solution at pH 7 containing different concentrations of complex $\mathbf{1}^{2-}$ (0.075-1 mM) with 0.1 M phosphate buffer, showing no evidences for adsorption of the oxidized species. GC disk was used as working electrode and the scan rate was set to 100 mV/s.

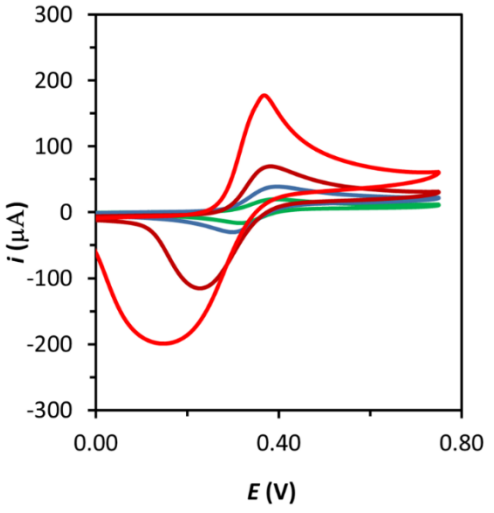

Figure S24. CV of an aqueous solution at pH 7 containing different concentrations of complex $\mathbf{1}^{2-}$ (1-10 mM) with 0.1 M phosphate buffer showing an increased reduction wave due to adsorption processes of the oxidized

species. GC disk was used as working electrode and the scan rate was set to 100 mV/s.

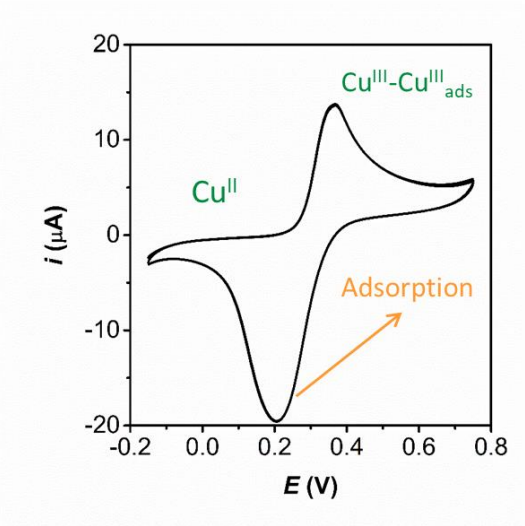

Figure S25. CV of an aqueous solution at pH 7 containing 5 mM of complex $\mathbf{1}^{2-}$ with 0.1 M phosphate buffer, showing the increase in the reductive charge derived from the desorption of the adsorbed, oxidized $\mathbf{1}^{-}$ complex. GC disk was used as working electrode and the scan rate was set to 100 mV/s.

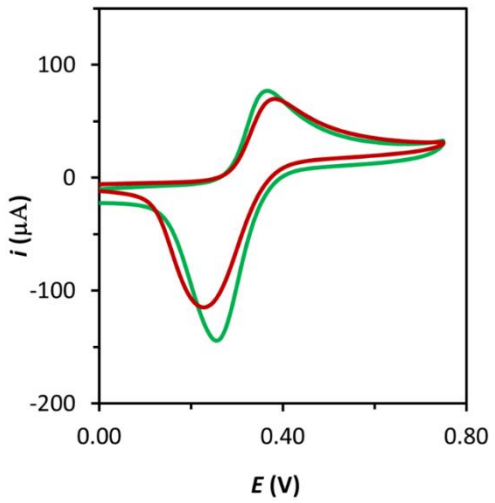

Figure S26. CV of an aqueous solution at pH 7 containing 5 mM of complex $\mathbf{1}^{2-}$ with 0.1 M phosphate buffer. BDD (red line) and GC (green line) disks were used as working electrode and the scan rate was set to 100 mV/s

7. Spectroscopic characterization of 1^- and 2^- in aqueous vs organic solutions

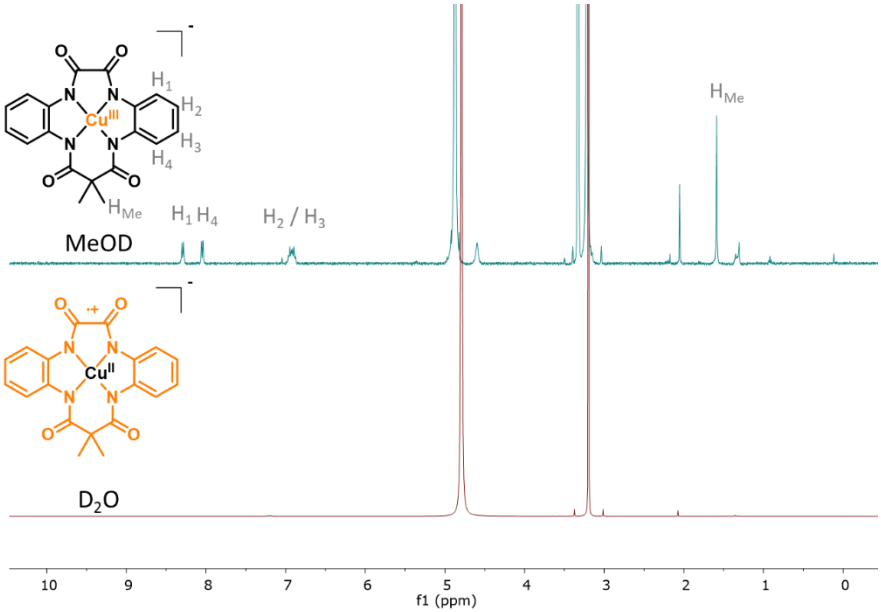

Figure S27. ^{1}H-NMR of the isolated oxidized species **1**$^-$ in MeOD and D_2O (400 MHz).

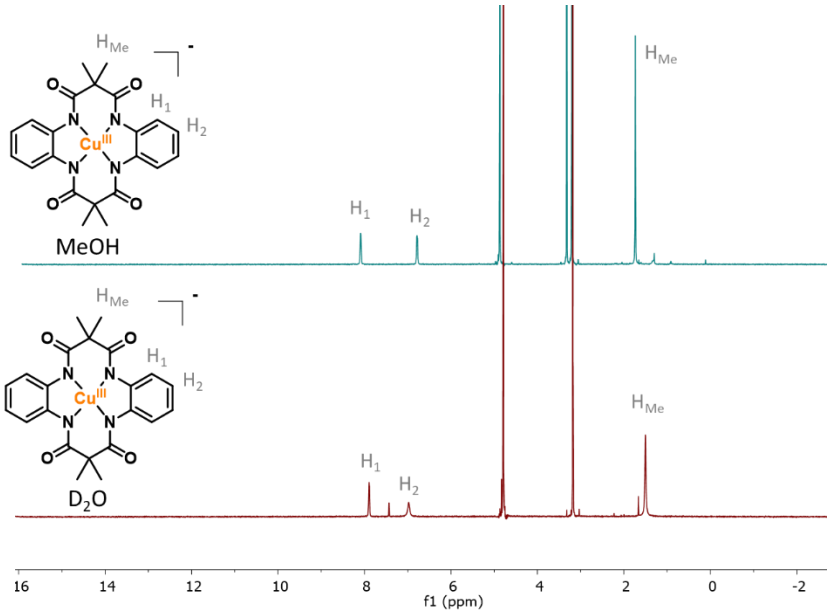

Figure S28. ^{1}H-NMR of the isolated oxidized species **2**$^{-}$ in MeOD and D_2O (400 MHz).

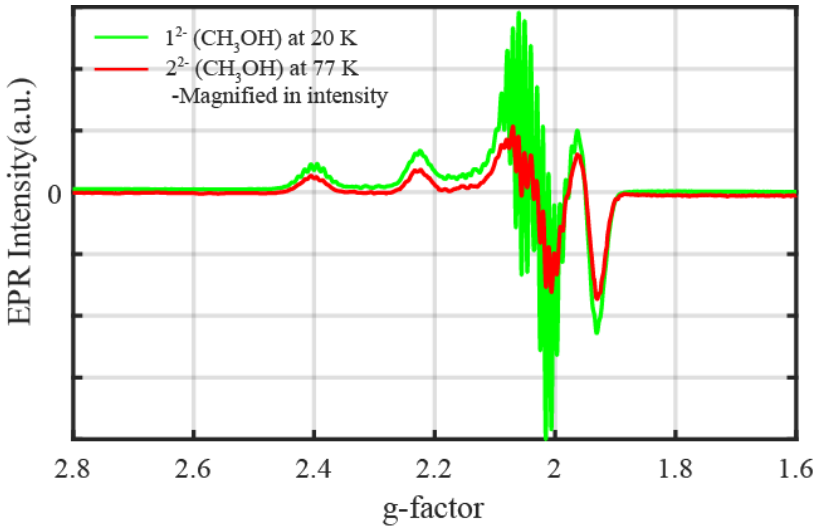

Figure S29. X-band EPR spectra of $\mathbf{1}^{2-}$ in CH_3OH (green trace recorded at 20 K) and $\mathbf{2}^{2-}$ in CH_3OH (red trace recorded at 77 K and magnified in intensity) . In aqueous solution dipole broadening occurs due to the difficulty of generating a good "glass" at low temperature. This provokes the presence of cracks and crystallites in the frozen solutions that are responsible for not providing a homogeneous path for the microwaves absorbed by the sample. Consequently, the hyperfine splitting arising due to the I =3/2 nuclear spin of Cu are broadened in the aqueous spectra (Figure S30 and Figure 5d) whereas in MeOH shown here not only the hyperfine coupling with the Cu can be clearly observed but also those of the four N with I = 1 nuclear spin.

Redox Metal–Ligand Cooperativity Enables Robust and Efficient Water Oxidation Catalysis at Neutral pH with Macrocyclic Copper Complexes

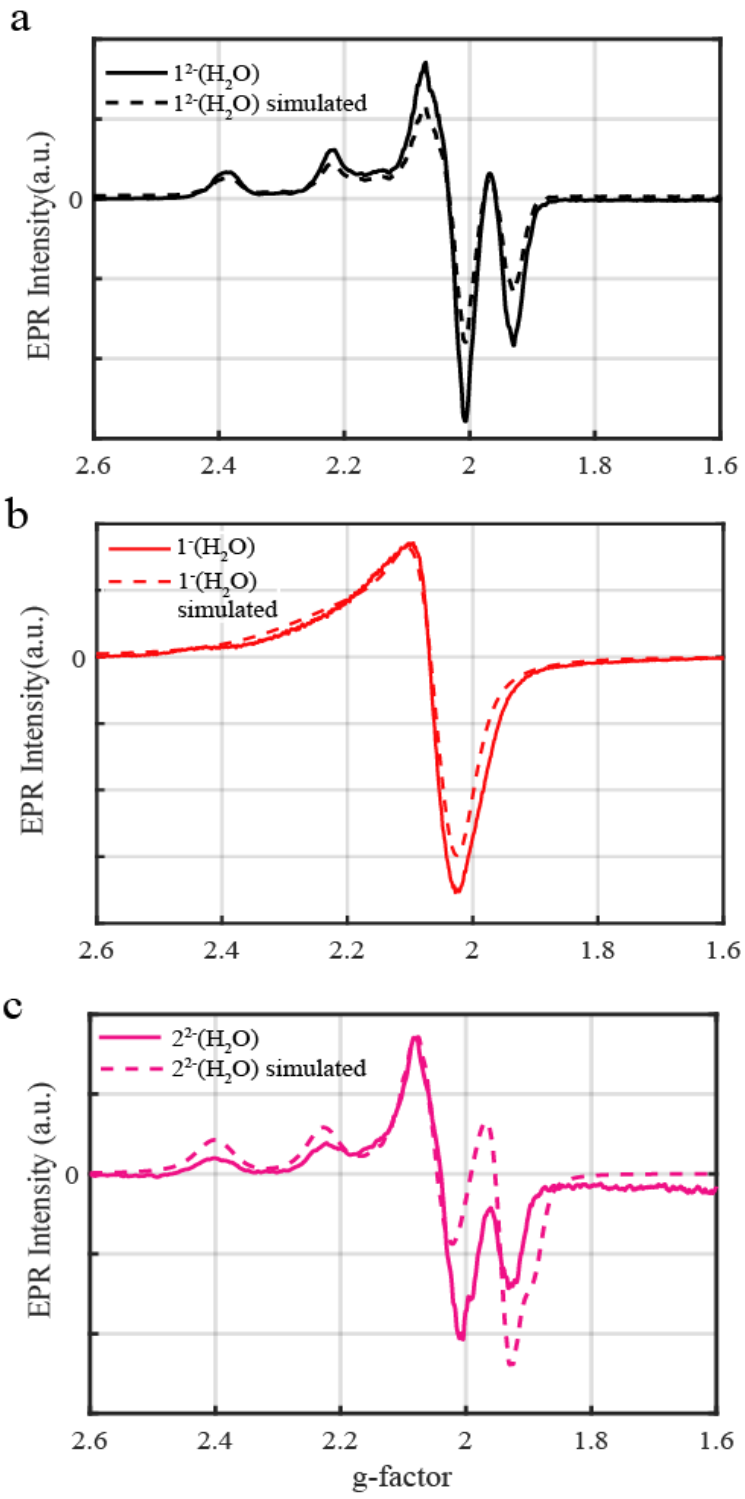

Figure S30. A. Simulation of $\mathbf{1}^{2-}(H_2O)$ g_{xx} = 2.138, g_{yy} = 2.045 and g_{zz} = 1.940 with A_{xx} = 215 G contribution. Hyperfine couplings with the four N with I = 1 nuclear spin were also added with A_{yy} = 20 G and A_{zz} = 13 G. **B**. Simulation of $\mathbf{1}^{-}(H_2O)$ assuming a triplet whereby g_{xx} = 2.230, g_{yy} = 2.050 and g_{zz} = 2.050. The simulated zero field splitting parameters D and E are 40 and 5 G respectively. **C**. Simulation of $\mathbf{2}^{2-}(H_2O)$ g_{xx} = 2.150, g_{yy} = 2.060 and g_{zz} = 1.937 with A_{xx} = 215 G contribution. Hyperfine couplings with the four N with I = 1 nuclear spin were also added with A_{yy} = 20 G and A_{zz} = 13 G.

8. XAS characterization of adsorbed layer on the electrodes

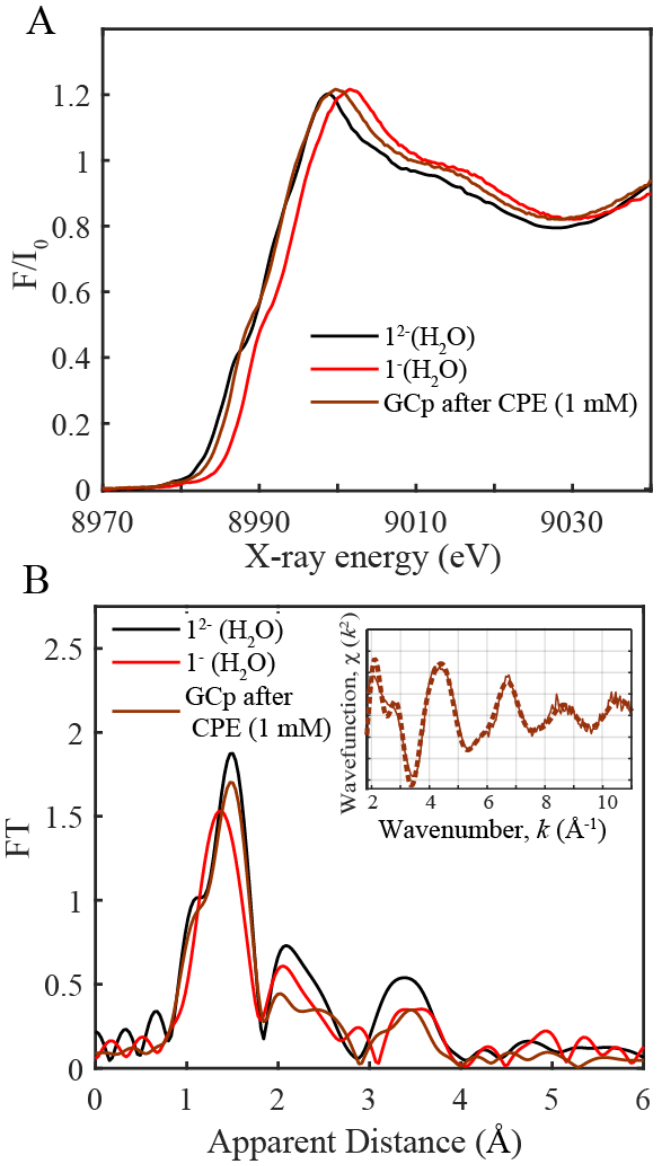

Figure S31. A, Normalized Cu K-edge XANES of $\mathbf{1}^{2-}$ and $\mathbf{1}^{-}$ in a pH 7 aqueous solution and GCp after CPE at 0.7 V in a 1 mM solution of the Cu(II) catalyst in water at pH 7. As observed in the graph, the XANES and EXAFS spectra of the electrode present similar features as those corresponding to the complex $\mathbf{1}^{2-}$.

B, Experimental Fourier transforms of k^2-weighted Cu EXAFS of $\mathbf{1}^{2-}$ and $\mathbf{1}^{-}$ in pH 7 aqueous solution and GCp after CPE at 0.7 V in a 1mM Cu(II) catalyst in water at pH 7. Inset, Fourier transforms, experimental results (solid line) and fitting (dashed line) of $k2\chi(k)$ for the GCp electrode sample.

9. Electrochemical water oxidation by 1^{2-} and 2^{2-}

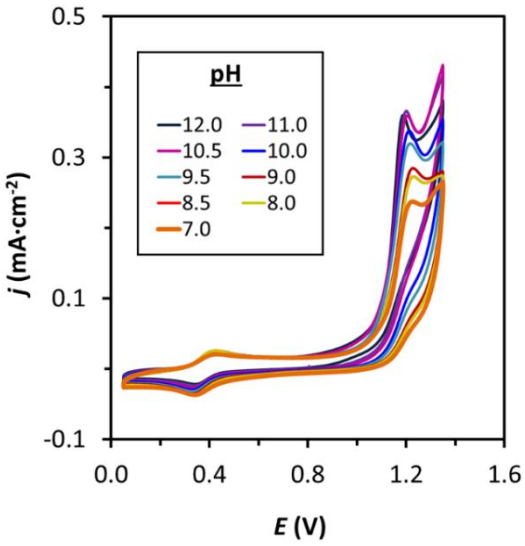

Figure S32. CV of a solution at different pH values containing 0.1 mM of complex $\mathbf{1}^{2-}$ at 100 mV·s^{-1} using a BDD as working electrode.

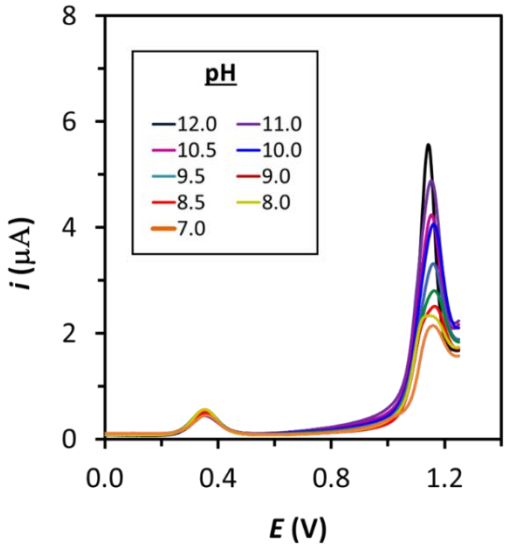

Figure S33. DPV of a solution at different pH values containing 0.1 mM of complex $\mathbf{1}^{2-}$, using a BDD as working electrode.

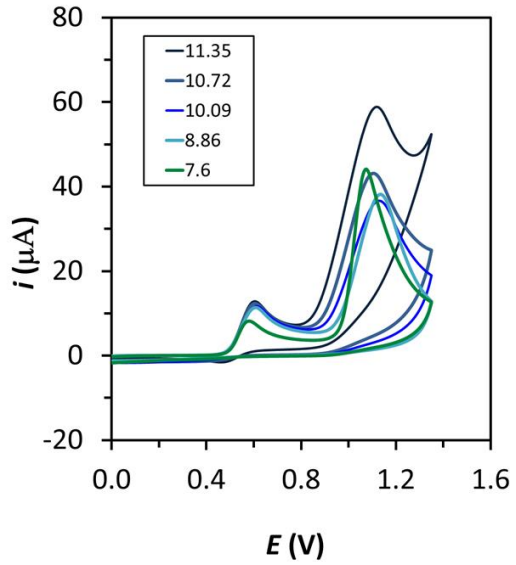

Figure S34. CV of a solution containing 0.1 mM of complex $\mathbf{2}^{2-}$ at different pH conditions and 100 $mV \cdot s^{-1}$ using a BDD as working electrode.

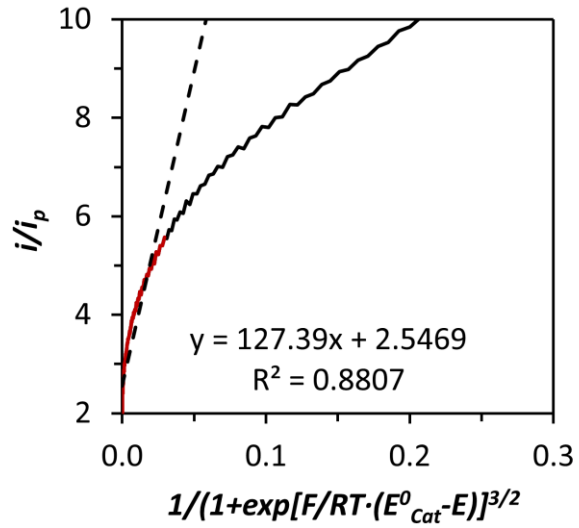

Figure S35. FOWA analysis based on 2nd order reaction in catalyst concentration.

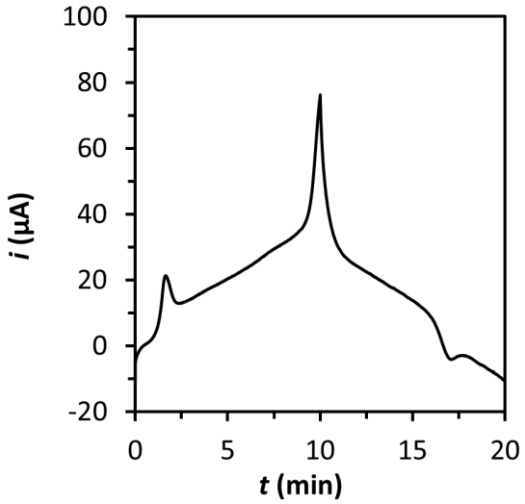

Figure S36. CV (*I* vs. *t*) of a pH 7 solution containing 0.1 mM of complex $\mathbf{1}^{2-}$ at 2 mV·s^{-1} using a OTTLE cell with a Pt working and counter electrode and a Ag pseudo reference.

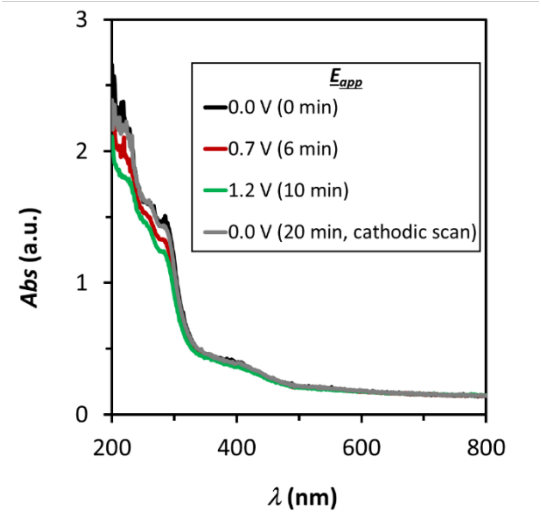

Figure S37. UV-vis spectra recorded in a spectroelectrochemical OTTLE cell using a 0.2 mM solution of $\mathbf{1}^{2-}$ in pH 7 phosphate buffer. Each line of the plot corresponds to the spectrum of the solution recorded at a certain potential (E_{app}) during a cyclic voltammetry at 10 mV·s^{-1} (CV in Figure S36). The potential used in this Figure were selected to show the UV-vis spectrum of the different

oxidation states of the complex observed in the CV: $\mathbf{1}^{2-}$ at 0.0 V (black trace), $\mathbf{1}^{-}$ at 0.7 V (red trace), catalytic resting state at 1.2 V (green trace), and $\mathbf{1}^{2-}$ again after catalytic turnover at 0.0 V (grey trace).

10. Electrochemical stability of complexes $\mathbf{1}^{2-}$ and $\mathbf{2}^{2-}$

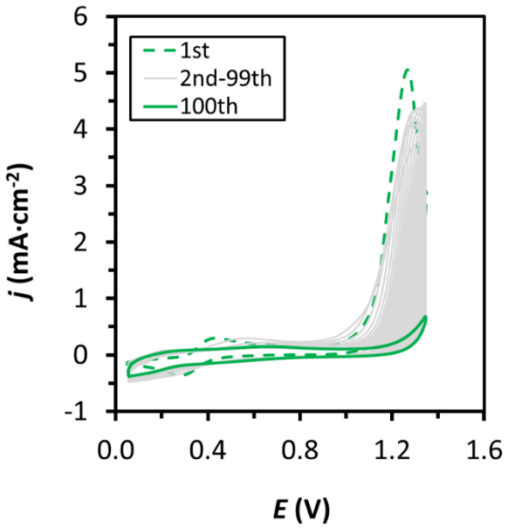

Figure S38. 100 consecutive CVs using 2 mM of complex $\mathbf{1}^{2-}$ in pH 7 aqueous solution with 0.1 M phosphate buffer. BDD disk as working electrode and scan rate 100 mV·s^{-1}. At this high concentration, adsorption of the complex lead to passivation of the electrode.

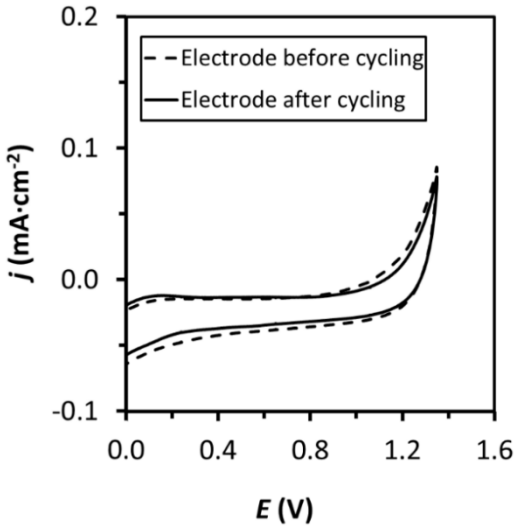

Figure S39. Rinse test of the BDD disk electrode in fresh pH 7 phosphate buffer solution before and after 100 CVs using 1 mM of complex $\mathbf{1}^{2-}$ (Figure S38).

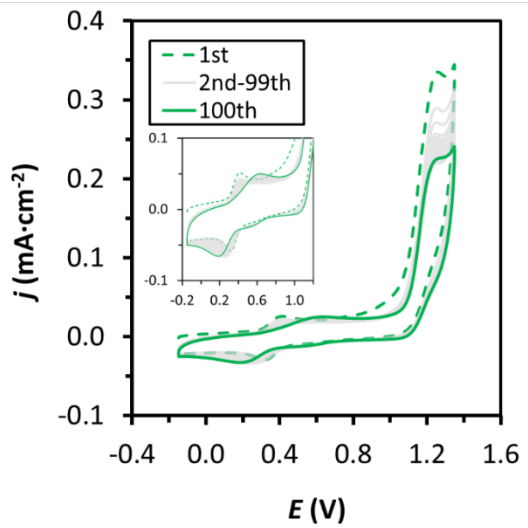

Figure S40. 100 consecutive CVs using 0.1 mM of complex $\mathbf{1}^{2-}$ in pH 7 aqueous solution with 0.1 M phosphate buffer. BDD disk as working electrode and scan rate 100 mV·s^{-1}. At this low concentration, adsorption of the complex and thus passivation are minimized over the 100 cycles, showing only small shift I the reversible wave and a slight attenuation of the catalytic wave due to the resistance added by the adsorbed layer.

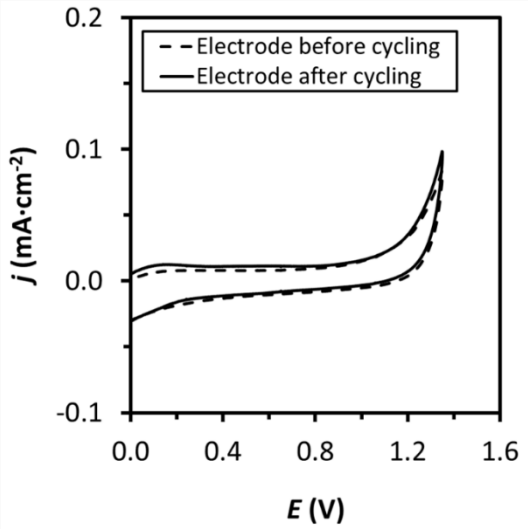

Figure S41. Rinse test of the BDD disk electrode in fresh pH 7 phosphate buffer solution before and after 100 CVs using 0.1 mM of complex $\mathbf{1}^{2-}$ (Figure S40).

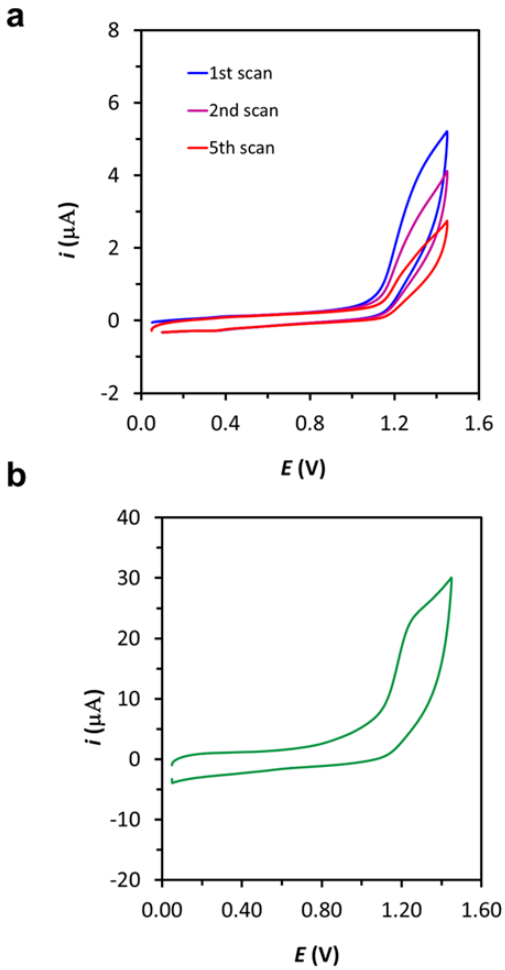

Figure S42. CVs using (a) 1 mM of ligand H_4L1 and (b) 1 mM of $[(L1)Zn]^{2-}$ in pH 7 aqueous solution with 0.1 M phosphate buffer. BDD disk as working electrode and scan rate 100 $mV \cdot s^{-1}$. This experiment shows the steady decrease of the current corresponding to oxidative degradation of free ligand under oxidative potentials.

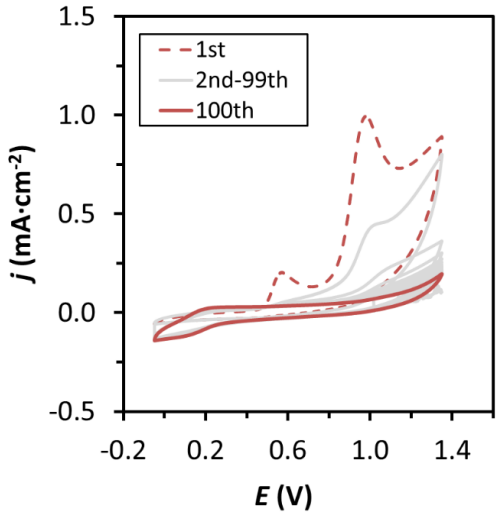

Figure S43. 100 consecutive CVs using 1 mM of complex $\mathbf{2}^{2-}$ in pH 7 aqueous solution with 0.1 M phosphate buffer. BDD disk as working electrode and scan rate 100 $mV \cdot s^{-1}$.

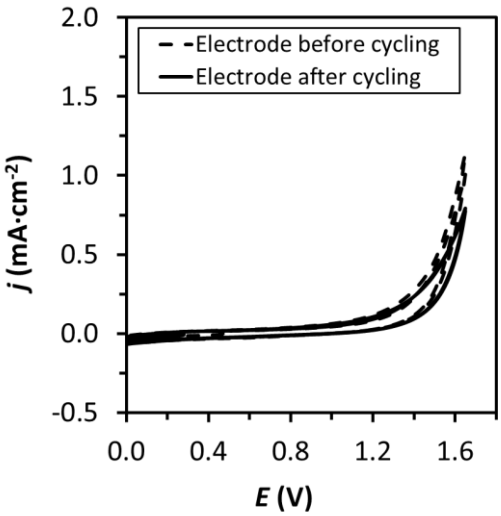

Figure S44. Rinse test of the BDD disk electrode in fresh pH 7 phosphate buffer solution before and after 100 CVs using 1 mM of complex $\mathbf{2}^{2-}$ (Figure S42). Degradation of complex $\mathbf{2}^{2-}$ under oxidative potentials does not lead to formation of electroactive layers on the surface of the electrode.

11. Controlled potential electrolysis and O_2 detection

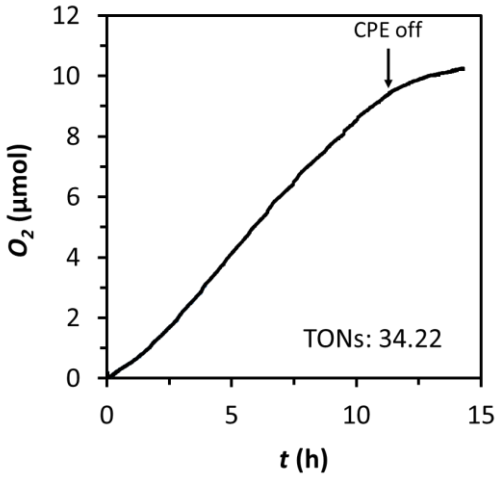

Figure S45. O_2 concentration measurement using a Clark electrode during CPE experiment at 1.2 V with $\mathbf{1}^{2-}$ as the catalyst and a BDDp as working electrode in pH 7 aqueous solution with *I*=0.1 M phosphate buffer. After the CPE, 34.22 TONs were obtained based on the total amount of catalyst added to the solution and the quantified oxygen evolved.

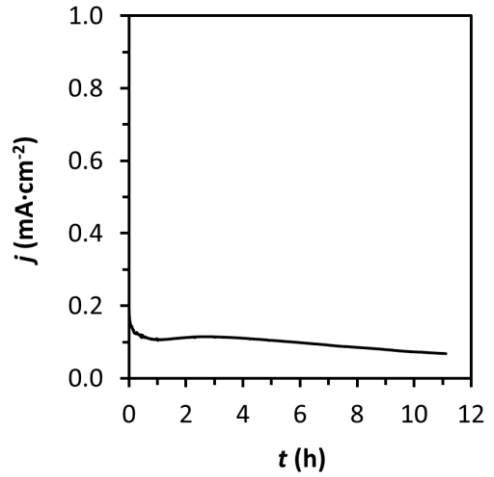

Figure S46. Intensity profile during CPE at 1.2 V using 0.1 mM of complex $\mathbf{1}^{2-}$ in pH 7 aqueous solution with *I*=0.1 M phosphate buffer. BDDp was used as working electrode.

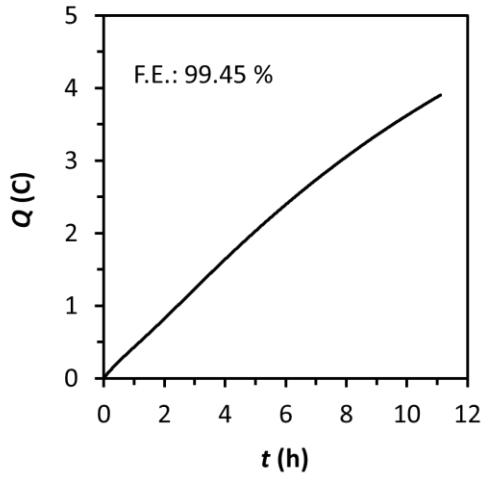

Figure S47. Charge profile during CPE at 1.2 V using 0.1 mM of complex $\mathbf{1}^{2-}$ in pH 7 aqueous solution with *I*=0.1 M phosphate buffer. BDDp was used as working electrode.

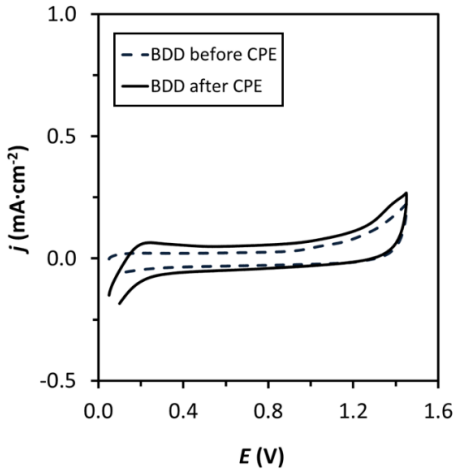

Figure S48. Rinse test of the BDDp electrode in fresh pH 7 phosphate buffer solution before (black dashed line) and after (black solid line) CPE at 1.2 V using 1 mM of complex $\mathbf{1}^{2-}$ (Figure S45).

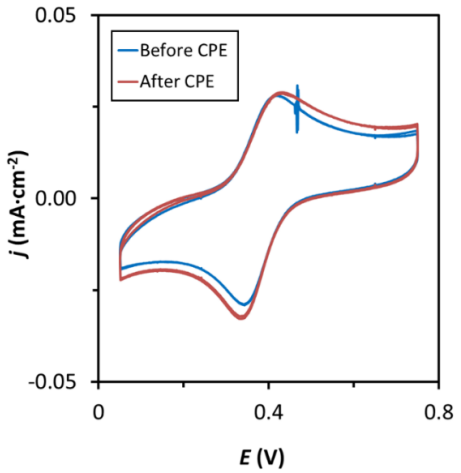

Figure S49. CV before and after a CPE at 1.2 V using 0.1 mM of complex $\mathbf{1}^{2-}$ in pH 7 aqueous solution with *I*=0.1 M phosphate buffer. BDDp was used as working electrode during CPE and BDD disk was used as working electrode for CV using 100 $mV \cdot s^{-1}$.

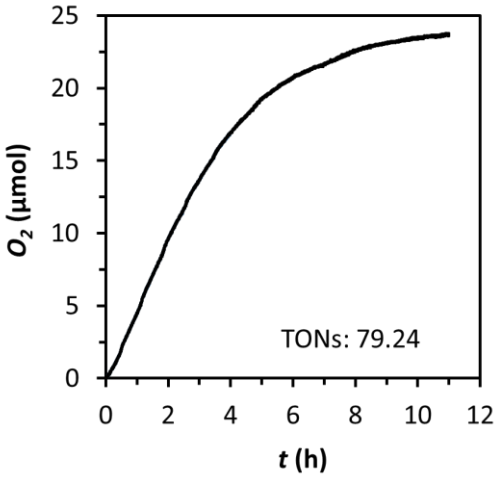

Figure S50. O_2 concentration measurement using a Clark electrode during CPE experiment at 1.2 V with $\mathbf{1}^{2-}$ as the catalyst and a GCp as working electrode^{-} in pH 7 aqueous solution with *I*=0.1 M phosphate buffer. After the CPE, 79.24 TONs were obtained based on the total amount of catalyst added to the solution and the quantified oxygen evolved.

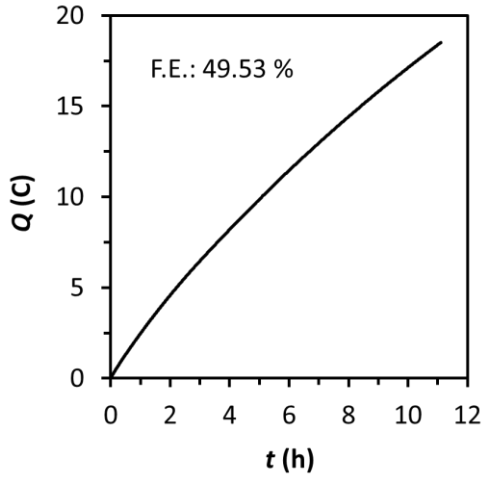

Figure S51. Charge profile during CPE at 1.2 V using 0.1 mM of complex $\mathbf{1}^{2-}$ in pH 7 aqueous solution with *I*=0.1 M phosphate buffer. GCp was used as working electrode.

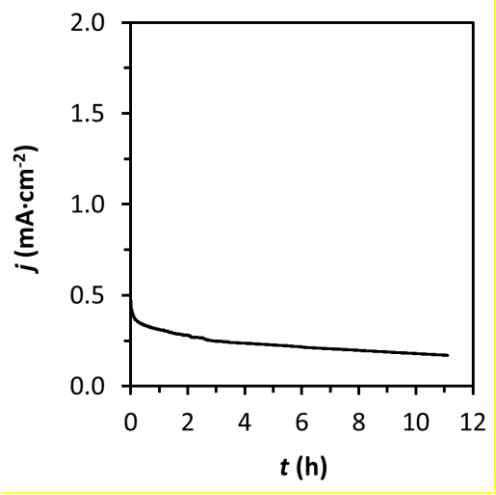

Figure S52. Intensity profile during CPE at 1.2 V using 0.1 mM of complex $\mathbf{1}^{2-}$ in pH 7 aqueous solution with *I*=0.1 M phosphate buffer. GCp was used as working electrode.

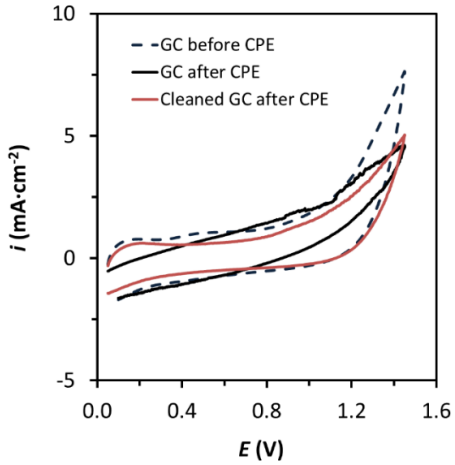

Figure S53. Rinse test of the GCp electrode in fresh pH 7 phosphate buffer solution before (black dashed line) and after (black solid line) CPE at 1.2 V using 1 mM of complex $\mathbf{1}^{2-}$ (Figure S50 and 51) and CV of the same electrode after polishing (solid red line).

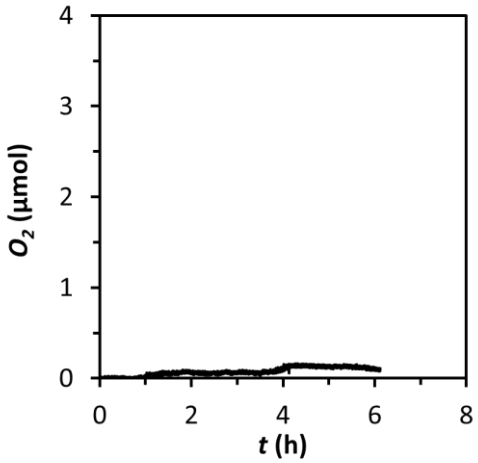

Figure S54. Intensity profile during CPE at 1.2 V in the absence of $\mathbf{1}^{2-}$ in pH 7 aqueous solution with *I*=0.1 M phosphate buffer. BDDp was used as working electrode.

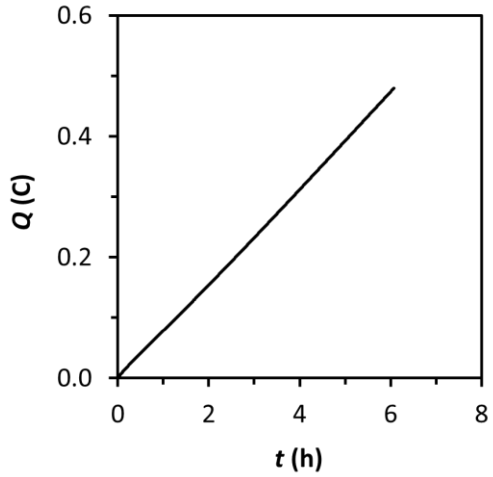

Figure S55. Charge profile during CPE at 1.2 V in the absence of $\mathbf{1}^{2-}$ in pH 7 aqueous solution with *I*=0.1 M phosphate buffer. BDDp was used as working electrode.

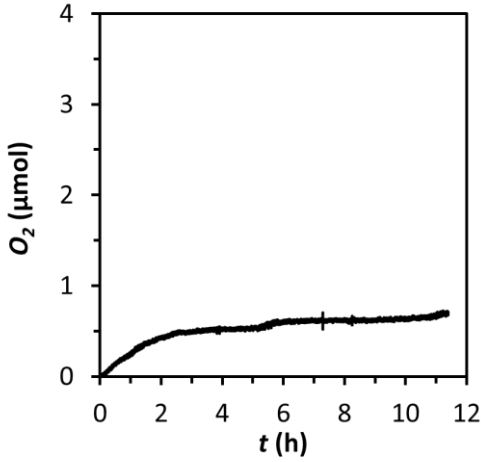

Figure S56. Intensity profile during CPE at 1.2 V using 0.1 mM $Cu(NO_3)_2$ in pH 7 aqueous solution with *I*=0.1 M phosphate buffer. BDDp was used as working electrode.

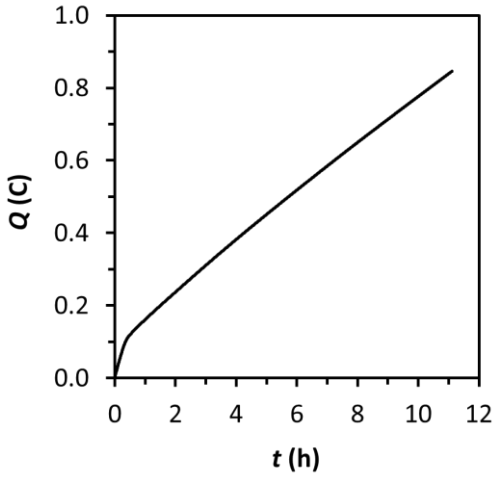

Figure S57. Charge profile during CPE at 1.2 V using 0.1 mM $Cu(NO_3)_2$ in pH 7 aqueous solution with *I*=0.1 M phosphate buffer. BDDp was used as working electrode.

12. Characterization of electrodes after O_2 evolution

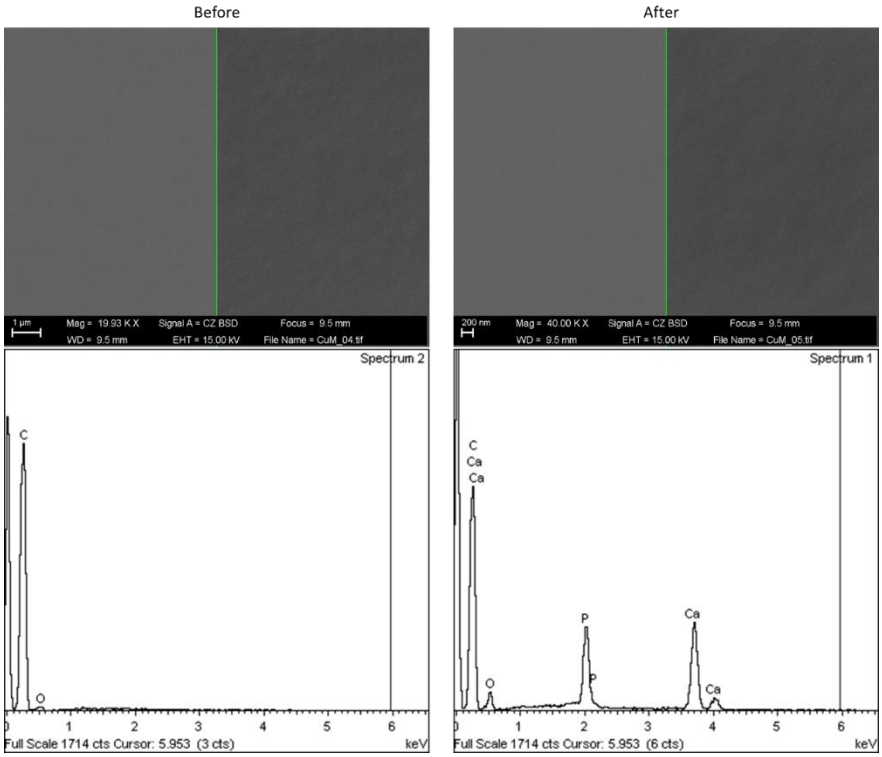

Figure S58. (Top) SEM images including both SEM micrographs (left picture) and corresponding back-scattered electron micrographs (righ picture). (Bottom) Corresponding EDX spectra of a GC plate electrode before and after CPE at 1.2 V using 0.1 mM of complex $\mathbf{1}^{2-}$ and subsequent rinse test analysis in fresh buffer solution.

Table S4. EDX analysis of a GC plate electrode before CPE at 1.2 V using 0.1 mM of complex $\mathbf{1}^{2-}$.

Element	App	Intensity	Weight%	Weight%	Atomic%
	Conc.	Corrn.		Sigma	
C K	72.09	2.0067	92.48	1.72	94.25
O K	1.27	0.4355	7.52	1.72	5.75
Totals			100.00		

Table S5. EDX analysis of a GC plate electrode before and after CPE at 1.2 V using 0.1 mM of complex $\mathbf{1}^{2-}$ and subsequent rinse test analysis in fresh buffer solution.

Element	App	Intensity	Weight%	Weight%	Atomic%
	Conc.	Corrn.		Sigma	
C K	41.15	0.8621	62.12	0.98	78.42
O K	3.53	0.4223	10.89	0.95	10.32
P K	10.36	1.4298	9.44	0.33	4.62
Ca K	13.07	0.9698	17.55	0.50	6.64
Totals			100.00		

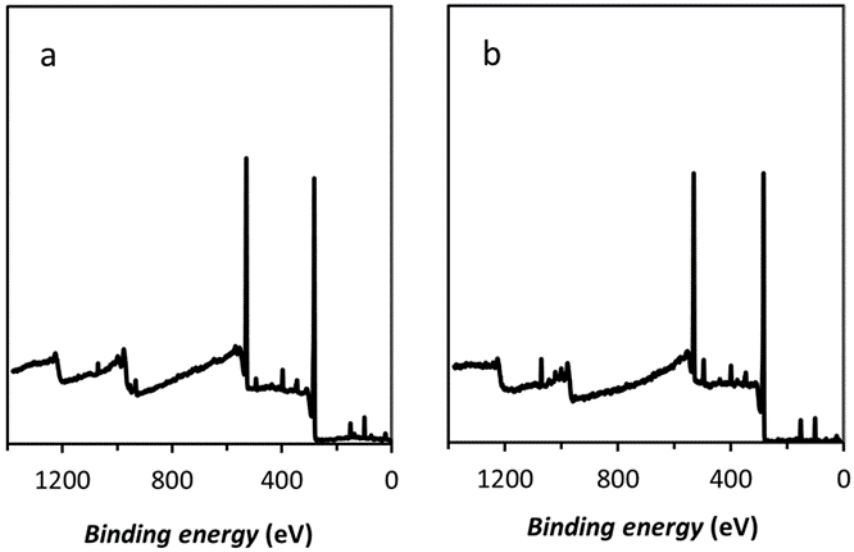

Figure S59. XPS survey scans of a GC electrode after CPE at 1.2 V (a) rinsed with fresh buffer solution and (b) further cycled in fresh buffer solution via rinse test.

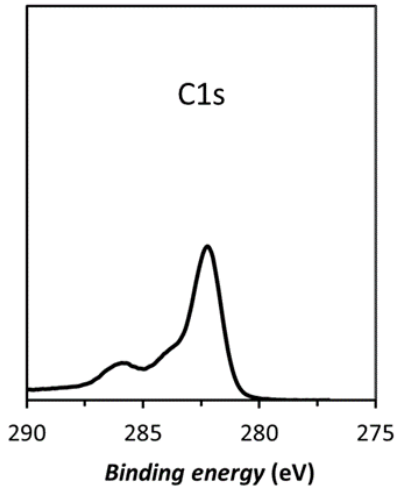

Figure S60. XPS spectrum of C1s of a GC electrode after CPE at 1.2 V, rinsed with fresh buffer solution and cycled in fresh buffer solution (rinse test).

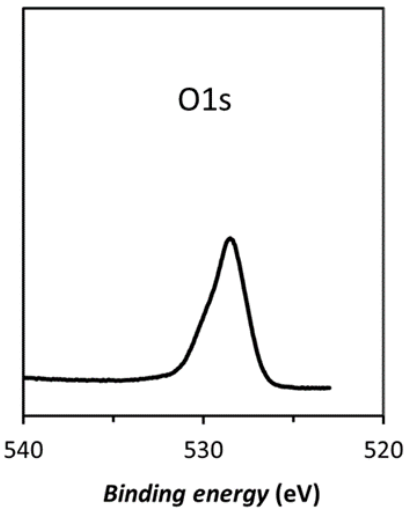

Figure S61. XPS spectrum of O1s of a GC electrode after CPE at 1.2 V, rinsed with fresh buffer solution and cycled in fresh buffer solution (rinse test).

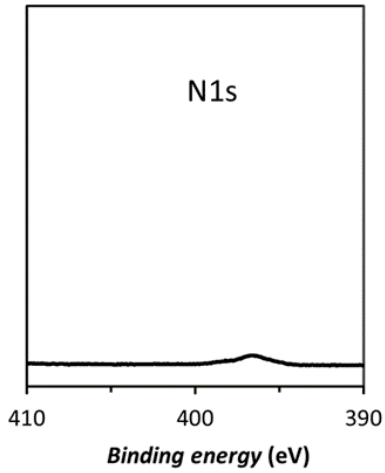

Figure S62. XPS spectrum of N1s of a GC electrode after CPE at 1.2 V, rinsed with fresh buffer solution and cycled in fresh buffer solution (rinse test).

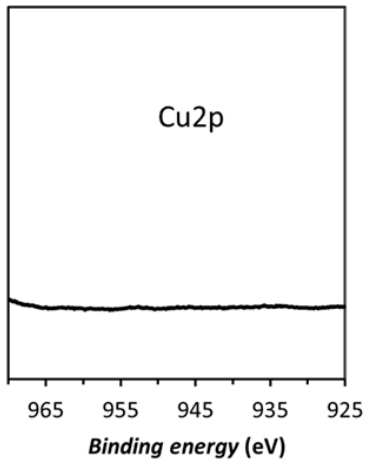

Figure S63. XPS spectrum of Cu2p of a GC electrode after CPE at 1.2 V, rinsed with fresh buffer solution and cycled in fresh buffer solution (rinse test).

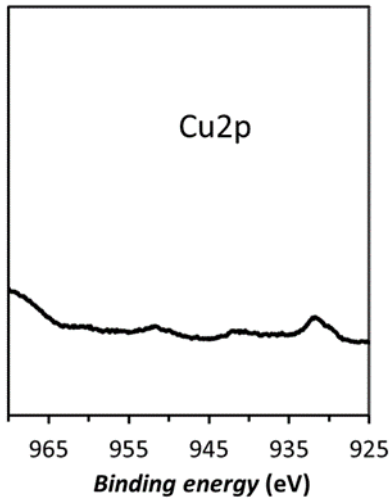

Figure S64. XPS spectrum of Cu2p of a GC electrode after CPE at 1.2 V and rinsed with fresh buffer solution.

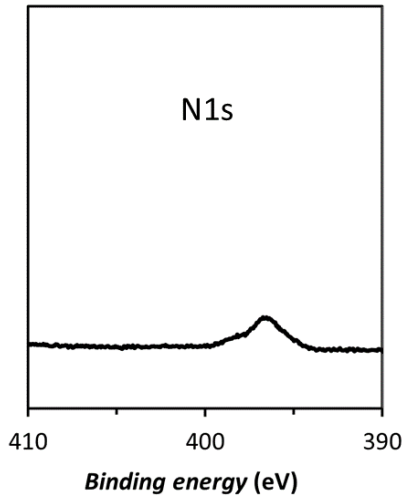

Figure S65. XPS spectrum of N1s of a GC electrode after CPE at 1.2 V and rinsed with fresh buffer solution.

13. Computational model of complexes 1^{2-} and 2^{2-}

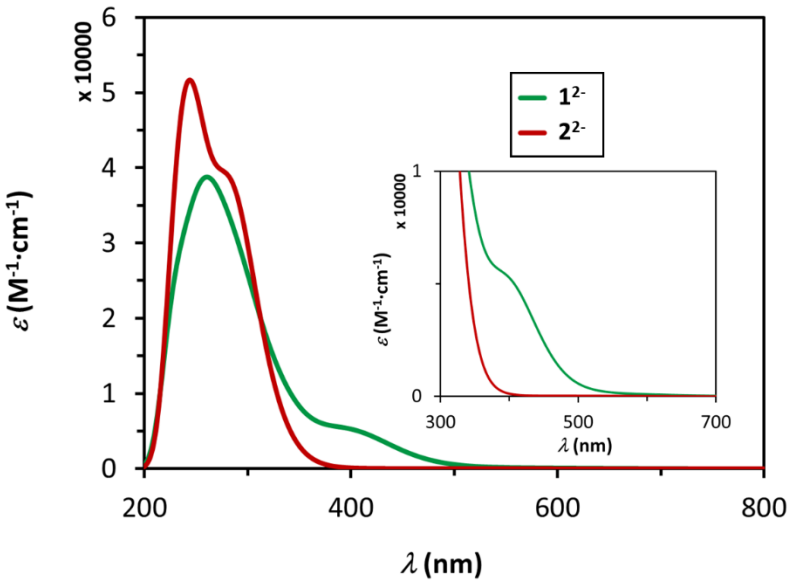

Figure S66. TD-DFT simulated UV-vis spectra of complexes $\mathbf{1}^{2-}$ (green trace) and $\mathbf{2}^{2-}$ (red trace) using water as solvent.

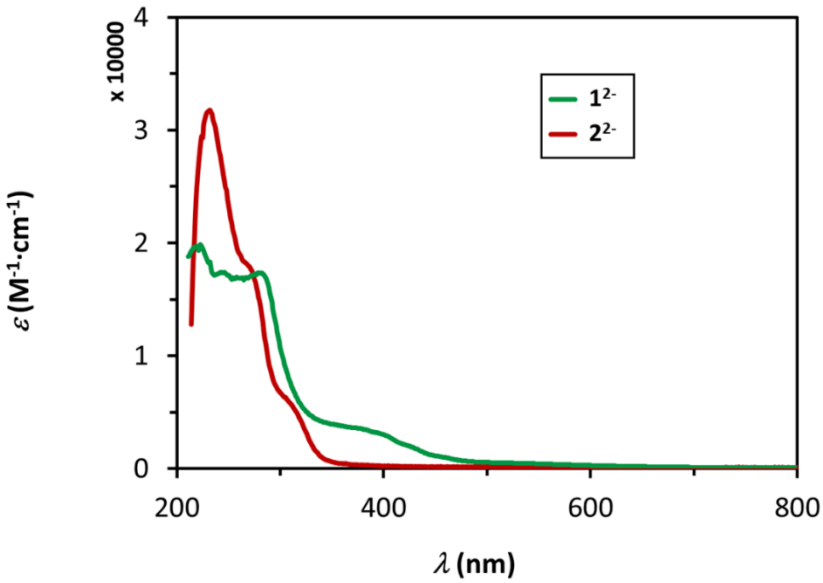

Figure S67. UV-vis spectra of a pH 7 aqueous solution containing 1 mM of either $\mathbf{1}^{2-}$ (green trace) or $\mathbf{2}^{2-}$ (red trace).

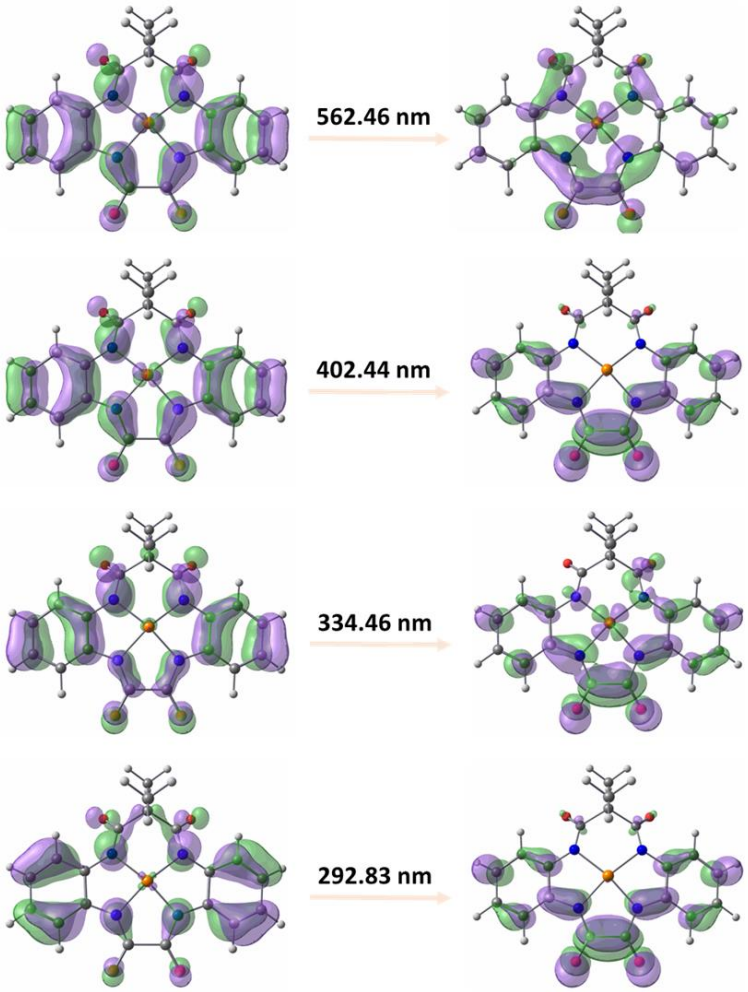

Figure S68. Representation of the main orbitals involved in the charge transfer at the different adsorption peaks simulated by TD-DFT for complex $\mathbf{1}^{2-}$.

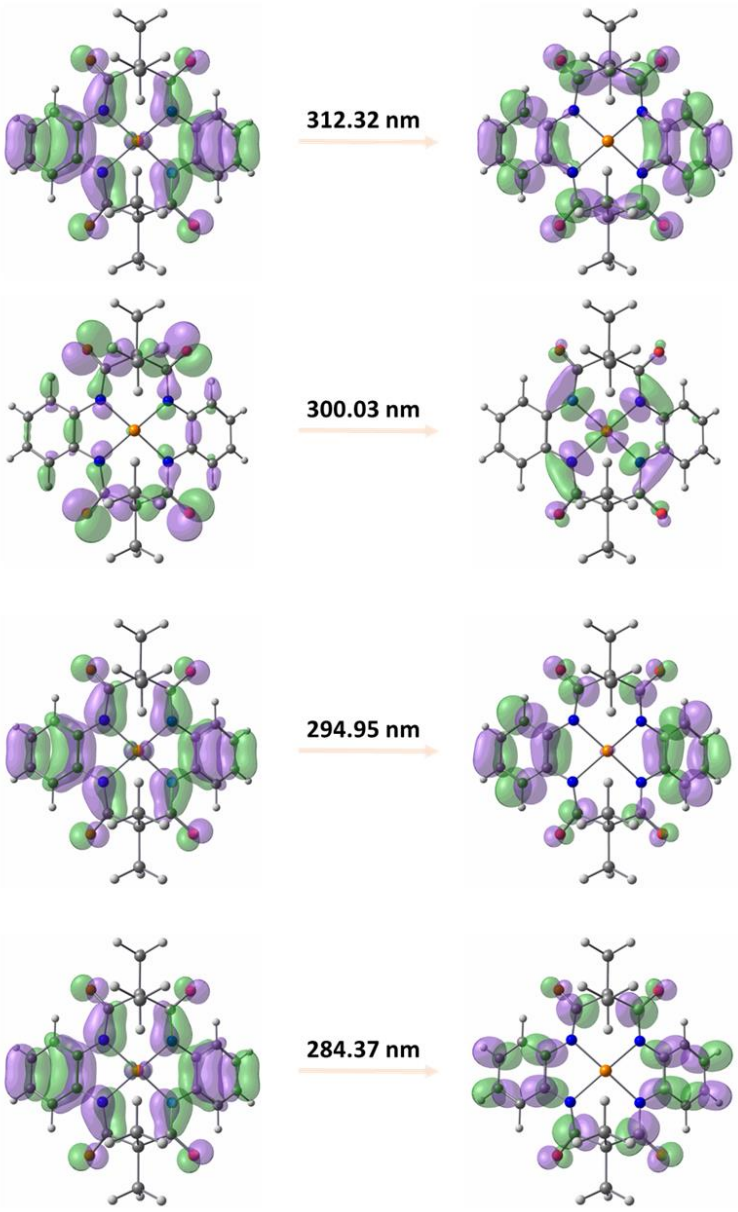

Figure S69. Representation of the main orbitals involved in the charge transfer at the different adsorption peaks simulated by TD-DFT for complex $\mathbf{2}^{2-}$.

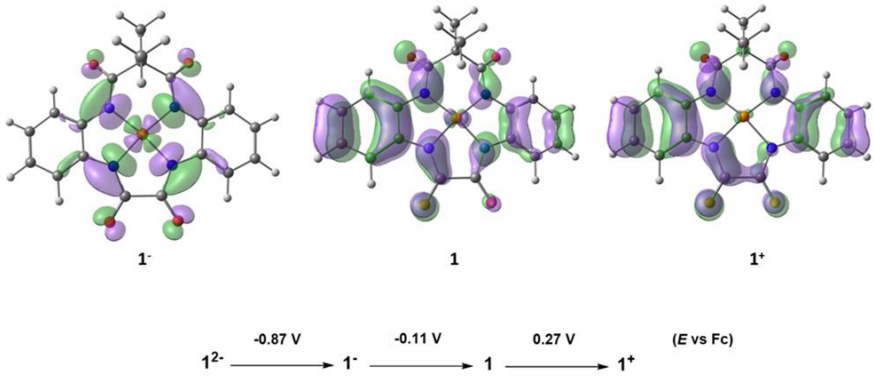

Figure S70. DFT optimized structures of **1** and $\mathbf{1}^{+}$ (with representation of the LUMO in the case of 1^{-} and SOMO for 1 and 1^{+}) and calculated redox potential (vs Fc) for the different oxidation states of complex $\mathbf{1}^{2-}$ in acetonitrile. As observed from the SOMO, the oxidation events leading to those species are centered on ligand π-orbitals.

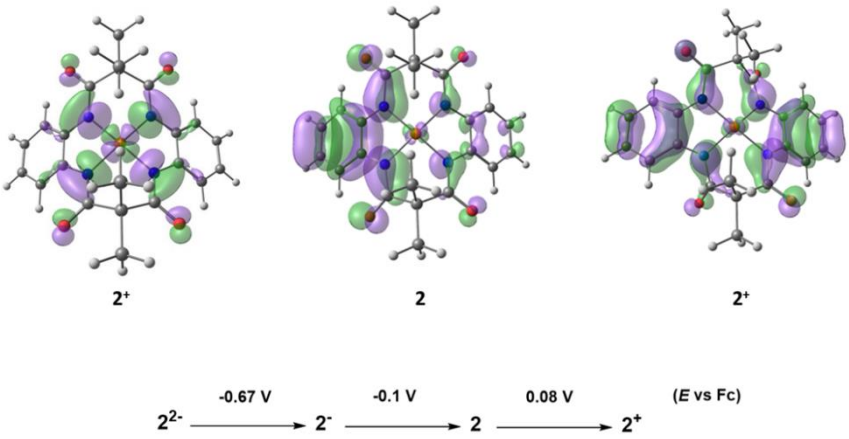

Figure S71. DFT optimized structures of **2** (with representation of the LUMO in the case of 1^- and 1^+ and SOMO for 1) and $\mathbf{2}^+$ and calculated redox potential (vs Fc) for the different oxidation states of complex $\mathbf{2}^{2-}$ in acetonitrile. As observed from the SOMO and LUMO, the oxidation events leading to those species are centered on ligand π-orbitals.

Scheme S1. Possible pathways for the oxidative activation of complex $\mathbf{1}^{2-}$.

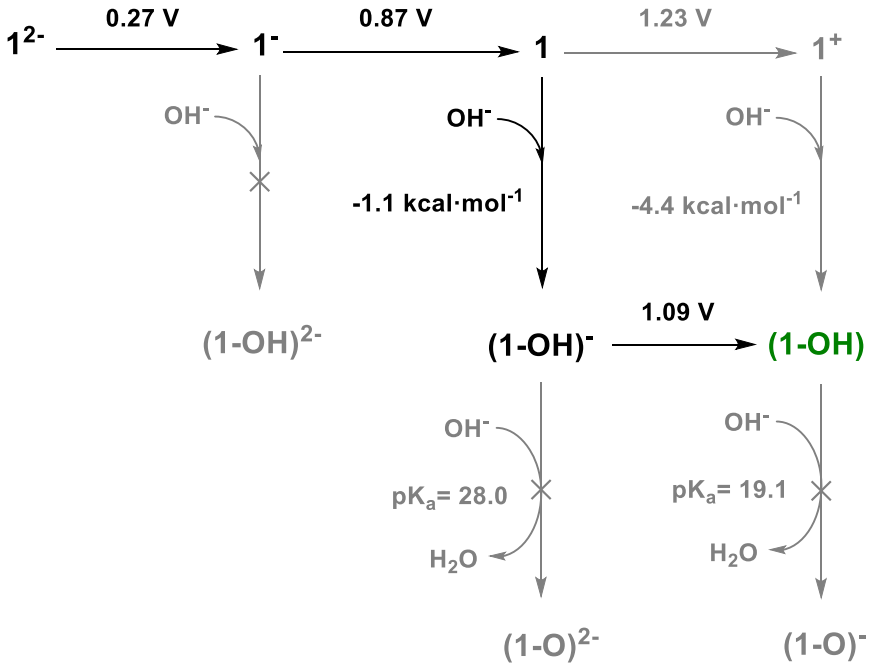

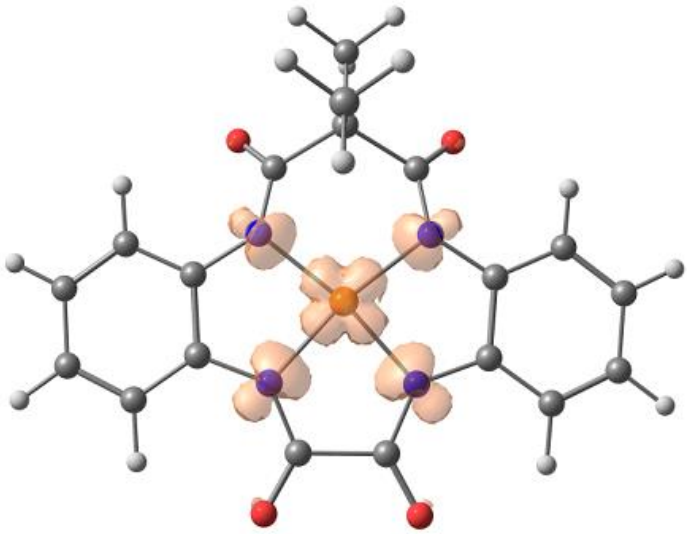

Figure S72. Optimized structure of complex $\mathbf{1}^{2-}$ and its calculated spin distribution.

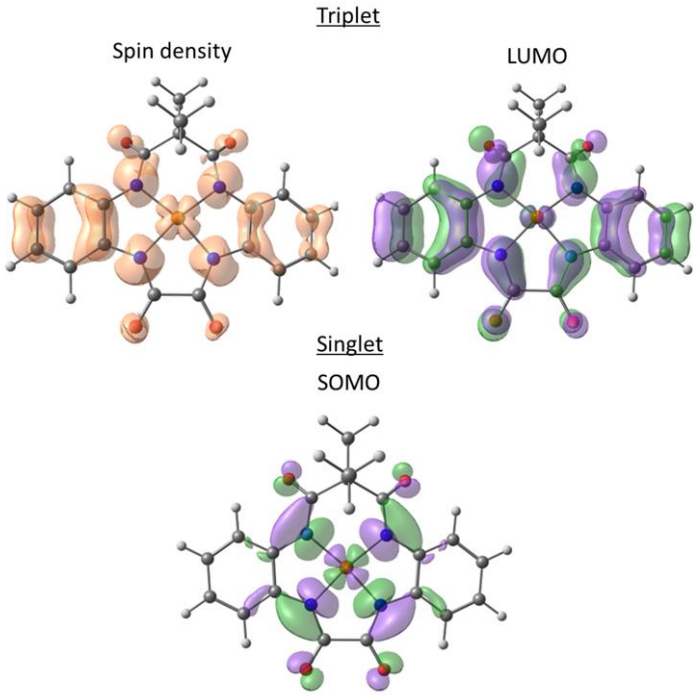

Figure S73. Optimized structure of complex $\mathbf{1}^-$ (triplet and singlet state) with spin density distribution (orange) and SOMO orbitals (green and purple).

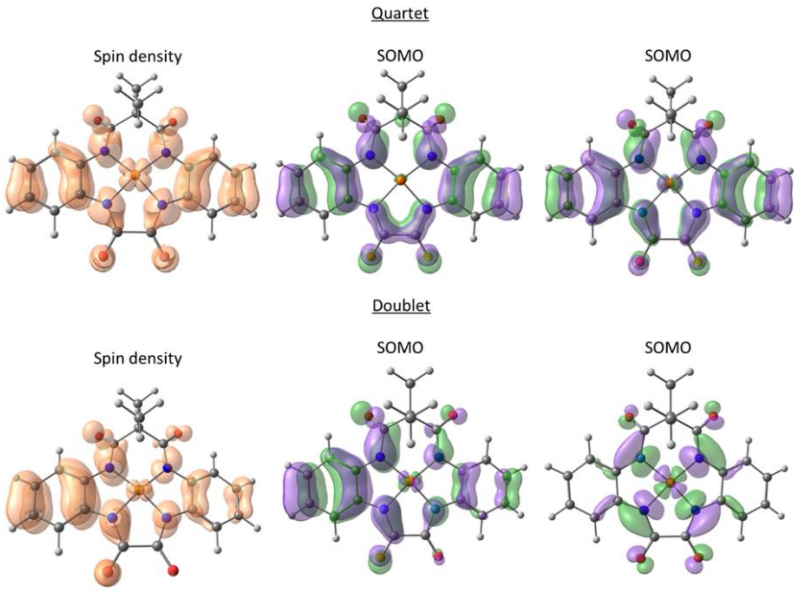

Figure S74. Optimized structure of complex **1** (quartet and doublet state) with spin density distribution (orange) and LUMO orbitals (green and purple).

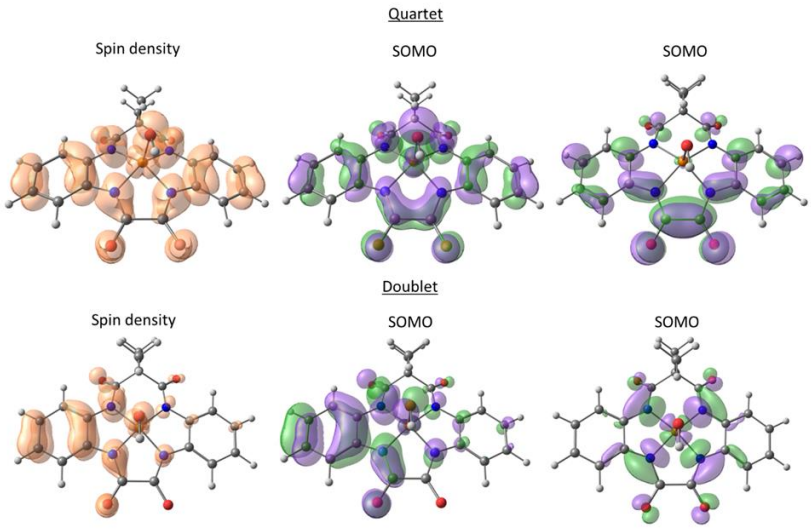

Figure S75. Optimized structure of complex **1(OH)**$^{-}$ (quartet and doublet state) with spin density distribution (orange) and LUMO orbitals (green and purple).

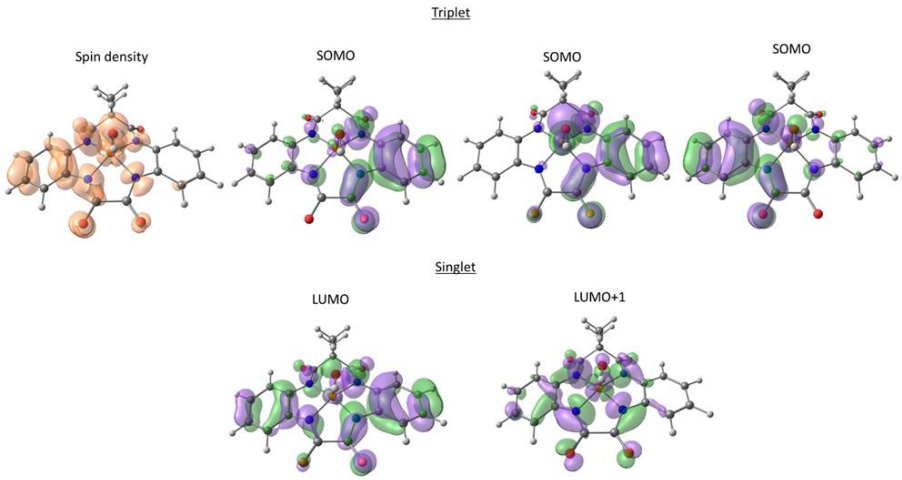

Figure S76. Optimized structure of complex **1(OH)** (triplet and singlet state) with spin density distribution (orange) and LUMO orbitals (green and purple).

Scheme S2. Mechanism for the O-O bond formation and O_2 evolution from the oxidized active species of catalyst $\mathbf{1}^{2-}$. Free energy is in kcal·mol^{-1} and the potential as expressed vs NHE.

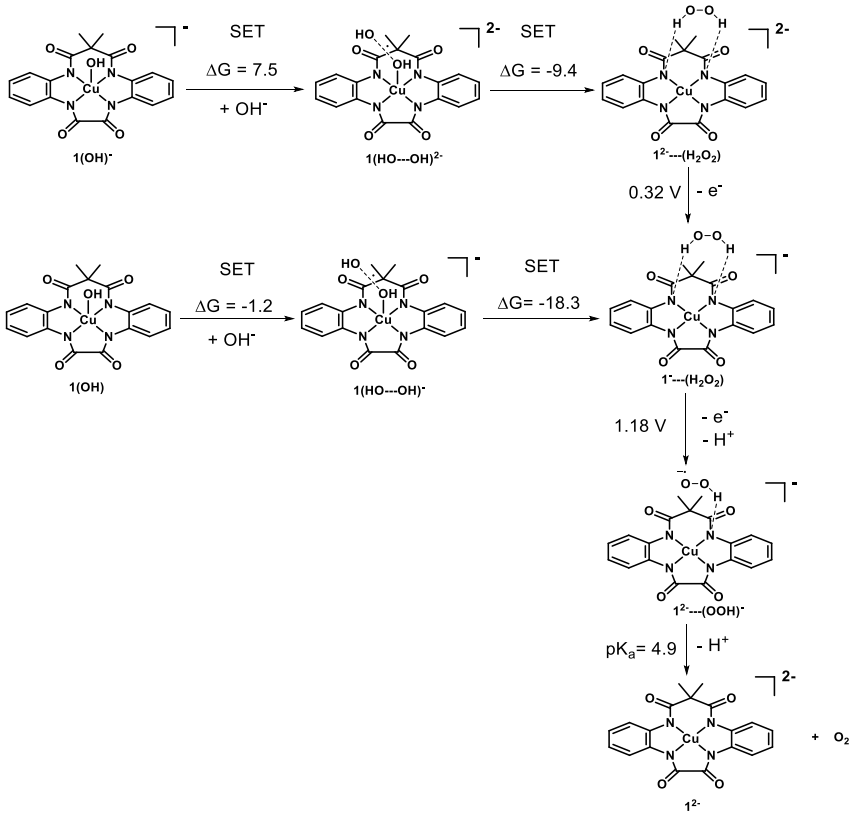

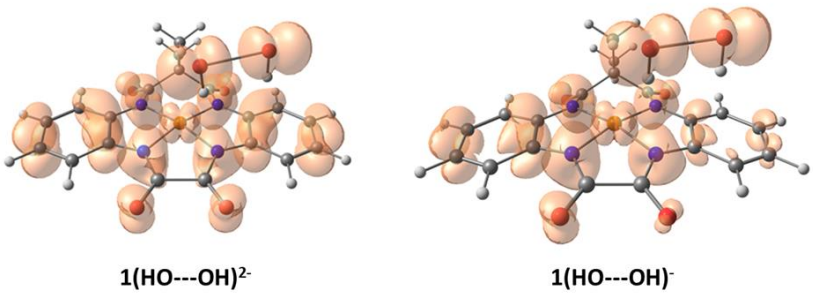

Figure S77. Optimized structure of the 2c-3e species **1(HO---OH)$^{2-}$** and **1(HO---OH)$^{-}$** (quintuplet and quartet state) with spin density distribution (orange).

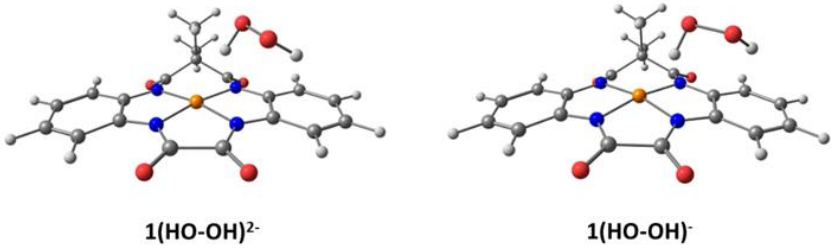

Scheme S78. Possible pathways for the oxidative activation of complex **2^{2-}**.

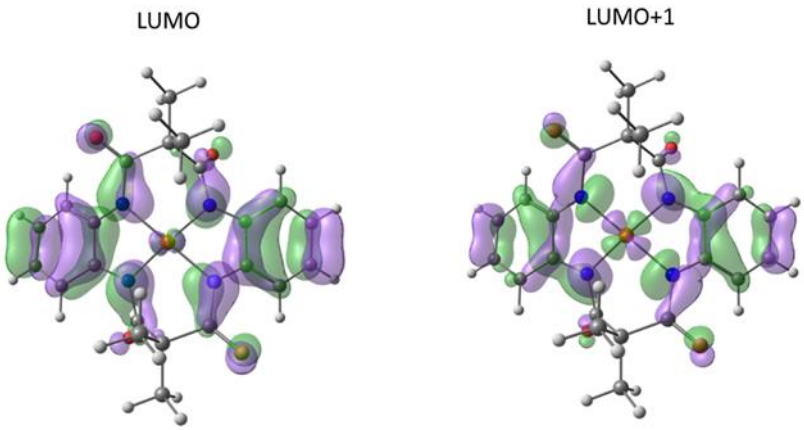

Figure S79. Optimized structure of complex $\mathbf{2}^{+}$ with representation of the LUMO and LUMO+1.

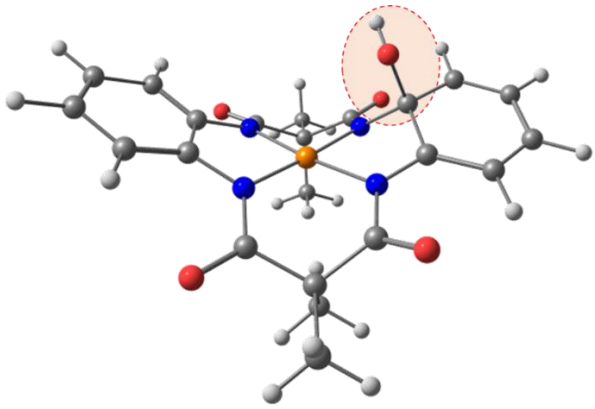

Figure S80. Optimized structure of complex **2(OH).**

XYZ coordinates available in the S.I.

https://dx.doi.org/10.1021/jacs.0c06515

References

(1) Stumpf, H. O.; Pei, Y.; Kahn, O.; Sletten, J.; Renard, J. P. *J. Am. Chem. Soc.* **1993**, *115*, 6738–6745.

(2) Garrido-Barros, P.; Funes-Ardoiz, I.; Drouet, S.; Benet-Buchholz, J.; Maseras, F.; Llobet, A. *J. Am. Chem. Soc.* **2015**, *137*, 6758–6761.

(3) Ruiz, R.; Surville-Barland, C.; Aukauloo, A.; Anxolabehere-Mallart, E.; Journaux, Y.; Cano, J.; Muñoz, M. C. *J. Chem. Soc., Dalt. Trans.* **1997**, 745-752.

(4) Simonelli, L.; Marini, C.; Olszewski, W.; Pérez, M. Á.; Ramanan, N.; Guilera, G.; Cuartero, V.; Klementiev, K. *Cogent Phys.* **2016**, *3*, 1231987.

(5) Nohara, I.; Prescimone, A.; Housecroft, C. E.; Constable, E. C. *Inorganics* **2019**, *7*, 11.

(6) Ravel, B.; Newville, M. *J. Synchrotron Radiat.* **2005**, *12* (4), 537–541..

(7) Rehr, J. J.; Albers, R. C.; Zabinsky, S. I. *Phys. Rev. Lett.* **1992**, *69*, 3397–3400.

(8) Koningsberger, D. C.; Prins, R. *X Ray Absorption: Principles, Applications, Techniques of EXAFS, SEXAFS and XANES.*; John Wiley & Sons, 1988 Ed.

(9) Costentin, C.; Drouet, S.; Robert, M.; Savéant, J. M. *J. Am. Chem. Soc* **2012**, *134*, 11235–11242.

(10) Zhang, T.; Wang, C.; Liu, S.; Wang, J.-L.; Lin, W. A. *J. Am. Chem. Soc.* **2014**, *136*, 273−281.

(11) Costentin, C.; Savéant, J. M. *ChemElectroChem.* **2014**, *1*, 1226–1236.

(12) Matheu, R.; Neudeck, S.; Meyer, F.; Sala, X.; Llobet, A. *ChemSusChem* **2016**, *9*, 3361–3369.

(13) Gaussian 09, Revision D.01, M. J. Frisch; G. W. Trucks, H. B. Schlegel, G. E. Scuseria, M. A. Robb, J. R. Cheeseman, G. Scalmani, V. Barone, B. Mennucci, G. A. Petersson, H. Nakatsuji, M. Caricato, X. Li, H. P. Hratchian, A. F. Izmaylov, J. Bloino, G. Zheng, J. L. Sonnenberg, M. Hada, M. Ehara, K. Toyota, R. Fukuda, J. Hasegawa, M. Ishida, T. Nakajima, Y. Honda, O. Kitao, H. Nakai, T. Vreven, J. A. Montgomery, Jr., J. E. Peralta, F. Ogliaro, M. Bearpark, J. J. Heyd, E. Brothers, K. N. Kudin, V. N. Staroverov, R. Kobayashi, J. Normand, K. Raghavachari, A. Rendell, J. C. Burant, S. S. Iyengar, J. Tomasi, M. Cossi, N. Rega, J. M. Millam, M. Klene, J. E. Knox, J. B. Cross, V. Bakken, C. Adamo, J. Jaramillo, R. Gomperts, R. E. Stratmann, O. Yazyev, A. J. Austin, R. Cammi, C. Pomelli, J. W. Ochterski, R. L. Martin, K. Morokuma, V. G. Zakrzewski, G. S99 A. Voth, P. Salvador, J. J. Dannenberg, S. Dapprich, A. D. Daniels, Ö. Farkas, J. B. Foresman, J. V. Ortiz, J. Cioslowski, and D. J. Fox, Gaussian, Inc., Wallingford CT, 2009.

(12) Becke, A. *J. Chem. Phys.* **1993**, *98*, 5648–5652.

(15) Grimme, S.; Ehrlich, S.; Goerigk, L. J. *Comput. Chem.* **2011**, *32* (1456).

(16) Hehre, W.J.; Ditchfield, R.; Pople, J. A. *J. Chem. Phys.* **1972**, *56*, 2257.

(17) Hariharan, P.C.; Pople, J. A. *Theor. Chim. Acta.* **1973**, *28*, 213–222.

(18) Francl, M.M.; Pietro, W. J.; Hehre, W. J. *J. Chem. Phys.* **1982**, *77*, 3654–3665.

(19) Hay, P. J.; Wadt, W. R. *J. Chem. Phys.* **1985**, *82*, 270-283.

(20) Schuchardt, K.L.; Didier, B. T.; Elsethagen, T.; Sun, L.; Gurumoorthi, V.; Chase, J.; Li, J.; Windus, T. L. *J. Chem. Inf.* **2007**, *47*, 1045-1052.

(21) Felier, D. *J. Comp. Chem.* **1996**, *17*, 1571–1586.

(22) Marenich, S. A. V.; Cramer, C. J.; Truhlar, D. G. *J. Phys. Chem. B.* **2009**, *113*, 6378-6396.

(23) J. A., Truhlar, D. G.; Cramer, C. J.; Lewis, A.; Bumpus, J. A. *J. Chem. Ed.* **2004**, *81*, 596-603.

(24) Marenich, A. V.; Majunmdar, A.; Lenz, M.; Cramer, C. J.; Truhlar, D. G. *Angew. Chem.* **2012**, *51*, 12810-12814.

(25) Winikoff, S.G.; Cramer, C. J. *Catal. Sci. Technol.* **2014**, *4*, 2484-2489.

(26) Ellis, W. C.; Tran, C. T.; Roy, R.; Rusten, M.; Fischer, A.; Ryabov, A. D.; Blumberg, B.; Collins, T. J. *J. Am. Chem. Soc.* **2010**, *132*, 9774–9781.

(27) Bruker. *Data Collection with APEX II Version V2013.4-1. Bruker*; 2007.

(28) Bruker. *Data Reduction with Bruker SAINT Version V8.30c. Bruker*; 2007.

(29) SADABS: V2012/1 Bruker (2001). Bruker AXS Inc., Madison, Wisconsin, USA Blessing, *Acta Cryst.* **1995**, *A51*, 33-38.

(30) TWINABS Version 2012/1 Bruker AXS scaling for twinned crystals; Blessing. *Acta Cryst.* **1995**, *A51*, 33–38.

(31) SHELXT; V2014/4 (Sheldrick 2014). Sheldrick, G. M. *Acta Cryst.* **2015**, *A71*, 3–8.

(32) Huebschle, C. B. .; Sheldrick, G. M. .; Dittrich, B. . ShelXle: A Qt Graphical User Interface for SHELXL. *J. Appl. Cryst.* **2011**, *44*, 1281–1284.

(33) SHELXL; SHELXL-2014/7 (Sheldrick 2014). Sheldrick, G. M. *Acta Cryst.* **2015**, *C71*, 3–

Chapter 4

Polymeric Cu-based Molecular Anodes: Application in Water Oxidation Catalysis

Chapter 4 describes the generation of molecular anodes based on first row transition metal WOCs. A reported rugged Cu-based molecular WOC was modified introducing two pyrenes in the ligand backbone, leading to the formation of two regioisomeric complexes, which were anchored on ITO electrodes through polymerization of the pyrene moieties. The new materials were tested toward water oxidation at pH between 7.5 and 10.

Project B. Polymeric Cu-based Molecular Anodes: Application in Water Oxidation Catalysis

Pelosin, P.; Gil-Sepulcre, M.; Pablo Garrido-Barros, Benet-Buchholz, J.; Llobet, A.

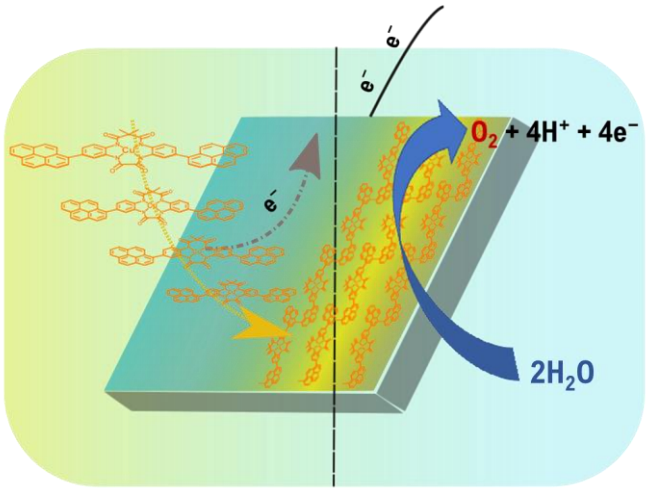

Abstract

Two regioisomeric copper based molecular oxidation catalysts (WOCs) with formula $[(L1)Cu]^-$, **1**$^-$, (H_4L1 = 15,15-dimethyl-3,10-di(pyren-1-yl)-8,13-dihydro-5H dibenzo[b,h][1,4,7,10]tetraazacyclotridecine-6,7,14,16(15H,17H)-tetraone), and $[(L2)Cu]^-$, **2**$^-$, (H_4L2 = 2-(1,2-dihydropyren-1-yl)-15,15-dimethyl-11-(pyren-1-yl)-8,13-dihydro-5H-dibenzo[b,h][1,4,7,10]tetraazacyclotridecine-6,7,14,16(15H,17H)-tetraone), have been synthesized and characterized. Both complexes contain two pyrene moieties which enable the anchoring via pyrene electropolymerization on GC (glassy carbon) and ITO (Indium tin oxide) electrodes covered with nano-ITO (n-ITO@GC and n-ITO@ITO) forming the hybrid electrodes *p*-**1**@ITO@GC, *p*-**2**@ITO@GC, *p*-**1**@ITO@ITO and *p*-**2**@ITO@ITO (where *p*- stands for polymer). The modified anodes were characterized by electrochemical techniques, UV-Vis and Raman spectroscopy. Their catalytic performance and stability were tested towards water oxidation catalysis at different pH values (7.5, 9 and 10). The best results were achieved at pH 10 with a Faradaic Efficiency (FE) of 74% (*p*-**1**@ITO@GC) and 66% (*p*-

2@ITO@GC) and an onset potential of 1.23 V and 1.21 V respectively for *p*-**1**@ITO@GC and *p*-**2**@ITO@GC.

Contributions

Pelosin Primavera performed the synthesis, characterization, and electrochemical experiments.

B.1 Introduction

The search for new renewables energetic sources, is becoming increasingly urgent because of the rise of greenhouse effect due to fossil fuels combustion.[1]The artificial photosynthesis is considered one of the most promising solution to the energetic problem, through the generation of solar fuels, such as hydrogen.[2] Unfortunately, the existing technologies for the production of solar fuels are often too expensive, for this reason, lately, the effort of many groups is focused on finding the way to have cheaper set ups lowering the cost of their components.[3]

Molecular water oxidation catalysts based on first row transition metals are economically advantageous respect to the molecular WOCs based on the metals of the 2nd and 3rd periods, for this reason, in the last years, there was a large increment in their development.[2,4] Further, the modification of the ligand scaffold with a linker can enable their anchoring on different type of electrodes, generating molecular anodes, which can be practically applied in the photoelectrochemical cell.[5,6]

The strategies adopted to anchor molecular WOCs depend on the material of the conductive support, as metal oxides (ITO, FTO, TiO_2) and carbon-based materials (glassy carbon, multi wall carbon nanotubes graphene etc.). In case of a metal oxide, the favored anchoring method is the formation of a covalent bond between the metal of the electrode and a carboxylic, sulphonic or phosphonic groups present on the ligand.[7–9] The main drawback is the instability of this bond at neutral-basic pH.[10,11] On the other hand, inserting a polycyclic aromatic hydrocarbon (PAH), as pyrene, in the ligand structure enable the anchoring through π- π interactions with a carbon-based electrode.[12]

A further anchoring methodology is the electropolymerization. In this case, the ligand is provided with a monomer able to polymerize on the electrode surface when a determined potential is applied. Some examples are the molecular electroanodes obtained polymerizing N-substituted pyrroles or C-substituted thiophenes.[13] Also pyrene, was proven to electropolymerize at relatively low potential, forming polymers with high condutivity,[14,15] on different supports such as multi wall carbon nanotubes (MWCNT), graphene nano sheets, glassy carbon and indium tin oxide,[15,16] but no reports are currently available about the use of this last strategy in the anchoring of molecular WOCs.

The development of technologies based on first row molecular WOCs needs the use of robust catalysts that have to be stable in aqueous solutions, where the catalytic reaction will occur. First row transition metal complexes are labile in coordinative solvents such as water. Further, their oxidation at high oxidation states is possible only at the cost of high energies, often leading to unwanted side reactions including ligand oxidation and even degradation of the entire complex. [4,17,18]

Recent studies revealed the rational design of a non-innocent ligands as a key point to have rugged first row transition metal based WOCs.[19–21] In particular, a recently reported tetra-amidate macrocycle ligand (TAML), was proven to work in combination with the central copper for the creation and delocalization of the positive charges necessary to oxidize water.[19] The size of the macrocycle was found of primary importance for achieving the right overlap of the π and d orbitals allowing a metal-ligand oxidation. Whereas, the delocalization of the positive charges was guaranteed thanks to the high conjugated system provided by the ligand framework, the macrocycle effect prevented the ligand protonation and the subsequent decoordination of the metal, allowing the WOC to work at neutral pH.

In this work, the ligand of this rugged copper WOC was further modified with two pyrene moieties. The synthesis leaded to the formation of two new regioisomers, whose pyrenes were disposed meta H_4L1 (15,15-dimethyl-3,10-di(pyren-1-yl)-8,13-dihydro-5H dibenzo[b,h][1,4,7,10]tetraazacyclotridecine-6,7,14,16(15H,17H)-tetraone) and para H_4L2 (2-(1,2-dihydropyren-1-yl)-15,15-dimethyl-11-(pyren-1-yl)-8,13-dihydro-5H-dibenzo[b,h][1,4,7,10]tetraazacyclotridecine-6,7,14,16(15H,17H)-tetraone) with regard to the oxalyl bridge present on the original macrocycle. The

influence of the relative position of pyrene moiety was studied by UV-Vis, electrochemistry and time-dependent density functional theory (TD-DFT) calculations.

Through electropolymerization of the pyrene in acetonitrile, the complexes were anchored on nano-ITO, forming the molecular anodes *p*-**1**@n-ITO@GC, *p*-**2**@n-ITO@GC and *p*-**1**@n-ITO@ITO, *p*-**2**@n-ITO@ITO where *p*- stands for polymer. The hybrid eletroanodes were further characterized through UV-Vis, electrochemical techniques and resonance Raman spectroscopy.

The water oxidation activity was tested at different pH values, confirming the oxidation of water to dioxygen through RRDE experiments.

B.2 Results

Synthesis, structural electronic and redox properties of 1^- and 2^-

The synthesis of the ligands H_4L1 and H_4L2 is depicted in the scheme 1. The first step consists in the monoprotection of a pyrene substituted 1,2-phenylenediamine, whose synthesis was already reported,[22] obtained adding a single equivalent of Di-tert-butyl decarbonate and giving the isomers 2.1, with the pyrene in meta and 2.2, with the pyrene in para respect to the protected amine. The subsequent procedure is similar to the one already reported for other tetra-amidate macrocycle ligands[23]. A methylmalonyl bridge is obtained through amide formation between two equivalents of 2.1 or 2.2 and one equivalent of dimethylmalonyl chloride. The half macrocycles 3.1 and 3.2, after an acidic deprotection, are closed forming other two amides with an equivalent of oxalyl dichloride, giving the two regioisomer macrocycles H_4L1 and H_4L2. See the Supporting Information for a more detailed description of each step.

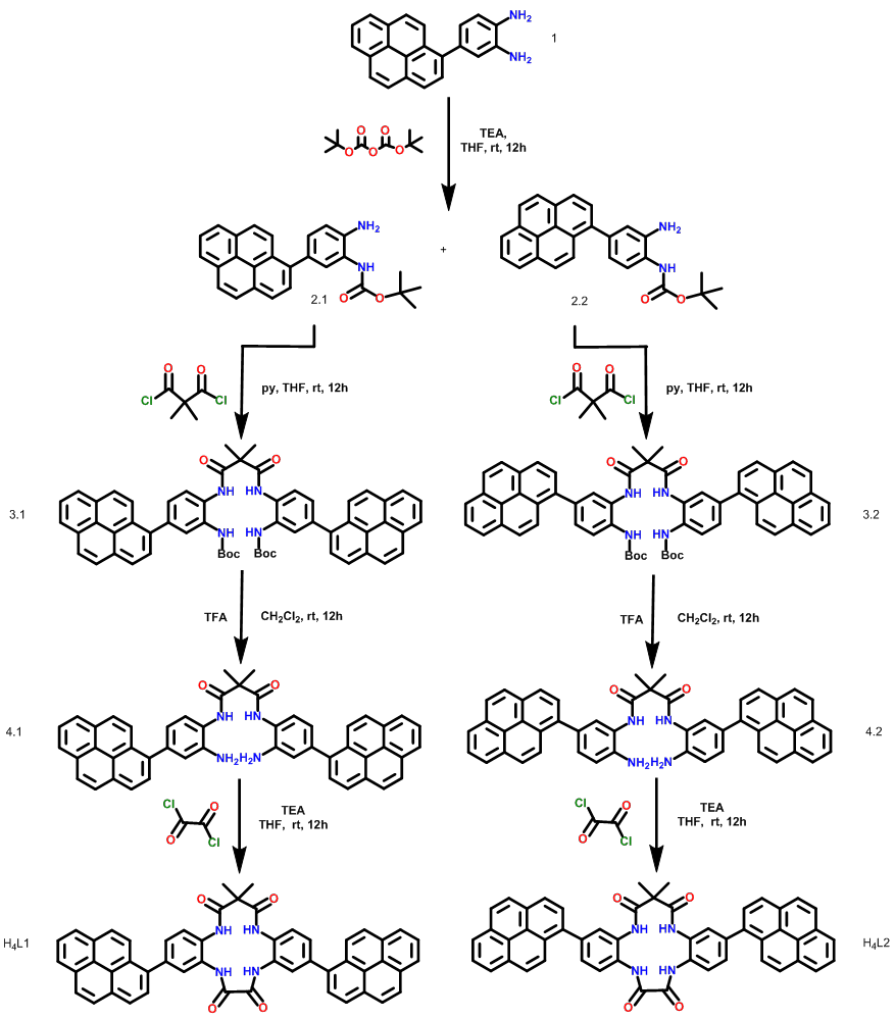

Scheme 1. Reaction scheme for the synthesis of ligands H_4L1 and H_4L2.

The copper complexes $\mathbf{1}^-$ and $\mathbf{2}^-$ are obtained by adding dropwise to a solution of the deprotonated ligand in DMF an equimolar solution of $Cu(ClO_4)_2$ in the same solvent. The solution is left to stir overnight at 50 °C. Afterwards, the solvent is removed and the products are isolated as brown solids after washing with cold methanol and diethyl ether.The complexes are characterized by mass spectrometry, X-Ray diffraction, spectroscopic and electrochemical techniques.The slow diffusion of diethyl ether in a solution of $\mathbf{1}^-$ in methanol allowed to get crystals suitable to X-ray diffraction, whose structure is reported

in Figure 1. The X-ray diffraction showed a mono-anionic complex, with an expected single molecule of tetramethyl ammonium acting as counterion. The oxidation state Cu(III) is confirmed also by the flat square planar geometry of the macrocycle, typical of d^8 metals, and the contraction of the Cu-N distance of **1**$^-$ respect to the unmodified macrocycle $[(MAC)Cu(II)]^{2-}$ [19] (1.79-1.87 Å and 2.07-1.85 Å, respectively) and the closer values to the Cu-N bond distances of the oxidized unmodified molecule $[Cu(III)MAC]^-$ (1.82-1.85 Å).

Table 1. Comparison of the Cu-N distances

Bond	**$[(MAC)Cu(II)]^{2-}$** [19]	**$[(MAC)Cu(III)]^-$** [19]	**1**$^-$
N1-Cu	2.076(8)	1.827(3)	1.7965(2)
N2-Cu	2.075(6)	1.855(3)	1.7986(2)
N3-Cu	1.857(8)	1.848(3)	1.8789(3)
N4-Cu	1.849(6)	1.831(3)	1.8477(2)

An additional analysis of the open circuit potential (OCP) over time of both complexes, confirmed the oxidation of the metal center from Cu(II) to Cu(III) by exposure to atmospheric oxygen. (Figure S21).

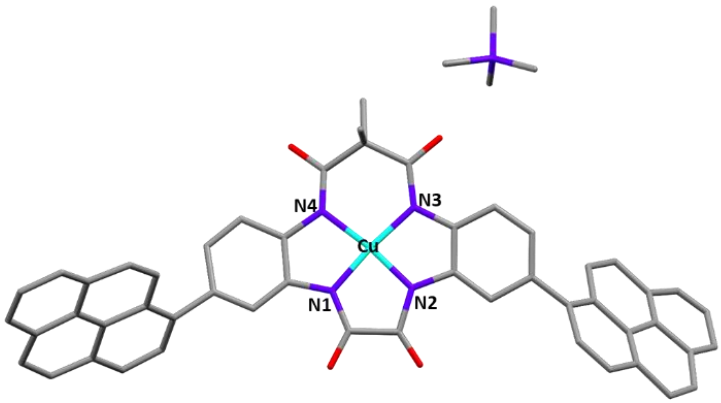

Figure 1. ORTEP drawing (thermal ellipsoids drawn at a 50% probability level) showing side views of the cationic structure of **1**$^-$. Color code: C, gray; N, blue; O, red; Cu, light blue.

The X-Ray structure further shows the pyrenes forming a dihedral angle of 120° with the phenyls of the macrocycle and laying at the opposite sides of the plane drawn by the macrocycle. This arrangement favors a CH-π (T-shaped

perpendicular) interaction with the pyrenes belonging a second molecule of complex in the packing of the structure, with an average distance between the plane of one pyrene and the C-H of the other of 2.7 Å, in agreement with the values found for this kind of interactions.(Figure S19).[24]

In the UV-Vis spectra of the complexes in propylene carbonate (Figure 2), the features of the pyrene mask all the characteristic bands of the macrocycle.[19] From the comparison of the spectra was possible to notice an absorption band at approx.430 nm for the complex $\mathbf{2}^{-}$, that is absent in $\mathbf{1}^{-}$. The time-dependent density functional theory (TD-DFT) reproduces well the experimental UV–vis spectra Figure 2 right.

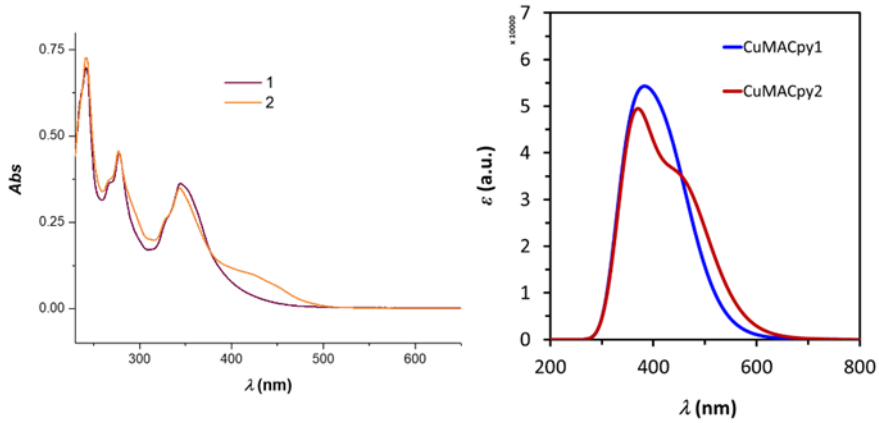

Figure 2. Left, UV-Vis spectra of $\mathbf{1}^{-}$ (violet) and $\mathbf{2}^{-}$ (orange) in propylene carbonate. Right, TD-DFT simulated UV-vis spectra of $\mathbf{1}^{-}$ (blue) and $\mathbf{2}^{-}$ (red).

The orbitals involved in the electronic transitions at lower energies are represented in Figure 3. Two main transitions can be appreciated for both $\mathbf{1}^{-}$ and $\mathbf{2}^{-}$ where in both cases there is a large degree of delocalization between the pyrene and the Cu-tetraamidate entities on the departing orbitals. However, on the arriving orbitals the electron density is mainly localized on the pyrene group in $\mathbf{1}^{-}$ while for $\mathbf{2}^{-}$ besides the pyrene a small electron density is observe on the oxalyl moiety. While this has little consequence on the first transition (357 nm for $\mathbf{1}^{-}$ *vs.* 364 nm for $\mathbf{2}^{-}$) it has a larger effect for the second transition (441 nm for $\mathbf{1}^{-}$ *vs*. 463 nm for $\mathbf{2}^{-}$). This shift to lower energy for $\mathbf{2}^{-}$ is now responsible for

the shoulder observed in the calculated spectra and can be extrapolated to the transition observed at low energy only for **2**$^{-}$.

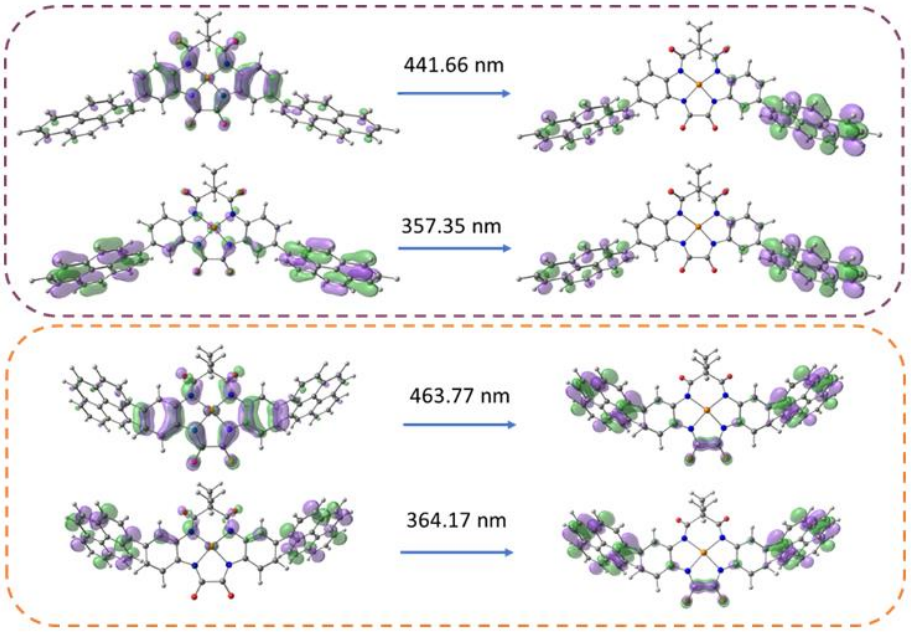

Figure 3. Representation of the main orbitals involved in the charge transfer at the different adsorption peaks simulated by TD-DFT for complex **1**$^{-}$ (top) and **2**$^{-}$ (bottom).

The ligands have, as well, specific features which can be associated to the different electronic distribution of the two regioisomers. The ligand H_4L2, in fact, absorb in a region closer to the visible range, between 307 and 449 nm, than H_4L1 (see Figure S20).

The redox properties of the two complexes were studied in CH_3CN containing 0.1 M of $TBAPF_6$ as supporting electrolyte (Figure 4). The cyclic voltammetry shows the presence of a reversible wave at -0.54 V and -0.56 V vs Fc/Fc^+ for **1**$^{-}$ and **2**$^{-}$, respectively, which can be associated with the Cu(III)/Cu(II) couple as compared to the unmodified complex that shows a reversible wave, associated with Cu(III)/Cu(II) at the similar potential of -0.60 V.[19]

Table 2. Comparison of the Cu(III)/Cu(II) $E_{1/2}$ in CH_3CN.

Entry	Complex	$E_{1/2}$ Cu(III)/Cu(II) (V vs. Fc/Fc^+)
1[tw]	$\mathbf{1}^-$	-0.54
2[tw]	$\mathbf{2}^-$	-0.56
3[19]	$[(MAC)Cu]^{2-}$	-0.60
4[20]	$[(L3)Cu]^{2-}$	-0.28
5[20]	$[(L4)Cu]^{2-}$	-0.33
6[a]	$[(L5)Cu]^-$	-0.57

Tw stands for this work. a) Not published results

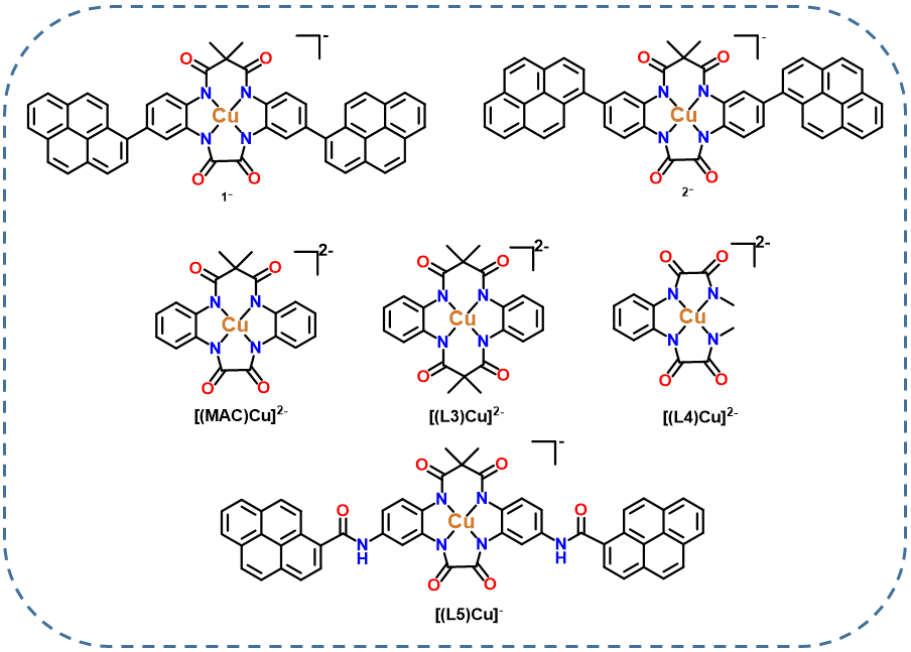

Chart 1. Drawing of the complexes structure whose $E_{1/2}$ is reported in table 2.

This lower potential of the unmodified complex was explained considering the σ-donor character of the coordinative amides able to stabilize the higher oxidation state of the metal. The higher or lower potentials needed in case of similar TAML based Cu complexes (see Table 2) are justified by the increase or decrease stabilization given by the ligand to the Cu(III) species. In general, the more electro-donating in the ligand the greater will be the stabilization of the oxidized species. Judging by the Cu(III/II) potentials in $\mathbf{1}^-$, $\mathbf{2}^-$ and $[(L5)Cu]^-$

compared to $[(MAC)Cu]^{2-}$, the presence of two pyrene group exert a small electron-withdrawing effect.

The higher energy required for the oxidation of the copper in $[(L3)Cu]^{2-}$ and $[(L4)Cu]^{2-}$ could be attributed to the lower σ-donation given by the ligand in comparison with $[(MAC)Cu]^{2-}$, whose smaller ring ensures a good overlap between the d-orbitals of the metal and the ones of the ligand.

Coming back to the CV of $\mathbf{1}^{-}$ and $\mathbf{2}^{-}$, at potential of circa 0.5 V vs Fc/Fc^{+} (see Figure 4) it is possible to observe the oxidation of the ligand with a reduction peak at 0.35 V *vs*. Fc/Fc^{+}. The pyrene could partially be the responsible of this redox process. The oxidation of this moiety is usually followed by a fast polymerization with a second molecule of pyrene as has been previously described for a related pyrene compound, *vide infra*.[15] The CV of Complex $\mathbf{1}^{-}$ shows a further process at 0.1 V whose nature is still not clear.

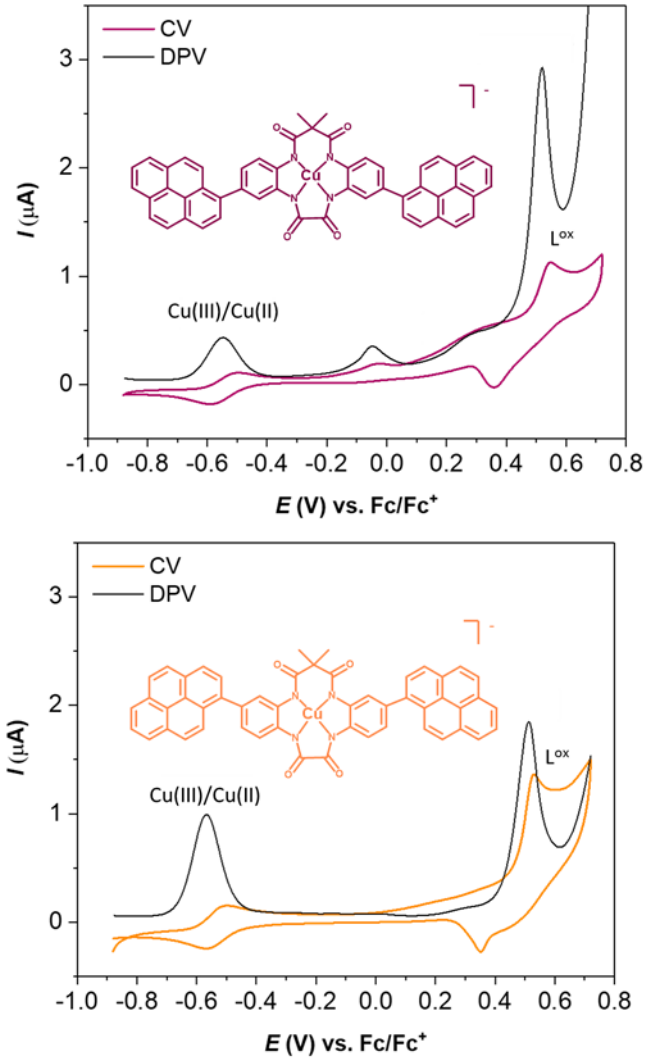

Figure 4. CV and DPV of 0.2 mM of $\mathbf{1}^-$ (top) and $\mathbf{2}^-$ (bottom) solution in CH_3CN with 0.1 $TBAPF_6$, at 10 mVs^{-1}, BDD (WE), Pt (CE), $Ag/AgNO_3$.

The comparison between the CVs of the complexes and the respective ligands in dimethylacetamide (DMA), where all compounds are fully soluble, is shown in Figure S25 and S26.

Pyrene polymerization on nano-ITO electrodes and characterization

The pyrene can be electropolymerize by slow sweep cyclic voltammetry going to potentials around 1.45 V vs NHE in organic aprotic solvents.[15]
The Scheme 2 depicts the process, which proceeds through the reaction between two radical cations and the following deprotonation of the carbons.[15,16] The positions were, most probably, the chain propagation occurs are 1,3, 6 and 8 and it is where the maximum unpaired electron density is situated.

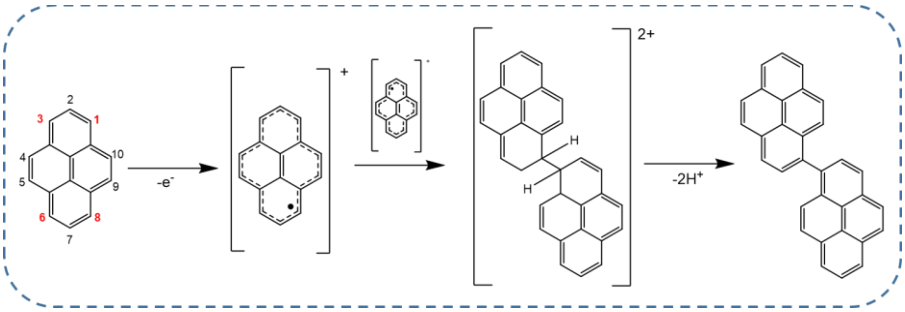

Scheme 2. Schematic representation of pyrene polymerization.[15]

In this study, the electropolymerization of the pyrene scaffold was used as anchoring strategy for complexes $\mathbf{1}^{-}$ and $\mathbf{2}^{-}$. The molecular anodes *p*-**1**@n-ITO@GC, *p*-**1**@n-ITO@ITO and *p*-**2**@n-ITO@GC, *p*-**2**@n-ITO@ITO were prepared by cycling GC or ITO electrodes covered with nano-ITO, in a 0.2 mM solution of $\mathbf{1}^{-}$ or $\mathbf{2}^{-}$ in CH_3CN containing 0.1 M of $TBAPF_6$ as supporting electrolyte, in a range of potential between -0.78 and 0.83 V vs Fc/Fc^{+} (-0.16 V to 1.45 V vs. NHE), see Figure 5 and Figure S27-S29.
During polymerization, it is possible to observe the lowering of the onset oxidative potential for the poly-pyrene, having a more extensively conjugated systems, which HOMO energies are higher than for the monomer.[15] New waves, rising during cycling, at potentials slightly lower than the pyrene oxidation process, around 0.2 – 0.4 V (see also Figure S27) could be attributed to the electroactivity of the polypyrene backbone of the polymer.[16] The wave increasing at -0.4 V is assigned toa metal center oxidation.
When ITO electrodes are used as support, it is possible to observe a thin brownish-orange film after the electropolymerization. The UV-Vis spectrum shows a wide band in the range of 350-600 nm (Figure S40). Further, resonance

Raman analysis of the ITO electrodes indicated the presence of pyrene with the typical peaks belonging to ring stretching at 1380 cm^{-1} and C-C stretching around 1240, 1590 and 1630 cm^{-1} (Figure S39).[25,26]

Due to its insolubility in acetonitrile, the ligand is dissolved in a DMF/MeCN (3:10) mixture, but, even after repetitive cycles at high potentials (Figure S28)., only a small amount of polymerized ligand was observed on the electrode by CV. This behavior could be attributed to the presence of DMF, which is probably able to solubilize the formed polymer and thus it does not stick at the electrode surface.

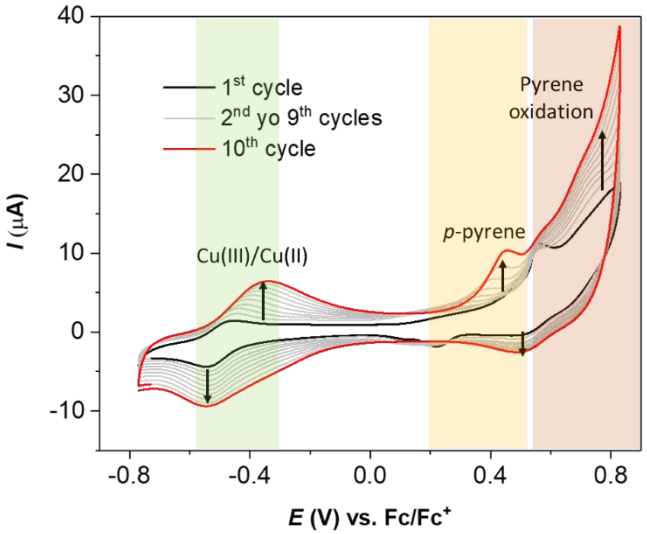

Figure 5. Electropolymerization of $\mathbf{1}^{-}$. 10 cycles in a CH_3CN solution 0.2 mM of $\mathbf{1}^{-}$, at 10 mVs^{-1}. n-ITO@ITO (WE), Pt (CE); $Ag/AgNO_3$ (RE).

The surface coverage (Γ, in nmol cm^{-2}) of the obtained electrode *p*-**1**@n-ITO@GC is calculated from the cyclic voltammogram of different samples in propylene carbonate, using the formula $\Gamma=Q/nSF$, where Q is the charge under the Cu(III)/Cu(II) wave, n is the number of electrons involved in the process, S is the area of the electrode and F is the Faraday constant. The Γ obtained were between the values of 11.6 and 4.22 nmol cm^{-2} (Figure S32).

The CV in propylene carbonate of *p*-**1**@n-ITO@GC, shown in Figure 6 top (violet line) shows three redox events. The first one with $E_{1/2}$ of -0.48 V vs Fc/Fc^{+} can be

associated with the Cu(III)/Cu(II). The same $E_{1/2}$ was recorded for the complex in solution in the same solvent (See Figure S24). The decrease in the ΔE_p from the 90 mV of the species in solution to 70 mV indicates a surface-confined redox process. The second wave around 0.0 V, could be related to the oxidation of the pyrene polymer, comparing the CV of the polymerized complex with the one of the polymerized pyrene (green line). The last wave at 0.8 V can be still related to the charge and discharge of the pyrene.[15]

The addition of a small amount of water (circa the 2% of the total volume) changes drastically the shape of the *p*-**1**@n-ITO@GC and pyrene cyclic voltammograms (Figure 6 bottom). A new wave appears at circa -0.65 V, at the same potential of the huge wave belonging to the pyrene polymer. The wave at 0.0 V disappear while the one of pyrene polymer, located at circa the same potential, decreases in intensity.

Further addition of water up to 7.5% in the total volume, move the wave associated to the Cu(III)/Cu(II) couple more and more to the anodic region, while the last wave, probably due to the charge and discharge of pyrene, loses its reversible character (see Figure S30 and S31).

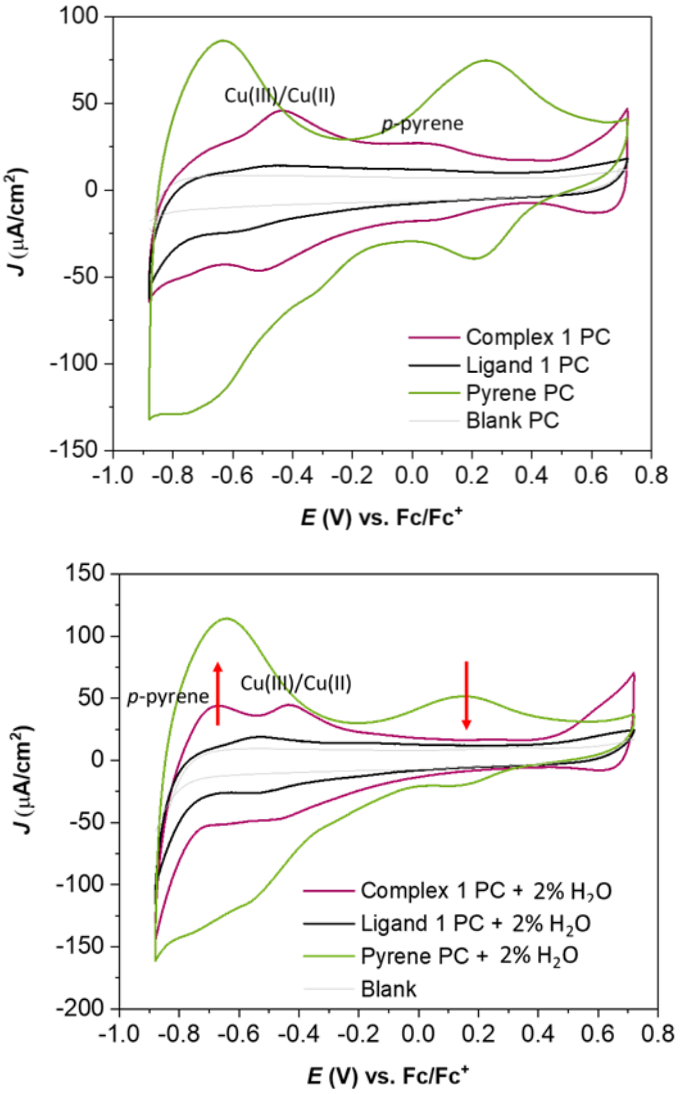

Figure 6. CV comparison between *p*-**1**@n-ITO@GC, (violet line), **L1**@ n-ITO@GC (black line), pyrene@n-ITO@GC (green line) and the blank (gray line) in propylene carbonate (top) and propylene carbonate with 2% water (bottom) at 10 mVs^{-1}. Pt (CE), $Ag/AgNO_3$ (RE).

Water Oxidation Catalysis

Redox behavior in water

The CV performed in 0.1 M borate buffer pH 10, shown in Figure 7, presents two close redox processes, at low potentials, one at circa 0.0 V, which can be related to the pyrene polymer (see Figure 6), and the other at 0.35 V probably due to the ligand-based oxidation of the TAML ligand, as reported previously for the unmodified complex $[(MAC)Cu]^{2-}$. A third irreversible process starts at circa 0.8 V, at similar potentials $[(MAC)Cu]^{-}$ undergoes to a second ligand-based oxidation leading to the formation of the species able to coordinate a molecule of OH^{-}, forming the intermediate $[(MAC)Cu\text{-}OH]^{-}$. The same process is possibly occurring also for the polymerized complex. At higher potentials, the irreversible wave could be associated to the attack of a second molecule of OH^{-} or H_2O, to the Cu-OH intermediate, leading to the formation of the O-O bond.

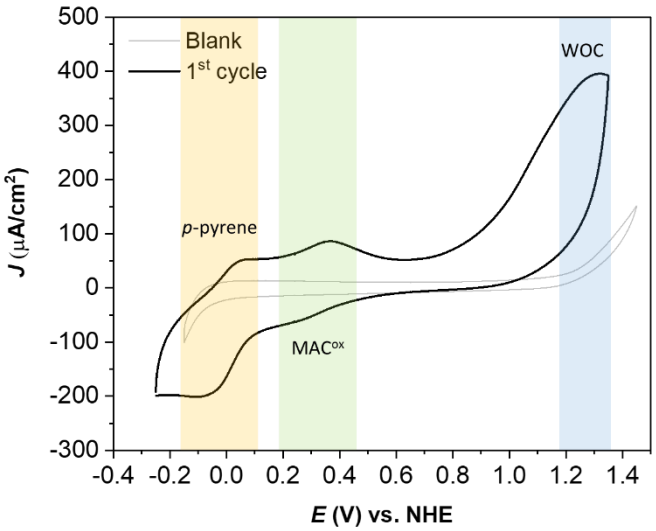

Figure 7. CV at 10 mVs^{-1} of *p*-**1**@n-ITO@GC, in 0.1 M borate buffer pH 10. Pt (CE), $Hg/HgSO_4$ (RE).

Oxygen Evolution

The oxygen evolution is monitored at the rotating ring disk electrode (RRDE). $\mathbf{1}^-$ and $\mathbf{2}^-$ are polymerized as previously described on the GC_{disk} of the RRDE modified with the nano-ITO. The experiment are carried out performing a linear sweep voltammetry (LSV) at the disk electrode, reaching the potential for the electrocatalytic water oxidation, while the platinum ring electrode is set at a potential were the oxygen is reduced, previously estimated through CV (Figure S34). When the oxygen produced at the disk reach the ring, this will reduce the O_2 and a negative current will be associated to the oxidative process responsible for the oxygen generation. The RRDE experiments were performed at pH 7.5, 9 and 10, through a linear sweep voltammetry (LSV) from -0.05 V to 1.75 V vs NHE. The results obtained for the electrode modified with $\mathbf{1}^-$ indicates the presence of an oxidative process, to which it is associated the generation of oxygen, with onset potential at 1.45 V, 1.32 V, and 1.23 V for pH 7.5, 9, and 10, respectively (Figure 8, Top). A similar behavior is observed for $\mathbf{2}^-$, where oxygen was detected at 1.49 V (pH 7.5), 1.32 V (pH 9) and at 1.21 V (pH 10).(Figure 8 bottom).
The efficiency of the process is calculated to be the 74% and the 66% at pH 10 for $\mathbf{1}^-$and $\mathbf{2}^-$**,** respectively. The relatively low efficiency could be explained by the possible side-processes involving the oxidation of the GC_{disk} electrode.

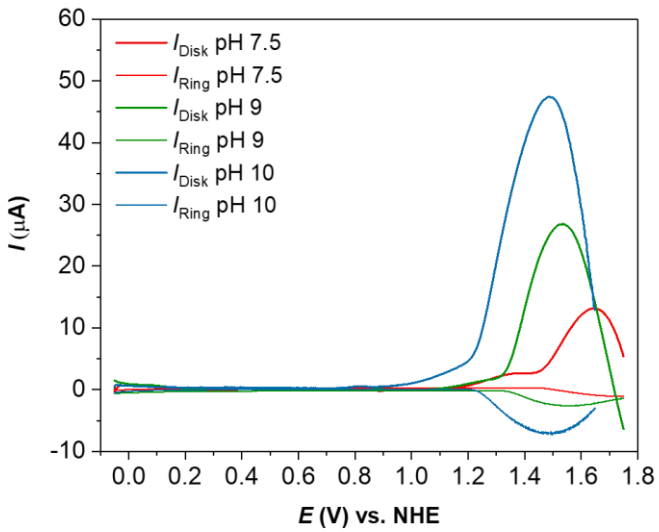

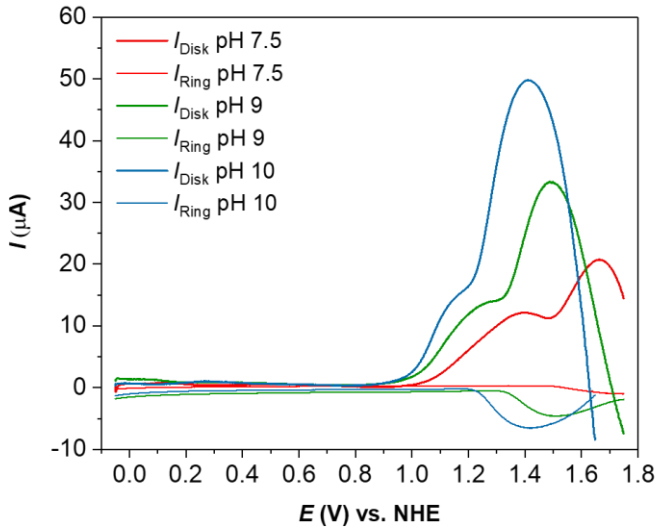

Figure 8. LSV of the modified *p*-**1**@n-ITO@GC (top) *p*-**2**@n-ITO@GC (bottom) RRDE in borate buffer at pH 7.5 (red line), 9 (green line) and 10 (blue line) under nitrogen atmosphere and at 1600 rpm and simultaneous oxygen reduction at Pt ring of the RRDE by CPE at 0.05 V (pH 7.5, red line), -0.05 V (pH 9, green line) and -0.15 V (pH 10, blue line). All the experiments are blank subtracted.

The pre-catalytic process, observed for *p*-**1**@nITO@GC and *p*-**2**@nITO@GC in the LSV recorded during the RRDE experiments, could be related to a further oxidation necessary to form a highly electrophilic intermediate able to trigger the oxygen evolution at relatively low pH values, as observed for the unmodified catalyst.[19] This last process has a strong pH dependency in case of $\mathbf{2}^{-}$, while for $\mathbf{1}^{-}$ looks almost to disappear at pH 10.
Further kinetic details, as the TOF, still need to be calculated.

In order to check the stability of the new molecular anodes, the electrodes *p*-**1**@n-ITO@GC was cycled above the potential triggering the catalysis in pure propylene carbonate and in a solution with just the 2% of water (Figure S36). At potentials of 0.8 V vs Fc/Fc^{+} (1.45 V vs. NHE) in pure organic solvent the organic polymeric structure anchored to the electrode undergoes to irreversible changes after the first anodic scan, but the wave corresponding to the Cu(III)/Cu(II) process maintains its reversibility. When 2% of water is added to

the system also the wave related to the metal center decreases its current, possibly indicating the depletion of the metal form the organic framework.
When the same experiment is tried in pure borate buffer pH 10, the decreasing of the wave at 0.35 V, associated to the ligand-based oxidation of the TAML is almost immediate, while the wave belonging to the pyrene polymer at circa 0.0 V was just slightly modified by the change of potential (Figure S37).
These data could indicate a degradation processes associated with the oxidation of the organic framework.
Considering these results, some analysis were performed to discard copper oxide (CuO) as responsible for the oxygen evolution. The comparison of the cyclic voltammogram in borate buffer pH 10 of an electrode modified with CuO, indicates that copper oxide is not active at the same conditions were the catalysts are (Figure S38). UV-Vis analysis of the ITO modified electrode does not show particular changes just the decrease in absorbance after the cyclic voltammetry in water (Figure S40). The resonance Raman spectra of the same electrode after cycling in water shows only the typical peaks of pyrene. At higher frequencies no peaks of typical of CuO are observed (Figure S39).[27,28]

B.3 Discussion and Conclusions

The modification of an already reported TAML macrocycle, with two pyrene moieties leaded to the formation of two new regioisomeric ligands, which, after addition of copper gave the complexes **1**$^{-}$ and **2**$^{-}$.
The X-Ray structure of **1**$^{-}$ indicated a complex with the typical flat square planar geometry of Cu d^8 and confirmed by X-ray crystallography.
The two complexes have different electronic properties, due to their distinct electronic distribution, with the isomer **2**$^{-}$ able to absorb light at higher wavelengths than **1**$^{-}$.
In the CV and DPV performed in acetonitrile the Cu(III)/Cu(II) couple potential appears at -0.54 V (**1**$^{-}$) and -0.56 V (**2**$^{-}$). A second wave at higher potentials is associated with the oxidation of the ligand framework, which will most likely involve both the amidate and the pyrene moieties.
The electropolymerization, of the complexes, which can be easily performed through oxidation of the pyrenes on nano-ITO, gives modified molecular anodes able to work in a pH range between 7.5 and 10.

The polymers can be further characterized on transparent ITO electrodes. The UV-Vis spectra indicated the presence of a high delocalized system with an intense absorbance in the range of 400-500 nm.

The stability of the system should be significantly optimized, and further studies have to be performed on the electrode surface to complete the characterization the anchored species before and after catalysis.

The suggested analysis are SEM and EDX, to obtain the morphology and the composition of the polymers, XPS, to have a deeper analysis of the surface composition, XAS, which will give the first coordination sphere of the complex and the oxidation state of the copper.

B.4 Acknowledgments

Support from MINECO, FEDER, and AGAUR is gratefully acknowledged through grants CTQ2016-80058-R, CTQ2015-73028-EXP, SEV 2013-0319, ENE2016-82025-REDT, CTQ2016-81923-REDC, and 2017-SGR-1631.

B.5 References

(1) IEA. https://www.iea.org/reports/world-energy-balances (accessed Oct 3, 2020).

(2) Berardi, S.; Drouet, S.; Francàs, L.; Gimbert-Suriñach, C.; Guttentag, M.; Richmond, C.; Stoll, T.; Llobet, A. *Chem. Soc. Rev.* **2014**, *43*, 7501–7519.

(3) Mckone, J. R.; Lewis, N. S.; Gray, H. B. *Chem. Mat.* **2014**, *26*, 407–414.

(4) Kärkäs, M. D.; Åkermark, B. *Dalt. Trans.* **2016**, *45*, 14421−14461.

(5) Bullock, R. M.; Das, A. K.; Appel, A. M. *Chem. Eur. J.* **2017**, *23*, 7626–7641.

(6) Materna, K. L.; Crabtree, R. H.; Brudvig, G. W. *Chem. Soc. Rev.* **2017**, *46*, 6099–6110.

(7) Francàs, L.; Richmond, C.; Garrido-barros, P.; Planas, N.; Roeser, S.; Benet-buchholz, J.; Escriche, L.; Sala, X.; Llobet, A. *Chem. Eur. J.* **2016**, *22*, 5261–5268.

(8) Chen, Z.; Concepcion, J. J.; Jurss, J. W.; Meyer, T. J. *J. Am. Chem. Soc.* **2009**, *131*, 15580–15581.

(9) Odrobina, J.; Scholz, J.; Pannwitz, A.; Franca, L.; Dechert, S.; Llobet, A.; Jooss, C.; Meyer, F. *ACS Catal.* **2017**, *7*, 2116–2125.

(10) Guerrero, G.; Mutin, P. H.; Vioux, A. *Chem. Mater.* **2001**, *13*, 4367–4373.

(11) Brennan, B. J.; Koenigsmann, C.; Materna, K. L.; Kim, P. M.; Koepf, M.; Crabtree, R. H.; Schmuttenmaer, C. A.; Brudvig, G. W. *J. Phys. Chem. C* **2016**, *120*, 12495–12502.

(12) Creus, J.; Matheu, R.; Peñafiel, I.; Moonshiram, D.; Blondeau, P.; Benet-Buchholz, J.; García-Antón, J.; Sala, X.; Godard, C.; Llobet, A. *Angew. Chemie - Int. Ed.* **2016**, *55*, 15382–15386.

(13) Mola, J.; Mas-marza, E.; Sala, X.; Romero, I.; Viæas, C.; Parella, T.; Llobet, A. *Angew. Chemie - Int. Ed.* **2008**, *47*, 5830–5832.

(14) Sayed-ahmad-baraza, Y.; Ewels, C.; Gaubicher, J. *J. Mater. Chem. A* **2017**, *5*, 1488–1494.

(15) Bachman, J. C.; Kavian, R.; Graham, D. J.; Young Kim, D.; Noda, S.; Nocera, D. G.; Shao-Horn, Y.; Lee, S. W. *Nat. Commun.* **2015**, *6*, 3–4.

(16) Waltman, R. J.; Bargon, J. *J. Electroanal. Chem.* **1985**, *194*, 49–62.

(17) Wu, X.; Li, F.; Zhang, B.; Sun, L. *J. Photochem. Photobiol. C Photochem. Rev.* **2015**, *25*, 71–89.

(18) Fukuzumi, S.; Hong, D. *Eur. J. Inorg. Chem.* **2014**, No. 4, 645–659.

(19) Garrido-Barros, P.; Moonshiram, D.; Gil-Sepulcre, M.; Pelosin, P.; Gimbert-Suriñach, C.; Benet-Buchholz, J.; Llobet, A. *J. Am. Chem. Soc.* **2020**, *142*, 17434–17446.

(20) Garrido-Barros, P.; Funes-Ardoiz, I.; Drouet, S. . B.-; Buchholz, J.; Maseras, F.; Llobet, A. *J. Am. Chem. Soc.* **2015**, *137*, 6758−6761.

(21) Garrido-Barros, P.; Funes-Ardoiz, I.; Drouet, S.; Benet-Buchholz, J.; Maseras, F.; Llobet, A. *J. Am. Chem. Soc.* **2015**, *137*, 6758–6761.

(22) Garrido-Barros, P.; Gimbert-Surinifach, C.; Moonshiram, D.; Picón, A.; Monge, P.; Batista, V. S.; Llobet, A. *J. Am. Chem. Soc.* **2017**, *139*, 12907–12910.

(23) Ellis, W. C.; McDaniel, N. D.; Bernhard, S.; Collins, T. J. *J. Am. Chem. Soc.* **2010**, *132*, 10990–10991.

(24) Hoque, A.; Gil-sepulcre, M.; Aguirre, A. De; Elemans, J. A. A. W.; Moonshiram, D.; Matheu, R.; Shi, Y.; Benet-buchholz, J.; Sala, X.; Malfois, M.; Solano, E.; Lim, J.; Garzón-manjón, A.; Scheu, C.; Lanza, M.; Maseras, F.; Gimbert-suriñach, C.; Llobet, A. *Nat. Chem.* **2020**, *12*, 1060–1066.

(25) Wang, X.; Hao, W.; Zhang, H.; Pan, Y.; Kang, Y.; Zhang, X.; Zou, M.; Tong, P.; Du, Y. *Spectrochim. Acta - Part A Mol. Biomol. Spectrosc.* **2015**, *139*, 214–221.

(26) Shinohara, H.; Yamakita, Y.; Ohno, K. *J. Mol. Struct.* **1998**, *442*, 221–234.

(27) Debbichi, L.; Marco De Lucas, M. C.; Pierson, J. F.; Krüger, P. *J. Phys. Chem. C* **2012**, *116*, 10232–10237.

(28) Hagemann, H.; Bill, H.; sadowski, W.; Walker, E.; François, M. *Solid State Commun.* **1990**, *73*, 447–451.

B.6 Supporting Information

Experimental Section

Materials

All general reagents and chemicals were used as purchased without further purification unless otherwise stated. The used solvents were HPLC grade. Air and moisture sensitive reactions were carried out under N_2 or Ar in oven-dried (120°C) glassware. Evaporation of solvents *in vacuo* was done with a *Büchi Rotevapor R-200* at 40°C. Water was deionized by passing through a nanopore Milli-Q purification system. Aqueous buffers (Ph 7.5, 9, 10 and 12, and ionic strenght of 0.1 M) were prepared using the necessary amount of boric acid and borax ($Na_2B_4O_7{\cdot}10H_2O$). Glassy Carbon Disk (GC), Platinum Disk (Pt), $Hg/HgSO_4$ and $Ag/AgNO_3$ electrodes were purchased from IJ-Cambria Ldt. Indium Tin Oxide (ITO) electrodes (Rs = 8−12 Ω) were purchased from ALPHA BIOTECH. Indium tin oxide nanopowder < 50 nm was purchased from Aldrich.

Instrumentation and measurements

NMR spectra were measured on a *Bruker AV-500* and *Bruker AV-400* spectrometers. All NMR experiments were performed at room temperature in corresponding deuterated solvents and using their residual proton signals as reference.

UV-Vis spectra were measured on a *Cary 50 UV-vis* spectrometer by *Varian Inc*.

Exact mass analyses were performed with a micrOTOF mass spectrometer (from Bruker company) using Electrospray ionization technique in methanol by direct injection and detecting with positive polarity.

Electrospray ionization mass spectra (ESI-MS) were performed on an *Agilent Technologies 6130-Quadrupole LC/MS* connected to an *Agilent Technologies HPLC-1200 series* or an *MicroTOF II (Bruker Daltonics): HPLC-MS-TOF* for high resolution. HR-MALDI mass spectra were measured on an *AutoFlex (Bruker Daltonics): MALDI-TOF-MS*.

Elemental Analysis of the samples was carried out in a Thermo Finnigan elemental analyzer Flash 1112 model.

IR spectrometry was performed using a FTIR-ATR TR0 equipment using the pure synthetized compounds as solids.

Resonance Raman Spectroscopy was performed in a Renishaw inVia Confocal Reflex RAMAN microscope instrument (Gloucestershire, UK), equipped with an Ar ion laser, operating at 405 nm. The spectrometer was equipped with a Peltier-cooled CCD detector (-70°C) coupled to a Leica DM-2500 microscope. Calibration was carried out with respect to Si standard.

Electrochemical measurements

Differential pulse voltammetry (DPV) and cyclic voltammetry (CV) were measured on a CHI660 potentiostat using a three-electrode cell. Glassy carbon (GC), boron-doped diamond (BDD) (d = 3 mm) or ITO (1 cm^2) working electrodes (WE) were employed while a Pt disk/mesh was used as counter electrode (CE) and a $Hg/HgSO_4$ (K_2SO_4 sat.) or $Ag/AgNO_3$ (0.01 M $AgNO_3$ in 0.1 M solution of $TBAPF_6$ in MeCN) electrodes were used as a references (RE). The working electrodes were polished with 0.05 micron alumina paste (GC) or with diamond paste (BDD) and washed with distilled water before each measurement. The ITO glass slides (1 cm^2) were immersed in the electrolyte solution and sonicated in MeOH (K_2CO_3 sat.) for 30 min and then rinsed with acetonitrile and water. CVs were typically recorded at different scan rates from 10 to 500 mV/s. DPVs were recorded with the following parameters: amplitude = 50 mV, step height = 4 mV, pulse width = 0.05 s. All redox potentials in the present work are reported versus either NHE by adding 0.648 V ($HgSO_4$) to the measured potential or versus Fc^+/Fc as internal standard. All the measurements were done applying IR compensation.

Surface coverage (Γ) calculation

The surface coverage (Γ) was calculated based on electrochemical measurements according to the following formula:

$$\Gamma(mol\ cm^{-2}) = \frac{Q}{n\ S\ F}$$

Q is the charge under the oxidative peak of the reversible, one-electron wave obtained by integration in the CV; n is the number of electrons involved in that oxidation process, which is 1; S is the geometrical surface of the electrode that

is 0.07 cm^{-2} and F is the Faradaic constant. In this work, the average surface coverage was calculated from 3 independent electrodes that were subjected to CV under same conditions. The error of the measurements was expressed as the standard deviation among the different values obtained.

Rotating Ring Disk

The oxygen evolution was monitored for the anchored species though an RRDE-3A Rotating Ring Disk Electrode from IJ-Cambria. The used electrode brings a central glassy carbon disk (GC_{disk}, 5 mm of diameter) a teflon middles ring (5 mm of diameter) and an external platinum ring (Pt_{ring}, 7 mm of diameter).
The solution is placed in a cell which can be hermetically closed with a Teflon stopper, having three holes where to place WE, CE and RE. Two smaller holes at the said are the entrance for the nitrogen flow tubes. The electrode are plugged to a IJ-Cambria CHI-770 potentiostat. Before the experiment in water the buffered solution is purged with nitrogen for at least 10 minutes.

Synthesis

Synthesis of tert-butyl (2-amino-5-(pyren-1-yl)phenyl)carbamate (2.1) and tert-butyl (2-amino-4-(pyren-1-yl)phenyl)carbamate (2.2).

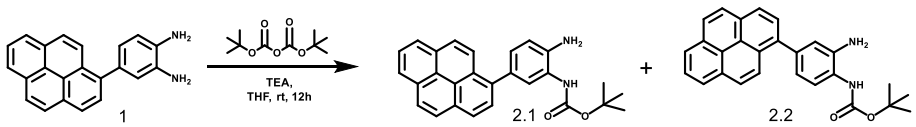

The synthesis of the Boc-mono protected adduct is performed solving 500 mg (1.6 mmol) of 1 in 40 mL of THF anhydrous. HPLC grade Et_3N (2 mmol, 213 mg, 1.3 eq) is added to the solution. Di-t-Butyl-dicarbonate (Boc2O) (1.5 mmol, 337 mg 1.05 eq) dissolved in 4 mL of THF anhydrous, is added drop-wise to the rapidly stirred solution. The reaction is performed under argon and allowed to proceed overnight. After evaporation of the solvent, the solid is purified by column chromatography. Silica was used as stationary phased and DCM used as mobile phase at low rate. The two regio-isomers are collected as third and fourth fraction respectively.

Isomer 2.1: Yield: 121 mg (0.296 mmol), 30%. MS (ESI positive mode, MeOH): m/z $[M+H]^+$ = 409.2 (Expected: 408.18).
^{1}H NMR (500 MHz, DMSO) δ 8.48 (H-NBoc, s, 1H), 8.31 (Pyrene, d, *J* = 7.9 Hz, 1H), 8.29 (Pyrene, dd, *J* = 7.6, 1.1 Hz, 1H), 8.27 – 8.22 (Pyrene, m, 2H), 8.18 (Pyrene, d, *J* = 4.6 Hz, 2H), 8.14 (Pyrene, d, *J* = 9.3 Hz, 1H), 8.07 (Pyrene, s, 1H), 7.95 (Pyrene, d, *J* = 7.9 Hz, 1H), 7.53 (H1, s, 1H), 7.14 (H3, dd, *J* = 8.1, 2.1 Hz, 1H), 6.92 (H2, d, *J* = 8.1 Hz, 1H), 5.14 (NH_2, s, 2H), 1.46 (Boc-CH_3, s, 9H).
^{13}C NMR (500 MHz, DMSO) δ 154.52 (NHCO-Boc), 138.59 (1C) 131.89 (1C), 131.35 (C3, 1C), 130.28 (1C), 128.90 (1C), 128.44 (1C), 128.41 (1C), 128.26 (1C), 128.01 (1C), 127.77 (1C), 127.11 (C1, 1C), 125.93 (1C), 125.87 (1C), 125.76 (1C), 125.51 (1C), 125.16 (1C), 125.04 (1C), 124.59 (1C), 116.57 (C2, 1C), 79.70 (Boc-C'-$(CH_3)_3$, 1C), 29.01 (Boc-C-$(C'H_3)_3$. 3C).

Isomer 2.2: Yield: 105 mg (0.257 mmol), 30%. MS (ESI positive mode, MeOH): m/z $[M+H]^+$ = 409.2 (Expected: 408.18).
^{1}H NMR (500 MHz, DMSO) δ 8.47 (H-NBoc, s, 1H), 8.34 – 8.25 (Pyrene, m, 3H), 8.22 – 8.13 (Pyrene, m, 4H), 8.08 (Pyrene, t, *J* = 7.6 Hz, 1H), 7.97 (Pyrene, d, *J* =

7.8 Hz, 1H), 7.45 (H2, d, *J* = 8.1 Hz, 1H), 6.97 (H1, d, *J* = 2.1 Hz, 1H), 6.79 (H3, dd, *J* = 8.1, 2.0 Hz, 1H), 5.09 (NH_2, s, 2H), 1.52 (Boc-CH_3, s, 9H).

^{13}C NMR (500 MHz, DMSO) δ 154.54 (NHCO-Boc), 141.86 (1C), 137.65 (1C), 131.84 (1C), 131.29 (1C), 130.63 (1C), 128.47 (1C), 128.23 (1C), 128.15 (1C), 128.01 (1C), 127.18 (1C), 126.02 (1C), 125.85 (1C), 125.67 (C2, 1C), 124.99 (1C), 124.13 (1C), 119.26 (C1, 1C), 118.30 (C3, 1C), 79.70 (Boc-C'-$(CH_3)_3$, 1C), 29.05 (Boc-C-$(C'H_3)_3$. 3C).

Synthesis of di-tert-butyl (((2,2-dimethylmalonyl)bis(azanediyl))bis(4-(pyren-1-yl)-2,1-phenylene))dicarbamate (3.1) and di-tert-butyl (((2,2-dimethylmalonyl)bis(azanediyl))bis(5-(pyren-1-yl)-2,1-phenylene))dicarbamate (3.2).

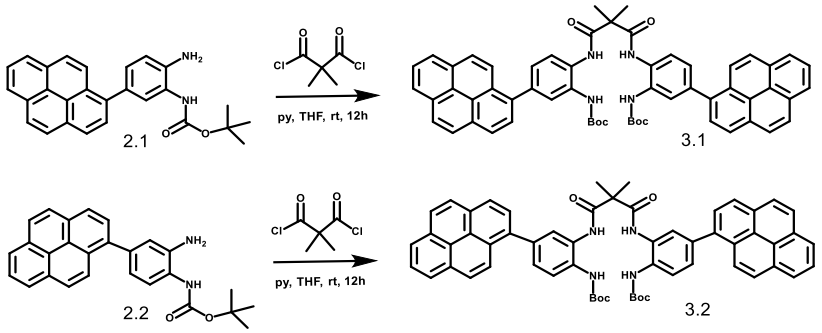

Anhydrous pyridine (2.5 mmol, 201 mg, 2.6 eq), is added to a solution of 2 (400 mg, 0.98 mmol) in 18 mL of THF anhydrous. A solution of Dimethylmalonyl chloride (0.49 mmol, 82 mg, 0.5 eq) in 6 mL of THF anhydrous is added dropwise. A pink-white solid (pyridinium chloride) is formed during the addiction. The solution is left to stir overnight under argon atmosphere. The solid is filtrated and the solvent removed to obtain the products 3.1 and 3.2 as a white solids. The isomers can be used directly or further purified by crystallization from boiling ethanol.

Isomer 3.1: Yield: 335 mg (0.364 mmol), 75%. MS (ESI negative mode, MeOH): m/z $[M-H]^-$ = 911.2 (Expected: 913.04).
^{1}H NMR (500 MHz, DMSO) δ 9.49 (H-NMalonyl, s, 1H), 8.89 (H-NBoc, s, 1H), 8.21 (Pyrene, d, *J* = 0.8 Hz, 2H), 8.19 – 8.12 (Pyrene, m, 2H), 8.08 (Pyrene, t, *J* = 7.6 Hz,

1H), 8.00 (Pyrene, d, *J* = 7.8 Hz, 1H), 7.78 – 7.74 (H1, H2, m, 2H), 7.38 (H3, dd, *J* = 8.1, 2.1 Hz, 1H), 1.66 (Malonyl-CH_3, s, 3H), 1.44 (Boc-CH_3, s, 9H).
^{13}C NMR (126 MHz, DMSO) δ 173.23 (NHCO-Malonyl), 154.58 (NHCO-Boc), 138.57 (1C), 137.21 (1C), 132.77 (1C), 131.82 (1C), 131.14 (2C), 129.77, 128.41 (2C), 127.21 (2C), 126.78, 125.86 (2C), 124.94 (2C), 80.65 (Boc-C'-$(CH_3)_3$, 1C), 52.11 (Malonyl-C'-$(CH_3)_2$), 28.89 (Malonyl-C-$(C'H_3)_3$. 3C) , 24.25 (Boc-C-$(C'H_3)_2$).

Isomer 3.2: Yield: 280 mg (0.306 mmol), 70%. MS (ESI negative mode, MeOH): m/z $[M-H]^-$ = 911.2 (Expected: 913.04).
^{1}H NMR (500 MHz, DMSO) δ 9.49 (H-NMalonyl, s, 1H), 8.87 (H-NBoc, s, 1H), 8.33 (Pyrene, t, *J* = 7.6 Hz, 2H), 8.26 (Pyrene, d, *J* = 7.5 Hz, 1H), 8.21 (Pyrene, s, 2H), 8.20 – 8.12 (Pyrene, m, 1H), 8.08 (Pyrene, t, *J* = 7.6 Hz, 1H), 7.99 (Pyrene, d, *J* = 7.9 Hz, 1H), 7.85 (H1, d, *J* = 2.1 Hz, 1H), 7.65 (H2, d, *J* = 8.2 Hz, 1H), 7.43 (H3, dd, *J* = 8.2, 2.2 Hz, 1H), 1.60 (Malonyl-CH_3, s, 3H), 1.28 (Boc-CH_3, s, 9H).

^{13}C NMR (126 MHz, DMSO) δ 173.00 (NHCO-Malonyl, 1C) , 154.59 (NHCO-Boc), 137.11 (1C), 137.07 (1C), 131.80 (1C), 131.66 (1C), 131.23 (1C), 130.98 (1C), 130.69 (1C), 128.54 (1C), 128.50 (1C), 128.36 (1C), 128.20 (1C), 127.89 (1C), 127.24 (1C), 126.19 (1C), 126.02 (1C), 125.80 (1C), 125.74 (1C), 125.38 (1C), 125.03(1C), 124.88 (1C), 80.48 (Boc-C'-$(CH_3)_3$, 1C) , 52.03 (Malonyl-C'-$(CH_3)_2$), 28.68 (Boc-C-$(C'H_3)_3$. 3C), 24.30 (Malonyl-C-$(C'H_3)_2$).

Synthesis of N1,N3-bis(2-amino-5-(pyren-1-yl)phenyl)-2,2-dimethylmalonamide (4.1) and N1,N3-bis(2-amino-4-(pyren-1-yl)phenyl)-2,2-dimethylmalonamide (4.2).

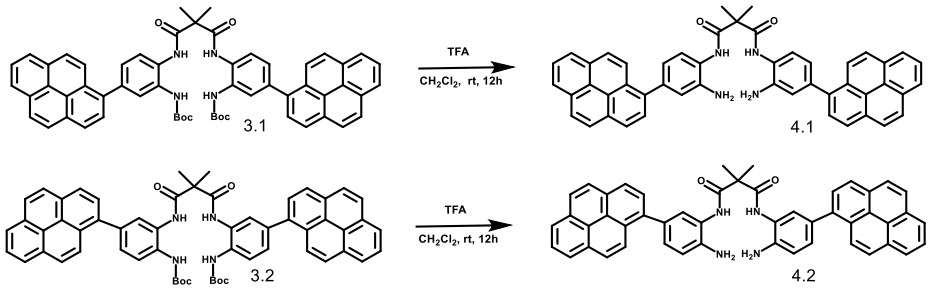

400 mg (0.438 mmol) of 3 are dissolved in 30 mL of DCM. Concentrated TFA (6.5 mmol, 749 mg 15 eq) is added slowly. The solution is left stirring overnight. The acid is neutralized with ice cold aqueous NaOH and the pH of the aqueous layer

was adjusted to 10.5. The mixture is extracted with dichloromethane (4 x 30 mL). The organic layers are dry on Na_2SO_4 anhydrous. The products 4.1 and 4.2 are obtained as brownish solids after evaporation of the solvent.

Isomer 4.1: Yield: 230 mg (0.323 mmol), 74%. MS (ESI negative mode, MeOH): m/z $[M-H]^-$ = 711.1 (Expected: 712.85).
^{1}H NMR (500 MHz, DMSO) δ 9.24 (H-NMalonyl, s, 1H), 8.35 (Pyrene, d, *J* = 7.9 Hz, 1H), 8.32 (Pyrene, d, *J* = 7.6 Hz, 1H), 8.28 (Pyrene, d, *J* = 7.6 Hz, 1H), 8.24 – 8.18 (Pyrene, m, 4H), 8.10 (Pyrene, d, *J* = 7.6 Hz, 1H), 8.01 (Pyrene, d, *J* = 7.8 Hz, 1H). 7.27 (H2, d, *J* = 7.8 Hz, 1H), 7.02 (H1, d, *J* = 2.0 Hz, 1H), 6.83 (H3, dd, *J* = 8.0, 2.0 Hz, 1H), 1.70 (Malonyl-CH_3, s, 3H).
^{13}C NMR (126 MHz, DMSO) δ 173.87 (NHCO-Malonyl, 1C), 144.75 (1C), 139.77 (1C), 138.51 (1C), 131.84 (1C), 131.27 (1C), 130.75 (1C), 128.48 (C2, 1C), 128.32 (1C), 128.24 (1C), 128.20 (1C), 128.10 (1C), 127.22 (1C), 126.09 (1C), 125.74 (1C), 125.69 (1C), 124.99 (1C), 124.94 (1C), 123.21 (1C), 118.99 (C3, 1C), 118.21 (C1, 1C), 51.79 (Malonyl-C'-$(CH_3)_2$), 24.49 (Malonyl-C-$(C'H_3)_2$).

Isomer 4.2: Yield: 202 mg (0.284 mmol), 65%. MS (ESI negative mode, MeOH): m/z $[M-H]^-$ = 711.1 (Expected: 712.85).
^{1}H NMR (500 MHz, DMSO) δ 9.71 (H-NMalonyl, s, 1H), 8.60 (Pyrene, t, *J* = 7.7 Hz, 2H), 8.56 – 8.47 (Pyrene, m, 5H), 8.44 – 8.36 (Pyrene, m, 2H), 8.27 (Pyrene, d, *J* = 7.9 Hz, 1H), 7.71 (H2, d, *J* = 2.1 Hz, 1H), 7.65 (H3, dd, *J* = 8.2, 2.1 Hz, 1H), 7.41 (H1, d, *J* = 8.2 Hz, 1H), 1.96 (Malonyl-CH_3, s, 3H).
^{13}C NMR (126 MHz, DMSO) δ 173.84 (NHCO-Malonyl, 1C), 152.30 (1C), 140.01 (1C), 137.86 (1C), 131.86 (1C), 131.29 (1C), 130.67 (1C), 130.47 (1C), 130.05 (1C), 129.75 (1C), 128.86 (1C), 128.41 (1C), 128.36 (1C), 128.22 (1C), 128.18 (1C), 127.91 (1C), 127.15 (1C), 125.97 (1C), 125.76 (1C), 125.73 (1C), 125.66 (1C), 125.57 (1C), 125.14 (1C), 124.99 (1C), 117.95 (1C), 51.80 (Malonyl-C'-$(CH_3)_2$), 24.36 (Malonyl-C-$(C'H_3)_2$).

Synthesis of 15,15-dimethyl-3,10-di(pyren-1-yl)-8,13-dihydro-5H dibenzo[b,h][1,4,7,10]tetraazacyclotridecine-6,7,14,16(15H,17H)-tetraone (5.1, H_4L1) and 2-(1,2-dihydropyren-1-yl)-15,15-dimethyl-11-(pyren-1-yl)-8,13-dihydro-5H-dibenzo[b,h][1,4,7,10]tetraazacyclotridecine-6,7,14,16(15H,17H)-tetraone (5.2, H_4L2).

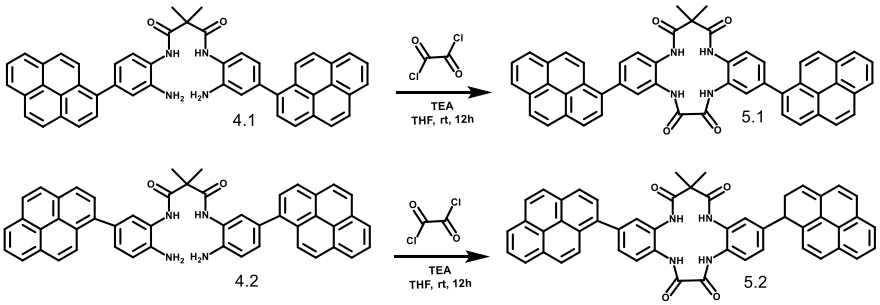

100 mg (0.14 mmol) of 4 are solved in 75 mL of THF anhydrous under argon atmosphere. Et_3N (0.3 mmol, 57 mg, 2.1 eq) is added to the mixture. A solution of Oxalyl dichloride 2M in DCM, (0.14 mmol, 70 µL, 1eq) in 12.5 mL of THF anhydrous is added dropwise. A white precipitate is immediately formed ($Et_3NH^+Cl^-$). The reaction is allowed to stir overnight. The $Et_3NH^+Cl^-$ is filtrated and the solvent removed. The obtained solid is washed with DCM.

Isomer 5.1: Yield: 27 mg (0.035 mmol), 25%. Elemental Analysis calc.(%) for $C_{51}H_{34}N_4O_4$: C 79.88, H 4.47, N 7.31; found (%): C 76.54, H 4.37, N 7.064. MS (MALDI$^+$ HCCA in TFA (H_2O):CH_3CN. Sample in DMSO): m/z [M+H]+ = 758.3 (Expected: 768.87).

^{1}H NMR (500 MHz, DMSO) δ 10.00 (H-NOxalyl, s, 1H), 9.81 (H-NMalonyl, s, 1H), 8.41 (Pyrene, d, *J* = 7.9 Hz, 1H), 8.33 (Pyrene, dd, *J* = 15.0, 7.6 Hz, 2H), 8.24 (Pyrene, d, *J* = 15.0 Hz, 4H), 8.15 – 8.07 (Pyrene, m, 2H), 7.92 (H1, s, 1H), 7.65 (H2, d, *J* = 8.1 Hz, 1H), 7.60 (H3, d, *J* = 8.4 Hz, 1H), 1.69 (Malonyl-CH_3, s, 3H).

^{13}C NMR (126 MHz, DMSO) δ 173.59 (NHCO-Oxalyl, 1C), 162.79 (NHCO-Malonyl, 1C), 139.23 (1C), 136.69 (1C), 131.82 (1C) , 131.21 (1C),130.97 (1C) 128.2–128.8 (C1, C2, C3, 1C), 127.83 (1C), 127.34 (1C), 126.35 (1C), 125.97 (1C), 125.89 (1C), 125.03 (1C), 124.87 (1C), 52.26 (Malonyl-C'-$(CH_3)_2$), 24.33 (Malonyl-C-$(C'H_3)_2$).

Isomer 5.2: Yield: 34 mg (0.044 mmol), 32%. Elemental Analysis calc.(%) for $C_{51}H_{34}N_4O_4$: C 79.88, H 4.47, N 7.31; found (%): C 77.59, H 4.59, N 7.15. MS (MALDI$^+$ HCCA in TFA (H_2O):CH_3CN. Sample in DMSO): m/z [M+H]+ = 823 (Expected: 768.87).

^{1}H NMR (500 MHz, DMSO) δ 9.97 (H-NOxalyl, s, 1H), 9.81 (H-NMalonyl, s, 1H), 8.41 (Pyrene, d, J = 7.8 Hz, 1H), 8.37 – 8.32 (Pyrene, m, 2H), 8.27 – 8.22 (Pyrene, m, 4H), 8.12 (Pyrene, t, J = 7.6 Hz, 1H), 8.08 (Pyrene, d, J = 7.8 Hz, 1H), 7.91 (H1, d, *J* = 8.1 Hz, 1H), 7.69 (H2, d, *J* = 2.1 Hz, 1H), 7.63 (H3, dd, *J* = 8.1, 2.1 Hz, 1H), 1.59 (Malonyl-CH_3, s, 3H).

^{13}C NMR (126 MHz, DMSO) δ 173.53 (NHCO-Oxalyl, 1C), 162.97 (NHCO-Malonyl, 1C), 138.93 (1C), 136.71 (1C), 131.77 (2C), 131.20 (2C), 129.66 (1C), 129.15 (1C), 128.80 (1C), 128.47 (C2, 1C), 128.24 (C3, 1C) 127.36 (1C), 126.45 (2C), 125.91 (C1, 1C), 125.20 (1C), 124.94 (2C), 52.21(Malonyl-C'-$(CH_3)_2$), 24.17 (Malonyl-C-$(C'H_3)_2$).

Synthesis of the complexes [(Cu)L1](NMe$_4$) and [(Cu)L2](NMe$_4$)

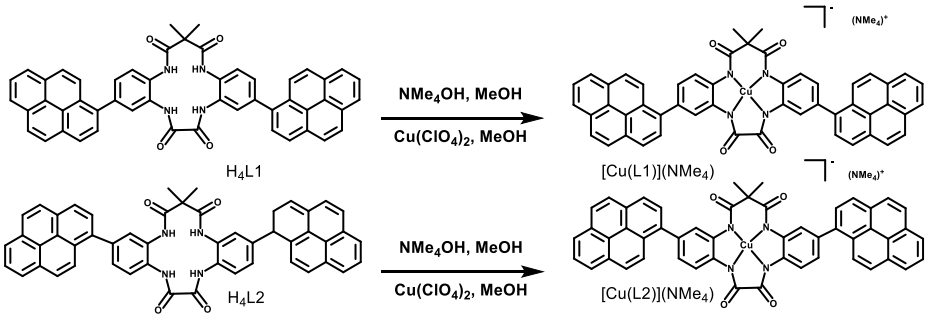

The ligand (10 mg, 0.013 mmol) is dispersed in 2.5 mL of DMF (concentration of 5 mM). After addition of (NMe_4)(OH), (10% in MeOH, 5.2 mg, 0.057 mmol, 4.4 eq), the mixture was stirred until complete dissolution, warming up at 50ºC. A solution in 2.5 mL of DMF of 5.3 mg (0.014 mmol) of $Cu(ClO_4)_2{\cdot}6H_2O$ (concentration of 5 mM) is added dropwise. After the Cu addition the mixture turns from yellow to deep brown The solution is left to stir overnight at 50 ºC. The solvent removed and the complex (brown) is washed with cold MeOH and Et_2O.

Isomer [(Cu)L1](NMe$_4$): Yield: 7.98 mg (0.0082 mmol) 63%. Elemental Analysis calc.(%) for $C_{59}H_{54}CuN_6O_4$: C 72.71, H 5.58, N 8.62; found (%): C 48.75, H 5.14, N

7.56. MS (MALDI$^-$, sample in DMSO:CH3CN (1:9), dctb in CH3CN): m/z [M-H]$^-$= 825.1 (expected 826.37).

Isomer [(Cu)L1](NMe$_4$): Yield: 7.22 mg (0.0074 mmol) 57%. Elemental Analysis calc.(%) for $C_{59}H_{54}CuN_6O_4$: C 72.71, H 5.58, N 8.62; found (%): C 30.99, H 5.46, N 6.81. MS (MALDI$^-$, sample in DMSO:CH3CN (1:9), dctb in CH3CN): m/z [M-H]$^-$= 825.1 (expected 826.37).

Spectroscopic characterization

NMR Spectroscopy

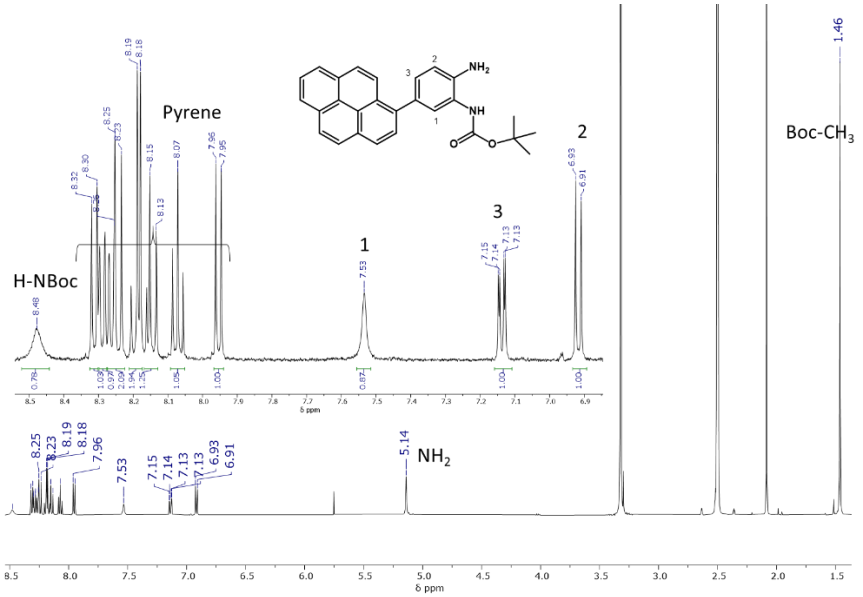

Figure S1. ^{1}H-NMR of tert-butyl (2-amino-5-(pyren-1-yl)phenyl)carbamate (2.1) in DMSO-d_6.

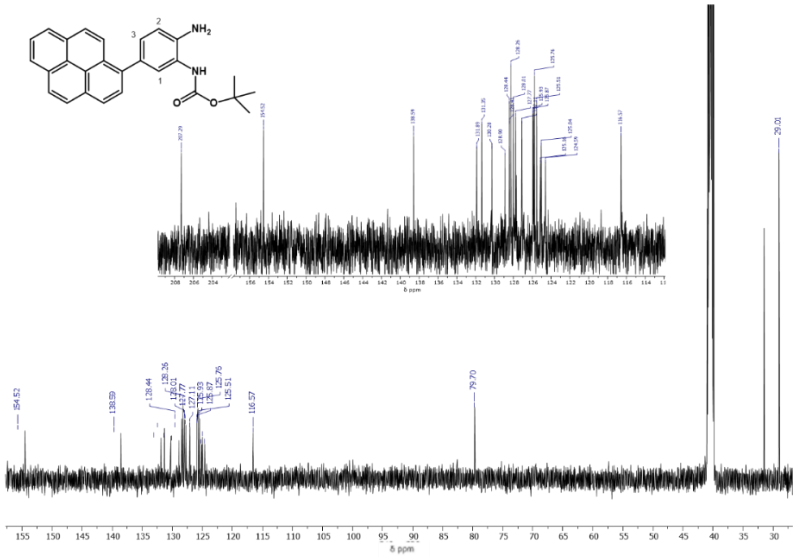

Figure S2. ^{13}C-NMR of tert-butyl (2-amino-5-(pyren-1-yl)phenyl)carbamate (2.1) in DMSO-d_6.

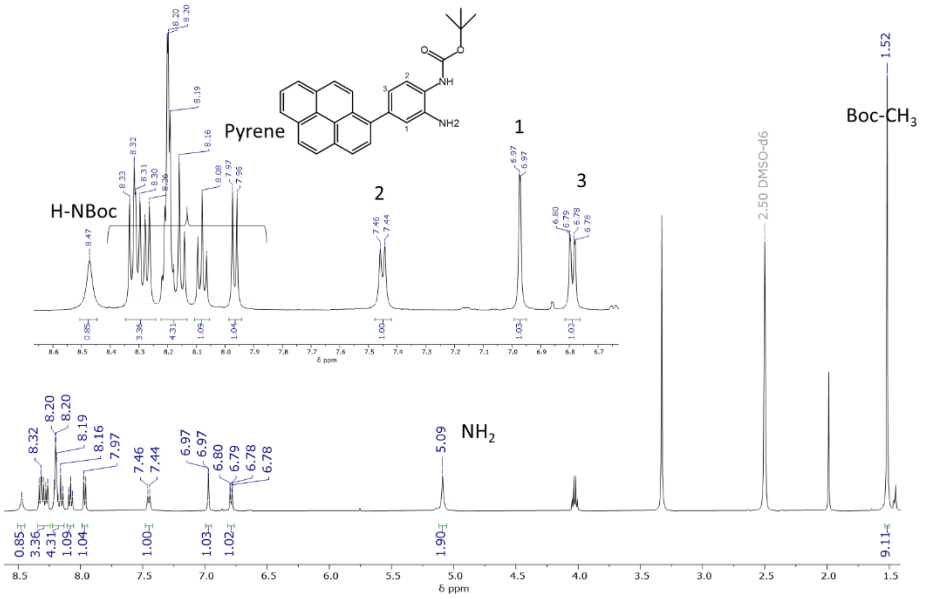

Figure S3. ^{1}H-NMR of tert-butyl (2-amino-4-(pyren-1-yl)phenyl)carbamate (2.2) in DMSO-d_6.

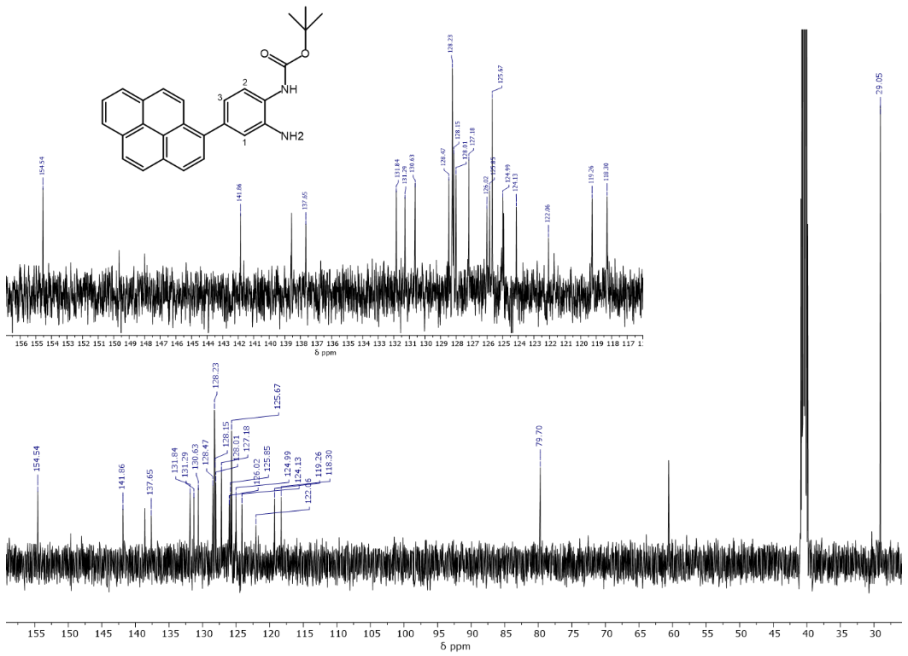

Figure S4. ^{13}C-NMR of tert-butyl (2-amino-4-(pyren-1-yl)phenyl)carbamate (2.2) in DMSO-d_6.

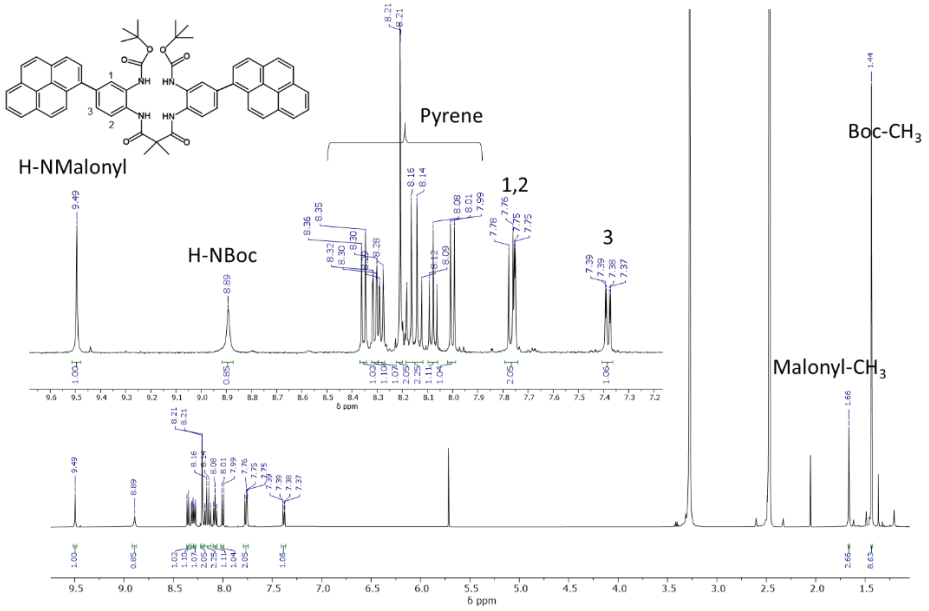

Figure S5. ^{1}H-NMR of di-tert-butyl (((2,2-dimethylmalonyl)bis(azanediyl))bis(4-(pyren-1-yl)-2,1-phenylene))dicarbamate (3.1) in DMSO-d_6.

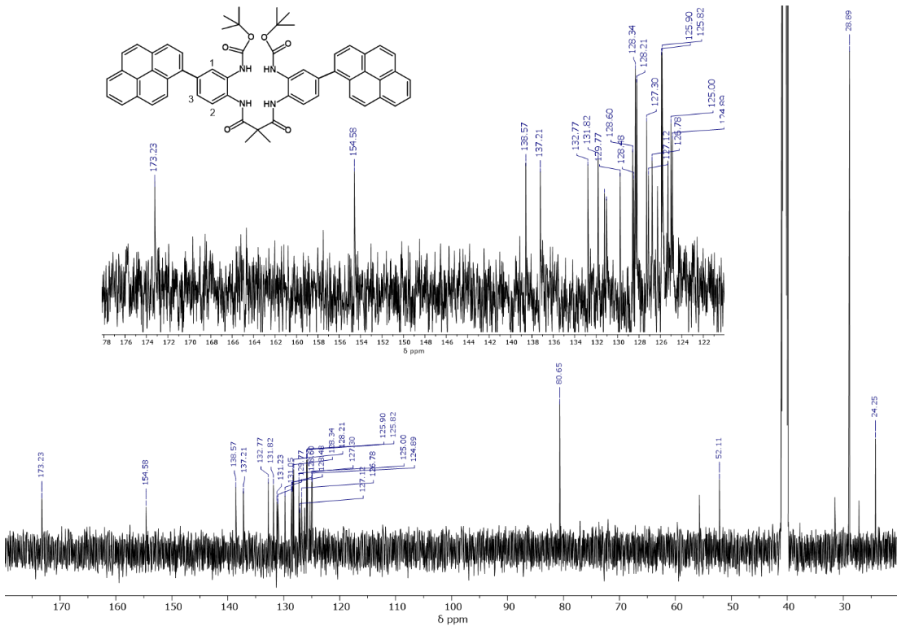

Figure S6. ^{13}C-NMR of di-tert-butyl (((2,2-dimethylmalonyl)bis(azanediyl))bis(4-(pyren-1-yl)-2,1-phenylene))dicarbamate (3.1) in DMSO-d_6.

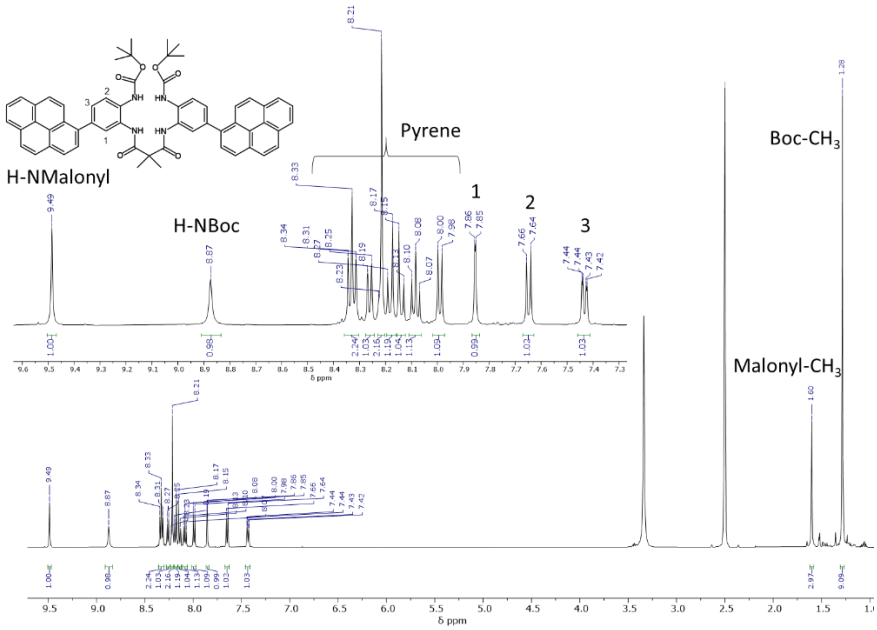

Figure S7. ^{1}H-NMR of di-tert-butyl (((2,2-dimethylmalonyl)bis(azanediyl))bis(5-(pyren-1-yl)-2,1-phenylene))dicarbamate (3.2) in DMSO-d_6.

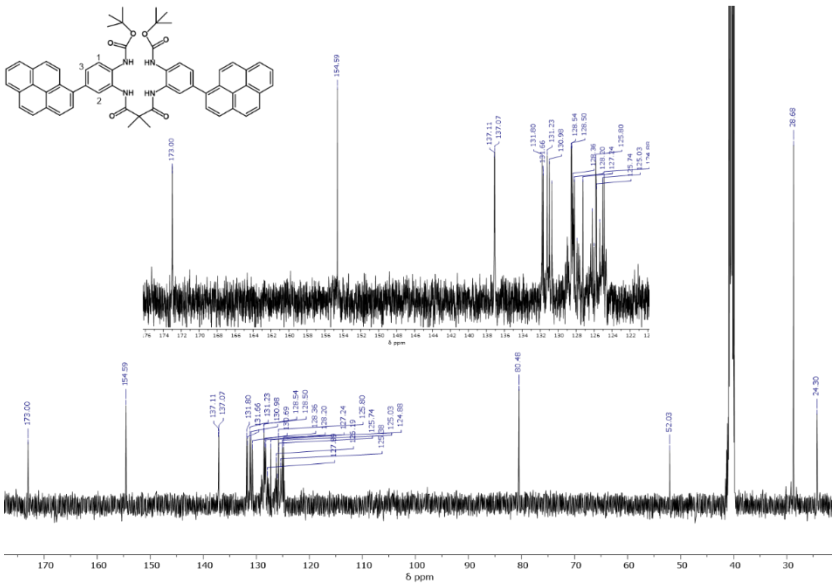

Figure S8. ^{13}C-NMR of di-tert-butyl (((2,2-dimethylmalonyl)bis(azanediyl))bis(5-(pyren-1-yl)-2,1-phenylene))dicarbamate (3.2) in DMSO-d_6.

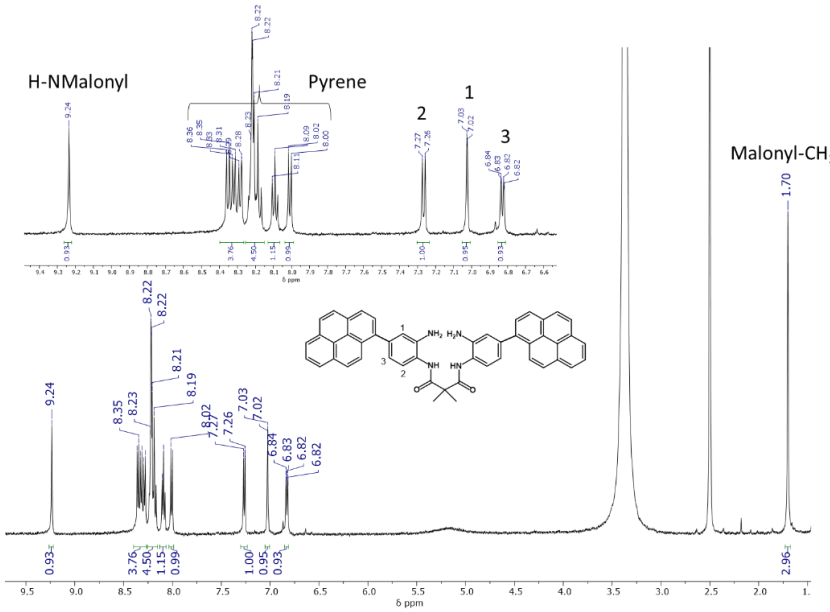

Figure S9. ^{1}H-NMR of N1,N3-bis(2-amino-5-(pyren-1-yl)phenyl)-2,2-dimethylmalonamide (4.1) in DMSO-d_6.

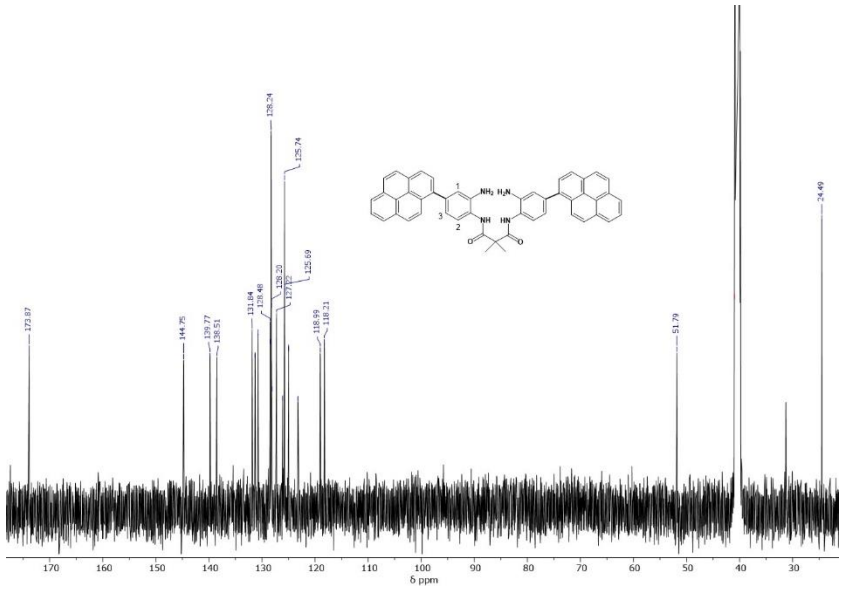

Figure S10. ^{13}C-NMR of N1,N3-bis(2-amino-5-(pyren-1-yl)phenyl)-2,2-dimethylmalonamide (6.1) in DMSO-d_6.

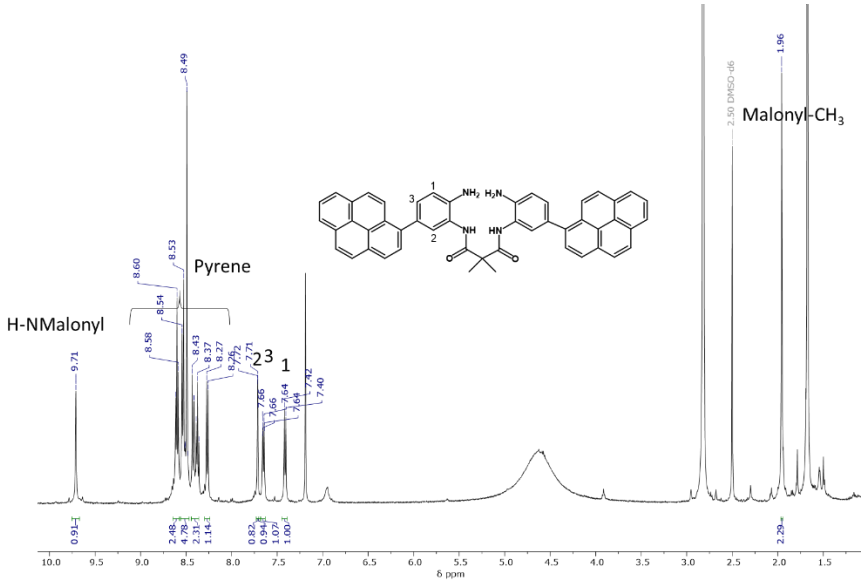

Figure S11. ^{1}H-NMR of N1,N3-bis(2-amino-4-(pyren-1-yl)phenyl)-2,2-dimethylmalonamide (4.2) in DMSO-d_6.

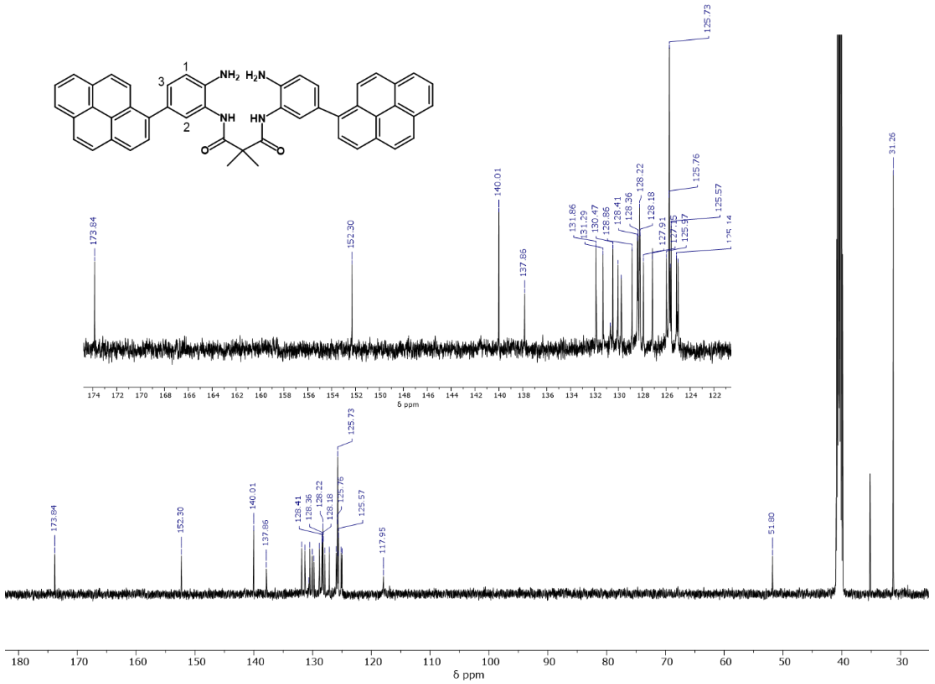

Figure S12. ^{13}C-NMR of N1,N3-bis(2-amino-4-(pyren-1-yl)phenyl)-2,2-dimethylmalonamide (4.2) in DMSO-d_6.

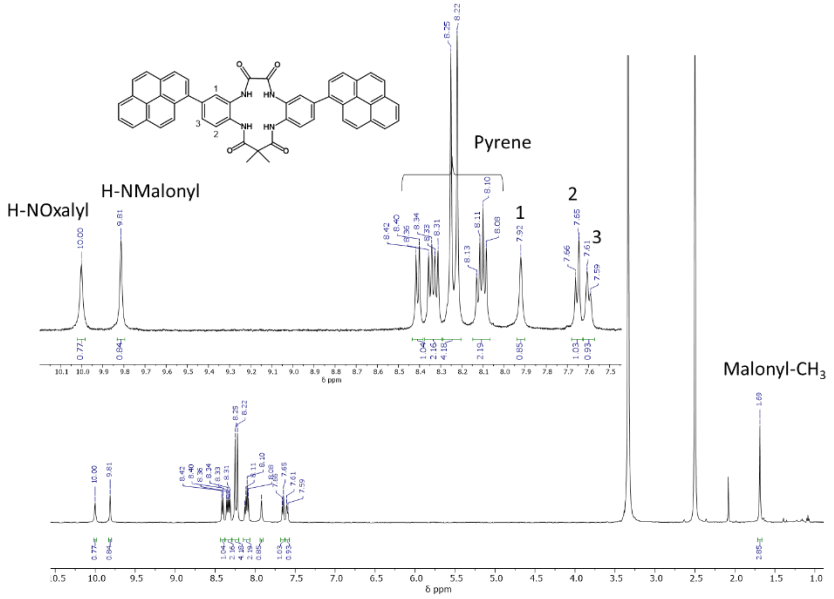

Figure S13. ^{1}H-NMR of 15,15-dimethyl-3,10-di(pyren-1-yl)-8,13-dihydro-5H dibenzo[b,h][1,4,7,10]tetraazacyclotridecine-6,7,14,16(15H,17H)-tetraone (5.1, H_4L1) in DMSO-d_6.

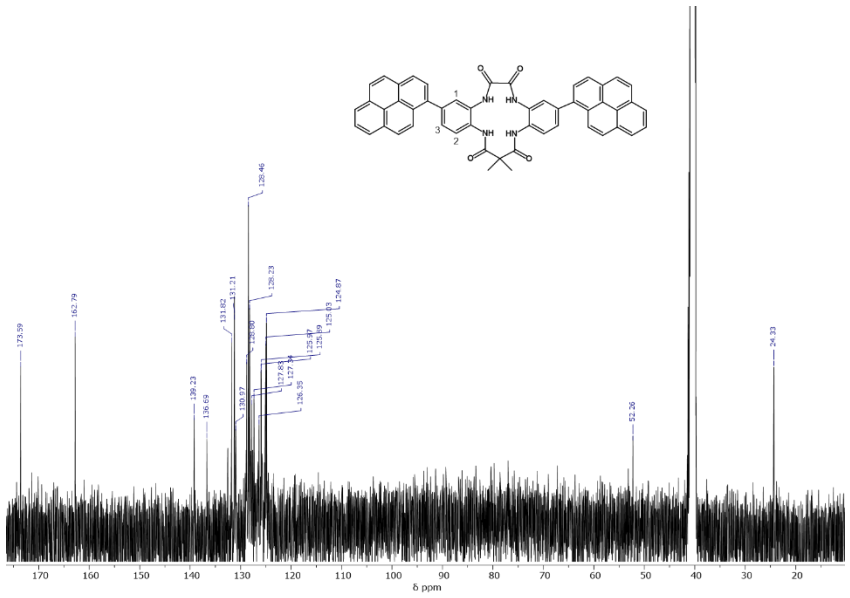

Figure S14. ^{13}C-NMR of 15,15-dimethyl-3,10-di(pyren-1-yl)-8,13-dihydro-5H dibenzo[b,h][1,4,7,10]tetraazacyclotridecine-6,7,14,16(15H,17H)-tetraone (5.1, H_4L1) in DMSO-d_6.

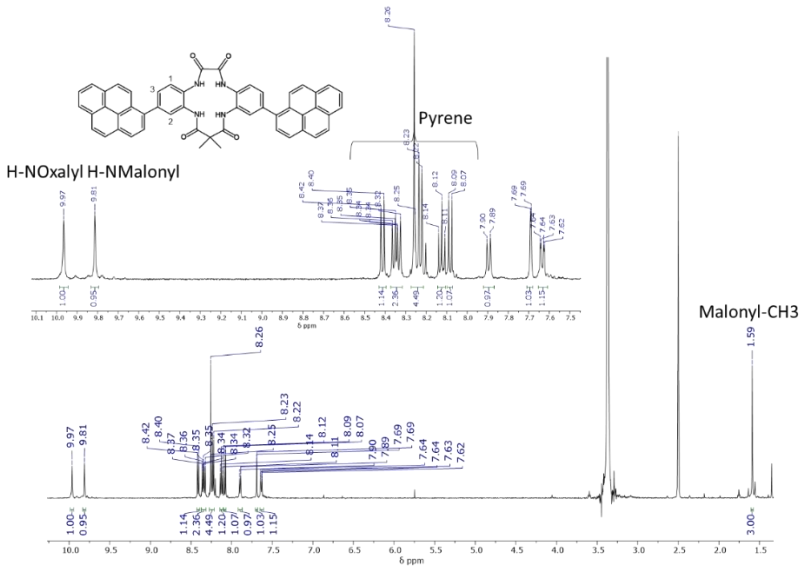

Figure S15. ^{1}H-NMR of 2-(1,2-dihydropyren-1-yl)-15,15-dimethyl-11-(pyren-1-yl)-8,13-dihydro-5H-dibenzo[b,h][1,4,7,10]tetraazacyclotridecine-6,7,14,16(15H,17H)-tetraone (5.2, H_4L2) in DMSO-d_6.

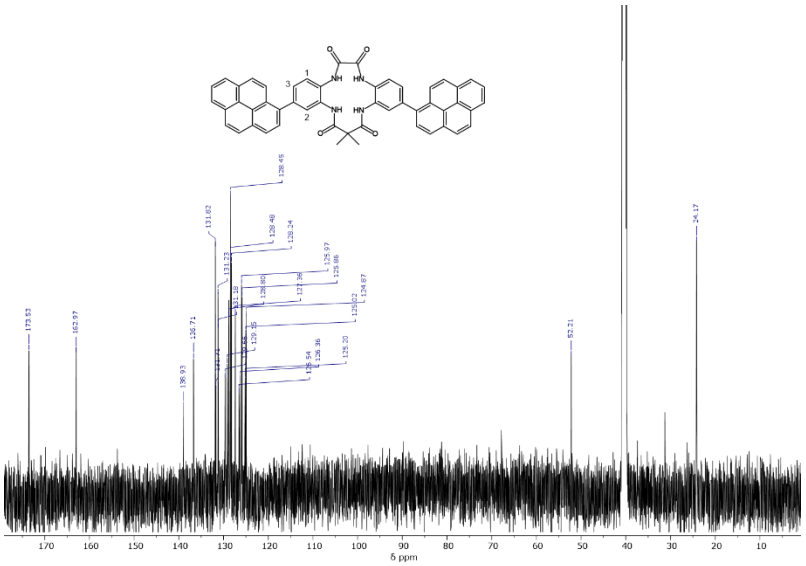

Figure S16. ^{13}C-NMR of 2-(1,2-dihydropyren-1-yl)-15,15-dimethyl-11-(pyren-1-yl)-8,13-dihydro-5H-dibenzo[b,h][1,4,7,10]tetraazacyclotridecine-6,7,14,16(15H,17H)-tetraone (5.2, H_4L2) in DMSO-d_6.

MS-Spectrometry

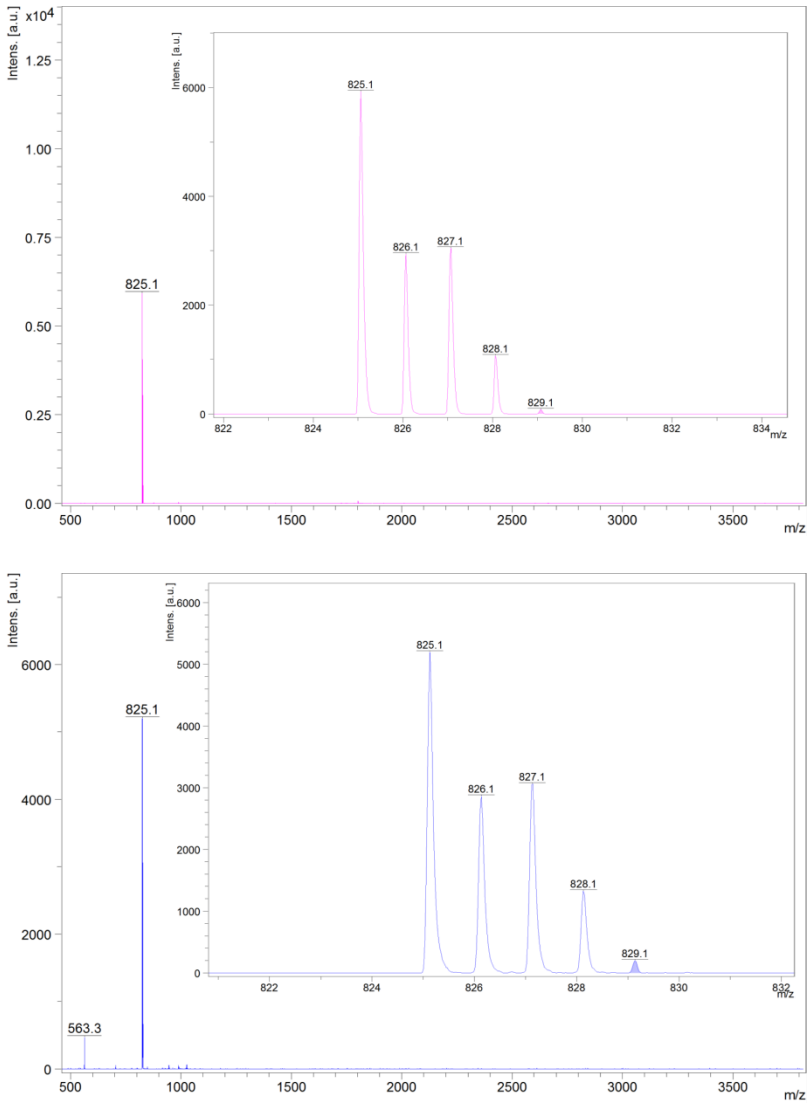

Figure S17. MALDI spectra of $\mathbf{1}^-$ and $\mathbf{2}^-$ negative mode. Insert: zoom on the molecular peak and the isotopic distribution.

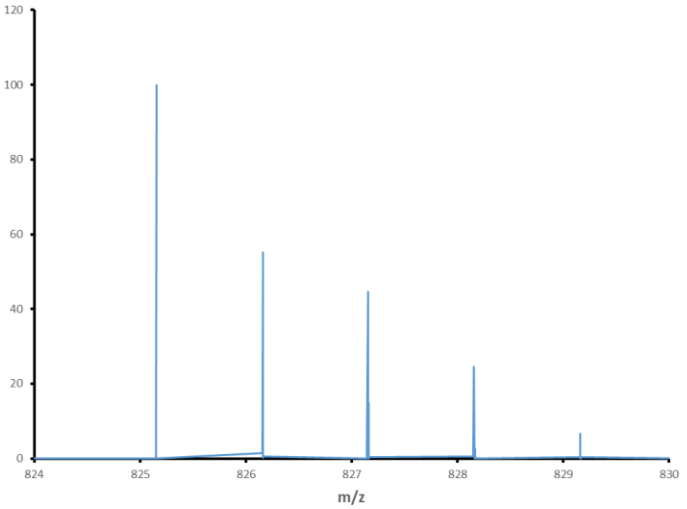

Figure S18. Simulate mass spectrum of the isotopic distribution for the complexes $\mathbf{1}^-$ and $\mathbf{2}^-$ (https://www.sisweb.com/mstools/isotope.htm).

X-Ray Chrystallography

Crystals preparation: Crystals of $\mathbf{1}^-$ were grown by slow diffusion of diethyl ether into an a methanolic solution of the corresponding complex. The measured crystals were prepared under inert conditions immersed in perfluoropolyether as protecting oil for manipulation.

Data collection: Crystal structure determination for compound $\mathbf{1}^-$ was carried out using a Rigaku diffractometer equipped with a Pilatus 200K area detector, a Rigaku MicroMax-007HF microfocus rotating anode with MoK_α radiation, Confocal Max Flux optics and an Oxford Cryosystems low temperature device Cryostream 700 plus (T = -173 ˚C). Full-sphere data collection was used with ω and φ scans. *Programs used:* Data collection and reduction with CrysAlisPro[1] V/.60A and absorption correction with Scale3 Abspack scaling algorithm.[2]

Structure Solution and Refinement: Crystal structure solution was achieved using the computer program SHELXT.[3] Visualization was performed with the program SHELXle.[4] Missing atoms were subsequently located from difference

Fourier synthesis and added to the atom list. Least-squares refinement on F^2 using all measured intensities was carried out using the program SHELXL 2015.[5] All non-hydrogen atoms were refined including anisotropic displacement parameters.

Comments to structure $\mathbf{1}^-$: In the structure of $\mathbf{1}^-$ the asymmetric unit contains one molecule of the metal complex, one tetramethyl ammonium cation and one diethylether molecule. The diethylether molecule is disordered in three orientations (ratio: 54:19:27). The structure is of excellent quality and no A- or B-alerts are present.

Table 1. Crystal data and structure refinement for **1**.

Identification code	**1**	
Empirical formula	C11.80 H10.40 Cu0.20 N O	
Formula weight	194.92	
Temperature	100(2)K	
Wavelength	0.71073 Å	
Crystal system	triclinic	
Space group	*P* -1	
Unit cell dimensions	a = 9.2856(6)Å	α = 92.124(4)°.
	b = 12.0608(6)Å	β = 91.751(4)°.
	c = 21.1489(8)Å	γ = 103.260(5)°.
Volume	2301.9(2) $Å^3$	
Z	10	
Density (calculated)	1.406 Mg/m^3	
Absorption coefficient	0.534 mm^{-1}	
F(000)	1020	
Crystal size	0.060 x 0.020 x 0.020 mm^3	
Theta range for data collection	2.255 to 29.410°.	
Index ranges	$-8 \le h \le 12, -16 \le k \le 15, -28 \le l \le 28$	
Reflections collected	25562	
Independent reflections	11211[R(int) = 0.0503]	
Completeness to theta =29.410°	88.0%	
Absorption correction	Multi-scan	
Max. and min. transmission	1.00 and 0.48	
Refinement method	Full-matrix least-squares on F^2	
Data / restraints / parameters	11211/ 420/ 736	
Goodness-of-fit on F^2	1.036	
Final R indices [I>2sigma(I)]	R1 = 0.0611, wR2 = 0.1565	
R indices (all data)	R1 = 0.0857, wR2 = 0.1686	
Largest diff. peak and hole	1.585 and -0.861 $e.Å^{-3}$	

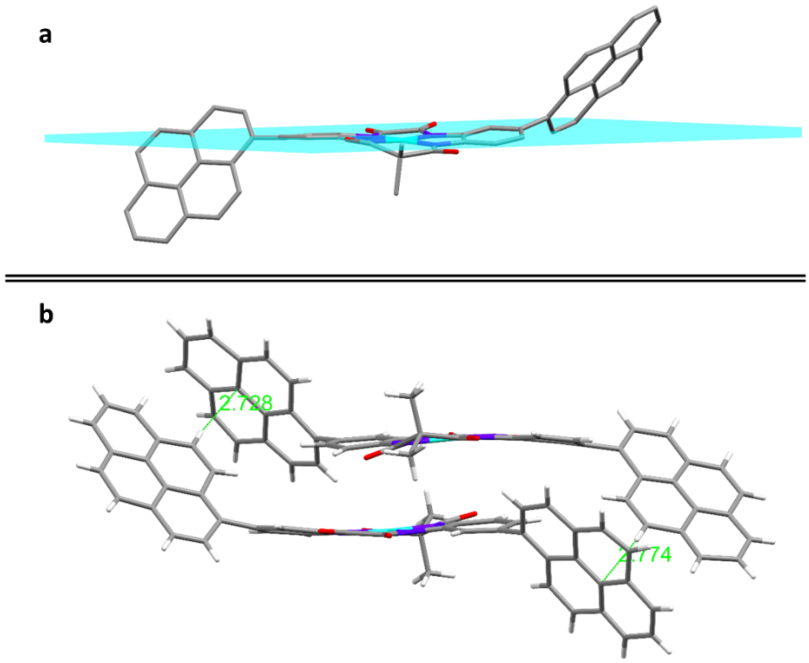

Figure S19. a) X-Ray structure of $\mathbf{1}^{-}$ showing the plane of the macrocycle. b) picture of the cell and CH-π interactions.

Characterization in organic solvents

UV-Vis Spectroscopy

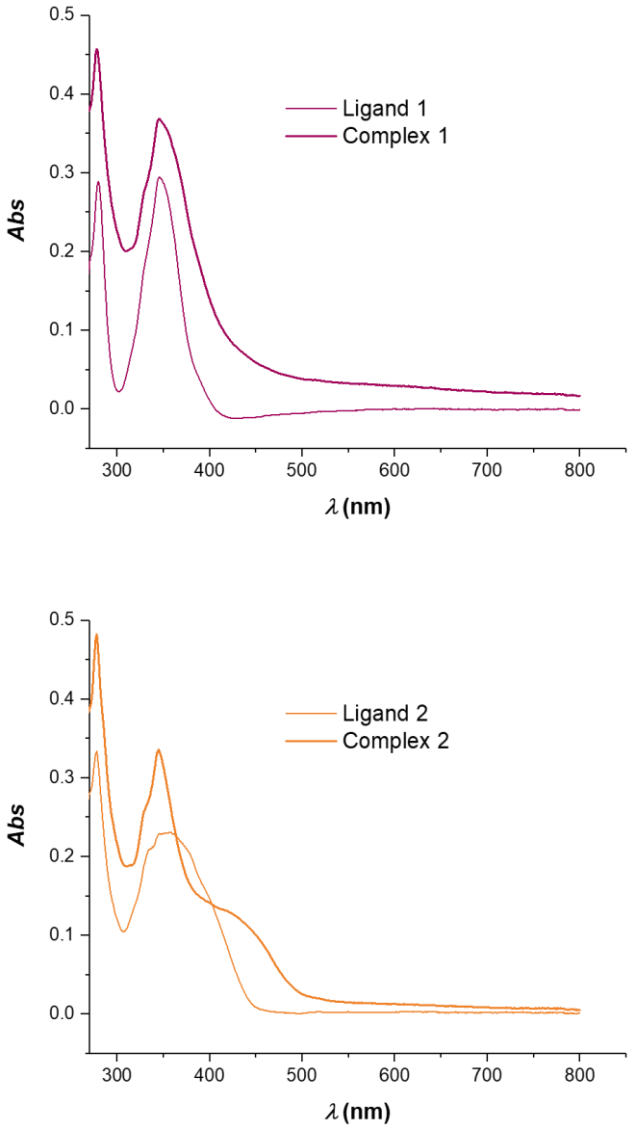

Figure S20. UV-Vis in DMA of $\mathbf{1}^-$ and H_4L1 (top) and $\mathbf{2}^-$ and H_4L2 (bottom).

Electrochemistry

The OCP of an aliquot took from the reaction mixture of complexation, run under Argon atmosphere, was measured at a first moment maintaining the solution under N_2 atmosphere and then exposing the system to oxygen (Figure S21). The OCP was increasing over time form an initial value of circa -0.60 V vs. Fc/Fc^+, on the left side of the Cu(III)/Cu(II) wave, to a final one of circa -0.50 V vs Fc/Fc^+, set at the i_p of the anodic process. This OCP, laying not so far form the middle of the Cu(III)/Cu(II) wave indicates the probable coexistence of the oxidized and not oxidize complexes, as can be clearly seen in the broad peaks of the ^{1}HNMR in DMSO-d_6 of the two molecules, indicating the presence of a paramagnetic Cu(II). A second ^{1}HNMR done adding I_2, shows well defined peaks, confirming the total oxidation to the diamagnetic Cu(III) (Figure S22).

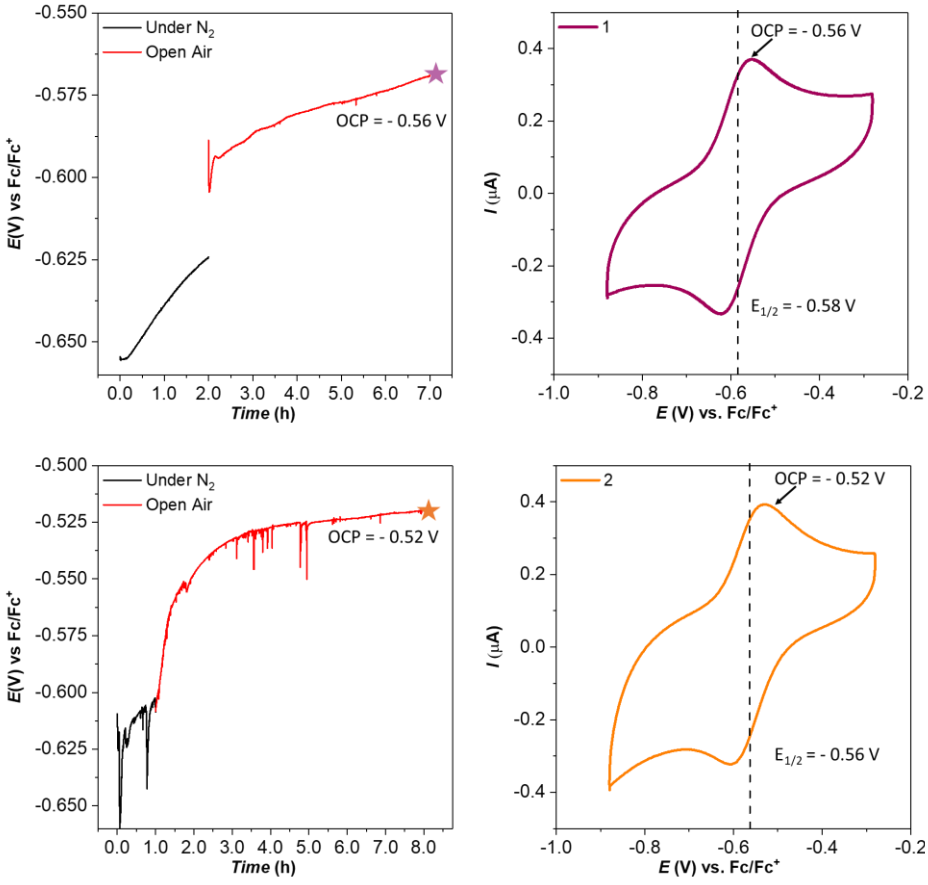

Figure S21. Left, open circuit potential (OPC) vs. time of a solution of $\mathbf{1}^-$ (top) and $\mathbf{2}^-$ (bottom) in DMF; right, CV of the first reversible wave associated with Cu(III)/Cu(II) process. BDD (WE), Pt (CE), $Ag/AgNO_3$ (RE).

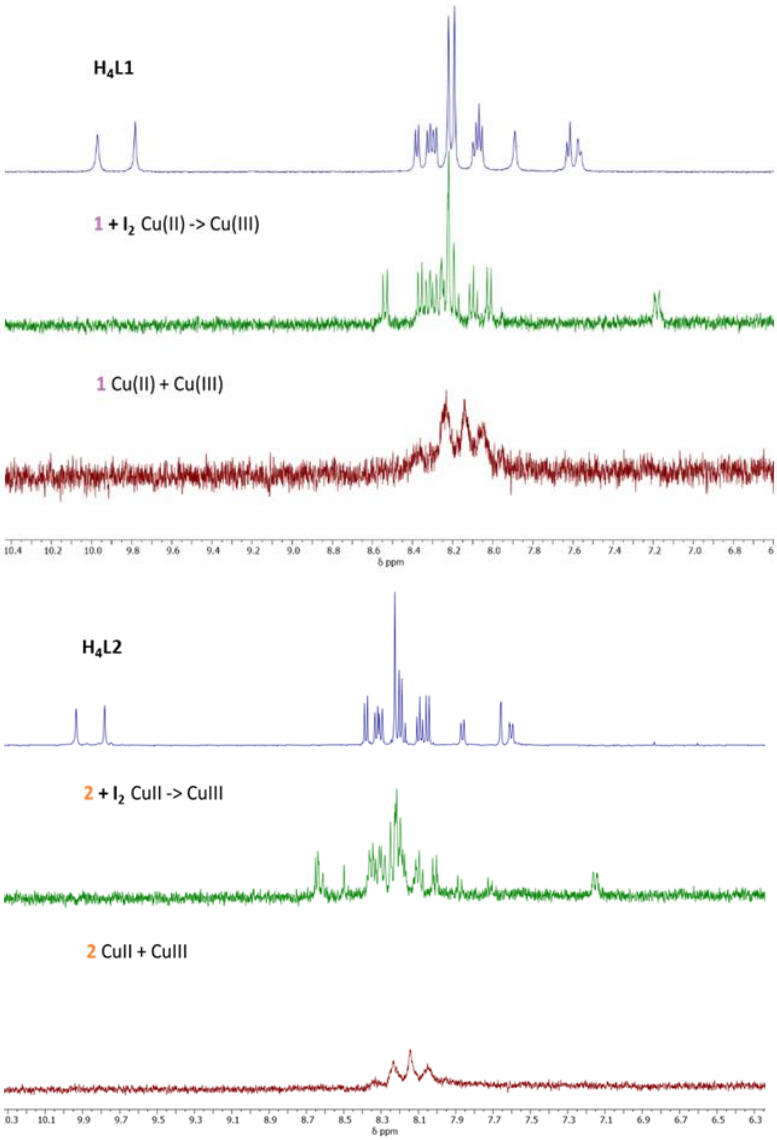

Figure 22. ^{1}HNMR in DMSO-d_6 of $\mathbf{1}^-$ (top) and $\mathbf{2}^-$ (bottom) before (red line), after the add of I_2 (green line) and the ligand (blue line).

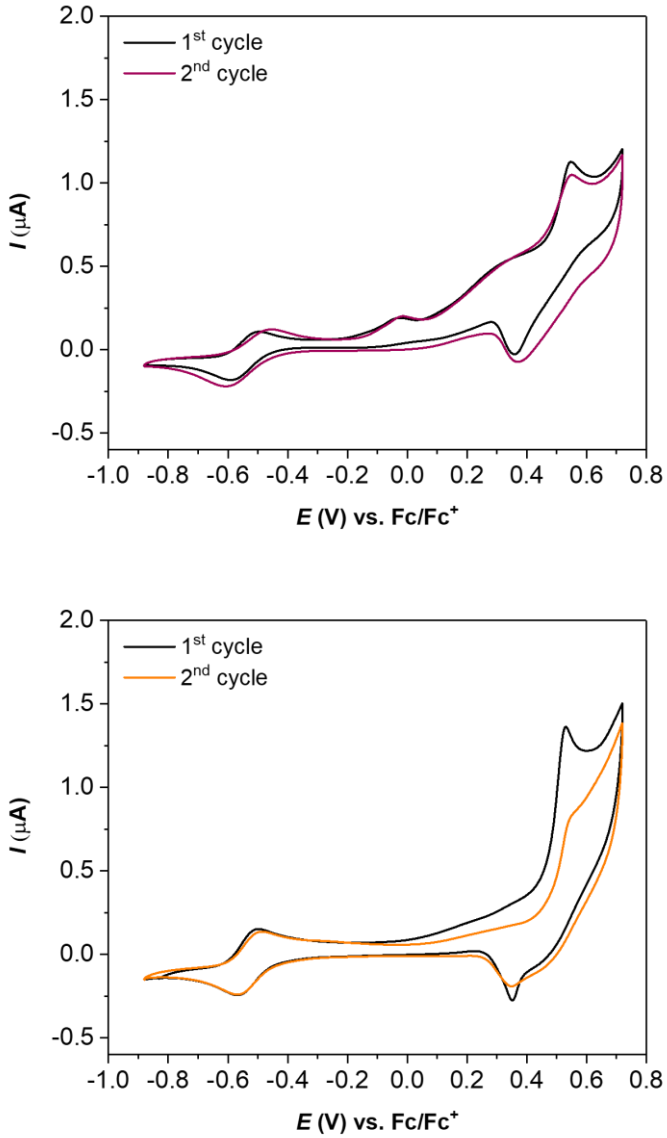

Figure S23. CV of the 1st (black line) and the 2nd (violet or orange lines) cycles of **1**$^{-}$ (left) and **2**$^{-}$ (right) 0.2 mM in CH_3CN with 0.1 M of $TBAPF_6$, 10 mVs^{-1}. BDD (WE), Pt (CE), $Ag/AgNO_3$ (RE).

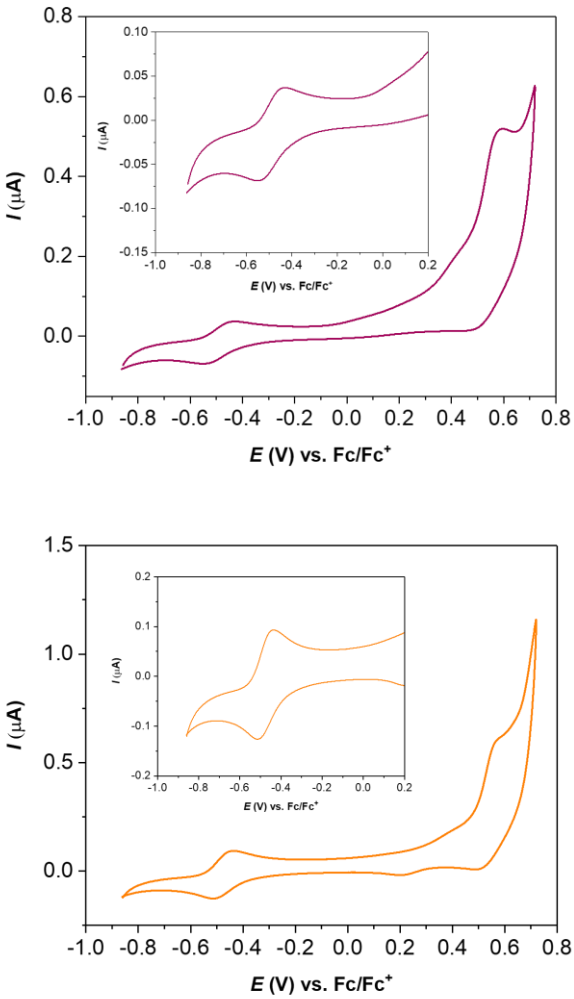

Figure S24. CV of $\mathbf{1}^-$ (top) and $\mathbf{2}^-$ (bottom) 0.2 mM in propylene carbonate (PC) with 0.1 M of $TBAPF_6$, 10 mVs^{-1}. BDD (WE), Pt (CE), $Ag/AgNO_3$ (RE).

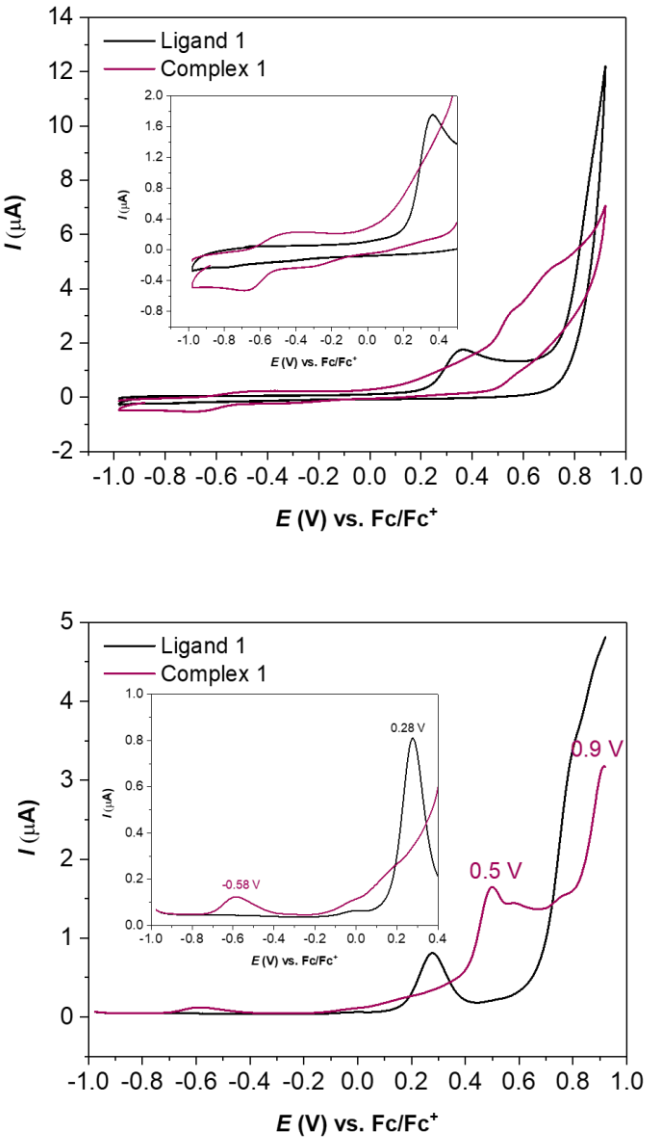

Figure S25. Comparison of the complex and the ligand $\mathbf{1}^{-}$.0.2 mM in DMA with 0.1 M of $TBAPF_6$. Top, CV, scan rate 10 mVs^{-1}; bottom, DPV. BDD (WE), Pt (CE), $Ag/AgNO_3$.(RE).

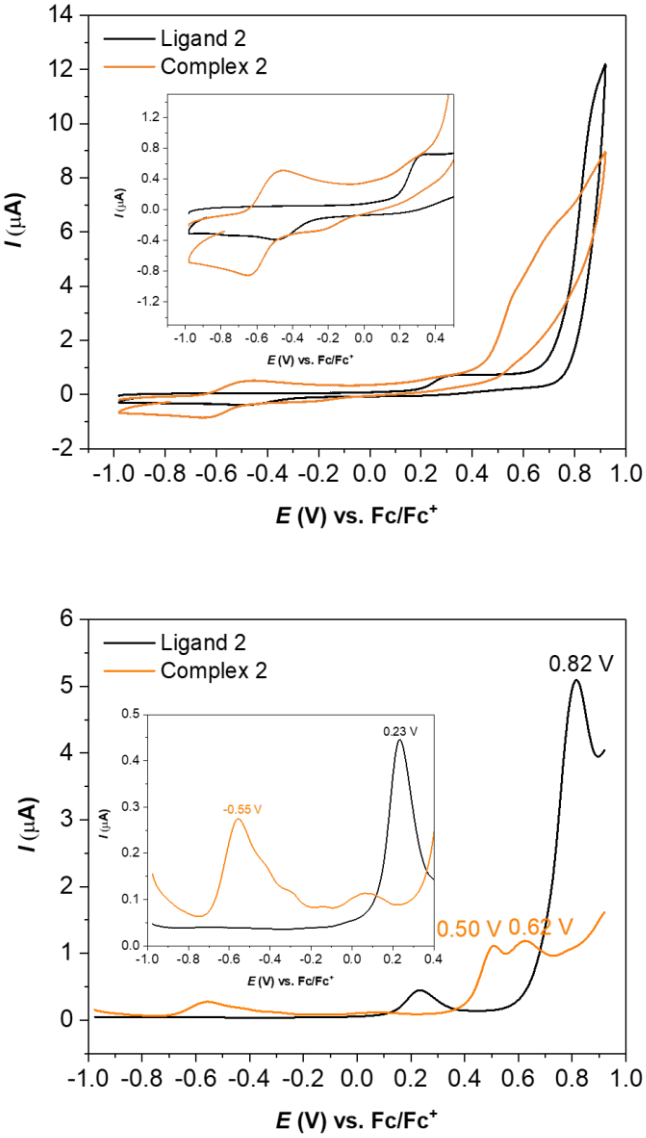

Figure S26. Comparison of the complex and the ligand $\mathbf{2}^{-}$.0.2 mM in DMA with 0.1 M of $TBAPF_6$. Top, CV, scan rate 10 mVs^{-1}; bottom, DPV. BDD (WE), Pt (CE), $Ag/AgNO_3$.(RE).

Preparation and characterization of hybrid materials.

As supportive material was used ITO nano-powder deposited on GC or ITO electrodes, due to its high electroactive surface area.

The ITO nano-powder is suspended in 9:1 MeOH:H_2O (~ 7 mg/mL): the suspension is left to sonicate 15 minutes. The nanoparticles suspension is added through a micropipette to the GC_{disk} of the RRDE electrode (10 µL), normal GC disk (5 µL) and to ITO plate (1 cm^2, 40 µL). The suspension is left to dry for 20 minutes, until a light-blue film is visible on the electrode's surface.[6]

The electrodes are then immersed in a solution 0.2 mM of the complexes or of the ligands in CH_3CN or DMA/CH_3CN 3:10 respectively with 0.1 M of $TBAPF_6$ and cycled repetitively in a range between -0.78 to 0.83 V vs Fc/Fc^+.

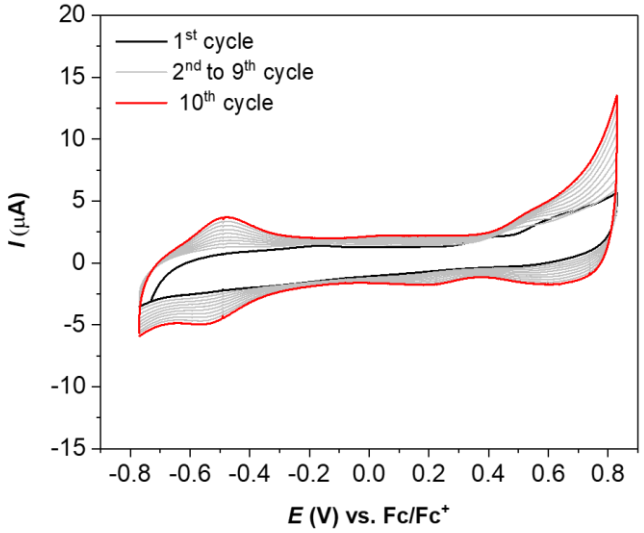

Figure S27. 10 CV cycles on the in a solution 0.2 mM of **1**$^-$ in CH_3CN with 0.1 M $TBAPF_6$ at 10 mVs^{-1}. n-ITO@GC (WE), Pt (CE), $Ag/AgNO_3$ (RE).

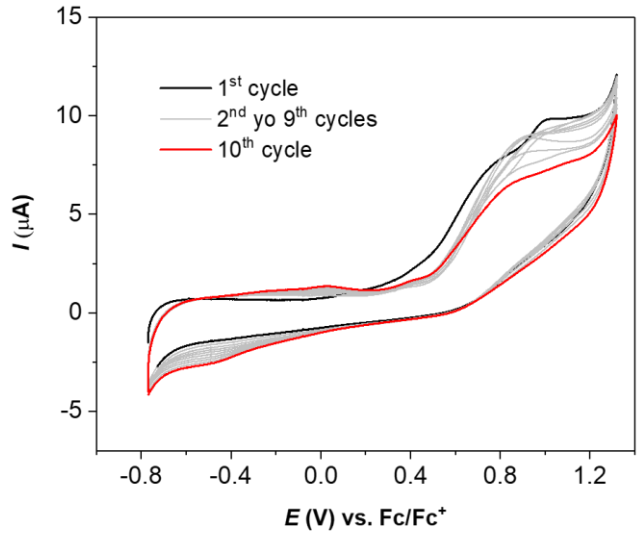

Figure S28. Left, 10 CV cycles on the in a solution 0.2 mM of $L1H_4$ in DMF/CH_3CN 3:10 with 0.1 M $TBAPF_6$ at 10 mVs^{-1}. n-ITO@GC (WE) Pt (CE), Ag/$AgNO_3$ (RE).

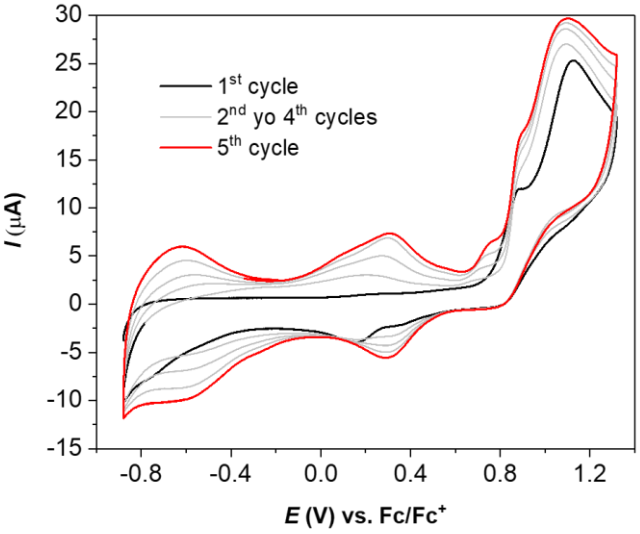

Figure S29. 5 CV cycles on the in a solution 0.2 mM of pyrene in CH_3CN with 0.1 M $TBAPF_6$ at 10 mVs^{-1}. n-ITO@GC (WE), Pt (CE), Ag/$AgNO_3$ (RE).

Characterization of the hybrid materials

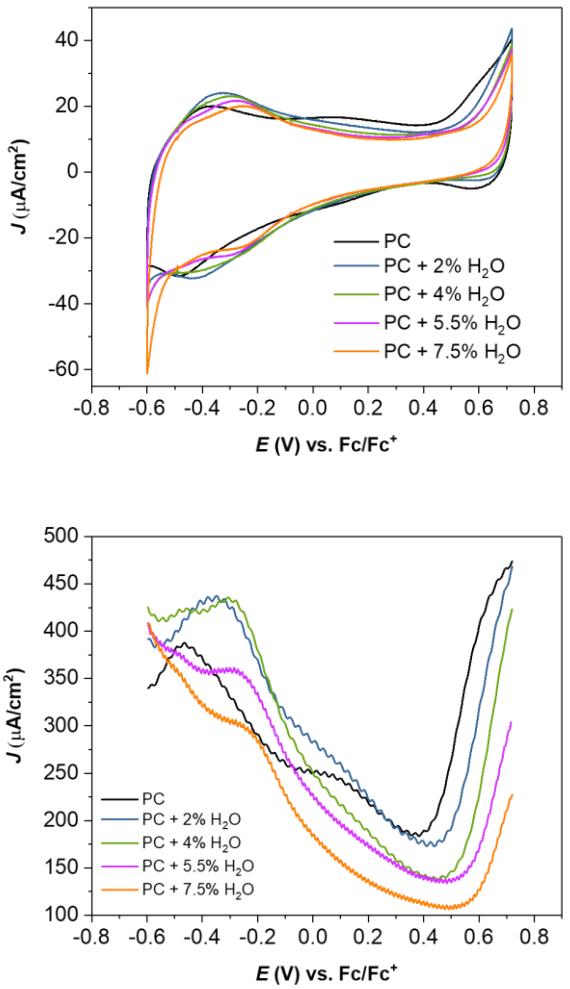

Figure S30. CV at 10 mVs^{-1}(top) and DPV (bottom) of *p*-**1**@n-ITO@GC in polypropylene carbonate (PC) (black line), PC + 2% H_2O (blue line); PC + 4% H_2O (green line); PC + 5.5% H_2O (violet line); PC + 7.5% H_2O (orange line). Pt, $Ag/AgNO_3$.

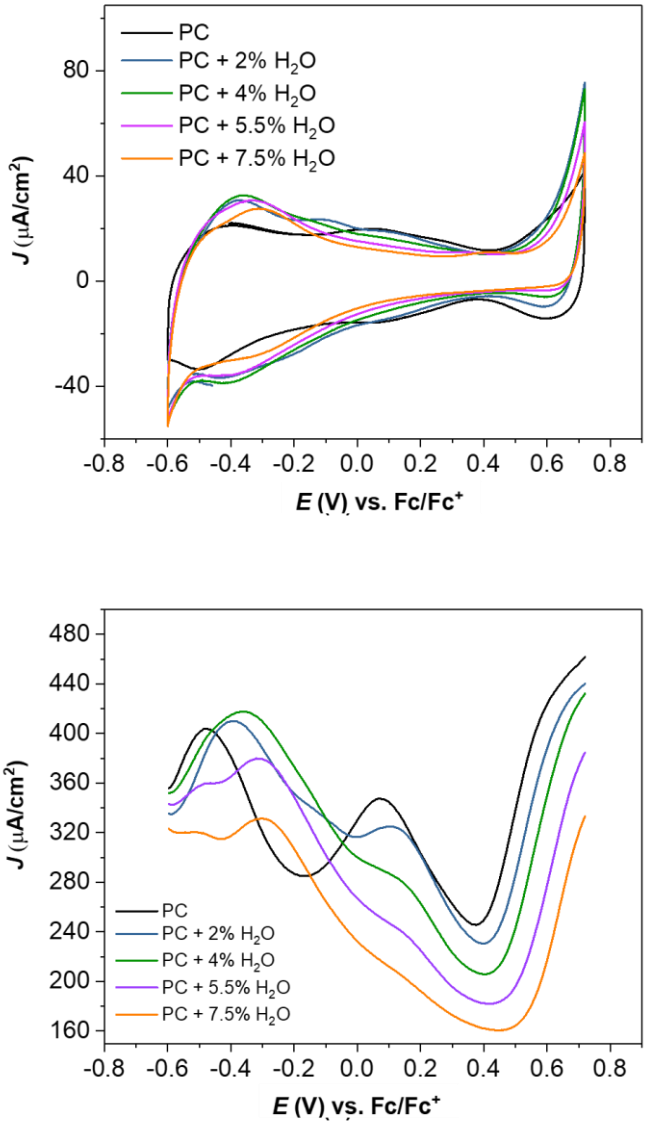

Figure S31. CV at 10 mVs^{-1} (top) and DPV (bottom) of *p*-**2**@n-ITO@GC in polypropylene carbonate (PC) (black line), PC + 2% H_2O (blue line); PC + 4% H_2O (green line); PC + 5.5% H_2O (violet line); PC + 7.5% H_2O (orange line). Pt, $Ag/AgNO_3$.

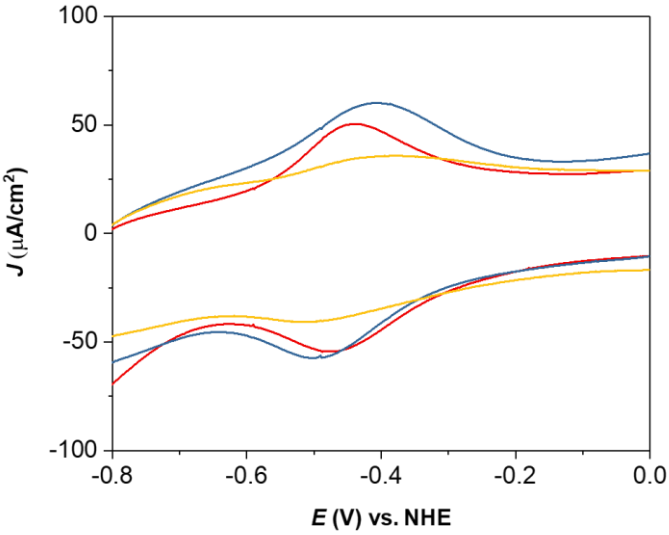

Figure S32. CVs of *p*-**1**@n-ITO@GC in propylene 10 mVs^{-1} of scan rate. The surface coverage, Γ, was calculated from the charge integrated under the background corrected oxidation peak.

O_2 evolution by RRDE

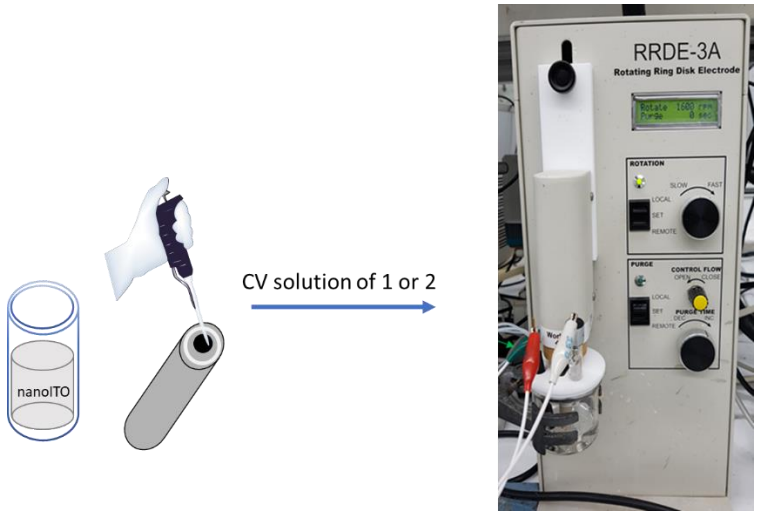

Scheme 1. Schematic representation of the RRDE electrode modification with **1** and **2**.

The efficiency of the RRDE (N) was quantify using the redox couple of $Fe(CN)_6^{4-}$ /$Fe(CN)_6^{3-}$, a well defined one-electron transfer process. 1 mM of $K_4Fe(CN)_6$ solutions in borate buffer 0.1 M at pH 7.5, 9 and 10 were prepared. The $Fe(CN)_6^{4-}$ was oxidized to $Fe(CN)_6^{3-}$ though an LSV at 10 mVs^{-1} at the GC_{disk} connected at the RRDE at a rotating speed of 1600 rpm, while the Pt_{ring}, set at a fix potential of 0.05 V, was reducing back the oxidized species to the original one. The efficiency is calculated as the rate of the intensity values of the GC_{disk} and the Pt_{ring} currents at the plateau (i GC_{disk}/i Pt_{ring}). The calculated efficiency was of 0.4, see Figure S23.

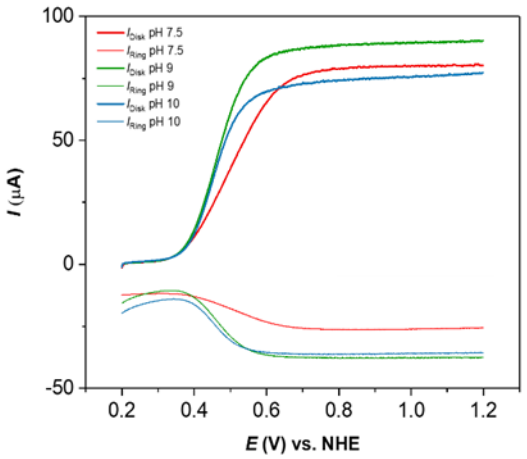

Figure S33. RRDE experiment using 1 mM of ferrocyanide $K_4Fe(CN)_6$ in pH 7.5 (red line), 9 (green line) and 10 (blue line) solution of borate buffer (0.1 M ionic strength). In the disk electrode, a LSV was performed at 10 $mV \cdot s^{-1}$ to oxidize to ferricyanide $Fe(CN)_6^{3-}$. In the ring electrode, a CPE was performed at 0.05 V to yield the reduction to the initial ferrocyanide $Fe(CN)_6^{4-}$. The rotation speed was 1600 rpm.

In order to set the potential of the Pt_{ring} at values where the oxygen reduction occurs, LSV at 10 mVs^{-1} were performed at the Pt_{ring} electrode toward negative potentials in presence (under air) and in absence of O_2 (N_2 atmosphere) in the same borate buffer solution 0.1 M pH 7.5, 9 and 10 used for the O_2 detection experiments. The used potentials were selected at the maximum of the reduction peaks detected in presence of O_2 but absent under N_2 atmosphere (Figure…), their values are of 0.05 (pH 7.5), -0.05 (pH 9) and -0.15 V (pH 10) vs NHE.[7]

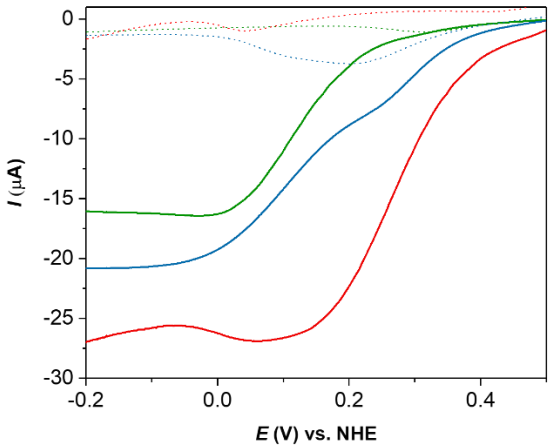

Figure S34. LSVs performed at 10 mV·s^{-1} with the Pt ring electrode in solutions with N_2 saturated (dot line) air saturated (straight line) at pH 7.5 (red line), 9 (green line) and 10 (blue line).

$$\varepsilon = 2 \cdot i_r / i_d \cdot N$$

In this equation, N is the collection efficiency previously calculated, and i_d and i_r are the values taken from the top of the peaks, where the intensity reaches a pseudo-stationary value before it starts to decrease due to electrode oxidative degradation. 2 is the number of electrons involved in the reaction of reduction of water to H_2O_2.

Stability

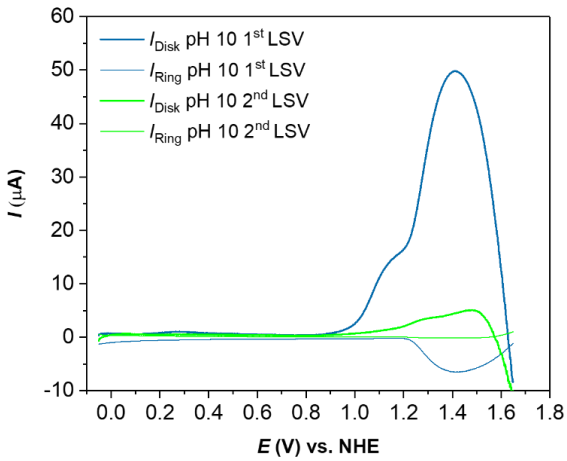

Figure S35. Comparison between the 1st and the 2nd LSV in borate buffer pH 10 of *p*-**1**@n-ITO@GC. Color code: 1st LSV, blue line; 2nd LSV, green line.

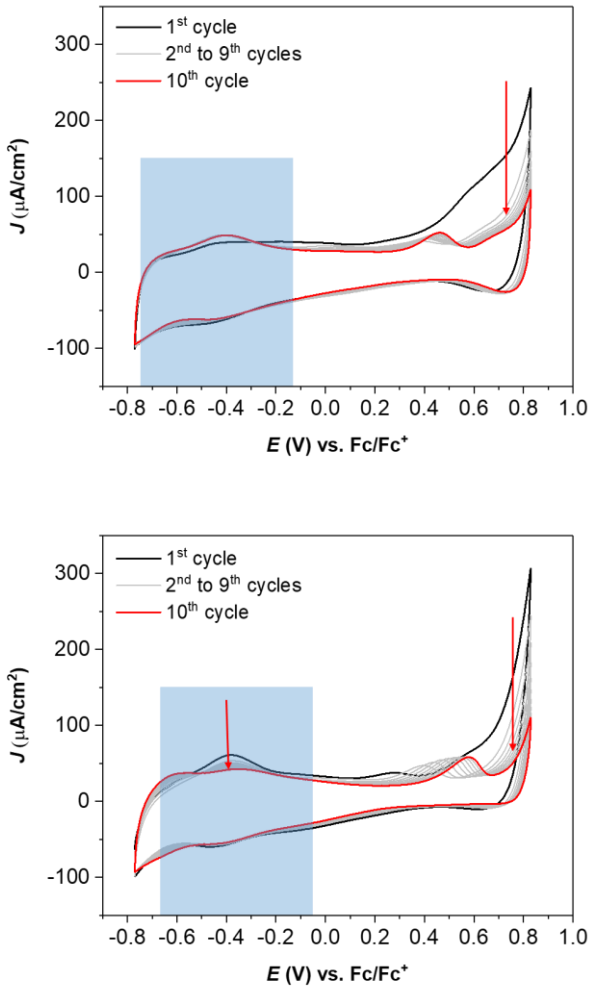

Figure S36. 10 CV cycles in pure propylene carbonate (top), and propylene carbonate + 2% of water (bottom) of *p*-**1**@n-ITO@GC. Color code: 1st cycle, black line; 2nd to 9th cycles, gray line; 10th cycle, red line. 10 mVs^{-1}. Pt (CE), $Hg/HgSO_4$ (RE).

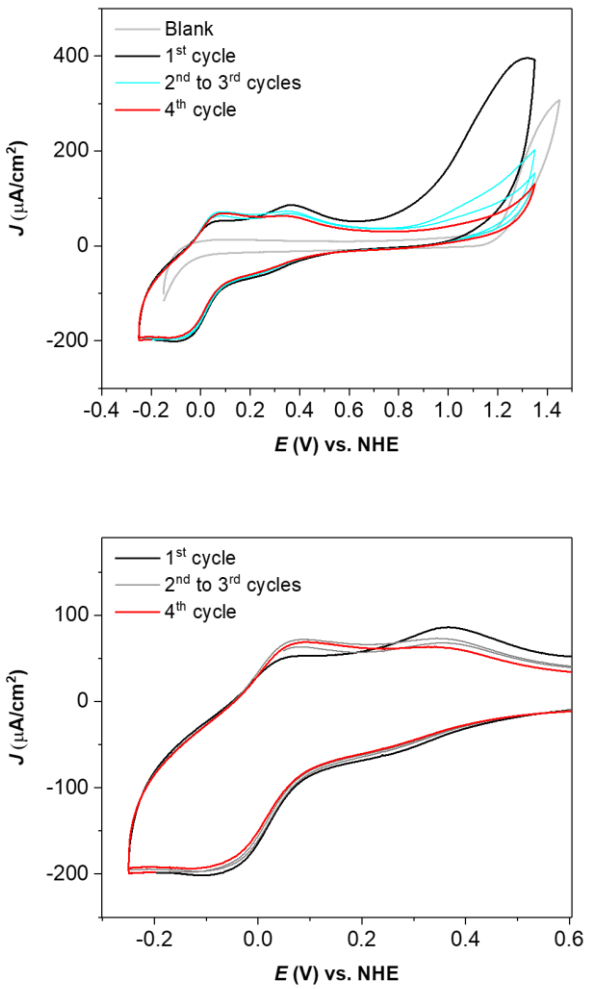

Figure S37. Top, CV in borate buffer pH 10, of *p*-**1**@n-ITO@GC. Bottom, zoom on the first waves. Color code: 1st cycle, black line; 2nd to 3rd cycle, cyan line; 4th cycle, red line; Blank, gray line. 10 mVs^{-1}. Pt (CE), $Hg/HgSO_4$ (RE).

The CuO modified electrodes were formed cycling a n-ITO@GC electrode in a solution 0.2 mM of $Cu(ClO_4)_2$. The so modified electrode is immersed in a solution of borate buffer pH 10 and cycled in the same range of potential used with $\mathbf{1}^-$ and $\mathbf{2}^-$.

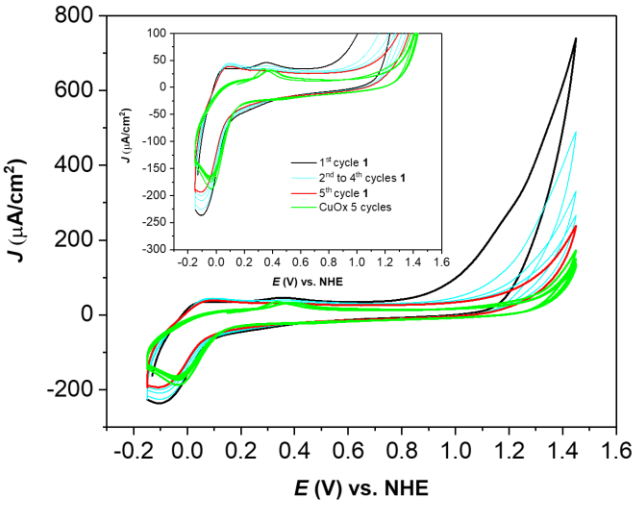

Figure S38. CV in borate buffer pH 10, of *p*-**1**@n-ITO@GC, at 10 mVs^{-1}. Pt (CE), $Hg/HgSO_4$ (RE).Right, zoom on the first waves. Color code: 1st cycle, black line; 2nd to 4th cycle, cyan line; 5th cycle, red line; CuO, green line.

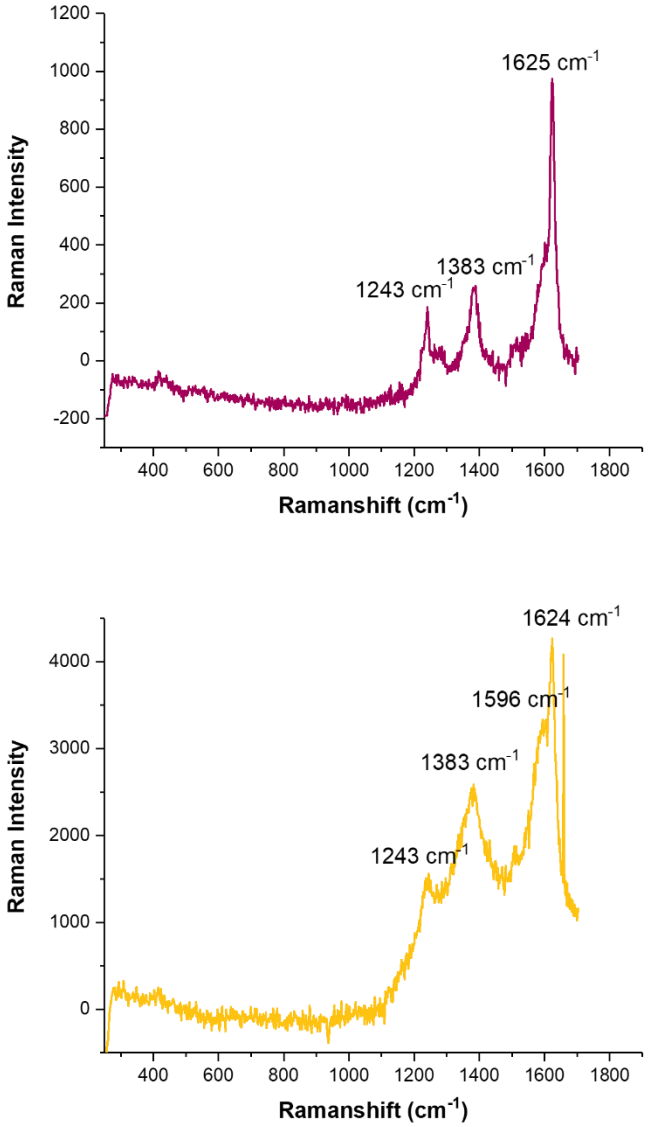

Figure S39. Raman spectra of *p*-**1**@n-ITO@ITO (top) and *p*-**2**@n-ITO@ITO (bottom) with excitation at 405 nm after cycling at pH 10, recorded at room temperature.

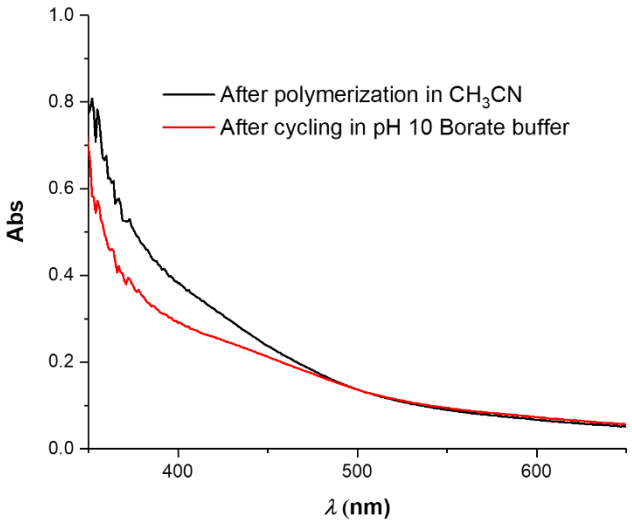

Figure S40. UV-Vis spectra of the *p*-**1**@n-ITO@ITO before (black line) and after (red line) cycling in borate buffer pH 10.

References

(1) Data collection and reduction with CrysAlisPro 1.171.39.12b (Rigaku OD, 2015). .

(2) Empirical absorption correction using spherical harmonics implemented in Scale3 Abspack scaling algorithm, CrysAlisPro 1.171.39.12b (Rigaku OD, 2015). .

(3) SHELXT; Sheldrick, G. M. *Acta Cryst.* **2015**, *A71*, 3–8.

(4) SHELXle; C.B. Huebschle, G. M. S. & B. D. *J. Appl. Cryst.* **2011**, *44*, 1281-1284.

(5) SHELXL; SHELXL-2014/7 (Sheldrick 2014). Sheldrick, G. M. *Acta Cryst.* **2015**, *C71*, 3–8.

(6) Concepcion, J. J.; Binstead, R. A.; Alibabaei, L.; Meyer, T. J. *Inorg. Chem.* **2013**, *52*, 10744–10746.

(7) McCrory, C. C. L.; Jung, S.; Peters, J. C.; Jaramillo, T. F. *J. Am. Chem. Soc.* **2013**, *135*, 16977–16987.

Chapter 5

Analysis of the Active Species Responsible for Water Oxidation Using a Pentanuclear Fe Complex

Chapter 5 is the revisited study of a pentanuclear iron complex claimed to work as molecular water oxidation catalyst. A deep analysis of the system after catalysis through techniques such as electrochemistry, UV-Vis, EDX, SEM, XPS and XAS, confirmed hematite as the real catalyst. This report with a detailed described methodology, can be considered as a user manual for researchers working with molecular non-noble metal based WOCs.

Chapter 5

Project C. Analysis of the Active Species Responsible for Water Oxidation Using a Pentanuclear Fe Complex

Pelosin, P.; Gil-Sepulcre, M.; Garrido-Barros, P.; Moonshiram, D.; Benet-Buchholz, J.; Gimbert-Suriñach, C.; Llobet, A. *iScience* 23, 101378, August 21, **2020**

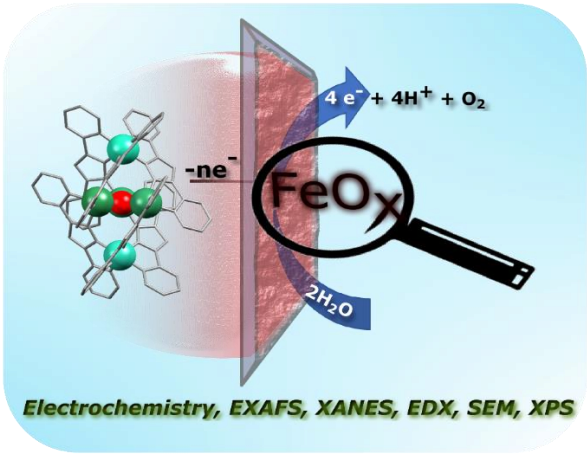

Abstract

Water splitting with sunlight is today one of the most promising strategies that can be used to start the imperatively needed transition from fossil to solar fuels. To achieve this, one of the key reactions that need to be mastered is the electrocatalytic oxidation of water to dioxygen. Great developments have been achieved using transition metal complexes mainly based on Ru, but for technological applications it is highly desirable to be able to use earth-abundant transition metals. The intrinsic chemistry of first row transition metals and in particular the lability of their M-L bonds in water imposes serious challenges for the latter to work as real molecular catalysts. The present work addresses this issue based on a molecular pentanuclear Fe5 complex and describes the different protocols and tests that need to be carried out in order to identify the real active species, responsible for the generation of dioxygen.

Contributions

Antoni Llobet conceived the idea of the project. Pelosin Primavera performed the synthesis, characterization, and electrochemical experiments. Marcos Gil-Sepulcre assisted with the electrochemical experiments. Dooshaye Moonshiram performed the XAS experiments. All authors contributed to the design of experiments, analysis of the results, and preparation of the manuscript.

C.1 Introduction

One of the main threats on the lifestyle of our modern societies is the increased global warming effect caused through the emission of greenhouse gases. The massive burning of fossil fuels over the course of the past decades has resulted in an alarming increase in carbon dioxide concentrations responsible for the global climate change and concomitant environmental issues. It is thus extremely urgent to replace fossil fuels by new energy conversion schemes based on clean and environmentally respectful fuels. A potential option is the production of H_2 through water splitting with sunlight ($h\nu$-WS) as indicated in Equation (1).

$$2H_2O_{(l)} + h\nu \rightarrow O_{2(g)} + 2H_{2(g)} \qquad \text{(Equation 1)}$$

$$2H_2O_{(l)} \rightarrow O_{2(g)} + 4H^{+}_{(aq)} + 4e^{-} \quad E° = 1{:}23 \text{ V } \textit{vs.} \text{ NHE at pH 0:0} \qquad \text{(Equation 2)}$$

$$2H^{+}_{(l)} + 2e^{-} \rightarrow H_{2(g)} \quad E° = 0.0 \text{ V } \textit{vs.} \text{ NHE at pH 0:0} \qquad \text{(Equation 3)}$$

Hydrogen generated in this manner is termed solar fuel. Furthermore, $h\nu$-WS is also termed as artificial photosynthesis[1–6] because there are a number of analogies with this reaction and the one that occurs in the natural photosynthesis summarized in Equation (4)[7–9]

$$6CO_{2(g)} + 6H_2O_{(l)} + h\nu \rightarrow C_6H_{12}O_{6(aq)} + 6O_{2(g)} \qquad \text{(Equation 4)}$$

From a chemical perspective these analogies include:
(1) Both reactions are thermodynamically uphill, driven by sunlight and require the participation of light harvesting agents that can transfer the sun's energy

into high-energy-density chemicals such as carbohydrates or H_2; (2) both processes need catalysts to speed up the redox reactions; and (3) the water oxidation reaction occurs in an identical fashion in natural photosynthesis and in $h\nu$-WS. In the former case a tetramanganese cluster located in photosystem II (PSII) is employed as a catalyst to speed up the water to dioxygen reaction.

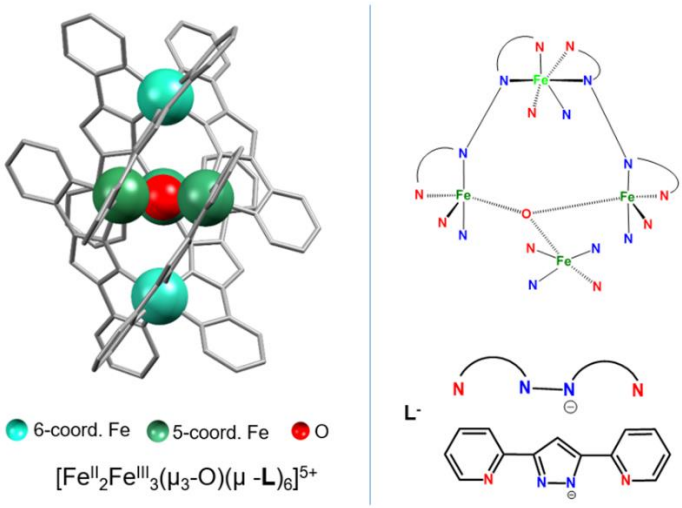

Figure 1. Left, ball and stick drawing of the cationic part of **[Fe$^{II}_2$Fe$^{III}_3$]**$^{5+}$. The Fe centers and the oxygen atoms are represented as green and red spheres, respectively. The two Fe(II) centers are situated in the equatorial plane of the bipyramid. The bpp$^-$ ligand is represented with gray sticks. H atoms are not drawn for simplicity reasons. Top right, partial representation of the upper part of bipyramidal structure of the **Fe$_5$**$^{5+}$ complex showing only two of the six bpp$^-$ ligands (for simplicity purposes) bridging axial and equatorial Fe centers. Bottom right, drawn structure of the bpp$^-$ (L$^-$) ligand and its representation using arcs connected with N.

The water oxidation reaction has long been regarded as a major bottleneck that ought to be solved to be able to develop devices based on $h\nu$-WS. However, during the last decade, a large degree of knowledge has been generated based on both oxide materials[10–12] and molecular transition metal complexes[13–16] In this context, the molecular water oxidation catalysis field has experienced a significant progress over the last 10 years powered by the promise of generating sustainable carbon neutral fuels based on water splitting[17–19]. A particularly noteworthy contribution has been the development of water oxidation catalysts

containing molecular Ru complexes owing to the high degree of understanding of their performance at a molecular level. This has been achieved thanks to a thorough description of their reactivity, electrochemical and spectroscopic properties, as well as a detailed characterization of their reaction intermediates, all combined with complementary computational models[20–22].

It would be very convenient to use non-toxic earth-abundant transition metal complexes such as Fe-based catalysts as water oxidation catalyst (WOCs) for the generation of technologically useful devices.
Few Fe based WOCs have been reported so far, but most of them are unfortunately not free from controversy since in most of the cases the real active catalytic species is most likely the corresponding oxide rather than the initial molecular complex[23,24]. Therefore, rigorous analysis of the active species is essential in order to achieve meaningful information of the catalytic species, not only in water oxidation but in the field of molecular electrocatalysis[25,26].

The present work analyses the water oxidation catalysis initially associated to the complex $[Fe_4^{II}Fe^{III}(\mu_3\text{-}O)(\mu\text{-}bpp)_6]^{3+}$, from now on labeled as $\mathbf{[Fe^{II}_4Fe^{III}]^{3+}}$ or $\mathbf{Fe_5}^{3+}$ [27], where bpp^- is the anionic tetradentate dinucleating bridging ligand 3,5-bis(2-pyridyl)pyrazolato; see Figure 1 for a drawing of its two electron oxidized derivative. The transformation of the metal complex into the corresponding oxide is a major concern here since it precludes the correlation of reactivity with the catalytic process and thus becomes a futile exercise. Such exercises could generate misleading information in the water oxidation field.

This manuscript summarizes the main critical tests that need to be carried out to prove the molecular nature of the catalytic processes using $\mathbf{Fe_5}^{3+}$ but that it obviously can be extended to other iron complexes as well as to other earth-abundant first row transition metal complexes.

C.2 Results

$\mathbf{Fe_5}^{n+}$ *Synthesis, Structure, and Redox Electronic Properties in MeCN.*

The reaction of $Fe(SO_4)\cdot 7H_2O$ and bpp^- in MeOH in an open atmosphere gives rise to the formation of a pentanuclear complex $[Fe^{II}_4Fe^{III}(\mu_3\text{-}O)(\mu\text{-}bpp)_6]^{3+}$,

[$Fe^{II}_4Fe^{III}$]$^{3+}$ or **Fe_5^{3+}**, with a relatively high isolated yield of~72%. Although UV-vis spectroscopy shows that the reactions proceed quantitatively (see Figure S3), the decrease in the isolated yield is due to the crystallization process and the follow-up operations needed to isolate a pure solid.

Complex **Fe_5^{3+}** can be cleanly and successively oxidized by two one-electron processes in MeCN reaching the high oxidation state complex [$Fe_2^{II}Fe_3^{III}(\mu_3\text{-}O)(\mu\text{-}bpp)_6$]$^{5+}$, **[$Fe^{II}_2Fe^{III}_3$]**$^{3+}$ or **Fe_5^{5+}**, whose crystal structure is shown in Figure 1. In the structure, the metal centers are situated at the vertex of a triangular bipyramid where the bpp^- acts as a bridging ligand between the axial and equatorial Fe, whereas the oxido group bridges the three Fe sites situated in the equatorial plane. The axial Fe sites are hexacoordinated (CN_6) with a distorted Oh symmetry, whereas the equatorial ones are pentacoordinated (CN_5) with a distorted C_{2v} symmetry. This crystal structure is very similar to the previously reported one for **Fe_5^{3+}** complex[27], except for a slightly shorter Fe-O and Fe-N distances as expected (Figure S1 and Table S1)[28].

It is important to realize here that the quantitative yield of this reaction implies that the pentanuclear structure is especially stable from a thermodynamic perspective given the large number of complexes that can be potentially formed by mixing the bpp^- ligand and the iron [$Fe^{II}(H_2O)_6$]$^{2+}$ (obtained from the dissolution of iron sulfate in water), as shown in Figure S2.
These potential complexes range from simple mononuclear complexes with different number of bbp^- ligands bonded to the Fe center to dinuclear, polynuclear, etc., again with different numbers of coordinated bpp^- ligands attached to Fe. The formation of **Fe_5^{3+}** as the only complex generated in this reaction points to a scenario whereby the Fe-N bond is forming and breaking easily in agreement with the lability of high spin Fe(II) and Fe(III) complexes[29]. This is exemplified in Figure S2 where the first Fe complexes that will most likely be made upon mixing Fe(II) and bpp^- are shown. The *fac*-[$Fe(L)_3$]$^-$ complex will end up acting as a capping group for the final **Fe_5^{3+}** complex. Only the [$Fe(L)(H_2O)_4$]$^+$ and the *cis,cis*-[$Fe(L)_2(H_2O)_2$] complexes will have the proper ligand geometrical coordination so that they can lead to the formation of *fac*-[$Fe(L)_3$]$^-$ without the need of additional ligand rearrangements. All the other complexes will need to rearrange, and thus Fe-N bonds will have to be broken and made anew to be able to lead to *fac*-[$Fe(HL)_3$]$^-$. Thus, all the potential complexes generated at the initial stages of the synthesis will reorganize in order to

converge to the most thermodynamically stable complex, which is, in this case, **Fe_5^{3+}**.

A parallel phenomenon also occurs with other metal complexes such as Mn that can achieve a similar structural arrangement with bpp^-, such as $[Mn^{II}_4Mn^{III}(\mu\text{-}bpp)_6(\mu_3\text{-}O)]^{3+}$, **$Mn_5^{3+}$**, and also with related linearly arranged tetranucleating ligands[30]. Although the **Fe_5^{3+}** is relatively stable in solution at low concentrations of water, the corresponding Mn analog, the **Mn_5^{3+}**, decomposes almost immediately to generate the free ligand and $[Mn(H_2O)_6]^{2+/3+}$ [31]. This indicates the capacity of H_2O to compete for the first coordination sphere of the Mn center, so that once a water molecule coordinates to a Mn center the whole structure collapses losing the stability provided by the pentanuclear arrangement.
In MeCN as solvent, the **Fe_5^{n+}** complex is a very rich molecule from a redox perspective accessing six
different oxidation states ranging from $[Fe^{II}_5(\mu_3\text{-}O)(\mu\text{-}bpp)_6]^{2+}$, **$Fe_5^{2+}$**, where all the iron centers have oxidation state II up to $[Fe^{III}_5(\mu_3\text{-}O)(\mu\text{-}bpp)_6]^{7+}$, **$Fe_5^{7+}$**, where now all Fe centers have oxidation state III. All the oxidation states can be accessed by successive one electron electrochemically quasireversible processes, as can be observed in the CV in Figure 2 and in agreement with a previous report[32] (see Figure S4 and Table S2 for further details).

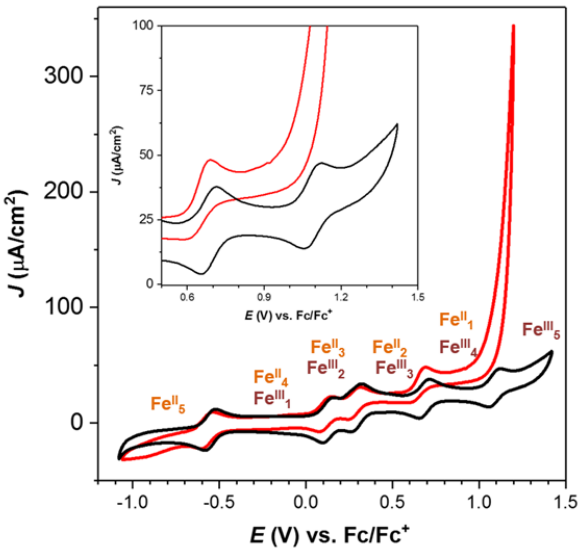

Figure 2. Cyclic voltammetry experiments for $\mathbf{Fe_5}^{3+}$ 0.2 mM dissolved in a 0.1 M TEAP MeCN solution ($V_i = V_f = -0.24$ V; $V_{C1} = -1.08$ V; $V_{C2} = 1.42$ V) black trace, and in a 10:1 MeCN:H_2O volume ratio ($V_i = V_f = -0.24$ V, $V_{C1} = -1.08$ V; $V_{C2} = 1.19$ V) red trace (background subtracted) at a scan rate of 10 mV/s. Labels indicate the oxidation state zones of predominance as a function of potential. The inset shows an enlargement of the 0.6–1.4 V zone.

All CVs in this work are carried out using a glassy carbon (GC) electrode as a working electrode, an Ag^+/Ag (0.01 M) as reference electrode and a Pt disk as auxiliary electrode unless explicitly mentioned. All potentials in this work are reported versus Fc/Fc^+. The fully reduced species $\mathbf{Fe_5}^{2+}$ is air sensitive and thus needs to be isolated in an inert atmosphere. The fully oxidized species, $\mathbf{Fe_5}^{7+}$, displays a chemically reversible behavior during the CV timescale, but on bulk electrolysis timescales it is not stable and decomposes, indicating the high reactivity of such a high oxidation state species. All other $\mathbf{Fe_5}^{n+}$ species in intermediate oxidation states are stable and can be isolated as solids in an open air atmosphere that is in accordance with a previous report[32]. The electronic structure of the six $\mathbf{Fe_5}^{n+}$ (n = 2–7) complexes at the different oxidation states has been unambiguously established based on EPR and magnetic measurements[32]. The six coordinated apical Fe(II) centers in $\mathbf{Fe_5}^{3+}$ have a low spin (LS) d^6 configuration, whereas two equatorial Fe(II) have a high spin (HS) d^6 and the third equatorial Fe(III) is a low spin d^5. On the other hand, for the highest

oxidation state complex, $\mathbf{Fe_5}^{7+}$, the apical Fe centers are LS, whereas the equatorial ones are HS.

Redox Properties in Aqueous MeCN

The Impact of [H_2O] in the Catalytic Activity

In water, the $\mathbf{Fe_5}^{3+}$ complex is not soluble, but it can be solubilized in mixtures of MeCN and H_2O. The latter is important since in the absence of water, the potential active species needed to enter into the water oxidation catalytic cycle cannot be formed. The electrochemical work reported here is carried out in mixtures of a MeCN solution containing 0.1 M tetraethyl ammonium perchlorate (TEAP) and water in a maximum 10:1 MeCN:H_2O volume ratio. This from now on will be referred in an abbreviated manner as 10:1 MeCN:H_2O.

In 10:1 MeCN:H_2O as solvent mixture the CV of $\mathbf{Fe_5}^{n+}$ is similar to the one reported in 0.1 M TEAP MeCN with a slight cathodic shift of roughly 40 mV for the wave associated with the $\mathbf{[Fe^{II}Fe^{III}_4]^{6+}/[Fe^{II}_2Fe^{III}_3]^{5+}}$ couple as can be observed in Figure 2. Furthermore, a large electrocatalytic current starting at 0.85 V is observed that is assigned to the oxidation of water to dioxygen. This electrocatalytic wave was wrongly assigned to the catalytic activity of a molecular $\mathbf{Fe_5}^{n+}$ complex[27]. It was proposed based CN_5 to CN_6. A series of oxidations and an additional water coordination to a neighboring Fe center was then proposed to occur so that a sufficiently reactive species would form an O-O bond that might finally release dioxygen. The transition state energy for the initial step, the coordination of water and the formation $[Fe^{III}_5(\mu_3\text{-}O)(\mu\text{-}bpp)_6]^{7+}$, is highly endergonic by 18.9 kcal/mol and is proposed to be the rate determining step (rds) of this catalytic cycle[33]. This is in agreement with the high stability of the $\mathbf{Fe_5}^{n+}$ structure and thus the large energy needed to disrupt it. On the other hand, it also points out that once a water molecule coordinates a metal center, the whole structure might collapse with the formation of multiple Fe complexes containing different ratios of aqua and bpp^- bonded ligands. If this disruption occurs in close proximity with a glassy carbon electrode the new species will generate FeOx as will be shown below.

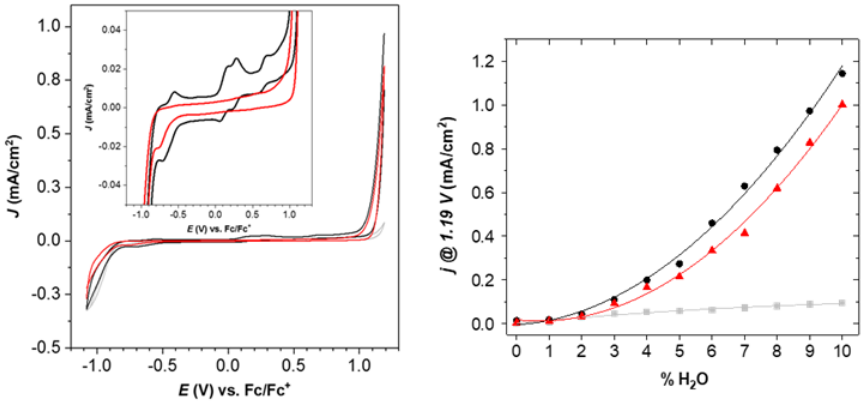

Figure 3. Left, black trace, CV of the third cycle for $\mathbf{Fe_5}^{3+}$ 0.2 mM dissolved in a 10:1 MeCN:H_2O solution ($V_i = V_f$ = -1.08 V; V_{C1} = 1.19 V) at a scan rate of 10 mV/s. Red trace, CV of the GC working electrode obtained in the previous experiment immersed in a clean electrolyte solution. Gray trace, CV of a bare GC electrode under the same conditions. Inset, enlargement in the zone of the non-catalytic waves of the complex. Right, plot of current density at 1.19 V under different MeCN:H_2O ratios obtained in the CV of: (1) black trace, after 2.5 cycles for a 0.2 mM $\mathbf{Fe_5}^{3+}$solution with a GC electrode as WE at the previous conditions; (2) red trace, after the previous 2.5 cycles the GC electrode obtained is immersed in a clean electrolyte solution ($V_i = V_f$ = 0.92 V; V_{C1} = 1.19 V); (3) gray trace, blank for a bare GC electrode.

Figure 3 left shows the third CV cycle of $\mathbf{Fe_5}^{3+}$ within the potential range of -1.08 to 1.19 V at a scan rate of 10 mV/s in 10:1 MeCN:H_2O solution (the first cycle is reported in Figure S5A). The waves associated with the $\mathbf{Fe_5}^{n+}$ molecular complex remain the same as in the first cycle (see Figure 2), whereas the catalytic current in the third cycle increases nearly five times from approximately 200 mA/cm^2 up to approximately 1.0 mA/cm^2 at 1.19 V. This unambiguously indicates the formation of new catalytically active species potentially adsorbed at the surface of the electrode. Indeed, transferring the glassy carbon electrode obtained after the CV into a clean electrolyte solution and scanning from 0.92 to 1.19 V shows a current density at 1.19 V that is close to 90% of the previous one. Furthermore, no redox waves associated with molecular $\mathbf{Fe_5}^{n+}$ complex can be observed when scanning within the -1.08 to 1.19 V potential range (see Figure 3 left). These two experiments point out that FeOx are the main species responsible for the electrocatalytic activity observed here, given its well-known catalytic behavior[34]. Furthermore, X-ray absorption spectroscopy (XAS) was also carried out on glassy

carbon plates, which gives additional support to the formation of FeOx adsorbed at the electrode surface as will be discussed later on.

A series of related experiments were also carried out by changing the relative concentration of H_2O from 1% to 10% in MeCN and are reported in the Figure S5B. In Figure 3 right a plot of the current density at 1.19 V versus the concentration of water is displayed for the initial $\mathbf{Fe_5}^{3+}$ solution and for the electrode obtained from this solution placed subsequently in a clean electrolyte solution. The very close values obtained here further point out that the $\mathbf{Fe_5}^{n+}$ species are a precursor for the generation of FeOx that is actually the active catalyst. The difference between the initial current density and the one obtained in a clean electrolyte solution can be due to ligand oxidation, the formation of transient active species generated during the decomposition process to FeOx, or from the partial solubilization of the FeOx from the electrode.

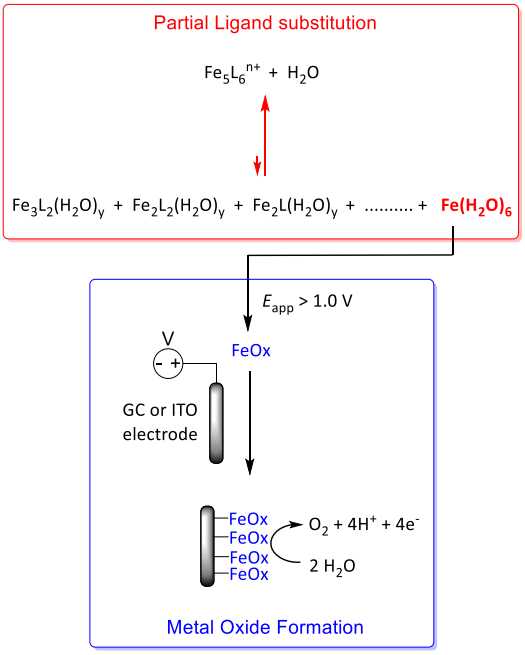

Figure 4. Potential non-isolated intermediate decomposition species formed from the $\mathbf{Fe_5}^{n+}$ complex toward the generation of free iron, $[Fe(H_2O)_6]^{n+}$, and the subsequent formation of the catalytically active species FeOx detected at the surface of an electrode.

As can be seen in Figure 3 right, the intensity of the wave at 1.19 V increases with the concentration of water thus clearly establishing a direct correlation between the H_2O concentration and the catalytic activity. This points out to the presence of a series of equilibria between the initial $\mathbf{Fe_5}^{n+}$ complex and FeOx as depicted in Figure 4. The larger the concentration of water, the larger is the equilibrium shift toward the aquated species, and thus a larger amount of FeOx will be deposited at the surface of the glassy carbon electrode. Furthermore, the increase in water concentration implies an increase in substrate concentration that can lead to a higher catalytic current.

The Influence of pH on the Stability of the Fe_5^{n+} Complex

The stability of Fe complexes is strongly dependent on pH as has been shown in a number of occasions for related ligands[35,36]. The main driving force for decomposition process is the lability of the bonded ligands that can be substituted by solvent water ligands. In acidic pH this substitution process will be further enhanced by the protonation of the bonded ligands that will be strongly dependent on pH. In this respect, the pKa of pyridinium ion is 5.5 and that of pyrazole is 14.2. However, when the Hbpp is coordinated to a transition metal as in the case of $[Ru(trpy)(Hbpp)]^{2+}$ (where trpy is 2,2':60,200-terpyridine), then the pKa of the pyrazole moiety becomes more acidic with pKa values in the range of 5–7 depending on the oxidation state of the metal[37]. In basic pH, the anionic OH^- ligand will be responsible for the substitution process and subsequent generation of FeOx[36,38].

For water oxidation catalysis, the fact that every oxygen molecule evolved generates four protons implies that the local pH will also be strongly reduced in the double layer during water oxidation electrocatalysis. This will in turn strongly effect the stability of the complex leading to decomposition reactions at low local pHs. For this reason, it is extremely important to carry out water oxidation catalysis in the presence of a buffer so that the pH can remain practically constant. This strong influence of pH into the electrocatalytic activity is clearly manifested by observing the current density in the CV at 1.19 V for $\mathbf{Fe_5}^{3+}$ in the presence and absence of buffer (see Figure S6 right). Indeed, in the absence of a buffer, the current density observed is 44% larger than the one in the presence of a non-coordinating borate buffer that clearly suggests the influence of the local pH on the equilibria proposed in Figure 4. CV experiments were also carried

out at different pH values, and it was found that from pH = 2–7, the behavior of the $\mathbf{Fe_5}^{n+}$ complex is basically the same[27]. However, below pH 2 the $\mathbf{Fe_5}^{3+}$ complex is not stable and decomposes to $[Fe^{II}(H_2O)_6]^{2+}$ and free ligand as is the case of related complexes reported in the literature[35,36]. Furthermore, no electrocatalytic activity is observed at pH values below 2. (see Figure S7 for further details).

The Formation of FeOx Films at the Surface of the GC Electrode

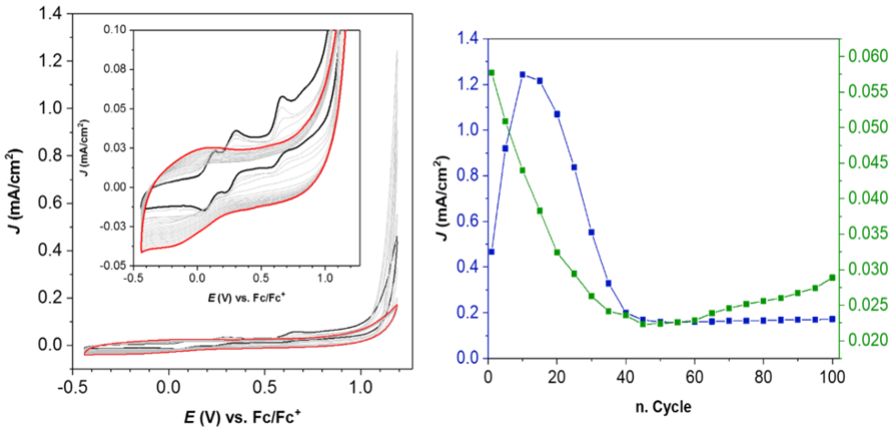

Figure 5. Left, 100 repetitive CVs for $\mathbf{Fe_5}^{3+}$ 0.2 mM dissolved in 10:1 MeCN:H_2O ($V_i = V_f$ = - 0.24 V, V_{C1} = -0.44 V; V_{C2} = 1.19 V). Color code: black trace, first cycle; red trace, last cycle; gray traces, intermediate cycles displayed every five cycles. Right, blue trace, plot of the current density at 1.19 V as a function of CV cycles. Green trace, plot of $i_{p,a}$ of the $[Fe^{II}Fe^{III}_4]^{6+}/[Fe^{II}_2Fe^{III}_3]^{5+}$ redox wave as a function of CV cycles.

The nature of the FeOx deposited at the surface of the GC electrode was evaluated by means of electrochemical, spectroscopic, and microscopy techniques. Figure 5 left shows the results of 100 repetitive CVs scans from -0.44 to 1.19 V for a 0.2 mM solution of $\mathbf{Fe_5}^{3+}$ in a 10:1 MeCN:H2O solution using a GC disk as a working electrode (GC). As it can be observed after the 100th cycle, the CV becomes nearly featureless with an increased double layer capacitance indicating that the initial electrode has lost its conductivity. A simply eye inspection of the electrode shows the formation of a film at the surface. Placing this electrode into a clean solution containing a ferrocene solution 0.2 mM

shows that the anodic III/II wave has lost 93.3% (see Figure S8) of its area with regard to a pristine electrode in exactly the same conditions, confirming the isolating nature of the oxide deposited at the electrode.

The SEM image of this electrode does not show any boundary or particle shapes, but rather a homogeneous surface with similar morphology as the GC electrode, and thus we attribute this to the formation of a film. The nature of this film was further evaluated based on energy-dispersive X-ray (EDX) spectroscopy, scanning electron microscopy (SEM), and X-ray photoelectron spectroscopy (XPS) displayed in the Supplemental Information (Figures S9 and S11 top, respectively). XANES (X-ray absorption near edge structure) and EXAFS (extended X-ray absorption fine structure analysis) were also carried out on the **Fe$_5$**$^{n+}$ complex before (Figures S19-S21, Table S3) and after bulk catalysis (Figure 6) in a glassy carbon plate following exactly the same protocol used for the CV with the GC disk electrode.

The XANES and EXAFS spectra shown in Figure 6 unequivocally show the spectral features of FeOx[39,40] at the electrode after the 100th cycle, thus discarding the potential surface absorption of the molecular **Fe$_5$**$^{n+}$ species. As observed by the red arrows in Figure 6B, a prominent increase in the amplitudes of the EXAFS peaks at apparent distances -1.5 and 2.5 Å are indeed observed in agreement with the EXAFS spectral features of Fe_2O_3 (shown in cyan).

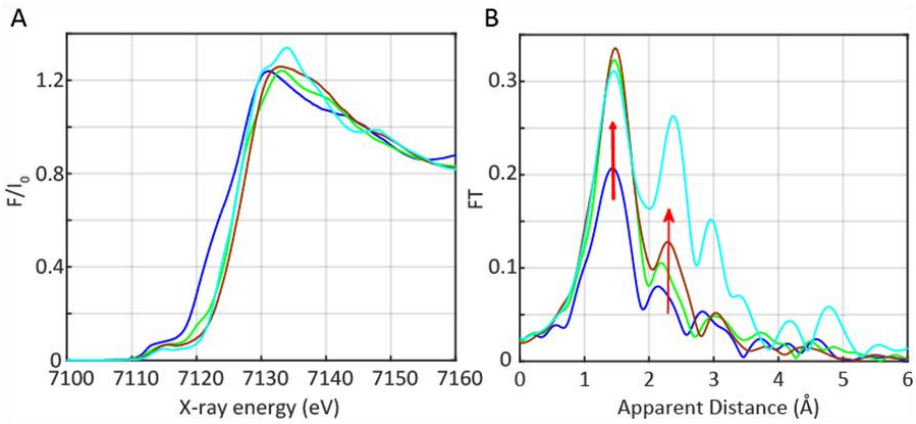

Figure 6. (A) Normalized Fe K-edge XANES of: (1) the **Fe$_5$**$^{3+}$ complex in a frozen mixture of 10:1 MeCN:H_2O (blue); (2) the frozen solution obtained after bulk electrolysis of **Fe$_5$**$^{3+}$ at an applied potential of 1.42 V for 30 min (green; see main text and Supplemental Information for further experimental details); (3) glassy carbon plate (used as a working electrode) obtained after 100 successive CV experiments carried out in the ranges of -0.44 to 1.19 V of 0.2 mM solution of the

Fe$_5$ $^{3+}$ complex in a mixture of 10:1 MeCN:H_2O (brown); (4) Fe_2O_3 powder (cyan). (B) Experimental Fourier transforms of k-weighted Fe EXAFS of the samples described in the left using the same color code. The red arrows indicate the main peaks associated with Fe_2O_3.

A closer inspection at the repetitive CV experiment provides additional insight into the progressive formation of the FeOx film. Figure 5 right shows a plot of the current density obtained at 1.19 V versus $i_{p,a}$ of the $[Fe^{II}Fe^{III}_4]^{6+}/[Fe^{II}_2Fe^{III}_3]^{5+}$ redox wave preceding the electrocatalytic current. During the first ten cycles, the electrocatalytic current at 1.19 V increases its intensity, whereas the $i_{p,a}$ of the $[Fe^{II}Fe^{III}_4]^{6+}/[Fe^{II}_2Fe^{III}_3]^{5+}$ wave decreases. This implies that the catalytic activity increases initially as active FeOx is being formed and deposited at the GC electrode. At the same time and owing to the formation of non-conductive FeOx (potentially due to a thicker layer or different morphology), the available conductive surface area decreases and thus the intensity of the molecular Fe5n+ waves decreases as well. The next 20 cycles show a decrease of both currents owing to the non-conductive nature of the film generated at the electrode. From 50 to 100 cycles, small amounts of isolating FeOx are further deposited, which generates a large increase of the capacitance at the electrode.

The Formation of FeOx Nanoparticles at the Surface of the GC Electrode

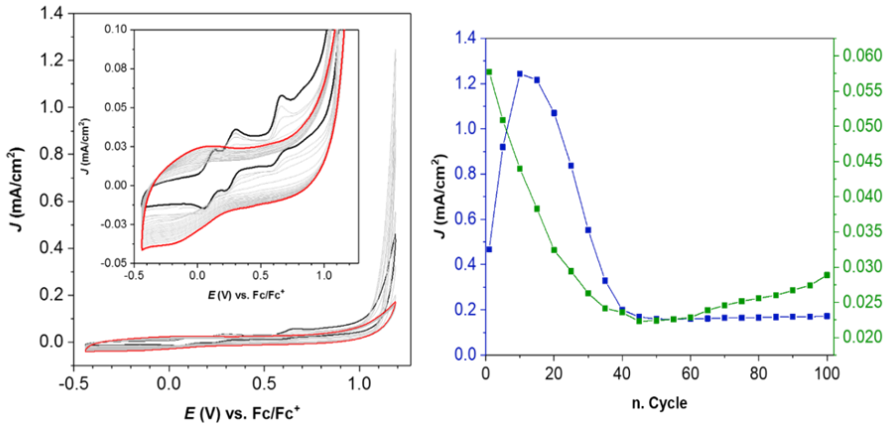

Figure 7. Left, 50 repetitive CVs for **Fe$_5$**$^{3+}$ 0.2 mMdissolved in 10:1 MeCN:H_2O (V_i = V_f = -0.24 V, V_{C1} = -1.08 V; V_{C2} = 1.19 V). Color code: black trace, first scan; red trace, last scan; gray traces, intermediate cycles displayed every five cycles. Right, blue trace, plot of the current density at

1.19 V as a function of CV cycles. Green trace, plot of $i_{p,a}$ of the $[Fe^{II}Fe^{III}_4]^{6+}/[Fe^{II}_2Fe^{III}_3]^{5+}$ redox wave as a function of CV cycles.

The performance of the $\mathbf{Fe_5}^{3+}$ complex was evaluated by multiple consecutive cycle voltammetric experiments under a different range of potentials. Figure 7 left shows 50 repetitive cyclic voltammetry experiments carried out in exactly the same conditions as the previous one but after changing the potential range from -1.08 to 1.19 V to fully reduce the initial complex all the way to the $Fe^{II}_5{}^{2+}$ species. Figure 7 right also shows the current density plot obtained at 1.19 V versus $i_{p,a}$ of the $[Fe^{II}Fe^{III}_4]^{6+}/[Fe^{II}_2Fe^{III}_3]^{5+}$ redox wave. As the number of cycles proceed, the catalytic intensity at 1.19 V increases owing to the increasing amount of FeOx adsorbed at the GC electrode until it reaches a plateau due to the saturation of the surface. On the other hand, the intensity of the molecular $\mathbf{Fe_5}^{n+}$ species waves decrease owing to a decrease of the concentration of the double layer caused by the formation of FeOx. As can be seen in the Figure 7, the FeOx deposited at the electrode is conductive. The formation of nanoparticles can be observed with SEM (see Figure S10) with an approximate diameter of about 40 nm. The conductivity of the material also enables us to observe the formation of other electroactive species growing at the double layer (see cathodic waves at -0.25 and 0.75 V in Figure 7 left). This suggests that the initial $\mathbf{Fe_5}^{n+}$ complex decomposes to other molecular species as indicated in Figure 4, before forming FeOx, which finally ends up being adsorbed at the surface of the electrode.

Potentiostatic Generation of FeOx

Potentiostatic experiments were carried out using a glassy carbon rod (GCrod) or indium tin oxide (ITO) as a working electrode as shown in the Supplemental Information (see Figures S12, S14, and S17). A controlled potential electrolysis (CPE) was performed with a GCrod as working electrode with 6.5 mL of a 0.2 mM (1.3 mmol) solution of $\mathbf{Fe_5}^{3+}$ and was carried out for 1 h at E_{app} = 1.19 V. During this time 1.05 C was passed together with the formation of 2.5 mmol of O_2 that accounts for 90 of faradaic efficiency (FE) (see Figures S12 and S13). Oxygen detection obtained through Clark electrode.

Potentiostatic experiments using ITO electrodes (S = 2 cm2) as working electrodes are shown in the Supplemental Information (Figures S14 and S17).

Same conditions previously described, 6.5 mL of a 0.2 mM (1.3 mmol) solution of $\mathbf{Fe_5}^{3+}$ was applied. One CPE was carried out for 1 h at E_{app} = 1.42 V. During this time 7.5 C (77 mmol of electrons/4 = 19.4 mmol of O_2) was obtained, which corresponds to a TN = 14.9 assuming a 100% FE (calculated for comparison purposes; see Figure S14). After the bulk electrolysis the ITO electrode was placed in a clean electrolyte solution and it showed the same activity as in the presence of the $\mathbf{Fe_5}^{3+}$ solution, demonstrating again that the water oxidation activity is due to the formation of FeOx at the surface of the electrode (Figure S15 left). Furthermore, a CV using a GC disk as working electrode was carried out for the $\mathbf{Fe_5}^{3+}$ solution obtained after the bulk electrolysis and showed no molecular species present indicating that the whole solution is transformed to FeOx (see Figures S15 and S16). An additional bulk electrolysis was carried out at E_{app} = 1.19 V (Figure S17) under the same conditions as in the previous case using an ITO electrode (S = 2 cm2), yielded 1 C (10.2 mmol of electrons/4 = 2.5 mmol of O_2), which corresponds to a TN = 1.9 assuming a 100% faradaic efficiency. The CV of the solution after the CPE shows that a significant amount of the initial complex together with other waves associated with potential decompositions of the initial $\mathbf{Fe_5}^{3+}$ complex is still present (Figure S18 right). This implies that the initial complex has only been partially decomposed to FeOx and that this process is taking place slowly and in parallel to the electrocatalytic formation of O_2 by the adsorbed FeOx.

C.3 Discussion and Conclusions

The compact structure of the $\mathbf{Fe_5}^{3+}$ complex is a highly stable structural arrangement and thus constitutes a thermodynamic sink in the sense that all intermediate species generated from the reaction of bpp^- and Fe(II) can break and form new Fe-N bonds until they end up trapped in $\mathbf{Fe_5}^{3+}$. This implies that bond formation and breaking acts as an automatic healing process that leads to the final $\mathbf{Fe_5}^{3+}$ complex. A similar type of phenomenon has been described in supramolecular chemistry for the generation of macrocycles and cages based on other transition metals [41]. This large stability is also displayed by related tetradentate linear ligands with Fe and other first row transition metal complexes such as Mn that generate virtually identical structures[42]. The large degree of stability is also manifested in the large energy value (18.9 kcal/mol)

calculated that is required to coordinate an additional water molecule to one of the equatorial Fe center, changing its first coordination sphere from CN_5 to CN_6.

These pentanuclear complexes are very stable from a thermodynamic perspective, but they also are highly labile owing to their high spin electronic configurations. Thus, although these complexes are stable in MeCN solution, they readily decompose in the presence of coordinating solvents such as water, where the latter competes for the first coordination sphere. This decomposition phenomenon involves the disruption of the whole complex leading to a structure crumbling effect that finally generates the $[M(H_2O)_6]^{2+/3+}$ and the free ligand as has been reported for the $\mathbf{Mn_5}^{3+}$ case. The $\mathbf{Fe_5}^{3+}$ complex is slightly more stable than its Mn analog and can tolerate concentrations up to 10:1 MeCN:H_2O at low oxidation states. However, the stability of the complex is reduced in its high oxidation state species even in MeCN. Although the $[Fe^{II}Fe^{III}_4]^{6+}$ decomposes completely in about 1 h, the $[Fe^{III}_5]^{7+}$ decomposes much faster and has not been isolated[32]. Electrochemically, the $[Fe^{II}Fe^{III}_4]^{6+}$ species are not stable in a 10:1 MeCN:H_2O solution as ascertained by CV leading to the aquated species (Figure 4).

Additionally, increasing the applied potential to the zone of predominance of the $[Fe^{III}_5]^{7+}$ species leads to the formation of FeOx concomitant with the generation of a large electrocatalytic water oxidation current. The fact that the foot of the electrocatalytic current is found at a 150 mV lower potential than the foot of the $[Fe^{III}_5]^{7+}$ /$[Fe^{II}Fe^{III}_4]^{6+}$ couple suggests that both the $[Fe^{II}Fe^{III}_4]^{6+}$ and the $[Fe^{III}_5]^{7+}$ might be responsible for the aquation of the $\mathbf{Fe_5}^{n+}$ species that leads to the formation of FeOx adsorbed at the electrode. Given the large stability of the $\mathbf{Fe_5}^{n+}$ structure, once a water adds to the first coordination sphere of an equatorial Fe center, the whole structure immediately crumbles giving rise to a large number of potential species as outlined in Figure 4. This view is also in agreement with the increased catalytic activity obtained upon increasing the H_2O concentration, which shifts the equilibria to the right as shown in Figure 3. These molecular high oxidation-state species generated at high potentials from the dismantling of the $\mathbf{Fe_5}^{n+}$ structure could potentially behave as water oxidation catalysts. However, in the present case, given the large activity associated with FeOx, the activity of the resulting decomposed species is small if not active at all, as evidenced by CV experiments in clean electrolyte solutions.

All these experiments suggest the presence of a very delicate equilibrium between the $[Fe^{II}Fe^{III}_4]^{6+}$ and the $[Fe^{III}_5]^{7+}$ species, and their aquated counterparts as proposed in Figure 4. An additional evidence of this delicate equilibrium is exemplified by the experiments carried out in the presence of triflic acid that completely suppresses catalysis. Furthermore, the experiments carried out at different pHs suggest the local pH close to the electrode can reach pH values as low as 1, in experiments carried out in the absence of a buffer, for instance, in a 10:1 MeCN:H_2O solvent. The low pH conditions could further help in the aquation of the $\mathbf{Fe_5}^{3+}$ complex and thus in the generation of FeOx.

An additional interesting point that also emerges from this work is how the nature of the FeOx formed at the surfaces of the electrode (conductive versus isolating; films versus nanoparticles), is strongly dependent on the potential range used to generate it. Furthermore, it is also striking to see the high activity of this FeOx adsorbed at the surface of the electrode that reaches current densities in the range of 3 mA/cm^2 at pH 7. In this regard, the high activity of the FeOx could lead to a misinterpretation of the results if the working electrodes are not properly evaluated in clean electrolyte solutions, since only very small amounts of the initial molecular complex are needed to be transformed into highly active FeOx.

Thus, in the hypothetical case that the stability of the complex in solutions after a bulk electrolysis experiment was checked, for instance, by UV-vis, MS, or DLS spectroscopy, it would appear as if the initial catalyst was intact as the initial concentration would remain practically the same. Several main conclusions can be inferred from the present work. In the first place, the auxiliary ligands used in WOCs with transition metals should contain oxidatively robust ligands given the high redox potentials of this reaction. Therefore, ligands containing benzyl pyridyl groups will be easily oxidized as has been shown in many cases[21,43,44]. Thus, they should not be used in their ligand framework. Second, special attention should be given to the stability of first row transition metals in water given the high lability of the M-L bond in this solvent[29]. The aqua substitution will foster the formation of oxides adsorbed at the surface of the electrode. Finally, the fact that the water oxidation reaction generates four protons per oxygen molecule implies that a buffer should always be used to avoid ligand decoordination and oxide formation.

C.4 Aknowledgments

Support fromMINECO, FEDER, and AGAUR is gratefully acknowledged through grants CTQ2016-80058-R, CTQ2015-73028-EXP, SEV 2013-0319, ENE2016-82025-REDT, CTQ2016-81923-REDC, and 2017-SGR-1631. D.M. acknowledges funding from the Severo Ochoa (SEV-2016-0686) Excellence Program from IMDEA Nanociencia. XAS experiments were performed at the CLAESS beamline at ALBA Synchrotron under proposal No. 20170913 and 2017032110.

C.5 References

(1) Grätzel, M. *Acc. Chem. Res.* **1981**, *14*, 376–384.

(2) Berardi, S.; Drouet, S.; Francàs, L.; Gimbert-Suriñach, C.; Guttentag, M.; Richmond, C.; Stoll, T.; Llobet, A. *Chem. Soc. Rev.* **2014**, *43* (22), 7501–7519

(3) Lewis, S. N. *Science* **2016**, *351,* 353–361.

(4) Nocera, D. G. *Acc. Chem. Res.* **2017**, *50* (3), 616–619.

(5) Guan, X.; Chowdhury, F. A.; Wang, Y.; Pant, N.; Vanka, S.; Trudeau, M. L.; Guo, L.; Vayssieres, L.; Mi, Z. *ACS Energy Lett.* **2018**, *3* (9), 2230–2231.

(6) Roger, I., Shipman, M. A. & Symes, M. D. *Nat. Rev. Chem.* **2017**, *1*, 301–313.

(7) Nelson, N.; Ben-Shem, A. *Nat. Rev. Mol. Cell Biol.* **2004**, *5* (12), 971–982.

(8) McEvoy, J. P.; Brudvig, G. W. *Chem. Rev.* **2006**, *106* (11), 4455–4483.

(9) Croce, R.; Van Amerongen, H. *Nat. Chem. Biol.* **2014**, *10* (7), 492–501.

(10) Smith, R. D. L.; Prevot, M. S.; Fagan, R. D.; Zhang, Z.; Sedach, P. A.; Siu, M. K. J.; Trudel, S.; Berlinguette, C. P. *Science* **2013**, *340*, 60–63.

(11) McCrory, C. C. L.; Jung, S.; Ferrer, I. M.; Chatman, S. M.; Peters, J. C.; Jaramillo, T. F. *J. Am. Chem. Soc.* **2015**, *137* (13), 4347–4357.

(12) Godwin, I.; Rovetta, A.; Lyons, M.; Coleman, J. *Curr. Opin. Electrochem.* **2018**, *7*, 31–35.

(13) Blakemore, J. D.; Crabtree, R. H. & Brudvig, G. W. *Chem. Rev.* **2015**, *115*, 12974–13005.

(14) Garrido-Barros, P.; Gimbert-Suriñach, C.; Matheu, R.; Sala, X.; Llobet, A. *Chem. Soc. Rev.* **2017**, *46* (20), 6088–6098.

(15) Matheu, R.; Garrido-Barros, P.; Gil-Sepulcre, M.; Sala, X.; Gimbert-Suriñach, C. *Nat. Rev. Chem.* **2019**, *2* (3), 331-341.

(16) Matheu, R.; Ertem, Z. M.; Gimbert-Suriñach, C.; Sala, X. and Llobet, A. *Chem. Rev.* **2019**, *119*, 3453–3471.

(17) Lewis, N. S.; Nocera, D. G. *Proc. Nat. Acad. Sci.* **2006**, *103*, 15729–15735.

(18) Lewis, N. S.; Nocera, D. G. *Proc. Nat. Acad. Sci.* **2007**, *104*, 20142–20142.

(19) Llobet, A.; Meyer, F. *Angew. Chem.* **2011**, *50*, 30–33.

(20) Ellis, W. C.; McDaniel, N. D.; Bernhard, S.; Collins, T. J. *J. Am. Chem. Soc.* **2010**, *132* (32), 10990–10991.

(21) Radaram, B.; Ive, A.; Singh, W. M.; Grudzien, R. M.; Reibenspies, J. H.; Webster, C. E.; Zhao, X. *Inorg. Chem.* **2011**, No. 50, 10564–10571.

(22) Keidel, A.; Lopez, I.; Staffa, J.; Kuhlmann, U.; Bozoglian, F.; Gimbert-Suriñach, C.; Benet, J.; Hildebrandt, P.; Llobet, A. *ChemSusChem* **2016**.

(23) Hoffert, W. A.; Mock, M. T.; Appel, A. M.; Yang, J. Y. *Eur. J. Inorg. Chem.* **2013**, 3846–3857.

(24) Pattanayak, S.; Chowdhury, R.; Garai, B.; Singh, K. K. *Chem. Eur.* **2017**, *23*, 3414–3424.

(25) Kaeffer, N.; Morozan, A.; Fize, J.; Martinez, E.; Guetaz, L.; Artero, V. *ACS Catal.* **2016**, No. 6, 3727−3737.

(26) Folkman, S. J.; Soriano-lopez, J.; Ramo, J.; Finke, R. G. *J. Am. Chem. Soc.* **2018**, *140*, 12040−12055.

(27) Okamura, M.; Kondo, M.; Kuga, R.; Kurashige, Y.; Yanai, T.; Hayami, S.; Praneeth, V. K. K.; Yoshida, M.; Yoneda, K.; Kawata, S.; Masaoka, S. A *Nature* **2016**, *530* (7591), 465–468.

(28) Sreerama, S. G.; Pal, S. *Eur. J. Inorg. Chem.* **2004**, *3*, 4718–4723.

(29) Helm, L.; Merbach, E. *Chem. Rev.* **2005**. 105, 1923–1960

(30) Bao, X.; Leng, J.-D.; Meng, Z.-S.; Lin, Z.; Tong, M.-L.; Nihei, M.; Oshio, H. *Chem.*

Eur. J. **2010**, 6169–6174.

(31) Romain, S.; Rich, J.; Sens, C.; Stoll, T.; Benet-Buchholz, J.; Llobet, A.; Rodriguez, M.; Romero, I.; Clérac, R.; Mathonière, C.; Duboc, C.; Deronzier, A.; Collomb, M. N. *Inorg. Chem.* **2011**, *50* (17), 8427–8436.

(32) Gouré, E.; Gerey, B.; Clémancey, M.; Pécaut, J.; Molton, F.; Latour, J. M.; Blondin, G.; Collomb, M. N. *Inorg. Chem.* **2016**, *55* (18), 9178–9186.

(33) Liao, R. Z.; Masaoka, S.; Siegbahn, P. E. M. *ACS Catal.* **2018**, *8* (12), 11671–11678.

(34) Formal, F.; Le; Pastor, E.; Tilley, S. D.; Mesa, C. A.; Pendlebury, S. R.; Gra, M.; Durrant, J. R. *J. Am. Chem. Soc.* **2015**, *137*, 6629−6637.

(35) Draksharapu, A.; Li, Q.; Logtenberg, H.; Van Den Berg, T. A.; Meetsma, A.; Killeen, J. S.; Feringa, B. L.; Hage, R.; Roelfes, G.; Browne, W. R. *Inorg. Chem.* **2012**, *51*, 900−913.

(36) Hong, D.; Mandal, S.; Yamada, Y.; Lee, Y.; Nam, W.; Llobet, A.; Fukuzumi, S. *Inorg. Chem.* **2013**, 52, 9522−9531.

(37) Sens, C.; Rodriguez, M.; Romero, I.; Llobet, A.; Parella, T.; Benet-buchholz, J. *Inorg. Chem.* **2003**, *42* (25), 8385–8394.

(38) Chen, G.; Chen, L.; Ng, S.; Man, W.; Lau, T. *Angew. Chem.* **2013**, *4*, 1789–1791.

(39) Kuzmin, A.; Chaboy, J. *IUCrJ* **2014**, *1*, 571–589.

(40) Tangwatanakul, W.; Sirisathitkul, C.; Limphirat, W.; Yimnirun, R. *Chin. J. Phys.* **2017**, *55*, 845.

(41) Cook, T. R.; Zheng, Y.; Stang, P. J. *Chem. Rev.* **2013**, *113*, 734−777.

(42) Kabata-pendias, A. and Mukherjee, A. B. *Trace Elements From Soil to Human*; Springer US, 2007.

(43) Sander, A. C.; Schober, A.; Dechert, S.; Meyer, F. *Eur. J. Inorg. Chem.* **2015**, 4348–4353.

(44) Wang, J.; Sahoo, P.; Lu, T. *ACS Catal.* **2016**, *6*, 5062−5068.

C.6 Supporting Information

Experimental Section

Materials

All the chemicals used in this work were provided by Sigma Aldrich and they have been used without further purification unless explicitly indicated. $FeSO_4 \cdot 7H_2O$ was purchased from Alfa-Aesar, 3,5-bis(2-pyridyl)pyrazole (Hbpp) was synthesized according to the published procedure [1]. $[Fe^{II}_4Fe^{III}(\mu_3\text{-}O)(\mu\text{-}bpp)_6](BF_4)_3$, (**$[Fe^{II}_4Fe^{III}]^{3+}$** or **$Fe_5^{3+}$**), was synthesized following a methodology previously described in the literature [2]. The solvents employed in this work were dried by a SPS® system and later degassed by bubbling nitrogen or argon before starting the reactions. All aqueous solutions used for electrochemical measurements were prepared with high purity de-ionized water obtained by passing distilled water through a nanopure Mili-Q water purification system. Glassy Carbon Disk (GC), Glassy Carbon Rod (GC_{rod}), Platinum Disk (Pt) and $Ag/AgNO_3$ were purchased from IJ-Cambria Ldt. Glassy Carbon Plates (Sigradur® K films 20 mm x 10 mm x 180 µm) were acquired from HTW Germany. Indium Tin Oxide (ITO) electrodes (Rs = 8−12 Ω) were purchased from ALPHA BIOTECH.

Instrumentation and Methods

Electrochemical measurements

Cyclic voltammetry (CV), Differential Pulse Voltammetry (DPV) and Controlled Potential Electrolysis (CPE) were carried out using a CHI660D potentiostat. Glassy carbon electrode (GC) (d = 3 mm), Glassy carbon Rod (GC_{rod}), Glassy carbon plate (GC_{plate}) or Indium Tin Oxide (ITO) electrode (S= 2 cm^2, Rs = 8−12 Ω) were employed as working electrode (WE). In case of Glassy carbon plate (GC_{plate}) or Indium Tin Oxide (ITO) the surface dipped in solution was 2 cm^2. Pt disk was employed as a counter electrode (CE) and $Ag/AgNO_3$ (0.01 M $AgNO_3$ in 0.1 M solution of $TBAPF_6$ in MeCN) as a reference (RE). Glassy carbon (GC) electrodes were polished with 1.0, 0.3 and 0.05 µm micron alumina paste, washed with distilled water and sonicated in acetone for 10 minutes before performing each experiment. All the potentials values reported in this work have

been measured vs $Ag/AgNO_3$ reference electrode and converted to Fc/Fc^+ by adding ferrocene/ferrocenium as internal standard ($E_{1/2}(Fc/Fc^+)$ ≈ -0.08 vs $Ag/AgNO_3$) at the end of each experiment ($E_{1/2}(Fc/Fc^+)$ ≈ + 0.548 V vs NHE).[3] All the electrochemical experiments carried out in acetonitrile (MeCN) were performed with the presence of 0.1 M tetraethyl ammonium perchlorate (TEAP) as supporting electrolyte.

Cyclic voltammetry (CV), differential pulse voltammetry (DPV): CV measurements were conducted under an N_2 atmosphere, unless otherwise stated at room temperature (24–25 °C), in a three-electrode cell. The scan rate was set at 10 mV/s unless otherwise stated. DPV was collected with amplitude= 50 mV, step height=4 mV, pulse width= 0.05 s, pulse period= 0.2 s and sampling width= 0.0167 s.

Controlled potential electrolysis (CPE): CPE experiments were carried out under an N_2 atmosphere, unless otherwise stated at room temperature (24–25 °C) in a gastight, two-compartment, three-electrode cell. In this case, ITO (S = 2 cm^2) or GC_{rod} were used as working electrode and Pt mesh was used as a counter electrode.

O_2 detection by Clark electrode: During the CPE experiment, the oxygen evolution was monitored with an OXNP type Clark electrode in gas phase (from Unisense Company). This electrode was positioned in the headspace of the compartment cell where the WE and the RE are placed. The oxygen was removed by bubbling nitrogen during 30 min. Once the Clark signal reached values close to 0 mV, the nitrogen flow was stopped and the base line was left to stabilize. The CPE was started once the oxygen sensor signal was stable. The experiment was performed under vigorous stirring. Calibration of the oxygen sensor was done by adding known amount of pure oxygen into the cell using a gas tight Hamilton syringe. The blank experiment followed the same procedure. The Faraday efficiency was determined according to the total charge passed during the CPE and the total amount of generated oxygen by considering that water oxidation is a 4 e^- oxidation process.

Solid State characterization of the electrodes.

SEM and EDX analyses were carried out on a JEOL JSM 6700F electron microscope working at 10 kV. XPS experiments were performed with a SPECS EA10P hemispherical analyser using a non-monochromated X-ray source (Al Kα line of 1486.6 eV and 300W). The direction of the X-ray source with respect to the sample was 90º and ultrahigh vacuum was maintained during the measurements, obtaining a residual pressure of 10^{-8} Pa.

Preparation of the electrodes: GC_{rod} electrodes (d= 3 mm), used for SEM and XPS analysis, were cut in pieces 4 mm tall. The pieces were left in 6 M H_2SO_4 aqueous solution overnight to avoid possible traces of metals during the measurements. Afterwards, they were sonicated in Milli-Q water for 30 min, polished with 1.0, 0.3 and 0.05 micron alumina paste, washed with distilled water and sonicated in acetone for 10 minutes. The experiments were performed covering the side of the electrode and leaving exposed only the top surface (S = 0.07 cm^2). The ITO glass slides (2 cm^2) were immersed in the electrolyte solution and sonicated in MeOH (K_2CO_3 sat.) for 30 min and then rinsed with acetonitrile and water. [2]

UV-vis spectrometry

UV-vis spectrometry was performed using a Cary 50 (Varian) UV-vis spectrophotometer.

X-ray Absorption Spectroscopy (XAS) Methods.

X-ray absorption spectra were collected at the CLAESS beamline at the ALBA synchrotron light source.[4] The radiation was monochromatized using a pair of Si(111) crystals. The intensity of the X-rays were monitored by three ion chambers (I_0, I_1 and I_2). I_0 placed before the sample was filled with 100% nitrogen while I_1 and I_2 placed after the sample were filled with 77 % N_2 and 23 % Kr. Fe metal was placed between ion chambers I_1 and I_2 and its absorption was recorded with each scan for energy calibration. The samples were measured in customized PEEK sample holders and measured with a defocused beam spot size of 500 x 500 µm using a liquid nitrogen cryostat cooled down to 77 K. Fluorescence absorption measurements were carried out with an Amptek silicon drift solid state detector (XR-100 SDD)[4] placed at 90 degrees to the incoming beam. The silicon drift detector was placed on a motorized stage allowing the

sample-detector distance to be easily changed between 30-110 mm[5]. Solid Fe_2O_3 diluted with BN powder, was pressed between kapton and mylar tape, and measured in the cryostat in transmission mode. Around 3 scans were collected on Fe_2O_3 and around 20-25 scans were collected on the solution and hybrid samples. Care was taken to measure at different spots on both the solution and hybrid samples in order to minimize radiation damage. No more than 2 scans were taken in this instance on each spot on the solution samples. All samples were also protected from the x-ray beam during spectrometer movements by a shutter synchronized with the scan program. Fe XAS energy was calibrated by the first maxima in the second derivative of the iron metal X-ray absorption near edge structure (XANES) spectrum.

Extended X-ray Absorption Fine Structure (EXAFS) Analysis

Athena software[6] was used for data processing. The energy scale for each scan was normalized using copper metal standard. Data in energy space were pre-edge corrected, normalized, deglitched (if necessary), and background corrected. The processed data were next converted to the photoelectron wave vector (k) space and weighted by *k*. The electron wave number is defined as $k = [2m(E - E_0)/\hbar^2]^{1/2}$, E_0 is the energy origin or the threshold energy. K-space data were truncated near the zero crossings k = 2 to 11.375 $Å^{-1}$ for the solid, solution and hybrid complexes, in Fe EXAFS before Fourier transformation. The k-space data were transferred into the Artemis Software for curve fitting. In order to fit the data, the Fourier peaks were isolated separately, grouped together, or the entire (unfiltered) spectrum was used. The individual Fourier peaks were isolated by applying a Hanning window to the first and last 15% of the chosen range, leaving the middle 70% untouched. Curve fitting was performed using *ab initio*-calculated phases and amplitudes from the FEFF[7] program from the University of Washington. *Ab initio*-calculated phases and amplitudes were used in the EXAFS equation

$$\chi(k) = S_0^2 \sum_j \frac{N_j}{kR_j^2} f_{eff_j}(\pi, k, R_j) e^{-2\sigma_j^2 k^2} e^{\frac{-2R_j}{\lambda_j(k)}} \sin(2kR_j + \phi_{ij}(k)) \qquad \text{(S2)}$$

where N_j is the number of atoms f_{effj} in the j^{th} shell; R_j the mean distance between the absorbing atom and the atoms in the j^{th} shell; (π,*k*, R_j) is the *ab initio* amplitude function for shell *j*, and the $e^{-2\sigma_j^2 k^2}$ Debye-Waller term accounts for damping due to static and thermal disorder in absorber-back scatterer distances. The mean free path term $e^{\frac{-2R_j}{\lambda_j(k)}}$ reflects losses due to inelastic scattering, where $\lambda_j(k)$, is the electron mean free path. The oscillations in the EXAFS spectrum are reflected in the sinusoidal term $\sin(2kR_j + \phi_{ij}(k))$, where $\phi_{ij}(k)$ is the *ab initio* phase function for shell *j*. This sinusoidal term shows the direct relation between the frequency of the EXAFS oscillations in k-space and the absorber-back scatterer distance. S_0^2 is an amplitude reduction factor.
The EXAFS equation[4] (Eq. S2) was used to fit the experimental Fourier isolated data (q-space) as well as unfiltered data (k-space) and Fourier transformed data (R-space) using *N*, S_0^2, E_0, *R,* and σ^2 as variable parameters (Table S3). *N* refers to the number of coordination atoms surrounding Fe for each shell. The quality of fit was evaluated by R-factor and the reduced Chi^2 value. The deviation in E_0 ought to be less than or equal to 10 eV. R-factor less than 2% denotes that the fit is good enough. R-factor between 2 and 5% denotes that the fit is correct within a consistently broad model. The reduced Chi^2 value is used to compare fits as more absorber-backscatter shells are included to fit the data. A smaller reduced Chi^2 value implies a better fit. Similar results were obtained from fits done in k, q, and R-spaces.

X-Ray Crystallography

Crystal preparation: Crystals of **$[Fe^{II}_2Fe^{III}_3]^{5+}$** were grown by slow evaporation of acetonitrile in ethyl ether, from a solution after the CPE at 1.19 V. The crystals were selected using a Zeiss stereomicroscope using polarized light and prepared under inert conditions immersed in perfluoropolyether as protecting oil for manipulation.

Data collection: Crystal structure determination for sample **$[Fe^{II}_2Fe^{III}_3]^{5+}$** was carried out using a Apex DUO Kappa 4-axis goniometer equipped with an APPEX 2 4K CCD area detector, a Microfocus Source E025 IuS using MoK_α radiation, Quazar MX multilayer Optics as monochromator and an Oxford Cryosystems low

temperature device Cryostream 700 plus (*T* = -173 °C). Full-sphere data collection was used with ω and φ scans. *Programs used:* Bruker Device: Data collection APEX-2 [8], data reductiesion Bruker Saint [9] V/.60A and absorption correction SADABS [10,11].

Structure Solution and Refinement: Crystal structure solution was achieved using the computer program SHELXT.[12] Visualization was performed with the program SHELX.[13]. Missing atoms were subsequently located from difference Fourier synthesis and added to the atom list. Least-squares refinement on F^2 using all measured intensities was carried out using the program SHELXL 2015[14] ll non-hydrogen atoms were refined including anisotropic displacement parameters.

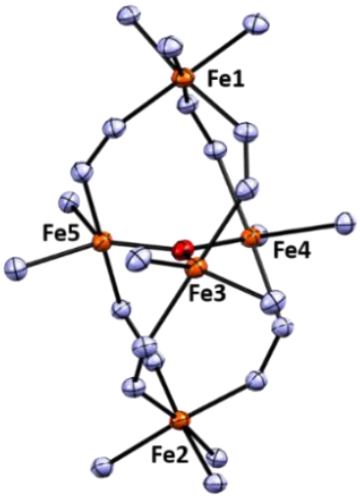

Figure S1. Schematic ORTEP drawing (ellipsoids 50 %) of $[Fe^{II}_2Fe^{III}_3]^{5+}$. The Fe centers are represented as orange ellipsoids and are numbered from 1 to 5. The further structure of bpp^- ligand, H atoms, counter ions and solvent molecules are not represented for simplicity reasons. Color code: red = O; orange = Fe; blue = N.

Table S1. Fe – O bond distances in Å for $[Fe^{II}_4Fe^{III}]^{3+}$ and $[Fe^{II}_2Fe^{III}_3]^{5+}$, extracted from X-ray structures.

Entry	Atoms	$[Fe^{II}_4Fe^{III}]^{3+}$	$[Fe^{II}_2Fe^{III}_3]^{5+}$
1	Fe_1 - O	3.85	3.84
2	Fe_2 - O	3.85	3.87
3	Fe_3 - O	1.93	1.80
4	Fe_4 - O	1.93	1.93
5	Fe_5 - O	1.99	1.94

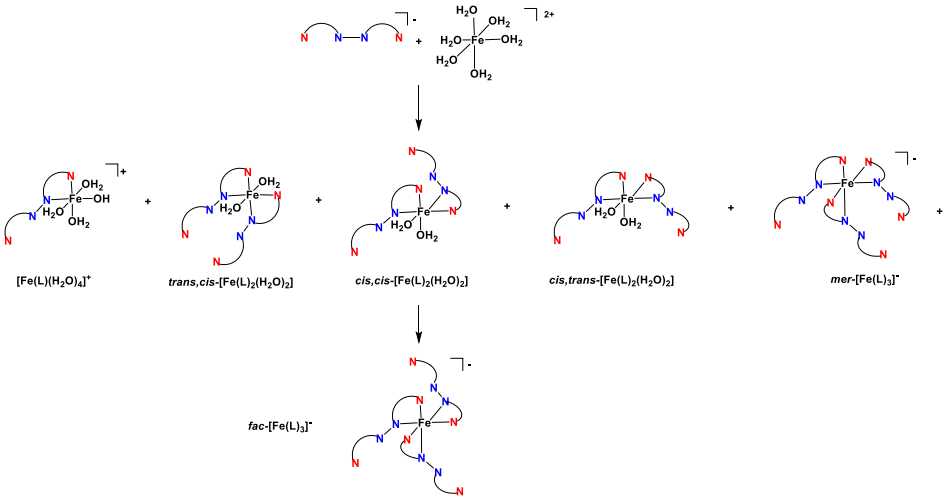

Figure S2. Potential non-isolated Fe complexes that can be formed at the Initial stages of the reaction of Fe(II) and L^- (bpp^-) to form $\mathbf{Fe_5}^{3+}$. The arcs connected with N represent the bpp^- ligand. Red N represent pyridyl groups whereas the blue ones represent pyrazolyl groups.

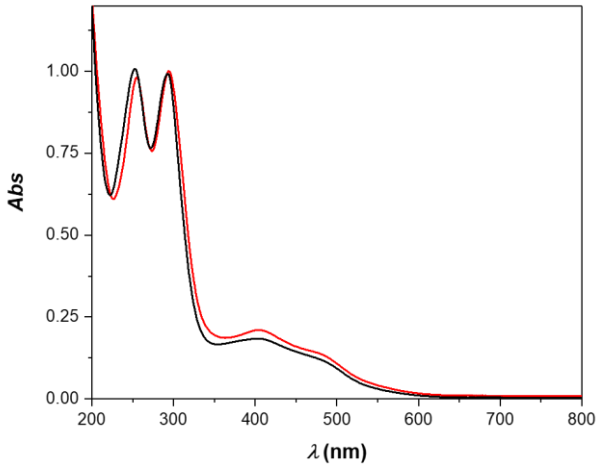

Figure S3. UV-Vis absorption spectrum in a MeOH:H_2O (10:3) solution of: a) black trace, a 0.07 mM of an isolated and crystallized sample of $[\mathbf{Fe_5}(BF_4)_3]\cdot 7H_2O$ and b) a diluted solution directly from the synthesis. A 0.2 cm path length quartz cuvette was used. For the $\mathbf{Fe_5}^{3+}$ 0.140 mg of $[\mathbf{Fe_5}(BF_4)_3]\cdot 7H_2O$ (MW, 2009.15, 0.07 μmols) dissolved in MeOH:H_2O (10:3) solution up to a total volume of 1.0 mL.

This generates a 0.07 mM solution of [**Fe$_5$**(BF$_4$)$_3$]. For the reaction mixture, the same procedure as in the synthesis was flollowed. A sample of $FeSO_4 \cdot 7H_2O$ (84 mg, 0.3 mmol; 0.05 M) + Hbpp (80 mg, 0.36 mmol; 0.06 M) + NaOH (14 mg, 0.36 mmol; 0.06 M) was dissolved with 10:3 MeOH:H_2O up to a total volume of 6 mL. Then the solution was stirred at RT for a few minutes. An aliquot of the resulting solution was diluted to reach a formal concentration of bpp^- of 0.42 mM.

Table S2. $E_{½}$ values for all the redox processes of Fe_5^{3+} in MeCN and 10:1 MeCN:H_2O containing TEAP (0.1 M) as supporting electrolyte. Related to Figure 2.

Entry	Redox Couple	$E_{1/2}$ (E (V) vs Fc/Fc^+)	
		CH_3CN	10:1 MeCN:H_2O
1	$[Fe^{II}_4Fe^{III}]^{3+}/[Fe^{II}_5]^{2+}$	-0.55	-0.57
2	$[Fe^{II}_3Fe^{III}_2]^{4+}/[Fe^{II}_4Fe^{III}]^{3+}$	0.13	0.11
3	$[Fe^{II}_2Fe^{III}_3]^{5+}/[Fe^{II}_3Fe^{III}_2]^{4+}$	0.30	0.29
4	$[Fe^{II}Fe^{III}_4]^{6+}/[Fe^{II}_2Fe^{III}_3]^{5+}$	0.68	0.64
5	$[Fe^{III}_5]^{7+}/[Fe^{II}Fe^{III}_4]^{6+}$	1.08	1.19 ($E_{p,a}$)

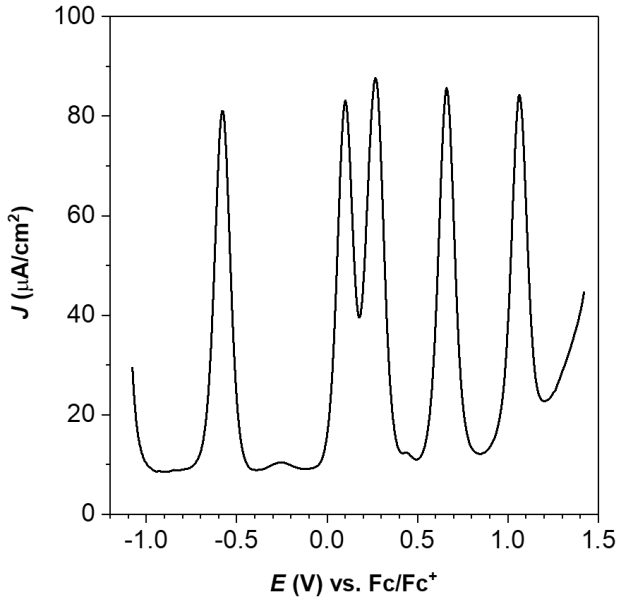

Figure S4. Differential Pulse Voltammetry. 0.2 mM solution of $\mathbf{Fe_5}^{3+}$ in MeCN (V_i -1.08 V; V_f = 1.42 V). Amplitude= 50 mV, step height= 4 mV, pulse width= 0.05 s, pulse period= 0.2 s and sampling width= 0.0167 s.

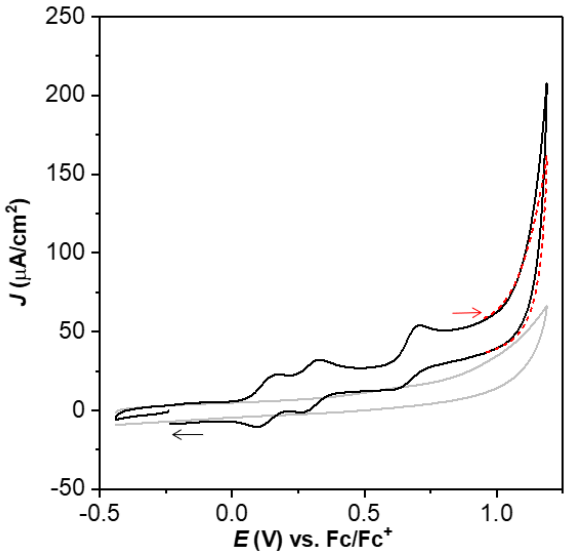

Figure S5A. Solid black trace, CV of the first cycle for $\mathbf{Fe_5}^{3+}$ 0.2 mM in MeCN containing 10% of H_2O at a scan rate of 10 mV/s. The black arrow indicates the scan direction. Dash red trace, base line subtracted CV of the GC working electrodes obtained in the previous experiment, immersed in a clean electrolyte solution of MeCN containing 10% of H_2O at a scan rate of 10 mV/s. The red arrow indicates scan direction. Gray trace, CV of a bare GC electrode in the same conditions.

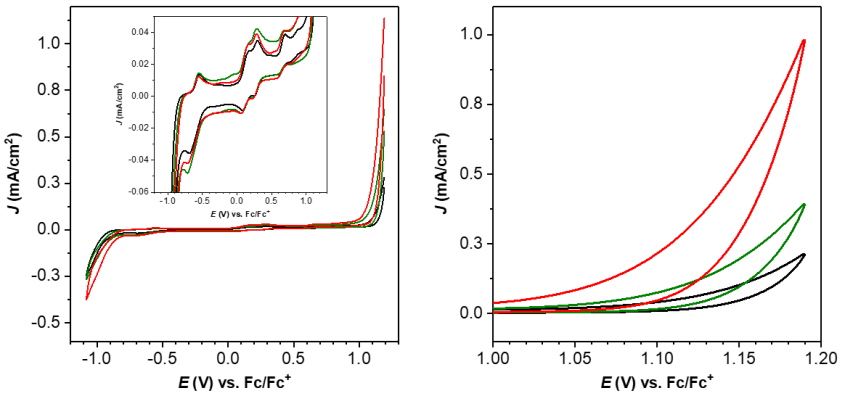

Figure S5B. Left, CV of the 2.5th for **Fe$_5$**$^{3+}$ 0.2 mM in MeCN containing 10% (red trace), 7 % (green trace) and 5 % (black trace) of H_2O at a scan rate of 10 mV/s (V_i = V_f = -1.08 V; V_{C1} = 1.19 V). *Inset*, enlargement on the wave of the complex. Right, CV of the GC working electrodes obtained in the previously mentioned experiments (left) under the same conditions immersed in a clean electrolyte solution (V_i = V_f = 0.92 V; V_{C1} = 1.19 V).

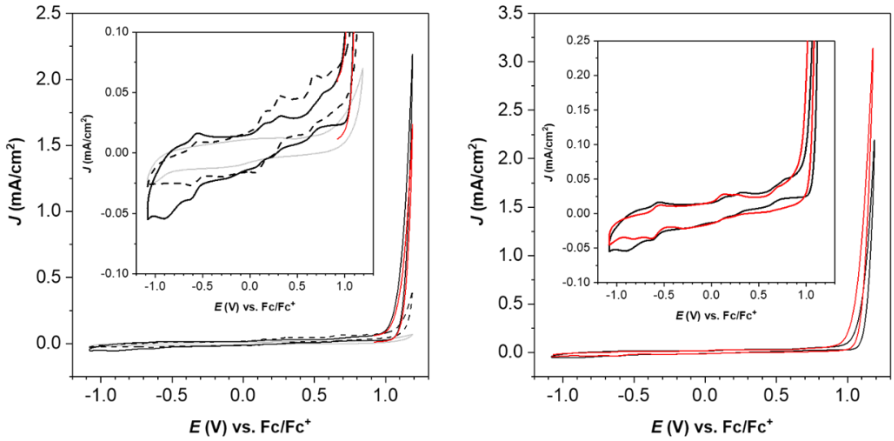

Figure S6. Left, black trace, CV of the 50th cycle for $\mathbf{Fe_5}^{3+}$ 0.2 mM dissolved in a 10:1 MeCN:H_2O solution (added H_2O contains 0.01 M borate buffer, pH 7.8) at a scan rate of 10 mV/s ($V_i = V_f$ = -1.08 V; V_{C1} = 1.19 V). Black dashed trace, CV of the 1st cycle. Red trace, CV of the GC working electrode obtained in the previous experiment immersed in a clean electrolyte solution. Gray trace, CV of a bare GC electrode under the same conditions. *Inset*, enlargement on the wave of the complex. Right, black trace, CV of the 50th cycle for $\mathbf{Fe_5}^{3+}$ 0.2 mM dissolved in a 10:1 MeCN:H_2O solution (added H_2O contains 0.01 M borate buffer, pH 7.8) at a scan rate of 10 mV/s ($V_i = V_f$ = -1.08 V; V_{C1} = 1.19 V). Red trace, CV of the 50th cycle for $\mathbf{Fe_5}^{3+}$ under the same conditions but adding pure H_2O.

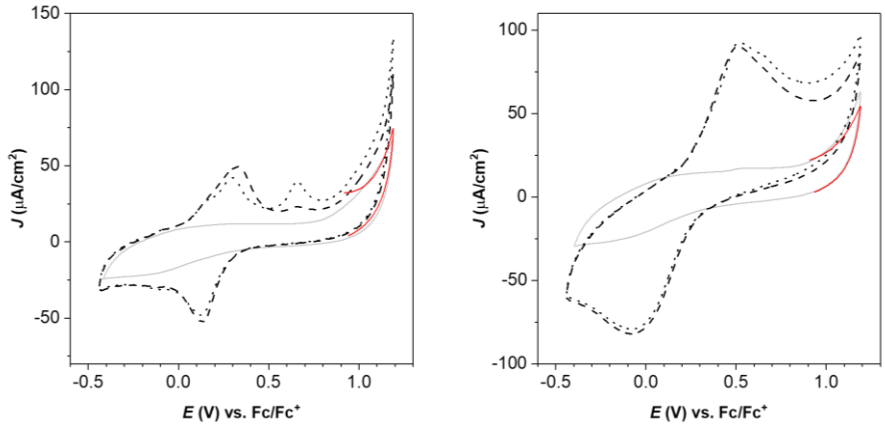

Figure S7. CVs for $\mathbf{Fe_5}^{3+}$ 0.2 mM dissolved in a 10:1 MeCN:H_2O solutions, performed with 0.1 M triflic acid solution pH 1 (left) and 0.3 M triflic acid solution

pH 0.5 (right), at a scan rate of 10 mV/s. *Color code:* black dotted trace, CV of the first cycle; black dashed trace, CV of the second cycle; red trace, CV of the GC working electrode obtained in the previous experiment immersed in a clean electrolyte solution. Gray trace, bare GC electrode. For black dotted, black dashed and grey traces, $V_i = V_f = -0.44$ V; $V_{C1} = 1.19$ V. For the red trace, $V_i = V_f = 0.92$ V; $V_c = 1.19$ V.

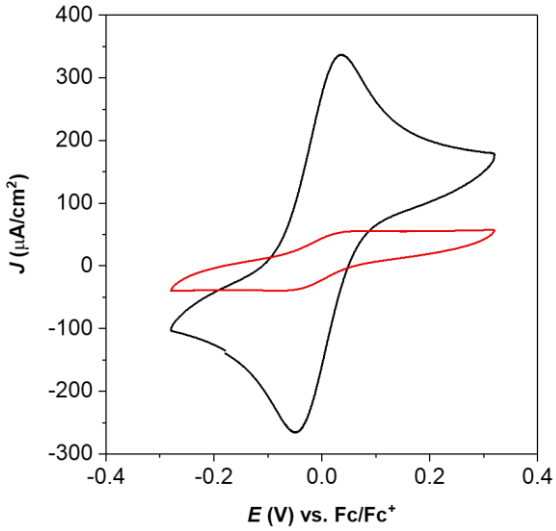

Figure S8. CVs of a 0.2 mM ferrocene solution in 10:1 MeCN:H_2O before (black trace) and after (red trace) cycling the GC electrode ($V_i = V_f = -0.44$ V, $V_{C1} = -0.44$ V; $V_{C2} = 1.19$ V) 100 times in a solution 0.2 mM of $\mathbf{Fe_5}^{3+}$ in a 10:1 MeCN:H_2O.

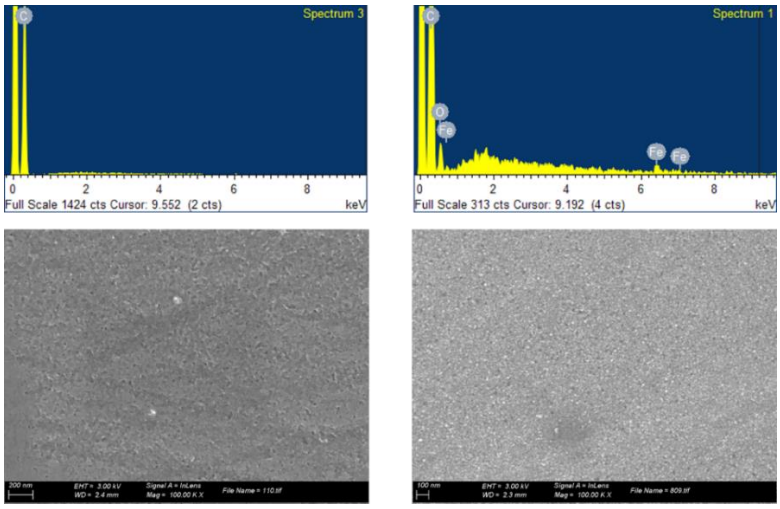

Figure S9. EDX analysis (top) and SEM pictures (bottom) of the GC_{rod} (d= 3 mm) surface after cycling 100 times ($V_i = V_f = -0.44$; $V_C = 1.19$ V) in a complex-free 10:1 MeCN:H_2O solution (left) and in a solution of $\mathbf{Fe_5}^{3+}$ 0.2 mM (right) in 10:1 MeCN:H_2O, at scan rate of 10 mV/s.

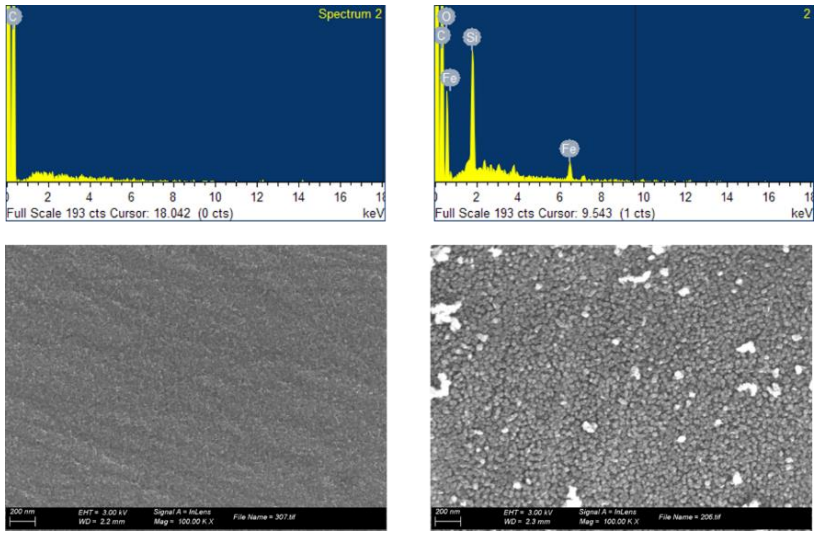

Figure S10. EDX analysis (top) and SEM pictures (bottom) of the GC_{rod} (d= 3 mm) surface after cycling 50 times ($V_i = V_f$ = -1.08; V_C = 1.19 V) in a complex-free 10:1 MeCN:H_2O solution (left) and in a solution of $\mathbf{Fe_5}^{3+}$ 0.2 mM (right) in 10:1 MeCN:H_2O, at scan rate of 10 mV/s.

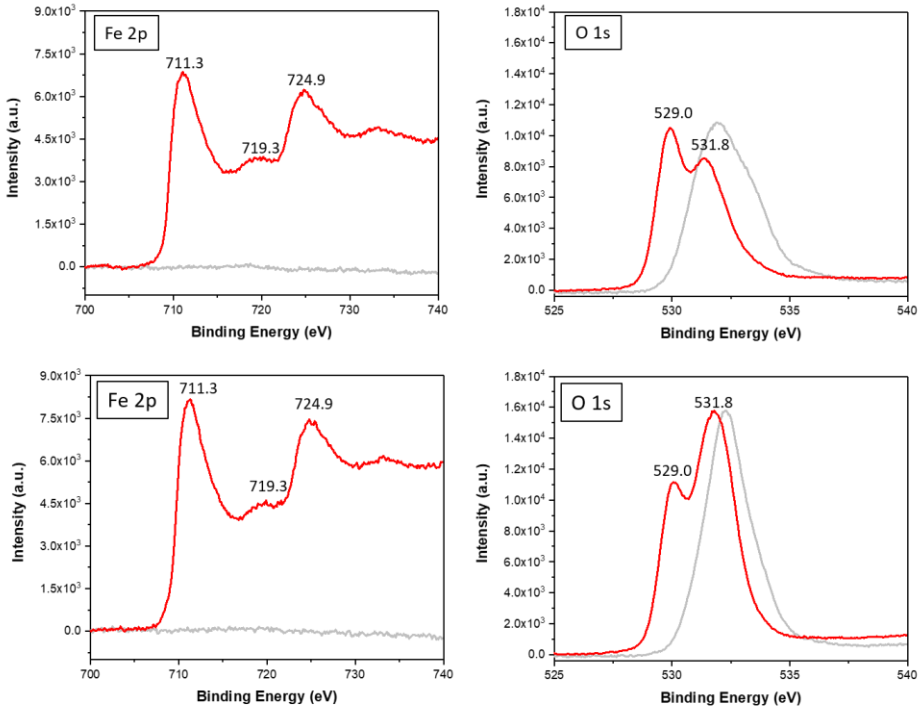

Figure S11. Fe 2p (left) and O 1s (right) XPS spectra of the GC_{rod} (d= 3 mm) surface after cycling in a solution of $\mathbf{Fe_5}^{3+}$ 0.2 mM (red trace) in 10:1 MeCN:H_2O and in a complex-free 10:1 MeCN:H_2O solution (gray trace), at scan rate of 10 mV/s. Top, 100 CV cycles, $V_i = V_f$ = -0.44; V_C = 1.19 V; Bottom, 50 CV cycles, $V_i = V_f$ = -1.08; V_C = 1.19 V. Energies have been calibrated according to the C 1s band of graphite at 284.2 eV.

Table S3. EXAFS Fits parameters

Sample	Fit	Peak	Shell,N	R, Å	E_0	ss.^{2} (10^{-3})	R-factor	Reduced Chi-square
Fe_5^{3+} powder	1	1	Fe-N/O, 5.4	2.03	-7.8	9.2	0.0028	236
	2	I,II	Fe-N/O, 5.4 Fe-C, 8	2.03 2.96	-7.9	9.3 52.2	0.0057	204
	3	all	Fe-N/O,5.4 Fe-C, 8 Fe-C, 21	2.04 2.93 3.09	-5.5	9.1 17.1 7.6	0.0005	27
	4	all	**Fe-N/O, 5.4** **Fe-C, 8** **Fe-C, 21** **Fe-C, 36**	**2.04** **2.98** **3.14** **3.56**	**-6.0**	**9.3** **16.6** **34.2** **10.3**	**0.0082**	**299**
Fe_5^{3+} dissolved in pure CH_3CN	5	1	Fe-N/O, 5.4	2.02	-7.6	11.7	0.0104	223
	6	I,II	Fe-N/O, 5.4 Fe-C, 8	2.02 2.99	-7.1	11.7 50.7	0.0224	187
	7	all	Fe-N/O, 5.4 Fe-C, 8 Fe-C, 21	2.04 2.95 3.12	-4.8	11.2 14.5 6.1	0.0083	117
	8	all	**Fe-N/O, 5.4** **Fe-C, 8** **Fe-C, 21** **Fe-C, 36**	**2.05** **2.98** **3.15** **3.54**	**-4.3**	**11.6** **11.2** **16.4** **13.9**	**0.0132**	**124**
Fe_5^{3+} dissolved in CH_3CN: H_2O (10:1)	9	1	Fe-N/O, 5.4	2.01	-8.7	11.6	0.0091	63
	10	I,II	Fe-N/O, 5.4 Fe-C, 8	2.02 3.03	-7.3	11.7 46.2	0.0196	52
	11	all	Fe-N/O, 5.4 Fe-C, 8 Fe-C, 21	2.03 2.97 3.14	-5.1	11.0 16.1 8.8	0.0089	40
	12	all	**Fe-N/O, 5.4** **Fe-C, 8** **Fe-C, 21** **Fe-C, 36**	**2.03** **2.98** **3.19** **3.50**	**-5.0**	**11.4** **10.3** **16.8** **10.6**	**0.0095**	**29**

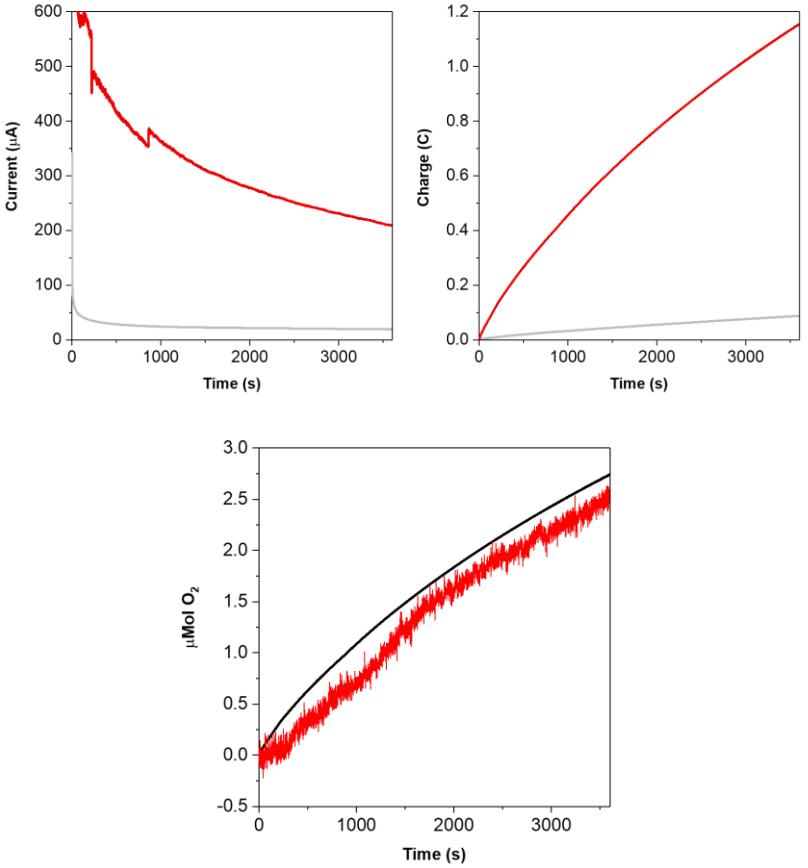

Figure S12. Current (left) and charge (right) profiles generated during the CPE experiment at E_{app} = 1.19 V performed under N_2 atmosphere with **Fe_5^{3+}** 0.2 mM in 6.5 mL 10:1 MeCN:H_2O solution (red trace) and with a complex-free 10:1 MeCN:H_2O solution (gray trace) during 3600 seconds. Charge, 1.05 C (blank subtracted) -> 10.8 μmols of e^-, TN = 2.1 (assuming 100 % of Faradaic efficiency; 1.9 with 90%). Electrodes: GC_{rod} (2 cm immersed in the solution) (WE), Pt mesh (CE), Ag/Ag^+ (RE).

Blank subtracted oxygen evolution (bottom) detected by a Clark electrode for the above CPE up to 3600 s. The ratio between the theoretical oxygen evolved (black line) calculated from the generated charge and the experimental oxygen evolved (red line), gives a Faradaic efficiency of 90 %.

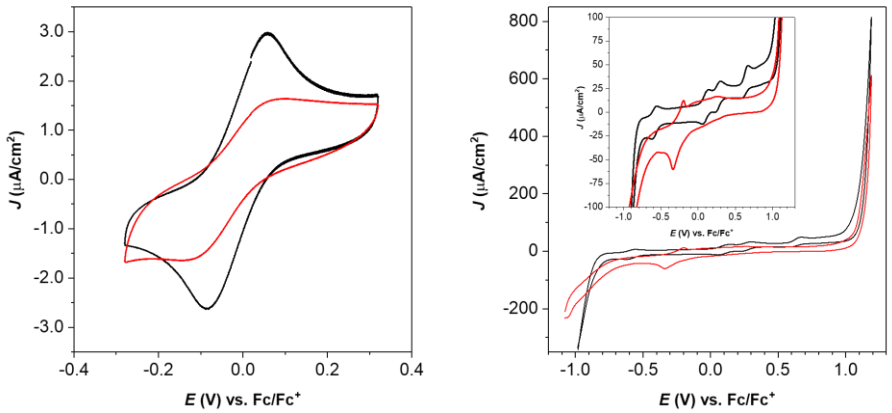

Figure S13. Left, CVs of GC_{rod} used in the previous experiment (CPE in Figure S12) in a 0.2 mM ferrocene solution in 10:1 MeCN:H_2O before (black trace) and after (red trace) the CPE experiment at a scan rate of 10 mV/s. Right, CVs of $\mathbf{Fe_5}^{3+}$ 0.2 mM in a 10:1 MeCN:H_2O solution using a GC disk as WE, before (black trace) and after (red trace) the CPE experiment (Figure S12), at a scan rate of 100 mV/s. Electrodes: GC disk (WE), Pt (CE), Ag/Ag^+ (RE).

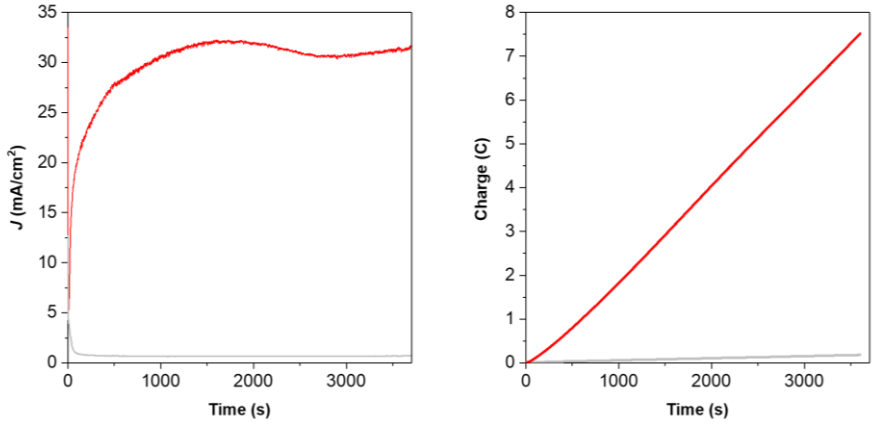

Figure S14. Current (left) and charge (right) profiles generated during the CPE experiment at E_{app} = 1.42 V performed under N_2 atmosphere with $\mathbf{Fe_5}^{3+}$ 0.2 mM in 6.5 mL 10:1 MeCN:H_2O solution (red trace) and with a complex-free 10:1 MeCN:H_2O solution (gray trace) during 3600 s. Charge, 7.5 C -> 77 μmols of e^-,

TON = 14.9 (assuming 100 % of Faradaic efficiency). Electrodes: ITO electrode (S = 2 cm^2) (WE), Pt mesh (CE), Ag/Ag^+ (RE).

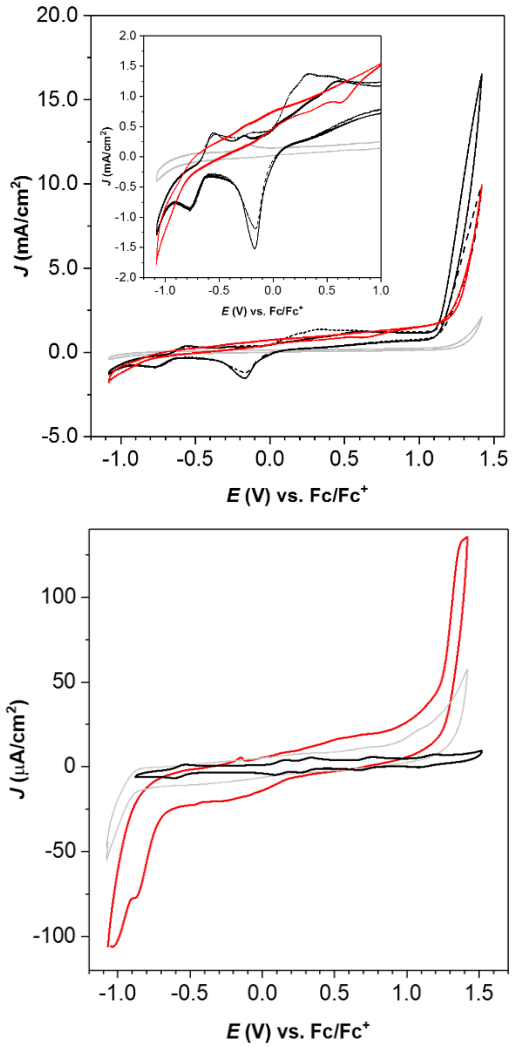

Figure S15. Left, black dashed trace, first CV cycle of $\mathbf{Fe_5}^{3+}$ 0.2 mM dissolved in 10:1 MeCN:H_2O before CPE experiment (Figure S14), at a scan rate of 100 mV/s ($V_i = V_f$ = -1.08 V; V_{C1} = 1.42 V). Black solid trace, second CV cycle. Red trace, CV of the ITO working electrode obtained after the previously mentioned CPE experiment immersed now in a clean electrolyte solution. Gray trace, CV of a bare ITO electrode under the same conditions. ITO electrode (S = 2 cm^2) (WE), Pt mesh (CE), Ag/Ag^+ (RE). Right, red trace, CV of $\mathbf{Fe_5}^{3+}$ 0.2 mM dissolved in 10:1 MeCN:H_2O after CPE experiment (Figure S14), at a scan rate of 100 mV/s ($V_i = V_f$ = -1.08 V; V_{C1} = 1.42 V). Black trace, CV of $\mathbf{Fe_5}^{3+}$ 0.2 mM dissolved in MeCN. Gray

trace, CV of a bare GC electrode under the same conditions. GC (WE), Pt mesh (CE), Ag/Ag^{+} (RE).

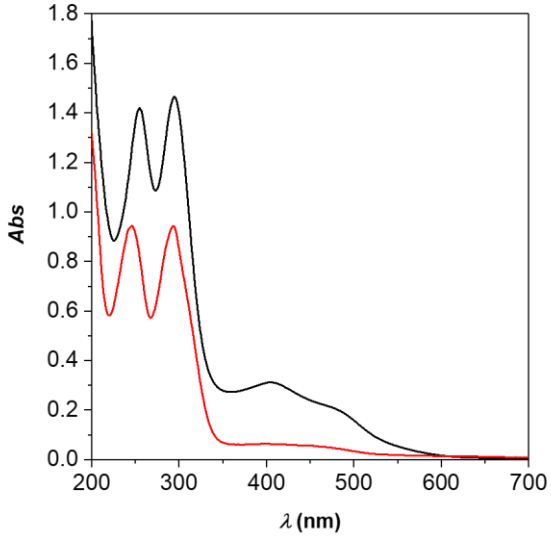

Figure S16. Comparison of UV-Vis absorption spectra of a 0.2 mM solution of $\mathbf{Fe_5}^{3+}$ in 10:1 MeCN:H_2O containing TEAP 0.1 M as supporting electrolyte before (black trace) and after (red trace) the CPE at E_{app}= 1.42 V.

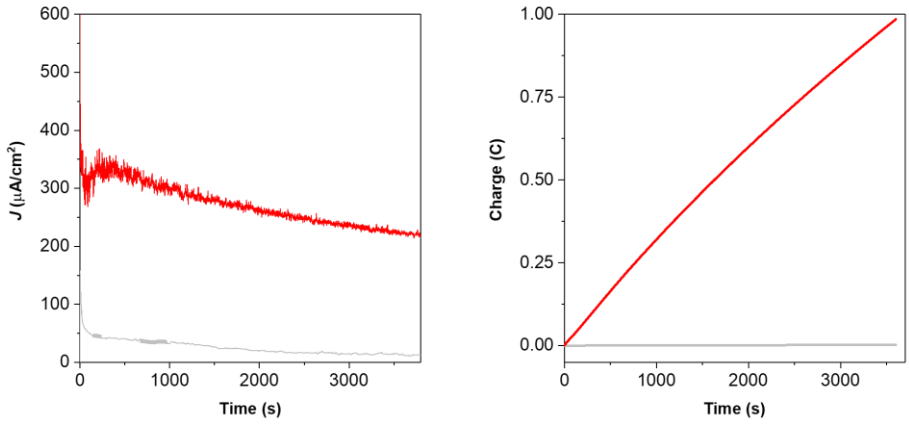

Figure S17. Current (left) and charge (right) profiles generated during the CPE experiment at E_{app}=1.19 V performed under N_2 atmosphere with **Fe$_5$**$^{3+}$ 0.2 mM in 6.5 mL 10:1 MeCN:H_2O solution (red trace) and with a complex-free 10:1 MeCN:H_2O solution (gray trace) during 3600 seconds. Charge, 0.98 C -> 10.2 µmols of e^-, TN = 1.9 (assuming 100 % of Faradaic efficiency). Electrodes: ITO electrode (S = 2 cm^2) (WE), Pt mesh (CE), Ag/Ag$^+$ (RE).

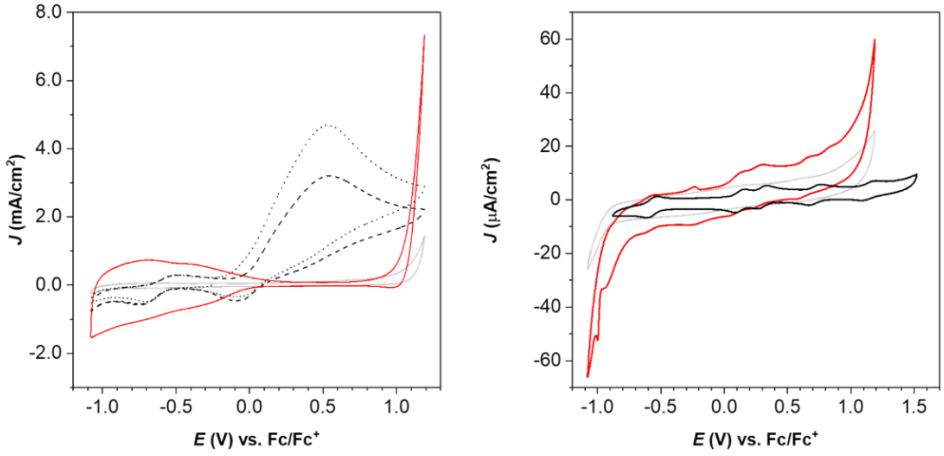

Figure S18. Left, black dotted trace, first CV cycle of **Fe$_5$**$^{3+}$ 0.2 mM dissolved in 10:1 MeCN:H_2O before CPE experiment (Figure S17) using ITO as WE, at a scan rate of 100 mV/s (V_i = V_f = -1.08 V; V_{C1} = 1.19 V). Black dashed trace, second CV cycle. Red trace, CV of the ITO working electrode obtained after CPE in Figures

S17, immersed in a clean electrolyte solution. Gray trace, CV of a bare ITO electrode under the same conditions. ITO electrode (S = 2 cm^2) (WE), Pt mesh (CE), Ag/Ag^+ (RE). Right, red trace, CV of $\mathbf{Fe_5}^{3+}$ 0.2 mM dissolved in 10:1 MeCN:H_2O after CPE experiment (Figure S17) using a GC working electrode, at a scan rate of 100 mV/s ($V_i = V_f$ = -1.08 V; V_{C1} = 1.19 V). Black trace, CV of $\mathbf{Fe_5}^{3+}$ 0.2 mM dissolved in MeCN. Gray trace, CV of a bare GC electrode under the same conditions. GC (WE), Pt mesh (CE), Ag/Ag^+ (RE).

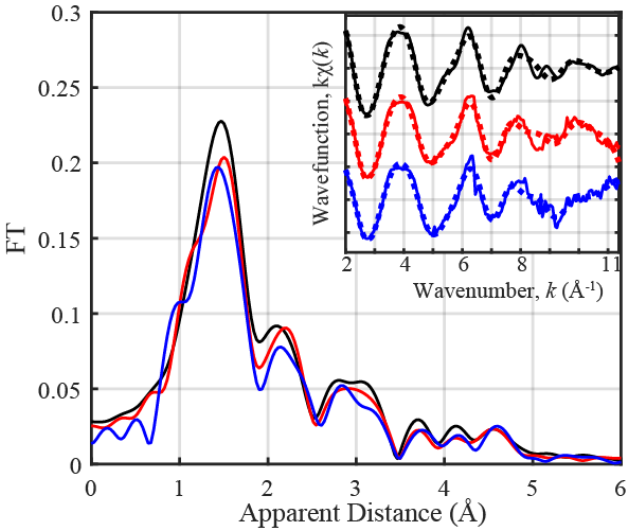

Figure S19. Fe_5^{3+} powder (black), Fe_5^{3+} dissolved in pure CH_3CN (red) and Fe_5^{3+} dissolved in CH_3CN: H_2O (10:1) (blue) together with EXAFS fits (Table S3) shown as an inset.

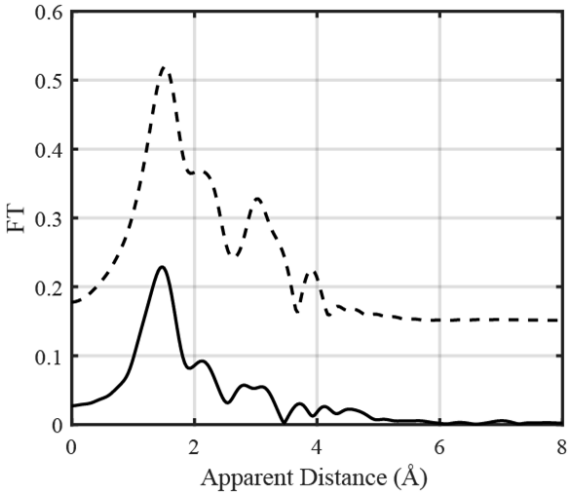

Figure S20. Experimental Fourier transforms of k-weighted Fe EXAFS of Fe_5^{3+} powder (solid black line) and EXAFS spectra simulated with FEFF software (dashed black line). for comparison. Coordinates of all atoms from X-ray structures [5] were used as input.

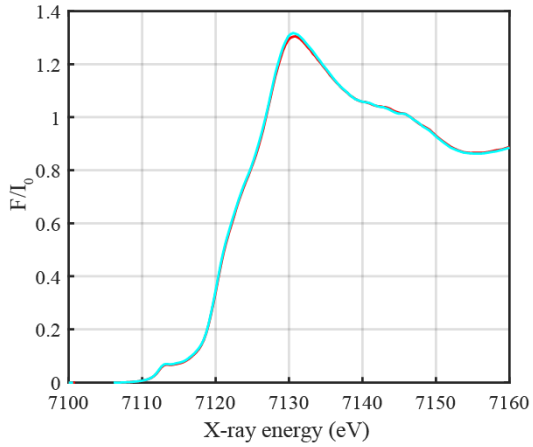

Figure S21. Normalized Fe K-edge. $\mathbf{Fe_5}^{3+}$ dissolved in pure CH_3CN (red) and $\mathbf{Fe_5}^{3+}$ dissolved in CH_3CN: H_2O (10:1) (cyan) frozen solution.

References

(1) Dowling, C.; Dinsdale, D. R.; Lemaire, M. T. **2015**, *774* (March), 769–774.

(2) Okamura, M.; Kondo, M.; Kuga, R.; Kurashige, Y.; Yanai, T.; Hayami, S.; Praneeth, V. K. K.; Yoshida, M.; Yoneda, K.; Kawata, S.; Masaoka, S. *Nature* **2016**, *530* (7591), 465–468.

(3) Addison, V. V. P. A. W.; Pavlishchuk, V. *Inorganica Chim. Acta* **2000**, *298* (1), 97–102.

(4) Simonelli, L.; Marini, C.; Olszewski, W.; Pérez, M. Á.; Ramanan, N.; Guilera, G.; Cuartero, V.; Klementiev, K. On. *Cogent Phys.* **2016**, *3*, 1231987..

(5) Koningsberger, D. C.; Prins, R. *X Ray Absorption: Principles, Applications, Techniques of EXAFS, SEXAFS and XANES*; Sons, J. W. &, Ed.; New York, 1988.

(6) Ravel, B.; Newville, M. *J. Synchrotron Radiat.* **2005**, *12* (4), 537–541.

(7) Rehr, J. J.; Albers, R. C.; Zabinsky, S. I. *Phys. Rev. Lett.* **1992**, *69*, 3397–3400.

(8) Bruker. *Data Collection with APEX II Version V2013.4-1. Bruker*; 2007.

(9) Bruker. *Data Reduction with Bruker SAINT Version V8.30c. Bruker*; 2007.

(10) SADABS: V2012/1 Bruker (2001). Bruker AXS Inc.

(11) Blessing. An Empirical Correction for Absorption Anisotropy. *Acta Cryst.* **1995**, No. A51, 33–38.

(12) SHELXT; V2014/4 (Sheldrick 2014). Sheldrick, G. M. No Title. *Acta Cryst.* **2015**, *A71*, 3–8.

(13) SHELXle; C.B. Huebschle, G. M. S. & B. D. *J. Appl. Cryst.* **2011**, *44*, 1281-1284.

(14) Sheldrick, G. M. *Acta Cryst.* **2015**, No. C71, 3–8.

Chapter 6

General Conclusions

According to the general objectives previously proposed, this chapter gather the final conclusions obtained.

Chapter 3. Redox Metal–Ligand Cooperativity Enables Robust and Efficient Water Oxidation Catalysis at Neutral pH with Macrocyclic Copper Complexes

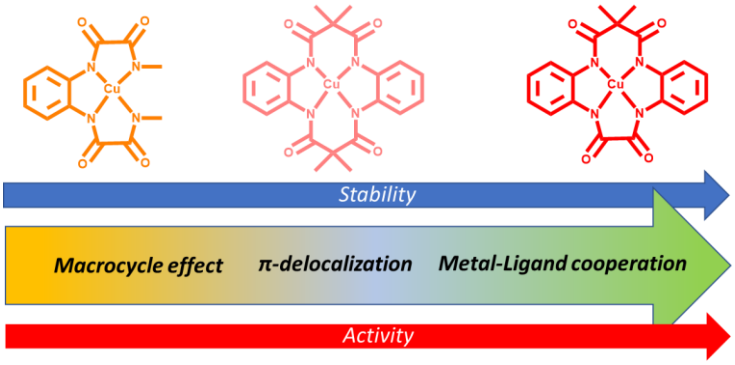

This study highlighted the importance of the ligand design when preparing new molecular WOCs based on first row transition metals.

The influence of the ligand on the activity and stability of three Cu-based WOCs, bringing different tetra-amide macrocycle ligands (TAML) was proven by electrochemical, ^{1}HNMR, EPR , UV-Vis, X-Ray, XAS and DFT analysis.

The 13-membered macrocycle ligand of one complex allowed an optimal overlap between the d orbitals of the metal and the π ones of the ligand, making possible a metal-ligand cooperation in the formation of positive charges, which were easily delocalized thanks to the ligand's extended aromatic system. This complex was proven to work at pH 7 with an overpotential of 200 mV and a k_{obs} of 140 s^{-1}. A second complex, bearing a 14-membered ring macrocycle as ligand, which was giving a lower overlap between the metal and ligand orbitals, did not allow a good charge delocalization and decomposed at the catalytic conditions. The macrocycle effect was proven by comparison with a third acyclic complex, able to work at basic pH, but decomposing at neutral pH at the contrary of the macrocycle.

Chapter 4. Polymeric Cu-base Molecular Anodes: Application in Water Oxidation Catalysis.

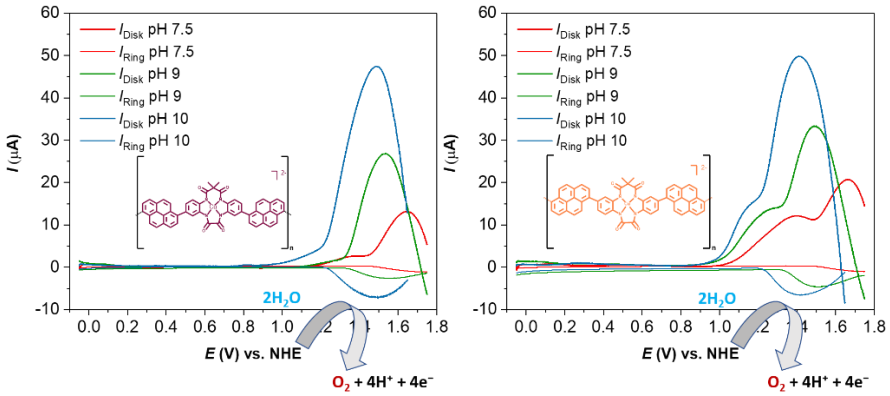

This chapter described the synthesis and the activity toward water oxidation of new polymeric Cu-based WOCs anchored on the surface of electrodes, to form novel molecular anodes.

The modification with pyrenes of the ligand of an already reported rugged molecular Cu-based WOC, gave two regioisomers, which differ for the position (para or meta) of the pyrenes respect to an oxalyl bridge present in the ligand structure.

Exploiting the capacity of the pyrene to electropolymerize, the two complexes were anchored on nano-ITO, giving molecular anodes which were tested through RRDE at pH 7.5, 9 and 10. Water oxidation occurred with similar overpotential and efficiency for both materials, with the best results at pH 10. The stability was thus tested at this pH, indicating a fast degradative pathway, whose nature has still to be investigated. Further experiments will be carried out to better characterize and improve the stability and activity of these new molecular anodes.

Chaper 5. Analysis of the Active Species Responsible for Water Oxidation Using a Pentanuclear Fe Complex

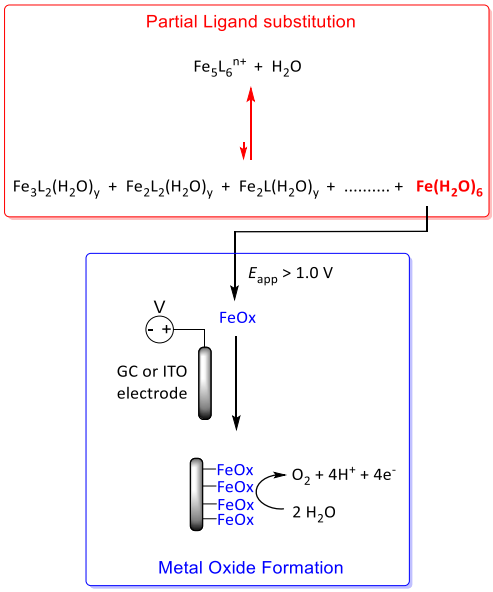

The revisited study on a pentanuclear iron complex claimed as molecular WOC, indicated that the true nature of the catalysis was heterogenous. The anomalous behaviour observed in the electrochemical experiments as the continuous growth of the catalytic wave, the lowering of the non-catalytic process's current and the dirty rinse tests, suggested the deposition of new species on the electrode surface. Deeper analysis of the electrode, through SEM, EDX, XPS and XAS, revealed that the real catalyst was hematite (α-Fe_2O_3).

Annexes

Glossary of terms and abbreviations

bpp- 3,5-bis(2-pyridyl)pyrazolate	3,5-bis(2-pyridyl)pyrazolate
bpy	2,2'-bipyridine
CPE	Controlled Potential Electrolysis
CV	Cyclic Voltammetry
BDD	Boron Doped Diamond
d	doublet
δ	Chemical shift
DCM	Dichloromethane
DFT	Density Functional Theory
dmso	Dimethyl sulfoxide
DPV	Differential Pulse Voltammetry
E	Potential
ECSA	Electrochemically Active Surface Area
ε	Extintion Coefficient
$E_{1/2}$	Half wave potential
EDX	Energy Dispersive X-Ray Spectroscopy
ESI-MS	Electrospray Ionization Mass Spectrometry
EXAFS	Extended X-Ray Absorption Fine Structure
FE	Faradaic Efficiency
FOWA	Foot of the Wave Analysis
GC	Glassy Carbon
H2bda	[2,2'-bipyridine]-6,6'-dicarboxylic acid
HER	Hydrogen Evolution Reaction
HEC	Hydrogen Evolution Catalyst
hν	Light
J	Coupling constant
λ	Wavelenght
M	Molar
I	Ionic force
I2M	Bimolecular Interaction Mechanism
i	Current
j	Current density
m/z	Mass-to-Charge ratio

MLCT	Metal to Ligand Charge Transfer
MS	Mass Spectrometry
η	Overpotential
NHE	Normal Hydrogen Electrode
NMR	Nuclear Magnetic Resonance
NOESY	Nuclear Overhauser Spectroscopy
NPs	Nanoparticles
OEC	Oxygen Evolving Center
PCET	Proton Coupled Electron Transfer
PEC	Photoelectrochemical cell
PEM	Proton Exchange Membrane
Ph	Phenyl
ppm	Parts per million
PSI	Photosystem I
PSII	Photosystem II
PT	Proton Transfer
PV	Photovoltaic
py	Pyridine
RDV	Rotating Disk Voltammetr
RF	Roughness Facto
RT	Room Temperature
S	Surface of the Electrode
s	Singlet
SCE	Saturated Calomel Electrode
SEM	Scanning Electron Microscopy
t	Triplet
$TEAPF_6$	Tetraethylammonium hexafluorophosphate
$TBAPF_6$	Tetra(N-butyl)ammonium hexafluorophosphate
TEM	Transmission Electron Microscopy
TEA	Trimethylamine
TOF	Turnover Frequency
TON	Turnover Number
trpy	2,2’:6’,2’’-terpyridine
UV-vis	Ultraviolet-visible Spectroscopy
v	Scan rate
vs.	versus
WNA	Water Nucleophilic attack
WO	Water Oxidation
WOC	Water Oxidation Catalyst
XANES	X-ray Absorption Near Edge Structure

XAS	X-Ray Absorption Spectroscopy
XPS	X-Ray Photoelectron Spectroscopy

UNIVERSITAT ROVIRA I VIRGILI
Water Oxidation Catalysis Using First Row Transition Metals
PRIMAVERA PELOSIN

UNIVERSITAT
ROVIRA i VIRGILI